Title
Ion Correlations and Transport in Li-Ion Battery Electrolytes

Author
Fong, Kara Danielle

Publication Date
2022

Peer reviewed|Thesis/dissertation

Ion Correlations and Transport in Li-Ion Battery Electrolytes

by

Kara Danielle Fong

A dissertation submitted in partial satisfaction of the

requirements for the degree of

Doctor of Philosophy

in

Chemical Engineering

in the

Graduate Division

of the

University of California, Berkeley

Committee in charge:

Professor Kristin A. Persson, Co-chair
Professor Bryan D. McCloskey, Co-chair
Professor Kranthi K. Mandadapu
Professor Mark Asta

Spring 2022

Ion Correlations and Transport in Li-Ion Battery Electrolytes

Abstract

Ion Correlations and Transport in Li-Ion Battery Electrolytes

by

Kara Danielle Fong

Doctor of Philosophy in Chemical Engineering

University of California, Berkeley

Professor Kristin A. Persson, Co-chair

Professor Bryan D. McCloskey, Co-chair

Li-ion batteries are among the leading technologies for electric vehicles and grid-scale renewable electricity storage, making them a crucial element in building a sustainable energy future. The performance of current Li-ion batteries is limited in large part by the properties of the electrolyte, which is responsible for transporting ions through the battery. Sluggish motion of Li-ions through the electrolyte restricts the rate at which the battery can be charged or discharged and lowers the energy efficiency of the system. Design of improved electrolyte formulations is hindered by our inability to connect our theoretical understanding of electrolyte transport across length scales, that is, to relate the macroscopic transport behavior probed experimentally to the molecular-level mechanisms governing ion motion. The most commonly used theories to describe continuum-level electrolyte transport, namely the Stefan-Maxwell equations, yield transport coefficients which lack clear physical interpretation at the atomistic level and cannot be easily computed from molecular simulations. This presents significant challenges in deciphering the mechanisms of ion motion from experimental measurements and understanding the physical phenomena that may be limiting battery performance.

Herein, we present the theoretical development and application of the Onsager transport framework to analyze transport at both the continuum and molecular levels. We discuss the integration of continuum mechanics, nonequilibrium thermodynamics, and electromagnetism to derive the governing equations of irreversible thermodynamics in electrolytes, including balance laws and internal entropy production. These relations yield the Onsager transport equations: linear laws relating the electrochemical potential gradients and fluxes of each species in solution. At the atomistic level, the transport coefficients emerging from this theory directly quantify ion correlations in the electrolyte; we show how these transport coefficients may be computed directly from molecular simulations using Green-Kubo rela-

tions derived from Onsager's regression hypothesis. At the continuum level, the Onsager transport framework provides the governing equations for solving macroscopic boundary value problems in an electrochemical cell. We demonstrate how the theory presented here may be directly related to existing frameworks for continuum-level modeling such as the Stefan-Maxwell equations and the Nernst-Planck equation for transport at infinite dilution. We further relate the Onsager transport coefficients to experimentally-measurable quantities such as the conductivity, transference number, and salt diffusion coefficient.

We demonstrate application of the Onsager transport framework by investigating the transport properties of potential next-generation battery electrolytes. In conventional batteries, the energy and power densities are limited by electrolytes with low Li-ion transference numbers (t_+), in which the majority of the electrolyte conductivity comes from motion of the anion, rather than the electrochemically-active Li-ion. Nonaqueous polyelectrolyte solutions, in which anion motion is slowed through covalent attachment to a polymer, have been recently suggested as high transference number alternatives to conventional Li-ion battery electrolytes. Initial experimental evidence on these nonaqueous polyelectrolyte solutions has been promising, with transference numbers reported to be at least twice that of conventional battery electrolytes. These experimental transference number measurements, however, are typically based on ideal solution approximations, i.e., the assumption that there no correlations between ions. Prior to this work, we lacked insight into the extent to which these assumptions hold for polyelectrolytes as well as the true transference number of these solutions. The non-idealities (ion correlations) contributing to the true transference number are very challenging to quantify experimentally yet are easily accessible through molecular dynamics simulations via the theoretical framework presented herein. Using this framework, we demonstrate that ion correlations are substantial in polyelectrolytes such that the rigorously computed transference number is actually lower than that of a conventional electrolyte. These efforts have thus suggested that — contrary to intuition — nonaqueous polyelectrolytes may not be promising for next-generation batteries, and they more broadly call into question some of the conventional paradigms employed for understanding and characterizing transport in polyelectrolytes. In this work, we first present detailed characterization of a specific polyelectrolyte which had been presented in the literature as particularly promising based on experimental ideal solution approximations. We subsequently construct a more general simulation model, which is agnostic to any specific polymer chemistry, and show that these surprising results hold universally across a broad range of polyelectrolytes. Finally, we present perspectives on how analyzing ion correlations in this manner has the potential to yield valuable insights across a wide class of electrolytes for energy storage applications.

Contents

List of Figures

Acknowledgments

I have had the honor of working with an incredible group of research mentors who have made my time at Berkeley so meaningful and formative. My advisors, Prof. Kristin Persson and Prof. Bryan McCloskey, gave me the freedom and independence to explore my interests but were always ready to provide guidance when I needed it. Kristin has always impressed me with the compassion with which she leads her group. She has taught me that a good advisor supports not only her students' intellectual growth, but also their mental and emotional well-being. Bryan has been a tremendous advocate for me over the years, and I greatly admire the genuine care and intentionality he puts into mentoring his students. He has been the calm voice of reason throughout the most stressful periods of graduate school and the faculty interview process.

Beyond my official advisors, one of the highlights of my PhD was working closely with Prof. Kranthi Mandadapu. Kranthi pushed me intellectually in ways that nobody had before and deeply changed my scientific philosophy. All of our long work sessions discussing (arguing) about electrolyte transport helped me build the confidence to defend my scientific ideas and were greatly impactful in influencing the work I want to do post-PhD.

I would also like to thank all of the members of the Persson Group and McCloskey Lab. Much of my doctoral work was done in collaboration with Julian Self, who has taught me a lot over the years about the battery field and computational chemistry. I have also thoroughly enjoyed interacting with my experimentalist counterparts on the polyelectrolyte project, Helen Bergstrom and Kyle Diederichsen, who have helped make sure my simulations always have some connection to experimental reality. I'd additionally like to acknowledge my undergraduate mentees, Lexi and Rachael, for helping me develop my skills and experience as a mentor.

My doctoral work would not have been possible without the support of all my friends. I am so grateful for the community in my research groups and in the CBE department as a whole, which have made grad school an enjoyable experience even when research progress was slow. I would like to specifically thank Nat, Helen, Ahmad, Oxana, Handong, Lori, Sarah, and Lance.

I am also incredibly grateful for my family, who patiently supported me through both the highs and lows of my PhD experience. They gave me the foundation I needed in graduate school by instilling in me an excitement for learning and the work ethic necessary to succeed. Finally, I give my deepest thanks to my fiancé Casey Wojcik for his constant love and support. I could not imagine a better partner for the grad school journey.

Chapter 1

Introduction[1]

1.1 Li-ion battery electrolytes

Lithium ion batteries (LIBs) are ubiquitous in applications ranging from electric vehicles to electric grids and consumer electronics. The increasing importance of this technology in society necessitates the development of batteries which charge faster, store more energy, and persist over longer lifetimes. Achieving these goals and developing next-generation battery technologies will likely require substantial advances in all components of the battery, from the cathode and anode chemistries to the cell design and manufacturing procedures. In this work, we focus on the electrolyte, which constitutes a major bottleneck in the performance of current battery technologies.

The electrolyte of a battery determines the rate at which ions can move across the cell and is thus a key determinant of the attainable charging and discharging rate of the battery. An ideal LIB electrolyte will have high ionic conductivity (κ), which allows for facile transport of ions through solution and minimizes ohmic resistance in the cell. Beyond the conductivity, the performance of a battery is additionally impacted by the cation transference number of the electrolyte (t_+), defined as the fraction of of the total conductivity attributed to motion of the cation, as opposed to the anion [2]. In a LIB, where the cation is the electroactive species, it is desirable to have a high value of t_+ (close to one). When t_+ is below unity, migration of the mobile anionic species results in the formation of concentration gradients, which generate additional overpotential in the cell. During battery discharging these concentration gradients deplete the population of ions in the porous cathode material, such that at sufficiently high discharging rates the concentration of Li^+ at the electrode surface may reach zero and cause the cell to fail. During the charging process, concentration gradients facilitate lithium plating at the anode [3], which can lead to degradation of the battery's performance or short-circuit of the device. Collectively, these phenomena associated with low t_+ severely limit the attainable

[1]Portions of this chapter are adapted from Ref. [1]: Fong, K. D., Bergstrom, H. K., McCloskey, B. D. & Mandadapu, K. K. Transport phenomena in electrolyte solutions: Non-equilibrium thermodynamics and statistical mechanics. *AIChE Journal* e17091 (2020).

energy density and rate capability of the battery.

The impact of low cation transference number on battery performance has been quantified by continuum-level simulations: Doyle, Fuller, and Newman [4] have modeled cells with a polymer-based electrolyte and lithium metal electrodes and found that increasing the cation transference number from 0.2 to 1 resulted in substantial improvements in cell performance, even when the conductivity was decreased by an order of magnitude. These improvements were particularly pronounced at high discharge rates. Diederichsen et al. [3] have extended these simulations to study cells with porous graphite and $LiCoO_2$ electrodes, finding that even modest increases in t_+ improve the attainable state of charge of the battery. Unfortunately, increasing the cation transference number typically decreases the total ionic conductivity. This challenging tradeoff between κ and t_+, as well as other transport parameters which impact battery performance, will be explored in more detail herein.

State-of-the-art LIB electrolytes have been optimized to balance the aforementioned transport properties with a diverse set of additional factors such as cost, safety, and stability [5]. These conventional formulations consist of a lithium salt, a mixture of carbonate-based solvents, and a collection of stabilizing additives [6]. The lithium salt is chosen such that it readily dissociates in solution and is stable against (electro)chemical decomposition; lithium hexafluorophosphate ($LiPF_6$) is the standard choice. The solvent mixture typically includes ethylene carbonate (EC), which contributes to the formation of a stable solid electrolyte interphase and possesses a high dielectric constant, and a linear carbonate such as dimethyl carbonate, diethyl carbonate, or ethyl methyl carbonate. While these linear carbonates have a very low dielectric constant, they possess a much lower viscosity than EC, which facilitates more rapid ion transport through the electrolyte. These solvents are not generally electrochemically stable under the operating voltages of a battery, and their degradation can limit the long-term stability of the cell. To address this challenge, it is common practice to add a small quantity of sacrificial additives, such as vinylene carbonate and fluoroethylene carbonate, which react at the electrode to form a stable interface [7, 8]. These standard electrolyte formulations have sufficiently high ionic conductivity (typically on the order of 10 S/cm), but they suffer from low cation transference numbers near 0.4 [9].

Notably, while the field has witnessed rapid development of new chemistries for other battery components such as the cathode in the past two decades, the central components of the industry-standard electrolyte have remained largely unchanged [10]. Work in recent years, however, has given rise to new frontiers in electrolyte research aimed towards producing systems with favorable properties ranging from facile Li-ion transport to non-flammability, mechanical robustness, and improved electrochemical stability [5]. These include polymer or gel-based electrolytes [11, 12], inorganic solid electrolytes such as ceramics and glasses [13, 14], and superconcentrated or solvent-in-salt systems [15, 16]. The development of these research-stage electrolytes, many of which possess unconventional transport mechanisms, has drawn our attention to the complexities of ion transport in electrochemical systems and the glaring gaps in our fundamental understanding of these processes. Realizing optimized electrolyte formulations for improved LIB performance is contingent on developing a deeper understanding and more rigorous formulation of the transport phenomena governing the

motion of charged species in solution.

1.2 Theories for electrolyte transport

Given that electrolyte solutions play a crucial role in a wide range of systems — from energy technologies such as batteries and fuel cells to biological, geological, and medical systems — extensive effort has been devoted to improving our theoretical understanding of electrolyte transport. However, despite nearly a century of progress since the pioneering work of Debye, Hückel, and Onsager [17–19], analytical models for predicting electrolyte transport properties remain elusive, particularly at non-dilute concentrations. The complexities induced by long-range electrostatic forces as well as short-range, specific chemical interactions create both conceptual as well as mathematical difficulties in working towards an all-encompassing theory for describing transport phenomena in electrolyte solutions.

The most ubiquitous framework for understanding transport of ions in concentrated electrolytes is the Stefan-Maxwell equations for multicomponent diffusion [2, 20, 21], originally derived from the kinetic theory of gases [22]. These equations relate the gradient in electrochemical potential $\overline{\mu}_i$ of a species i to the velocities $\boldsymbol{v}_j$ of each of the species j in solution:

$$c_i \boldsymbol{\nabla} \overline{\mu}_i = \sum_{j \neq i} K^{ij} (\boldsymbol{v}_j - \boldsymbol{v}_i) \ , \tag{1.1}$$

where c_i is the concentration of species i and K^{ij} are the Stefan-Maxwell transport coefficients. These equations may be interpreted as a force balance: the thermodynamic force acting on species i (the left side of the equation) is balanced by the frictional forces between species i and each of the other species in solution. It is assumed that this frictional force is proportional to the difference in velocities of the two species. The Stefan-Maxwell transport coefficients may also be expressed in terms of binary interaction diffusion coefficients D^{ij} as

$$K^{ij} = \frac{RT c_i c_j}{c_{\mathrm{T}} D^{ij}} \ , \tag{1.2}$$

where R is the ideal gas constant, T is temperature, and c_{T} is the total concentration of the system.[2]

Alternatively, transport in electrolyte solutions can be analyzed based on the classical theories of thermodynamics of irreversible processes developed by Onsager [23, 24], Prigogine [25] and de Groot and Mazur [26]. This framework uses the rate of internal entropy production (dissipation) to relate thermodynamic driving forces and corresponding fluxes with a matrix of transport coefficients:

$$\boldsymbol{J}_i = \sum_j \boldsymbol{L}^{ij} \boldsymbol{X}_j \ , \tag{1.3}$$

[2]Throughout this text, the same symbol c_i will be used to denote concentration as both number per volume and mole per volume. It is implied that concentration is in units of mole per volume when appearing with the quantity RT, and in units of number per volume when appearing with $k_{\mathrm{B}}T$ where k_{B} is the Boltzmann constant.

where $\boldsymbol{J}_i$ is the flux of species i, $\boldsymbol{X}_j$ is the thermodynamic driving force acting on species j, and $\boldsymbol{L}^{ij}$ are the Onsager transport coefficients. The forms of $\boldsymbol{J}_i$ and $\boldsymbol{X}_j$ will be derived herein.

Although both frameworks are consistent with thermodynamics and have been shown to effectively model electrolyte transport, the less common Onsager transport framework possesses several advantages over the Stefan-Maxwell equations. Unlike the Stefan-Maxwell transport coefficients K^{ij} (or D^{ij}), the Onsager transport coefficients L^{ij} can be computed directly from molecular simulations using Green-Kubo relations [27, 28] (which will be derived herein for multicomponent electrolyte solutions). This allows facile computation of all transport properties even in complex solutions which are challenging to characterize experimentally, such as those with multiple salt species. The Green-Kubo relations also allow direct physical interpretation of L^{ij} as the extent of correlation between the motion of species i and j. The Stefan-Maxwell coefficients, D^{ij}, however, have a less intuitive meaning and can even diverge to positive or negative infinity under certain conditions [29], making interpretation of transport phenomena challenging. Furthermore, the Onsager transport coefficients can be used directly to solve boundary value problems and obtain concentration profiles in an electrochemical system, while the Stefan-Maxwell transport matrix $\boldsymbol{K}$ must be inverted in order to be used in this manner.

Based on these advantages, we argue that the Onsager transport equations could become a simple and useful framework to study electrolyte transport, as is already the case in other fields such as in the study of membrane permeability [30, 31]. Rigorous formulation of the Onsager transport equations for electrolytes, however, requires integration of the principles of continuum mechanics, electromagnetism, and non-equilibrium thermodynamics. We are unaware of any work which has developed the underlying irreversible thermodynamics in their entirety rather than addressing special limiting cases. The classic texts of de Groot and Mazur [26]; Prigogine [25]; and Hirschfelder, Curtiss, and Bird [22] each formulate balance laws and the corresponding forces/fluxes in fluid mixtures but do not consider the impact of external electromagnetic fields. Katchalsky and Curran [32] and Kjelstrup and Bedeaux [33] both present a theory for irreversible processes which accounts for electrostatic work but do not include momentum conservation, yielding an incomplete picture of entropy production in electrolytes. The classic text of Newman and Thomas-Alyea [2] and related works [34, 35] introduce Stefan-Maxwell and Onsager-like transport equations for electrolytes, albeit without discussion of the momentum, energy, and entropy balances of continuous media upon which these equations are built. Kovetz [36] formulates rigorous balance laws in the presence of electromagnetic fields but does not consider multicomponent systems. None of the aforementioned existing works address problems which require coupling of electromagnetic effects, momentum transport, and multicomponent diffusion.

1.3 Central contributions of this work

The primary aims of this dissertation are twofold: (i) we work to develop a more complete theory of electrolyte transport, denoted the Onsager transport framework, and (ii) we apply this transport framework to the study of polyelectrolyte solutions, which have been recently proposed as candidates for next-generation Li-ion battery electrolytes. The key contributions in each of these areas are summarized below.

Theoretical development of the Onsager transport framework

By integrating the classical frameworks of continuum mechanics and linear irreversible thermodynamics with the theory of electromagnetism, we have formulated continuum-level governing equations for mass, momentum, and energy transport as well as entropy production in electrolyte solutions. These equations allow us to capture the coupling of simultaneous gradients in temperature, concentration, pressure, and electric potential, which allows for rigorous prediction of macroscopic transport behavior under experimentally-relevant conditions without many of the simplifying assumptions inherent to previous theories. We furthermore derive Green-Kubo relations to directly compute the transport parameters emerging from these equations from molecular simulations. These equations relate the nonequilibrium transport behavior of an electrolyte with flux-flux correlations at equilibrium, thereby providing a quantitative mapping between macroscopic transport and molecular-scale ion motion. This mapping provides a powerful lens for intuitively interpreting transport and gives physical insight into the types of atomistic processes governing macroscopic ion transport. The Onsager transport equations may further be combined to yield experimentally-measurable transport quantities such as the conductivity and transference number. By establishing these connections, this work bridges a crucial gap between theory, simulation, and experiment in the field of electrolyte transport.

Elucidating the nature of ion transport in polyelectrolyte solutions for Li-ion batteries

Application of the Onsager transport framework has demonstrated critical flaws in the standard methods for experimentally characterizing transport in polyelectrolyte solutions, and it has challenged the intuitive understanding of anionic polyelectrolytes as having high cation transference number. Over the past several years, nonaqueous polyelectrolytes have been presented as promising high transference number alternatives to conventional LIB electrolytes: it is thought that appending the anions of the electrolyte to the backbone of a polymer chain will slow their motion relative to the cation, thereby increasing the cation transference number. Experimental characterization of the transference number via the Nernst-Einstein (ideal solution) approximation corroborates this intuition, yielding transference numbers approaching unity. By using molecular dynamics simulations to access the Onsager transport coefficients, we have computed the rigorous transference number (accounting for solution

non-idealities) for a range of polyelectrolyte solutions. We have established that the Nernst-Einstein assumption as used in existing experimental works does not yield a physically meaningful approximation for polyelectrolyte transport due the substantial anion-anion and cation-anion correlations in these systems, and that t_+ is generally lower in a polyelectrolyte than in a conventional LIB electrolyte formulation. These results have therefore dispelled the notion that polyelectrolytes may yield promising transport behavior for next-generation batteries.

These computational results have directly inspired new experiments: my colleagues at Berkeley are currently testing the theoretical predictions of this dissertation by designing new model polyelectrolyte systems and developing methods to more accurately measure the transference number in polyelectrolytes. Preliminary data shows strong support for the conclusions presented herein.

1.4 Dissertation outline

This dissertation is organized as follows. Chapters 2 and 3 are devoted to the theoretical development of the Onsager transport framework. In Chapter 2, we use Maxwell's equations and balance laws of mass, momentum, energy, and entropy to derive continuum-level governing equations for transport in electrolyte solutions. We then simplify these balance laws using linear constitutive relations and introduce the diffusive transport coefficients L^{ij} relating electrochemical potential gradients and diffusive fluxes within the system. In Chapter 3, we build upon the results of Chapter 2 to derive Green-Kubo relations for L^{ij}, which allow us to compute these transport coefficients from molecular simulations. Next, in Chapter 4 we provide contextualization for our derived transport framework by providing physical interpretation for the Onsager transport coefficients and relating our expressions to other commonly used frameworks for analyzing electrolyte transport, including the Stefan-Maxwell equations and the Nernst-Planck equation for infinitely dilute solutions. We furthermore demonstrate the application of the Onsager transport framework to a model electrolyte (lithium chloride in dimethyl sulfoxide). Chapters 5 and 6 are dedicated to applying the Onsager transport framework to polyelectrolyte solutions: Chapter 5 uses all-atom molecular dynamics simulations to gain detailed insight into the structure and dynamics of an experimentally-realized nonaqueous polyelectrolyte solution, while Chapter 6 employs coarse-grained molecular dynamics simulations to draw more general conclusions as to transport in oligomeric polyions and polymerized ionic liquids. Finally, in Chapter 7 we summarize the primary contributions of this dissertation and present potential avenues for future work, in which we anticipate applying the Onsager transport framework may be used to answer extant questions in electrolyte transport. Additional thermodynamic derivations are presented in Appendix A, and methods are presented in Appendix B.

Chapter 2

Continuum Mechanics and Linear Irreversible Thermodynamics of Electrolyte Solutions[1]

In this chapter, we derive the governing equations of irreversible thermodynamics in electrolyte solutions. The theories here are built upon on the work of Onsager [23, 24], Prigogine [25], de Groot and Mazur [26], Katchalsky and Curran [32], and Kovetz [36]. These classical works are extended to simultaneously describe the phenomena of electromagnetism (Maxwell's equations) and transport of mass, linear and angular momentum, and energy. The resulting balance laws are generally applicable for electrolytes with an arbitrary number of components, without assuming electroneutrality. We then invoke the second law of thermodynamics to analyze entropy production, enabling the formulation of linear laws relating the thermodynamic forces and fluxes within the electrolyte.

2.1 Balance laws

Mass balance

The mass balance for electrolyte solutions is identical to that of mixtures of uncharged species. Consider a volume $\mathcal{P}$ with a local density $\rho(\boldsymbol{x}, t)$ at any position $\boldsymbol{x}$ and time t, defined as the mass per unit volume. Let $\rho_i(\boldsymbol{x}, t)$ be the mass of species i per unit volume, such that $\rho \coloneqq \sum_i \rho_i$. The linear momentum density of species i is given by $\rho_i \boldsymbol{v}_i$, where $\boldsymbol{v}_i$ is the velocity of species i. Let us define the total momentum density at any point in $\mathcal{P}$ as $\rho \boldsymbol{v} \coloneqq \sum_i \rho_i \boldsymbol{v}_i$. The quantity $\boldsymbol{v} = \sum_i \frac{\rho_i}{\rho} \boldsymbol{v}_i$ is the mass-averaged velocity of all species. Utilizing these definitions, the rate of change in total mass of species i in $\mathcal{P}$ is equivalent to

[1] This chapter is closely adapted from portions of Ref [1]: Fong, K. D., Bergstrom, H. K., McCloskey, B. D. & Mandadapu, K. K. Transport phenomena in electrolyte solutions: Non-equilibrium thermodynamics and statistical mechanics. *AIChE Journal* e17091 (2020).

the flux of i in and out of the surface area of $\mathcal{P}$, denoted as $\partial\mathcal{P}$. This yields the global form of the balance of mass:

$$\frac{d}{dt}\int_{\mathcal{P}} \rho_i dv = -\int_{\partial\mathcal{P}} \rho_i(\boldsymbol{v}_i - \boldsymbol{v})\cdot\boldsymbol{n} da \ , \tag{2.1}$$

where $\boldsymbol{n}$ is the outward normal of surface $\partial\mathcal{P}$. Based on Eq. (2.1), let the diffusive flux of species i be defined as $\boldsymbol{j}_i \coloneqq \rho_i(\boldsymbol{v}_i - \boldsymbol{v})$, such that

$$\frac{d}{dt}\int_{\mathcal{P}} \rho_i dv = -\int_{\partial\mathcal{P}} \boldsymbol{j}_i\cdot\boldsymbol{n} da \ . \tag{2.2}$$

Note that $\sum_i \boldsymbol{j}_i = 0$. Applying the Reynolds transport theorem and the divergence theorem, we obtain

$$\int_{\mathcal{P}} (\dot{\rho}_i + \rho_i \boldsymbol{\nabla}\cdot\boldsymbol{v}) dv = -\int_{\mathcal{P}} \boldsymbol{\nabla}\cdot\boldsymbol{j}_i dv \ , \tag{2.3}$$

where the notation $\dot{(\ )}$ refers to the substantial or material derivative, $\dot{(\ )} = \frac{d}{dt}(\ ) = \frac{\partial}{\partial t}(\ ) + \boldsymbol{\nabla}(\ )\cdot\boldsymbol{v}$. Further simplification using the localization theorem gives the local form of the species mass balance as

$$\dot{\rho}_i + \rho_i \boldsymbol{\nabla}\cdot\boldsymbol{v} = -\boldsymbol{\nabla}\cdot\boldsymbol{j}_i \ . \tag{2.4}$$

Alternatively, Eq. (2.4) can be expressed in terms of the concentration of species i, $c_i \coloneqq \rho_i/M_i$ where M_i is the molecular weight of species i, as

$$\dot{c}_i + c_i \boldsymbol{\nabla}\cdot\boldsymbol{v} = -\boldsymbol{\nabla}\cdot(c_i(\boldsymbol{v}_i - \boldsymbol{v})) = -\boldsymbol{\nabla}\cdot\boldsymbol{J}_i \ , \tag{2.5}$$

where $\boldsymbol{J}_i \coloneqq c_i(\boldsymbol{v}_i - \boldsymbol{v})$. Note that $\boldsymbol{J}_i$ and $\boldsymbol{j}_i$ are simply related by a factor of M_i, i.e., $M_i\boldsymbol{J}_i = \boldsymbol{j}_i$.

The species mass balance can be used to obtain the total mass balance of the electrolyte. Summing Eq. (2.4) over all species and invoking the relation $\sum_i \boldsymbol{j}_i = 0$, we obtain

$$\dot{\rho} + \rho\boldsymbol{\nabla}\cdot\boldsymbol{v} = 0 \ . \tag{2.6}$$

For incompressible systems, i.e., constant density, the mass balance leads to

$$\boldsymbol{\nabla}\cdot\boldsymbol{v} = 0 \ . \tag{2.7}$$

Charge balance and Maxwell's equations

We now review the fundamentals of electromagnetism, generally following the philosophy of Kovetz [36]. While most electrolyte applications will involve electroneutral systems, linear dielectrics, and no magnetic effects, in this and the following sections we consider the most general case of both electric and magnetic fields in a non-electroneutral dielectric with arbitrary polarization and magnetization. This general theory enables us to treat more complex

electrolyte systems and allows a deeper understanding of the underlying assumptions invoked when we do consider more conventional systems.

Much of electromagnetism is based on the key assumption that electric charge is conserved, i.e., the charge contained in a volume $\mathcal{P}$ changes only via flux of charges through the surface of the volume, $\partial\mathcal{P}$. The charge conservation law can be expresed mathematically as

$$\int_{\mathcal{P}} \frac{\partial q}{\partial t} dv = -\int_{\partial\mathcal{P}} \tilde{\boldsymbol{j}} \cdot \boldsymbol{n} da \ , \tag{2.8}$$

where q is the total charge density and $\tilde{\boldsymbol{j}} \cdot \boldsymbol{n} da$ is the total amount of charge passing through the area element da in the direction of $\boldsymbol{n}$ per unit time. The quantity $\tilde{\boldsymbol{j}}$ is called the current density. Alternatively, this charge balance can be written in terms of the substantial derivative of q as

$$\frac{d}{dt}\int_{\mathcal{P}} q dv = -\int_{\mathcal{P}} \boldsymbol{\nabla} \cdot (\tilde{\boldsymbol{j}} - q\boldsymbol{v}) dv = -\int_{\mathcal{P}} \boldsymbol{\nabla} \cdot \boldsymbol{\mathcal{J}} dv \tag{2.9}$$

where $\boldsymbol{\mathcal{J}} \coloneqq \tilde{\boldsymbol{j}} - q\boldsymbol{v}$ is the conduction current density. The corresponding local form of the charge balance law is

$$\dot{q} + q\boldsymbol{\nabla} \cdot \boldsymbol{v} = -\boldsymbol{\nabla} \cdot \boldsymbol{\mathcal{J}} \ . \tag{2.10}$$

The principle of charge conservation and its invariance to coordinate transformations in four-dimensional space-time motivates the first pair of Maxwell's equations,

$$q = \boldsymbol{\nabla} \cdot \boldsymbol{D} \ , \tag{2.11}$$

and

$$\tilde{\boldsymbol{j}} = \boldsymbol{\nabla} \times \boldsymbol{H} - \frac{\partial \boldsymbol{D}}{\partial t} \ , \tag{2.12}$$

where $\boldsymbol{D}$ and $\boldsymbol{H}$ are the charge and current potentials, respectively [36].

The second pair of Maxwell's equations are formulated by assuming the existence of two vector fields, the electric field $\boldsymbol{E}$ and magnetic field $\boldsymbol{B}$, which obey the relations

$$\boldsymbol{\nabla} \cdot \boldsymbol{B} = 0 \tag{2.13}$$

and

$$\frac{\partial \boldsymbol{B}}{\partial t} = -\boldsymbol{\nabla} \times \boldsymbol{E} \ . \tag{2.14}$$

As the electromagnetic field is conservative, $\boldsymbol{E}$ and $\boldsymbol{B}$ can be written in terms of electric and magnetic potentials denoted as ϕ and $\boldsymbol{A}$, respectively, as

$$\begin{aligned} \boldsymbol{B} &= \boldsymbol{\nabla} \times \boldsymbol{A} \ , \\ \boldsymbol{E} &= -\frac{\partial \boldsymbol{A}}{\partial t} - \boldsymbol{\nabla}\phi \ . \end{aligned} \tag{2.15}$$

For a system with no magnetic field, as is often the case in physically relevant electrolyte applications, we may simply write $\boldsymbol{E} = -\boldsymbol{\nabla}\phi$.

The two pairs of Maxwell's equations are related by the aether constitutive relations [36],

$$\boldsymbol{D} = \epsilon_0 \boldsymbol{E} \ , \tag{2.16}$$

where ϵ_0 is the vacuum permittivity, and

$$\boldsymbol{B} = \mu_0 \boldsymbol{H} \ , \tag{2.17}$$

where μ_0 is the permeability.

The quantities $\tilde{\boldsymbol{j}}$, $\boldsymbol{E}$, and $\boldsymbol{H}$ depend on the choice of reference frame. In merging the theory of electromagnetism with continuum mechanics, it is convenient to re-cast Maxwell's equations in terms of quantities that are invariant under Galilean transformations (note that the charge, charge potential, magnetic field, and conduction current density are Galilean invariants). For a material with velocity $\boldsymbol{v}$, we can define the Galilean invariants $\boldsymbol{\mathcal{E}}$, called the electromotive intensity, and $\boldsymbol{\mathcal{H}}$, the magnetomotive intensity, as

$$\boldsymbol{\mathcal{E}} = \boldsymbol{E} + \boldsymbol{v} \times \boldsymbol{B} \tag{2.18}$$

and

$$\boldsymbol{\mathcal{H}} = \boldsymbol{H} - \boldsymbol{v} \times \boldsymbol{D} \ . \tag{2.19}$$

In terms of these Galilean invariants, Eq. (2.12) and Eq. (2.14) become

$$\boldsymbol{\mathcal{J}} = \boldsymbol{\nabla} \times \boldsymbol{\mathcal{H}} - \overset{*}{\boldsymbol{D}} \tag{2.20}$$

and

$$\overset{*}{\boldsymbol{B}} = -\boldsymbol{\nabla} \times \boldsymbol{\mathcal{E}} \tag{2.21}$$

respectively, where we use the notation $\overset{*}{\boldsymbol{A}}$ to denote the flux derivative [36], i.e. $\overset{*}{\boldsymbol{A}} = \frac{\partial \boldsymbol{A}}{\partial t} + (\boldsymbol{\nabla} \cdot \boldsymbol{A})\boldsymbol{v} - \boldsymbol{\nabla} \times (\boldsymbol{v} \times \boldsymbol{A})$.

All of the electromagnetism equations introduced thus far provide a microscopic picture of the system by accounting for the charge of each individual particle comprising the body. However, when considering charges in a dielectric medium rather than in vacuum, it is typically more convenient to decompose the total charge density of the system q into the free charge density (q^{f}) and bound charge density (q^{b}). This decomposition yields

$$q = q^{\mathrm{f}} + q^{\mathrm{b}} \tag{2.22}$$

and correspondingly

$$\tilde{\boldsymbol{j}} = \tilde{\boldsymbol{j}}^{\mathrm{f}} + \tilde{\boldsymbol{j}}^{\mathrm{b}} \ . \tag{2.23}$$

Equation (2.23) leads naturally to the quantities $\boldsymbol{\mathcal{J}}^{\mathrm{b}} = \tilde{\boldsymbol{j}}^{\mathrm{b}} - q^{\mathrm{b}}\boldsymbol{v}$ and $\boldsymbol{\mathcal{J}}^{\mathrm{f}} = \tilde{\boldsymbol{j}}^{\mathrm{f}} - q^{\mathrm{f}}\boldsymbol{v}$. In an electrolyte, free charges correspond to mobile ions in solution, while bound charges are

those of the solvent molecules comprising the dielectric medium, which result in polarization $\boldsymbol{P}$ and magnetization $\boldsymbol{M}$. The quantities $\boldsymbol{P}$ and $\boldsymbol{M}$ are related to the bound charge and current density by

$$q^{\mathrm{b}} = -\boldsymbol{\nabla} \cdot \boldsymbol{P} \tag{2.24}$$

and

$$\tilde{\boldsymbol{j}}^{\mathrm{b}} = \boldsymbol{\nabla} \times \boldsymbol{M} + \frac{\partial \boldsymbol{P}}{\partial t} \ . \tag{2.25}$$

Defining the Lorentz magnetization (a Galilean invariant) as $\boldsymbol{\mathcal{M}} = \boldsymbol{M} + \boldsymbol{v} \times \boldsymbol{P}$, we can also write

$$\boldsymbol{\mathcal{J}}^{\mathrm{b}} = \boldsymbol{\nabla} \times \boldsymbol{\mathcal{M}} + \overset{*}{\boldsymbol{P}} \ . \tag{2.26}$$

From the distinction between free and bound charge we can write the first pair of Maxwell's equations (Eq. (2.11) and (2.12)) in matter as

$$q^{\mathrm{f}} = \boldsymbol{\nabla} \cdot \boldsymbol{D}^{\mathrm{f}} \ , \tag{2.27}$$

and

$$\tilde{\boldsymbol{j}}^{\mathrm{f}} = \boldsymbol{\nabla} \times \boldsymbol{H}^{\mathrm{f}} - \frac{\partial \boldsymbol{D}^{\mathrm{f}}}{\partial t} \ , \tag{2.28}$$

where

$$\boldsymbol{D}^{\mathrm{f}} = \boldsymbol{D} + \boldsymbol{P} \tag{2.29}$$

and

$$\boldsymbol{H}^{\mathrm{f}} = \boldsymbol{H} - \boldsymbol{M} \ . \tag{2.30}$$

In terms of Galilean invariants, Eq. (2.28) is

$$\boldsymbol{\mathcal{J}}^{\mathrm{f}} = \boldsymbol{\nabla} \times \boldsymbol{\mathcal{H}}^{\mathrm{f}} - \overset{*}{\boldsymbol{D}}^{\mathrm{f}} \ , \tag{2.31}$$

where

$$\boldsymbol{\mathcal{H}}^{\mathrm{f}} = \boldsymbol{\mathcal{H}} - \boldsymbol{\mathcal{M}} \ . \tag{2.32}$$

In the following sections, we derive the balances of linear momentum, angular momentum and energy of a body in the presence of an electromagnetic field. The most rigorous approach for doing so is based on knowing the conserved quantities of the electromagentic field. To this end, it is known that solutions to Maxwell's equations Eqs. (2.11)-(2.14) with the aether constitutive relations Eqs. (2.16) and (2.17) in vacuum can also be expressed as stationary points of an action functional in space-time corresponding to a Maxwell Lagrangian $\mathcal{L}$ [37–39]. The existence of such a Lagrangian and its invariance under translations in space-time and Lorentz transformations allows us to apply Noether's theorem to identify the conserved quantities of the electromagnetic field, namely the linear momentum $\epsilon_0 \boldsymbol{E} \times \boldsymbol{B}$, angular momentum $\epsilon_0 \boldsymbol{x} \times (\boldsymbol{E} \times \boldsymbol{B})$, and energy $\frac{1}{2}\left(\epsilon_0 E^2 + \frac{1}{\mu_0} B^2\right)$ [39]. Given these expressions, one may express the total linear and angular momentum, and energy per unit volume of a body in the presence of an electromagnetic field to be $\rho \boldsymbol{g} = \rho \boldsymbol{v} + \epsilon_0 \boldsymbol{E} \times \boldsymbol{B}$, $\boldsymbol{x} \times \rho \boldsymbol{g}$, and $\rho \bar{e} =$

$\rho e + \frac{1}{2}\left(\epsilon_0 E^2 + \frac{1}{\mu_0} B^2\right)$, respectively, where e is the energy per unit mass of the body (including kinetic and interatomic potential energies) but without the energy of the electromagnetic field. Ideally, one would formulate the balance laws based on the time changes of these compound quantities, which is the approach followed by Kovetz [36]. However, in light of familiarity of the principles of momentum and energy transport in chemical engineering and continuum mechanics, in what follows, we proceed to derive the local forms of balance laws starting from a physically intuitive perspective by capturing the effects of the electromagentic field through the Lorentz force, and then end with the forms of momentum and energy balances in terms of the compound fields.

Linear momentum balance

In this section, we derive equations for the balance of linear momentum in an electrolyte. As mentioned before, we begin with a physically intuitive derivation in which the influence of the electromagnetic field is captured through the Lorentz force. This is the form conventionally presented in electromagnetism texts [40, 41] and provides a valid description of momentum transport within a body. We will argue, however, that this approach is less convenient when describing the boundary conditions of a system and may lead to incorrect interpretations of surface forces at a material boundary. We will end with an alternate form of the momentum balance which is more generally applicable. The formulation of these two forms of the linear momentum balance as well as the corresponding forms of the angular momentum balance largely follows the approach of Steigmann [42], who has reinterpreted Kovetz's work from a continuum mechanics perspective.

The global balance of momentum says that changes in total momentum in a body $\mathcal{P}$ must be balanced by the sum of all forces acting on the body:

$$\frac{d}{dt}\int_{\mathcal{P}} \rho \boldsymbol{v} dv = \int_{\mathcal{P}} \sum_i \rho_i \boldsymbol{b}_i dv + \int_{\partial\mathcal{P}} \boldsymbol{t} da + \boldsymbol{F} \ , \tag{2.33}$$

where $\boldsymbol{b}_i$ denotes non-electromagnetic body forces (such as gravity) acting on species i and $\boldsymbol{t}$ is a surface force density. By Cauchy's lemma and tetrahedron argument, $\boldsymbol{t}$ may be rewritten in terms of the stress tensor $\boldsymbol{T}$ as $\boldsymbol{t} = \boldsymbol{T}\boldsymbol{n}$ [36, 42], where, recall, $\boldsymbol{n}$ is the outward normal vector. The quantity $\boldsymbol{F}$ is the Lorentz force exerted on the body from the electromagnetic field:

$$\boldsymbol{F} = \int_{\mathcal{P}} (q\boldsymbol{E} + \tilde{\boldsymbol{j}} \times \boldsymbol{B}) dv \ . \tag{2.34}$$

Recall that in writing the Lorentz force in terms of the total charge and current density, we are capturing effects of the electromagnetic field on both the free ions in solution as well as the solvent medium.

The Lorentz force can be rewritten in terms of Galilean invariants, $\boldsymbol{\mathcal{E}}$ and $\boldsymbol{\mathcal{J}}$, using Eq. (2.18) and $\boldsymbol{\mathcal{J}} = \tilde{\boldsymbol{j}} - q\boldsymbol{v}$:

$$\boldsymbol{F} = \int_{\mathcal{P}} (q\boldsymbol{E} + \tilde{\boldsymbol{j}} \times \boldsymbol{B}) dv = \int_{\mathcal{P}} (q\boldsymbol{\mathcal{E}} + \boldsymbol{\mathcal{J}} \times \boldsymbol{B}) dv \ . \tag{2.35}$$

The local form of Eq. (2.33) is then given by

$$\rho\dot{\boldsymbol{v}} = \boldsymbol{\nabla}\cdot\boldsymbol{T} + \sum_i \rho_i \boldsymbol{b}_i + q\boldsymbol{\mathcal{E}} + \boldsymbol{\mathcal{J}}\times\boldsymbol{B}\ . \tag{2.36}$$

In a dielectric medium, Eq. (2.36) is more useful if written in terms of free (rather than total) charges. After some manipulation using Eqs. (2.22) through (2.32), it can be shown that Eq. (2.36) can alternatively be expressed as

$$\begin{aligned}\rho\dot{\boldsymbol{v}} = \boldsymbol{\nabla}\cdot[\boldsymbol{T} - \boldsymbol{\mathcal{E}}\otimes\boldsymbol{P} - (\boldsymbol{\mathcal{M}}\cdot\boldsymbol{B})\boldsymbol{I} + \boldsymbol{\mathcal{M}}\otimes\boldsymbol{B}] + \sum_i \rho_i\boldsymbol{b}_i \\ + q^{\mathrm{f}}\boldsymbol{\mathcal{E}} + \boldsymbol{\mathcal{J}}^{\mathrm{f}}\times\boldsymbol{B} + \boldsymbol{P}\cdot\boldsymbol{\nabla}\boldsymbol{\mathcal{E}} + \boldsymbol{\mathcal{M}}\cdot\boldsymbol{\nabla}\boldsymbol{B} + \boldsymbol{\mathcal{M}}\times(\boldsymbol{\nabla}\times\boldsymbol{B}) + \overset{*}{\boldsymbol{P}}\times\boldsymbol{B}\ ,\end{aligned} \tag{2.37}$$

where $\boldsymbol{I}$ is the identity tensor. In most physically-relevant scenarios, q^{f} and $\tilde{\boldsymbol{j}}^{\mathrm{f}}$ are typically zero due to the condition of electroneutrality, a consequence of the substantial energy requirements for separating charges by a macroscopic distance. As can be seen from Eq. (2.37), however, even under this condition the electric field still alters the momentum of the system via the polarization and magnetization of the dielectric medium. In some situations, electroneutrality may be violated, namely within the electric double layers at charged interfaces. The violation of electroneutrality may also be important for nanoconfined systems where the size of the double layer is comparable to the length scale of the fluid region [43, 44]. In what follows, we aim to maintain generality and carry out the majority of derivations without assuming electroneutrality whenever possible.

It is important to note that the the Lorentz force $\boldsymbol{F}$ need not vanish at a material boundary. Thus, the surface force $\boldsymbol{t}$ in Eq. (2.33) and corresponding stress tensor $\boldsymbol{T}$ do not describe the overall traction on the surface of a body. In order to quantify the overall surface forces and formulate boundary conditions, it is necessary to rewrite the Lorentz force in terms of the divergence of some quantity $\boldsymbol{T}_{\mathrm{M}}$ (called the Maxwell stress tensor) representing the surface stress induced by the electromagnetic field. In the remainder of this section, we use Maxwell's equations to derive the form of $\boldsymbol{T}_{\mathrm{M}}$ and rewrite the linear momentum balance in a form more amenable to boundary condition analysis. Let us begin by revisiting the quantity $q\boldsymbol{E} + \tilde{\boldsymbol{j}}\times\boldsymbol{B}$. We can rewrite this quantity using Eqs. (2.11), (2.12), (2.16), and (2.17) as

$$q\boldsymbol{E} + \tilde{\boldsymbol{j}}\times\boldsymbol{B} = \epsilon_0(\boldsymbol{\nabla}\cdot\boldsymbol{E})\boldsymbol{E} + \frac{1}{\mu_0}(\boldsymbol{\nabla}\times\boldsymbol{B})\times\boldsymbol{B} - \epsilon_0\frac{\partial\boldsymbol{E}}{\partial t}\times\boldsymbol{B}\ . \tag{2.38}$$

The last term on the right side of Eq. (2.38) can be rewritten as

$$\begin{aligned}\epsilon_0\frac{\partial\boldsymbol{E}}{\partial t}\times\boldsymbol{B} &= \epsilon_0\frac{\partial}{\partial t}(\boldsymbol{E}\times\boldsymbol{B}) - \epsilon_0\boldsymbol{E}\times\frac{\partial\boldsymbol{B}}{\partial t} \\ &= \epsilon_0\frac{\partial}{\partial t}(\boldsymbol{E}\times\boldsymbol{B}) + \epsilon_0\boldsymbol{E}\times(\boldsymbol{\nabla}\times\boldsymbol{E})\ .\end{aligned} \tag{2.39}$$

In the last equality we have used Eq. (2.14). Substituting Eq. (2.39) into Eq. (2.38) yields

$$\begin{aligned} q\boldsymbol{E} + \tilde{\boldsymbol{j}} \times \boldsymbol{B} = \epsilon_0 \Big[(\boldsymbol{\nabla} \cdot \boldsymbol{E})\boldsymbol{E} - \boldsymbol{E} \times (\boldsymbol{\nabla} \times \boldsymbol{E}) \Big] \\ + \frac{1}{\mu_0} \Big[(\boldsymbol{\nabla} \cdot \boldsymbol{B})\boldsymbol{B} - \boldsymbol{B} \times (\boldsymbol{\nabla} \times \boldsymbol{B}) \Big] - \epsilon_0 \frac{\partial}{\partial t} (\boldsymbol{E} \times \boldsymbol{B}) \ . \end{aligned} \tag{2.40}$$

Note that the term $(\boldsymbol{\nabla} \cdot \boldsymbol{B})\boldsymbol{B}$ is equal to zero by Eq. (2.13) and is only added such that the electric and magnetic field terms appear symmetrically in the equation. We can further simplify Eq. (2.40) by using the vector identity $\boldsymbol{A} \times (\boldsymbol{\nabla} \times \boldsymbol{A}) = \frac{1}{2}\boldsymbol{\nabla} A^2 - \boldsymbol{A} \cdot \boldsymbol{\nabla}\boldsymbol{A}$, which yields

$$\begin{aligned} q\boldsymbol{E} + \tilde{\boldsymbol{j}} \times \boldsymbol{B} = \epsilon_0 \Big[(\boldsymbol{\nabla} \cdot \boldsymbol{E})\boldsymbol{E} + \boldsymbol{E} \cdot (\boldsymbol{\nabla}\boldsymbol{E}) \Big] + \frac{1}{\mu_0} \Big[(\boldsymbol{\nabla} \cdot \boldsymbol{B})\boldsymbol{B} + \boldsymbol{B} \cdot (\boldsymbol{\nabla}\boldsymbol{B}) \Big] \\ - \frac{1}{2}\boldsymbol{\nabla} \Big[\epsilon_0 E^2 + \frac{1}{\mu_0} B^2 \Big] - \epsilon_0 \frac{\partial}{\partial t} (\boldsymbol{E} \times \boldsymbol{B}) \ . \end{aligned} \tag{2.41}$$

We may now define the Maxwell stress tensor $\boldsymbol{T}_{\mathrm{M}}$ as

$$\boldsymbol{T}_{\mathrm{M}} = \left[\epsilon_0 \boldsymbol{E} \otimes \boldsymbol{E} + \frac{1}{\mu_0} \boldsymbol{B} \otimes \boldsymbol{B} \right] - \frac{1}{2} \left[\epsilon_0 E^2 + \frac{1}{\mu_0} B^2 \right] \boldsymbol{I} \tag{2.42}$$

and express Eq. (2.41) as

$$\frac{\partial}{\partial t} (\epsilon_0 \boldsymbol{E} \times \boldsymbol{B}) - \boldsymbol{\nabla} \cdot \boldsymbol{T}_{\mathrm{M}} + q\boldsymbol{E} + \tilde{\boldsymbol{j}} \times \boldsymbol{B} = 0 \ . \tag{2.43}$$

Eq. (2.43) is the local statement of conservation of momentum for the electromagnetic field itself, and the quantity $\epsilon_0 \boldsymbol{E} \times \boldsymbol{B}$ is the momentum density of an electromagnetic field [40]. The overall Lorentz force thus becomes

$$\boldsymbol{F} = \int_{\mathcal{P}} (\boldsymbol{\nabla} \cdot \boldsymbol{T}_{\mathrm{M}}) dv - \int_{\mathcal{P}} \frac{\partial}{\partial t} (\epsilon_0 \boldsymbol{E} \times \boldsymbol{B}) dv \ . \tag{2.44}$$

For the case of time-independent fields, Eq. (2.44) shows how the Lorentz force may be equivalently interpreted in terms of surface forces or traction. Using the definition of the substantial derivative and the Reynolds transport theorem, Eq. (2.44) can be rewritten as

$$\boldsymbol{F} = \int_{\mathcal{P}} (\boldsymbol{\nabla} \cdot \boldsymbol{T}_{\mathrm{M}}) dv - \frac{d}{dt} \int_{\mathcal{P}} \big(\epsilon_0 \boldsymbol{E} \times \boldsymbol{B} \big) dv + \int_{\mathcal{P}} \boldsymbol{\nabla} \cdot \big(\epsilon_0 (\boldsymbol{E} \times \boldsymbol{B}) \otimes \boldsymbol{v} \big) dv \ . \tag{2.45}$$

Defining a new quantity,

$$\hat{\boldsymbol{T}} = \boldsymbol{T}_{\mathrm{M}} + \epsilon_0 (\boldsymbol{E} \times \boldsymbol{B}) \otimes \boldsymbol{v} \ , \tag{2.46}$$

the Lorentz Force can be rewritten as

$$\boldsymbol{F} = \int_{\mathcal{P}} (\boldsymbol{\nabla} \cdot \hat{\boldsymbol{T}}) dv - \frac{d}{dt} \int_{\mathcal{P}} \big(\epsilon_0 \boldsymbol{E} \times \boldsymbol{B} \big) dv \ . \tag{2.47}$$

In Eq. (2.47) we have decomposed the Lorentz force into two contributions. The first is from surface stresses induced by the electromagnetic field, and the second represents the electromagnetic contributions to the total momentum. Given Eq. (2.47), we can now reformulate the global form of the momentum balance in Eq. (2.33) as

$$\frac{d}{dt}\int_{\mathcal{P}} \rho(\boldsymbol{v} + \epsilon_0 \boldsymbol{E}\times\boldsymbol{B}/\rho)dv = \int_{\mathcal{P}} \sum_i \rho_i \boldsymbol{b}_i dv + \int_{\mathcal{P}} \boldsymbol{\nabla}\cdot(\boldsymbol{T}+\hat{\boldsymbol{T}})dv \ . \tag{2.48}$$

Finally, defining the composite stress tensor $\bar{\boldsymbol{T}} = \boldsymbol{T} + \hat{\boldsymbol{T}}$ and a modified momentum density $\boldsymbol{g} = \boldsymbol{v} + \epsilon_0 \boldsymbol{E}\times\boldsymbol{B}/\rho$, Eq. (2.48) reduces to

$$\frac{d}{dt}\int_{\mathcal{P}} \rho \boldsymbol{g} dv = \int_{\mathcal{P}} \sum_i \rho_i \boldsymbol{b}_i dv + \int_{\mathcal{P}} (\boldsymbol{\nabla}\cdot\bar{\boldsymbol{T}})dv, \tag{2.49}$$

with the local form of the balance

$$\rho\dot{\boldsymbol{g}} = \boldsymbol{\nabla}\cdot\bar{\boldsymbol{T}} + \sum_i \rho_i \boldsymbol{b}_i \ . \tag{2.50}$$

The quantity $\boldsymbol{g}$, as mentioned before, is a more general representation of the momentum per unit mass in a body subject to electromagnetic fields, as it captures the momentum of the electrolyte body as well as that of the electromagnetic field itself [36]. Thus, we can interpret our original momentum balance (Eq. (2.36)) as accounting for changes in momentum of only the body $\mathcal{P}$ (considering the electromagnetic field only as an external force), while in Eq. (2.50) we account for momentum changes in both the body $\mathcal{P}$ and the electromagnetic field together. Either form is valid within the bulk of the body, but only Eq. (2.50) provides a transparent description of behavior at a material boundary, where the overall surface force per unit area or traction is given by $\bar{\boldsymbol{t}} = \bar{\boldsymbol{T}}\boldsymbol{n}$ (and not $\boldsymbol{T}\boldsymbol{n}$, as may be incorrectly concluded from Eq. (2.36)).

The forms of the linear momentum balances derived in this section are generally applicable to any body subject to an electromagnetic field. In Sec. 2.2, we will assume linear constitutive relations and derive the forms of the momentum balance that are applicable to most liquid electrolyte solutions.

Angular momentum balance

We now present the balance of angular momentum in two forms. The first is based on the linear momentum balance of the form Eq. (2.36), which considers the momentum of the body to be $\rho\boldsymbol{v}$. The second treats the momentum of both the body and the electromagnetic field, captured in the quantity $\boldsymbol{g}$, as in Eq. (2.50). We will analyze the implications that these angular momentum balances have on the symmetry of the stress tensor in each of these forms.

Based on Eq. (2.36), the angular momentum balance can be written as

$$\frac{d}{dt}\int_{\mathcal{P}}(\boldsymbol{x}\times\rho\boldsymbol{v})dv=\int_{\partial\mathcal{P}}(\boldsymbol{x}\times\boldsymbol{T}\boldsymbol{n})da+\int_{\mathcal{P}}\boldsymbol{x}\times\left(\sum_i\rho_i\boldsymbol{b}_i+q\boldsymbol{E}+\tilde{\boldsymbol{j}}\times\boldsymbol{B}\right)dv\ . \tag{2.51}$$

Incorporating the Reynolds transport theorem and overall mass balance (Eq. (2.6)) to simplify the left side of Eq. (2.51) gives

$$\int_{\mathcal{P}}\rho\boldsymbol{x}\times\dot{\boldsymbol{v}}dv=\int_{\partial\mathcal{P}}(\boldsymbol{x}\times\boldsymbol{T}\boldsymbol{n})da+\int_{\mathcal{P}}\boldsymbol{x}\times\left(\sum_i\rho_i\boldsymbol{b}_i+q\boldsymbol{E}+\tilde{\boldsymbol{j}}\times\boldsymbol{B}\right)dv\ . \tag{2.52}$$

Comparing with Eq. (2.36), we may eliminate the second term on the right side and write

$$\int_{\mathcal{P}}\boldsymbol{x}\times(\boldsymbol{\nabla}\cdot\boldsymbol{T})dv=\int_{\partial\mathcal{P}}(\boldsymbol{x}\times\boldsymbol{T}\boldsymbol{n})da\ . \tag{2.53}$$

Rearranging and applying the localization theorem yields

$$\varepsilon_{ijk}T_{kj}=0\ , \tag{2.54}$$

where ε_{ijk} is the Levi-Civita symbol. This leads to the familiar result that the stress tensor is symmetric,

$$\boldsymbol{T}=\boldsymbol{T}^T\ . \tag{2.55}$$

Now let us write the overall angular momentum balance based on Eq. (2.50):

$$\frac{d}{dt}\int_{\mathcal{P}}(\boldsymbol{x}\times\rho\boldsymbol{g})dv=\int_{\partial\mathcal{P}}(\boldsymbol{x}\times\bar{\boldsymbol{T}}\boldsymbol{n})da+\int_{\mathcal{P}}\boldsymbol{x}\times\left(\sum_i\rho_i\boldsymbol{b}_i\right)dv\ . \tag{2.56}$$

Analogous simplifications allow us to conclude that

$$\int_{\mathcal{P}}(\boldsymbol{v}\times\rho\boldsymbol{g}+\boldsymbol{x}\times(\boldsymbol{\nabla}\cdot\bar{\boldsymbol{T}}))dv=\int_{\partial\mathcal{P}}(\boldsymbol{x}\times\bar{\boldsymbol{T}}\boldsymbol{n})da\ , \tag{2.57}$$

or

$$\varepsilon_{ijk}(\bar{T}_{kj}+\rho v_k g_j)=0\ . \tag{2.58}$$

Thus, the overall stress tensor $\bar{\boldsymbol{T}}$ which is relevant in the boundary conditions of the body is only symmetric in the case where $v_k g_j = v_j g_k$. This will in general only be true if their is no electric or magnetic field. However, we can show that the result in Eq. (2.58) is equivalent to Eq. (2.55) by incorporating the anti-symmetric portions of $\bar{\boldsymbol{T}}$ and $\rho\boldsymbol{v}\otimes\boldsymbol{g}$ into Eq. (2.58):

$$\varepsilon_{ijk}(\bar{T}_{kj}+\rho v_k g_j)=\varepsilon_{ijk}(T_{kj}+\epsilon_0\varepsilon_{klm}E_lB_mv_j+\epsilon_0\varepsilon_{jlm}E_lB_mv_k)=0\ . \tag{2.59}$$

The last two terms on the right side cancel, leading once again to Eqs. (2.54) and (2.55).

Energy balance

We now develop expressions for conservation of energy in electrolyte systems. As with the momentum balances, we develop two forms of this balance law: one which considers the energy of only the electrolyte body and one which includes the energy of both the body and the electromagnetic field.

The first of these forms of the global energy balance can be formulated by balancing the total change in energy with all of the sources of heat and work on the system. This yields

$$\frac{d}{dt}\int_{\mathcal{P}}\rho e dv = \int_{\mathcal{P}}\rho r dv - \int_{\partial\mathcal{P}}\boldsymbol{J}_{\mathrm{q}}\cdot\boldsymbol{n}da + \int_{\partial\mathcal{P}}\boldsymbol{t}\cdot\boldsymbol{v}da + \int_{\mathcal{P}}\sum_i \rho_i\boldsymbol{b}_i\cdot\boldsymbol{v}_i dv + \int_{\mathcal{P}}\mathbb{P}^{\mathrm{EM}}dv\ , \quad (2.60)$$

where e is total energy per unit mass, r is energy per mass produced through body heating, and $\boldsymbol{J}_{\mathrm{q}}$ is the heat flux vector. Again we emphasize that e is the energy of the body $\mathcal{P}$, which is affected by the electromagnetic field, but it does not include the energy of the electromagnetic field itself. The quantities $\boldsymbol{t}\cdot\boldsymbol{v}$ and $\sum_i \rho_i\boldsymbol{b}_i\cdot\boldsymbol{v}_i$ give the rate of work done by surface and body forces, respectively. In the last term of Eq. (2.60), $\mathbb{P}^{\mathrm{EM}}$ represents the rate of work done on the body by the electromagnetic field via the Lorentz force. Evaluating this power requires introducing a microscopic picture of charge transport in terms of the positions and velocities of individual particles, $\boldsymbol{r}^\alpha$ and $\boldsymbol{v}^\alpha$, respectively.[2] The current density $\tilde{\boldsymbol{j}}$, for example, may be written on a microscopic level as $\tilde{\boldsymbol{j}} = \sum_\alpha \hat{q}^\alpha\boldsymbol{v}^\alpha\Delta(\boldsymbol{x}-\boldsymbol{r}^\alpha)$, where $\hat{q}^\alpha$ is the charge (not the charge density) of particle α and $\Delta(\boldsymbol{x}-\boldsymbol{r}^\alpha)$ is a coarse-graining function connecting the microscopic particle picture to the continuum level. The Lorentz force acting on an individual particle $\boldsymbol{F}^\alpha$ is

$$\boldsymbol{F}^\alpha = \hat{q}^\alpha\boldsymbol{E} + \hat{q}^\alpha\boldsymbol{v}^\alpha\times\boldsymbol{B}\ . \quad (2.61)$$

The power corresponding to this Lorentz force is

$$\mathbb{P}^{\mathrm{EM}} = \sum_\alpha(\boldsymbol{F}^\alpha\cdot\boldsymbol{v}^\alpha)\Delta(\boldsymbol{x}-\boldsymbol{r}^\alpha) = \left[\sum_\alpha\hat{q}^\alpha\boldsymbol{v}^\alpha\cdot\boldsymbol{E} + \sum_\alpha\hat{q}^\alpha(\boldsymbol{v}^\alpha\times\boldsymbol{B})\cdot\boldsymbol{v}^\alpha\right]\Delta(\boldsymbol{x}-\boldsymbol{r}^\alpha) = \tilde{\boldsymbol{j}}\cdot\boldsymbol{E}\ . \quad (2.62)$$

The global energy balance can thus be expressed as

$$\frac{d}{dt}\int_{\mathcal{P}}\rho e dv = \int_{\mathcal{P}}\rho r dv - \int_{\mathcal{P}}\boldsymbol{\nabla}\cdot\boldsymbol{J}_{\mathrm{q}}dv + \int_{\mathcal{P}}\boldsymbol{\nabla}\cdot(\boldsymbol{T}^T\boldsymbol{v})dv + \int_{\mathcal{P}}\sum_i\rho_i\boldsymbol{b}_i\cdot\boldsymbol{v}_i dv + \int_{\mathcal{P}}\tilde{\boldsymbol{j}}\cdot\boldsymbol{E}dv\ , \quad (2.63)$$

with the corresponding local form

$$\rho\dot{e} = \sum_i\rho_i\boldsymbol{b}_i\cdot\boldsymbol{v}_i + \boldsymbol{\nabla}\cdot(\boldsymbol{T}^T\boldsymbol{v}) + \rho r - \boldsymbol{\nabla}\cdot\boldsymbol{J}_{\mathrm{q}} + \tilde{\boldsymbol{j}}\cdot\boldsymbol{E}\ . \quad (2.64)$$

[2]Throughout the text, superscript Greek indices (α, β) denote individual particles, while subscript Latin indices (i, j) denote species of a given type.

We can simplify this energy balance by incorporating the momentum balance as written in Eq. (2.36), yielding

$$\rho\dot{e} = \rho\dot{\boldsymbol{v}}\cdot\boldsymbol{v} + \boldsymbol{T}:\boldsymbol{\nabla v} + \rho r - \boldsymbol{\nabla}\cdot\boldsymbol{J}_{\mathrm{q}} + \sum_i \boldsymbol{j}_i\cdot\boldsymbol{b}_i + \boldsymbol{\mathcal{J}}\cdot\boldsymbol{\mathcal{E}}\ . \tag{2.65}$$

Note that for body forces such as gravity which act uniformly on all species, $\sum_i \boldsymbol{j}_i\cdot\boldsymbol{b}_i = 0$.

Let us rewrite the local energy balance Eq. (2.65) in terms of free and bound charges, rather than the total charge. Substituting Eq. (2.26), the quantity $\boldsymbol{\mathcal{J}}\cdot\boldsymbol{\mathcal{E}}$ in Eq. (2.65) can be rewritten as

$$\boldsymbol{\mathcal{J}}\cdot\boldsymbol{\mathcal{E}} = \boldsymbol{\mathcal{J}}^{\mathrm{f}}\cdot\boldsymbol{\mathcal{E}} + \boldsymbol{\mathcal{J}}^{\mathrm{b}}\cdot\boldsymbol{\mathcal{E}} = \boldsymbol{\mathcal{J}}^{\mathrm{f}}\cdot\boldsymbol{\mathcal{E}} + \boldsymbol{\mathcal{E}}\cdot\overset{*}{\boldsymbol{P}} + \boldsymbol{\mathcal{E}}\cdot\boldsymbol{\nabla}\times\boldsymbol{\mathcal{M}}\ . \tag{2.66}$$

Using Eq. (2.21), the last term in this equation can be rewritten as $\boldsymbol{\mathcal{E}}\cdot\boldsymbol{\nabla}\times\boldsymbol{\mathcal{M}} = \boldsymbol{\nabla}\cdot(\boldsymbol{\mathcal{M}}\times\boldsymbol{\mathcal{E}}) - \boldsymbol{\mathcal{M}}\cdot\overset{*}{\boldsymbol{B}}$. Thus, we have

$$\boldsymbol{\mathcal{J}}\cdot\boldsymbol{\mathcal{E}} = \boldsymbol{\mathcal{J}}^{\mathrm{f}}\cdot\boldsymbol{\mathcal{E}} + \boldsymbol{\mathcal{E}}\cdot\overset{*}{\boldsymbol{P}} + \boldsymbol{\nabla}\cdot(\boldsymbol{\mathcal{M}}\times\boldsymbol{\mathcal{E}}) - \boldsymbol{\mathcal{M}}\cdot\overset{*}{\boldsymbol{B}}\ . \tag{2.67}$$

We can further simplify by noting that for two vectors $\boldsymbol{A}$ and $\boldsymbol{B}$, $\boldsymbol{A}\cdot\overset{*}{\boldsymbol{B}} = \boldsymbol{A}\cdot\dot{\boldsymbol{B}} + \big[(\boldsymbol{A}\cdot\boldsymbol{B})\boldsymbol{I} - \boldsymbol{A}\otimes\boldsymbol{B}\big]:\boldsymbol{\nabla v}$. Equation (2.65) is thus

$$\begin{aligned}\rho\dot{e} = \rho\dot{\boldsymbol{v}}\cdot\boldsymbol{v} + [\boldsymbol{T}+(\boldsymbol{\mathcal{E}}\cdot\boldsymbol{P})\boldsymbol{I} - \boldsymbol{\mathcal{E}}\otimes\boldsymbol{P} - (\boldsymbol{\mathcal{M}}\cdot\boldsymbol{B})\boldsymbol{I} + \boldsymbol{\mathcal{M}}\otimes\boldsymbol{B}]:\boldsymbol{\nabla v}\\ + \rho r - \boldsymbol{\nabla}\cdot\bar{\boldsymbol{J}}_{\mathrm{q}} + \sum_i \boldsymbol{j}_i\cdot\boldsymbol{b}_i + \boldsymbol{\mathcal{J}}^{\mathrm{f}}\cdot\boldsymbol{\mathcal{E}} + \boldsymbol{\mathcal{E}}\cdot\dot{\boldsymbol{P}} - \boldsymbol{\mathcal{M}}\cdot\dot{\boldsymbol{B}}\ ,\end{aligned} \tag{2.68}$$

where we have defined the quantity $\bar{\boldsymbol{J}}_{\mathrm{q}} = \boldsymbol{J}_{\mathrm{q}} + \boldsymbol{\mathcal{E}}\times\boldsymbol{\mathcal{M}}$ as a modified heat flux vector.

Equation (2.68) is the form of the energy balance which will be useful in deriving internal entropy production. However, we can also express the energy balance in terms of $\boldsymbol{g}$, the momentum of the body including the electromagnetic field, and $\bar{\boldsymbol{T}}$, the composite stress tensor used in the momentum balance as written in Eq. (2.50). To do so, let us rewrite the quantity $(\tilde{\boldsymbol{j}}\cdot\boldsymbol{E})$ in terms of the applied electric and magnetic fields. Using Eqs. (2.12), (2.16), and (2.17), we can write

$$\begin{aligned}\tilde{\boldsymbol{j}}\cdot\boldsymbol{E} &= \frac{1}{\mu_0}\boldsymbol{E}\cdot(\boldsymbol{\nabla}\times\boldsymbol{B}) - \boldsymbol{E}\cdot\epsilon_0\frac{\partial\boldsymbol{E}}{\partial t}\\ &= \frac{1}{\mu_0}\big(-\boldsymbol{\nabla}\cdot(\boldsymbol{E}\times\boldsymbol{B}) + \boldsymbol{B}\cdot(\boldsymbol{\nabla}\times\boldsymbol{E})\big) - \boldsymbol{E}\cdot\epsilon_0\frac{\partial\boldsymbol{E}}{\partial t}\ .\end{aligned} \tag{2.69}$$

Applying Eq. (2.14), we obtain

$$\tilde{\boldsymbol{j}}\cdot\boldsymbol{E} = -\boldsymbol{\nabla}\cdot\left(\frac{1}{\mu_0}\boldsymbol{E}\times\boldsymbol{B}\right) - \frac{1}{\mu_0}\boldsymbol{B}\cdot\frac{\partial\boldsymbol{B}}{\partial t} - \epsilon_0\boldsymbol{E}\cdot\frac{\partial\boldsymbol{E}}{\partial t}\ . \tag{2.70}$$

Thus,

$$\int_{\mathcal{P}} \tilde{\boldsymbol{j}} \cdot \boldsymbol{E} dv = -\int_{\mathcal{P}} \left[\boldsymbol{\nabla} \cdot \left(\frac{1}{\mu_0} \boldsymbol{E} \times \boldsymbol{B} \right) + \frac{1}{\mu_0} \boldsymbol{B} \cdot \frac{\partial \boldsymbol{B}}{\partial t} + \epsilon_0 \boldsymbol{E} \cdot \frac{\partial \boldsymbol{E}}{\partial t} \right] dv \ . \tag{2.71}$$

Recall that the electromagnetic energy per volume $\tilde{u}_{\mathrm{EM}}$ can be expressed as $\tilde{u}_{\mathrm{EM}} = \frac{1}{2}(\epsilon_0 E^2 + \frac{1}{\mu_0} B^2)$, and consequently $\frac{\partial}{\partial t}(\tilde{u}_{\mathrm{EM}}) = \epsilon_0 \boldsymbol{E} \cdot \frac{\partial \boldsymbol{E}}{\partial t} + \frac{1}{\mu_0} \boldsymbol{B} \cdot \frac{\partial \boldsymbol{B}}{\partial t}$. Thus, we can rewrite Eq. (2.71) as

$$\int_{\mathcal{P}} \tilde{\boldsymbol{j}} \cdot \boldsymbol{E} dv = -\int_{\mathcal{P}} \left[\boldsymbol{\nabla} \cdot \left(\frac{1}{\mu_0} \boldsymbol{E} \times \boldsymbol{B} \right) - \boldsymbol{\nabla} \cdot (\tilde{u}_{\mathrm{EM}} \boldsymbol{v}) \right] dv - \frac{d}{dt} \int_{\mathcal{P}} \tilde{u}_{\mathrm{EM}} dv \ . \tag{2.72}$$

When written in terms of partial (as opposed to substantial) derivatives, the local form of Eq. (2.72) is

$$\frac{\partial \tilde{u}_{\mathrm{EM}}}{\partial t} = -\tilde{\boldsymbol{j}} \cdot \boldsymbol{E} - \boldsymbol{\nabla} \cdot \left(\frac{1}{\mu_0} \boldsymbol{E} \times \boldsymbol{B} \right) \ . \tag{2.73}$$

Equation (2.73) is the energy balance of the electromagnetic field alone [45], where the change in energy of the electromagnetic field is balanced by the work done by the Lorentz force (the first term on the right side) and the energy flux of the field (the second term). The latter quantity, $\frac{1}{\mu_0} \boldsymbol{E} \times \boldsymbol{B} =: \boldsymbol{S}$, is referred to as the Poynting vector.

We may now proceed by integrating the electromagnetic energy balance in Eq. (2.72) with the energy balance for the system as a whole. To this end, incorporating the definition of $\tilde{u}_{\mathrm{EM}}$ and applying the divergence theorem to the first term on the right side of Equation (2.72), we obtain

$$\begin{aligned} \int_{\mathcal{P}} \tilde{\boldsymbol{j}} \cdot \boldsymbol{E} dv = \int_{\partial \mathcal{P}} \left[\frac{1}{2} \left(\epsilon_0 E^2 + \frac{1}{\mu_0} B^2 \right) \boldsymbol{v} - \left(\frac{1}{\mu_0} \boldsymbol{E} \times \boldsymbol{B} \right) \right] \cdot \boldsymbol{n} da \\ - \frac{d}{dt} \int_{\mathcal{P}} \left[\frac{1}{2} \left(\epsilon_0 E^2 + \frac{1}{\mu_0} B^2 \right) \right] dv \ . \end{aligned} \tag{2.74}$$

After some manipulation using Eqs. (2.17)-(2.19) and (2.42), it can be shown that the integrand of the first term on the right-hand side can be rewritten as

$$\begin{aligned} \frac{1}{2} \left(\epsilon_0 E^2 + \frac{1}{\mu_0} B^2 \right) \boldsymbol{v} \cdot \boldsymbol{n} - \left(\frac{1}{\mu_0} \boldsymbol{E} \times \boldsymbol{B} \right) \cdot \boldsymbol{n} &= -\boldsymbol{\mathcal{E}} \times \boldsymbol{\mathcal{H}} \cdot \boldsymbol{n} + \boldsymbol{T}_{\mathrm{M}} \boldsymbol{v} \cdot \boldsymbol{n} + \epsilon_0 [(\boldsymbol{v} \otimes \boldsymbol{E} \times \boldsymbol{B}) \boldsymbol{v}] \cdot \boldsymbol{n} \\ &= -\boldsymbol{\mathcal{E}} \times \boldsymbol{\mathcal{H}} \cdot \boldsymbol{n} + \hat{\boldsymbol{T}} \boldsymbol{n} \cdot \boldsymbol{v} \ . \end{aligned} \tag{2.75}$$

In the second equality we have made use of the symmetry of $\boldsymbol{T}_{\mathrm{M}}$. Therefore,

$$\int_{\mathcal{P}} \tilde{\boldsymbol{j}} \cdot \boldsymbol{E} dv = \int_{\mathcal{P}} \boldsymbol{\nabla} \cdot (\hat{\boldsymbol{T}}^T \boldsymbol{v} - \boldsymbol{\mathcal{E}} \times \boldsymbol{\mathcal{H}}) dv - \frac{d}{dt} \int_{\mathcal{P}} \left[\frac{1}{2} \left(\epsilon_0 E^2 + \frac{1}{\mu_0} B^2 \right) \right] dv \ . \tag{2.76}$$

Substituting this expression into the global energy balance (Eq. (2.63)) yields

$$\frac{d}{dt} \int_{\mathcal{P}} \rho \bar{e} dv = \int_{\mathcal{P}} \rho r dv - \int_{\mathcal{P}} \boldsymbol{\nabla} \cdot (\boldsymbol{J}_{\mathrm{q}} + \boldsymbol{\mathcal{E}} \times \boldsymbol{\mathcal{H}}) dv + \int_{\mathcal{P}} \boldsymbol{\nabla} \cdot (\bar{\boldsymbol{T}}^T \boldsymbol{v}) dv + \int_{\mathcal{P}} \sum_i \rho_i \boldsymbol{b}_i \cdot \boldsymbol{v}_i dv \ . \tag{2.77}$$

Here we have defined the quantity $\bar{e} = e + \frac{1}{2}(\epsilon_0 E^2 + \frac{1}{\mu_0} B^2)/\rho$, which is the energy per unit mass of the system including the vacuum energy of the electromagnetic field. The quantity $\boldsymbol{\mathcal{E}} \times \boldsymbol{\mathcal{H}}$ may be interpreted as an additional flux of energy from the electromagnetic field; this term is the Galilean invariant analogue of the Poynting vector introduced in Eq. (2.73). The corresponding local form of Eq. (2.77) is

$$\rho \dot{\bar{e}} = \boldsymbol{\nabla} \cdot (\bar{\boldsymbol{T}}^T \boldsymbol{v}) + \rho r + \sum_i \rho_i \boldsymbol{b}_i \cdot \boldsymbol{v}_i - \boldsymbol{\nabla} \cdot (\boldsymbol{J}_\mathrm{q} + \boldsymbol{\mathcal{E}} \times \boldsymbol{\mathcal{H}}) \ . \tag{2.78}$$

We can now incorporate the momentum balance. Taking the dot product of $\boldsymbol{v}$ with both sides of Eq. (2.50) and subtracting the resulting equation from Eq. (2.78), we obtain

$$\rho \dot{\bar{e}} = \rho \dot{\boldsymbol{g}} \cdot \boldsymbol{v} + \bar{\boldsymbol{T}} : \boldsymbol{\nabla} \boldsymbol{v} + \rho r + \sum_i \boldsymbol{j}_i \cdot \boldsymbol{b}_i - \boldsymbol{\nabla} \cdot (\boldsymbol{J}_\mathrm{q} + \boldsymbol{\mathcal{E}} \times \boldsymbol{\mathcal{H}}) \ . \tag{2.79}$$

We may analogously rewrite the alternate form of the local energy balance, Eq. (2.79), in terms of free charges. Using Eq. (2.32), the quantity $\boldsymbol{\mathcal{E}} \times \boldsymbol{\mathcal{H}}$ becomes $\boldsymbol{\mathcal{E}} \times \boldsymbol{\mathcal{H}}^\mathrm{f} + \boldsymbol{\mathcal{E}} \times \boldsymbol{\mathcal{M}}$. As in Eq. (2.68), we may utilize the definition of the modified heat flux vector $\bar{\boldsymbol{J}}_\mathrm{q} = \boldsymbol{J}_\mathrm{q} + \boldsymbol{\mathcal{E}} \times \boldsymbol{\mathcal{M}}$ to write

$$\rho \dot{\bar{e}} = \rho \dot{\boldsymbol{g}} \cdot \boldsymbol{v} + \bar{\boldsymbol{T}} : \boldsymbol{\nabla} \boldsymbol{v} + \rho r + \sum_i \boldsymbol{j}_i \cdot \boldsymbol{b}_i - \boldsymbol{\nabla} \cdot (\bar{\boldsymbol{J}}_\mathrm{q} + \boldsymbol{\mathcal{E}} \times \boldsymbol{\mathcal{H}}^\mathrm{f}) \ . \tag{2.80}$$

Entropy balance

In this section, we will introduce the entropy balance and the second law of thermodynamics for electrolyte solutions. In doing so we provide a rigorous derivation for the rate of internal entropy production for multicomponent systems in the presence of electromagnetic fields. We will ultimately simplify this result specifically for an electrolyte with no applied magnetic field. This section is an extension of the work of de Groot and Mazur [26] to charged systems in the presence of electromagnetic fields.

To begin, we postulate that the total change in entropy in the system can be written as

$$\rho \dot{s} = -\boldsymbol{\nabla} \cdot \boldsymbol{J}_\mathrm{s} + \rho \sigma_\mathrm{e} + \rho \sigma_\mathrm{i} \ , \tag{2.81}$$

where s is the entropy per unit mass, $\boldsymbol{J}_\mathrm{s}$ is entropy flux, σ_e is entropy production from body forces, and σ_i is internal entropy production ($\sigma_\mathrm{i} \geq 0$ by the second law of thermodynamics). Following Sahu et al. [46] and Mandadapu [47], the components of this entropy balance can be obtained by working with the Helmholtz free energy. The Helmholtz free energy per volume, $\tilde{f}$, can be written as [36, 48]

$$\tilde{f} = \rho e - \frac{1}{2} \rho \boldsymbol{v} \cdot \boldsymbol{v} - \rho T s - \boldsymbol{\mathcal{E}} \cdot \boldsymbol{P} \ . \tag{2.82}$$

Taking the substantial derivative of both sides and incorporating the mass balance (Eq. (2.6)), Eq. (2.82) becomes

$$\rho \dot{s} = \frac{1}{T} \left[\rho \dot{e} - \rho \dot{\boldsymbol{v}} \cdot \boldsymbol{v} - \dot{\tilde{f}} - \tilde{f} (\boldsymbol{I} : \boldsymbol{\nabla} \boldsymbol{v}) - \rho s \dot{T} - \boldsymbol{\mathcal{E}} \cdot \dot{\boldsymbol{P}} - \dot{\boldsymbol{\mathcal{E}}} \cdot \boldsymbol{P} - (\boldsymbol{\mathcal{E}} \cdot \boldsymbol{P})(\boldsymbol{I} : \boldsymbol{\nabla} \boldsymbol{v}) \right] \ . \tag{2.83}$$

Incorporating the energy balance in Eq. (2.68) allows us to rewrite Eq. (2.83) as

$$\begin{aligned}\rho\dot{s} = \frac{1}{T}\Bigg[&- \dot{\tilde{f}} - \tilde{f}(\boldsymbol{I} : \boldsymbol{\nabla v}) + [\boldsymbol{T} - \boldsymbol{\mathcal{E}} \otimes \boldsymbol{P} - (\boldsymbol{\mathcal{M}} \cdot \boldsymbol{B})\boldsymbol{I} + \boldsymbol{\mathcal{M}} \otimes \boldsymbol{B}] : \boldsymbol{\nabla v} + \rho r \\ &+ \sum_i \boldsymbol{j}_i \cdot \boldsymbol{b}_i - \boldsymbol{\nabla} \cdot \bar{\boldsymbol{J}}_{\mathrm{q}} + \boldsymbol{\mathcal{J}}^{\mathrm{f}} \cdot \boldsymbol{\mathcal{E}} - \dot{\boldsymbol{\mathcal{E}}} \cdot \boldsymbol{P} - \boldsymbol{\mathcal{M}} \cdot \dot{\boldsymbol{B}} - \rho s \dot{T} \Bigg] .\end{aligned} \tag{2.84}$$

Equation (2.84) can be simplified further by evaluating $\dot{\tilde{f}}$ in terms of its natural variables. In Appendix A.1, we argue that $\tilde{f}$ is a function of $N+3$ quantities: $[T,\, c_1, c_2, ..., c_N,\, \boldsymbol{\mathcal{E}},\, \boldsymbol{B}]$, which leads to

$$\dot{\tilde{f}} = \frac{\partial \tilde{f}}{\partial T}\dot{T} + \sum_i \frac{\partial \tilde{f}}{\partial c_i}\dot{c}_i + \frac{\partial \tilde{f}}{\partial \boldsymbol{\mathcal{E}}} \cdot \dot{\boldsymbol{\mathcal{E}}} + \frac{\partial \tilde{f}}{\partial \boldsymbol{B}} \cdot \dot{\boldsymbol{B}} . \tag{2.85}$$

Substituting Eq. (2.85) into Eq. (2.84) yields

$$\begin{aligned}\rho\dot{s} = \frac{1}{T}\Bigg[&- \dot{T}\left(\rho s + \frac{\partial \tilde{f}}{\partial T}\right) - \sum_i \frac{\partial \tilde{f}}{\partial c_i}\dot{c}_i - \left(\boldsymbol{P} + \frac{\partial \tilde{f}}{\partial \boldsymbol{\mathcal{E}}}\right) \cdot \dot{\boldsymbol{\mathcal{E}}} - \left(\boldsymbol{\mathcal{M}} + \frac{\partial \tilde{f}}{\partial \boldsymbol{B}}\right) \cdot \dot{\boldsymbol{B}} - \tilde{f}(\boldsymbol{I} : \boldsymbol{\nabla v}) \\ &+ [\boldsymbol{T} - \boldsymbol{\mathcal{E}} \otimes \boldsymbol{P} - (\boldsymbol{\mathcal{M}} \cdot \boldsymbol{B})\boldsymbol{I} + \boldsymbol{\mathcal{M}} \otimes \boldsymbol{B}] : \boldsymbol{\nabla v} + \rho r + \sum_i \boldsymbol{j}_i \cdot \boldsymbol{b}_i - \boldsymbol{\nabla} \cdot \bar{\boldsymbol{J}}_{\mathrm{q}} + \boldsymbol{\mathcal{J}}^{\mathrm{f}} \cdot \boldsymbol{\mathcal{E}} \Bigg] .\end{aligned} \tag{2.86}$$

We now invoke the local equilibrium assumption,

$$\rho s = -\left(\frac{\partial \tilde{f}}{\partial T}\right)_{c_1, c_2, ..., c_N, \boldsymbol{\mathcal{E}}, \boldsymbol{B}} , \tag{2.87}$$

and define the chemical potential of species i as

$$\mu_i \coloneqq \left(\frac{\partial \tilde{f}}{\partial c_i}\right)_{T, c_{j \neq i}, \boldsymbol{\mathcal{E}}, \boldsymbol{B}} . \tag{2.88}$$

These definitions along with the mass balance (Eq. (2.5)) allow us to rewrite Eq. (2.86) as

$$\begin{aligned}\rho\dot{s} = \frac{\boldsymbol{\tau} : \boldsymbol{\nabla v}}{T} + \frac{\rho r}{T} + \frac{\sum_i \boldsymbol{j}_i \cdot \boldsymbol{b}_i}{T} + \frac{1}{T}\sum_i \mu_i \boldsymbol{\nabla} \cdot \boldsymbol{J}_i - \frac{\boldsymbol{\nabla} \cdot \bar{\boldsymbol{J}}_{\mathrm{q}}}{T} + \frac{1}{T}\boldsymbol{\mathcal{J}}^{\mathrm{f}} \cdot \boldsymbol{\mathcal{E}} \\ - \frac{1}{T}\left(\boldsymbol{P} + \frac{\partial \tilde{f}}{\partial \boldsymbol{\mathcal{E}}}\right) \cdot \dot{\boldsymbol{\mathcal{E}}} - \frac{1}{T}\left(\boldsymbol{\mathcal{M}} + \frac{\partial \tilde{f}}{\partial \boldsymbol{B}}\right) \cdot \dot{\boldsymbol{B}} ,\end{aligned} \tag{2.89}$$

where $\boldsymbol{\tau}$ is defined as

$$\boldsymbol{\tau} = \boldsymbol{T} + \left(\sum_i \mu_i c_i - \tilde{f}\right)\boldsymbol{I} - \boldsymbol{\mathcal{E}} \otimes \boldsymbol{P} - (\boldsymbol{\mathcal{M}} \cdot \boldsymbol{B})\boldsymbol{I} + \boldsymbol{\mathcal{M}} \otimes \boldsymbol{B} , \tag{2.90}$$

which can also be expressed in terms of $\bar{\boldsymbol{T}}$ as

$$\begin{aligned}\boldsymbol{\tau} = \bar{\boldsymbol{T}} - \epsilon_0(\boldsymbol{E}\times\boldsymbol{B})\otimes\boldsymbol{v} - \epsilon_0\boldsymbol{E}\otimes\boldsymbol{E} - \frac{1}{\mu_0}\boldsymbol{B}\otimes\boldsymbol{B} + \frac{1}{2}\left[\epsilon_0 E^2 + \frac{1}{\mu_0}B^2\right]\boldsymbol{I} \\ + \left(\sum_i \mu_i c_i - \tilde{f}\right)\boldsymbol{I} - \boldsymbol{\mathcal{E}}\otimes\boldsymbol{P} - (\boldsymbol{\mathcal{M}}\cdot\boldsymbol{B})\boldsymbol{I} + \boldsymbol{\mathcal{M}}\otimes\boldsymbol{B}\ .\end{aligned} \tag{2.91}$$

Rearranging, Eq. (2.89) becomes

$$\begin{aligned}\rho\dot{s} = -\boldsymbol{\nabla}\cdot\left(\frac{\bar{\boldsymbol{J}}_\mathrm{q} - \sum_i \mu_i\boldsymbol{J}_i}{T}\right) + \frac{\rho r}{T} + \frac{\boldsymbol{\tau}:\boldsymbol{\nabla}\boldsymbol{v}}{T} - \frac{1}{T}\left(\boldsymbol{P} + \frac{\partial\tilde{f}}{\partial\boldsymbol{\mathcal{E}}}\right)\cdot\dot{\boldsymbol{\mathcal{E}}} - \frac{1}{T}\left(\boldsymbol{\mathcal{M}} + \frac{\partial\tilde{f}}{\partial\boldsymbol{B}}\right)\cdot\dot{\boldsymbol{B}} \\ -\bar{\boldsymbol{J}}_\mathrm{q}\cdot\frac{\boldsymbol{\nabla}T}{T^2} - \sum_i\left[\boldsymbol{\nabla}\left(\frac{\mu_i}{T}\right) - \frac{M_i\boldsymbol{b}_i}{T}\right]\cdot\boldsymbol{J}_i + \frac{\boldsymbol{\mathcal{J}}^\mathrm{f}\cdot\boldsymbol{\mathcal{E}}}{T}\ .\end{aligned} \tag{2.92}$$

To convert the entropy balance in Eq. (2.92) into the form of Eq. (2.81), we express $\boldsymbol{\mathcal{J}}^\mathrm{f}$ in terms of the fluxes of ionic species:

$$\boldsymbol{\mathcal{J}}^\mathrm{f} = \tilde{\boldsymbol{j}}^\mathrm{f} - q^\mathrm{f}\boldsymbol{v} = \sum_i z_i c_i F(\boldsymbol{v}_i - \boldsymbol{v}) = \sum_i z_i F\boldsymbol{J}_i\ , \tag{2.93}$$

where F is Faraday's constant. Note that while the sum over i in this expression includes all types of species in the system, the factor of z_i (the charge valency of species i) means that net neutral species such as solvent do not contribute to the free charge conduction current density. In contrast, quantities such as $\sum_i \mu_i\boldsymbol{J}_i$ are influenced by both charged and neutral species. Substitution of Eq. (2.93) into Eq. (2.92) yields

$$\begin{aligned}\rho\dot{s} = -\boldsymbol{\nabla}\cdot\left(\frac{\bar{\boldsymbol{J}}_\mathrm{q} - \sum_i \mu_i\boldsymbol{J}_i}{T}\right) + \frac{\rho r}{T} + \frac{\boldsymbol{\tau}:\boldsymbol{\nabla}\boldsymbol{v}}{T} - \frac{1}{T}\left(\boldsymbol{P} + \frac{\partial\tilde{f}}{\partial\boldsymbol{\mathcal{E}}}\right)\cdot\dot{\boldsymbol{\mathcal{E}}} - \frac{1}{T}\left(\boldsymbol{\mathcal{M}} + \frac{\partial\tilde{f}}{\partial\boldsymbol{B}}\right)\cdot\dot{\boldsymbol{B}} \\ -\bar{\boldsymbol{J}}_\mathrm{q}\cdot\frac{\boldsymbol{\nabla}T}{T^2} - \sum_i\left[\boldsymbol{\nabla}\left(\frac{\mu_i}{T}\right) - \frac{z_i F\boldsymbol{\mathcal{E}}}{T} - \frac{M_i\boldsymbol{b}_i}{T}\right]\cdot\boldsymbol{J}_i\ .\end{aligned} \tag{2.94}$$

Eq. (2.94) is the most general form of the entropy balance for a mixture subject to an electromagnetic field. Comparing to Eq. (2.81), we can deduce that the entropy flux is

$$\boldsymbol{J}_\mathrm{s} = \frac{\bar{\boldsymbol{J}}_\mathrm{q} - \sum_i \mu_i\boldsymbol{J}_i}{T}\ , \tag{2.95}$$

the external entropy production is

$$\rho\sigma_\mathrm{e} = \frac{\rho r}{T}\ , \tag{2.96}$$

and the internal entropy production is

$$\begin{aligned}\rho\sigma_{\mathrm{i}} = \frac{\boldsymbol{\tau}:\boldsymbol{\nabla v}}{T} - \frac{1}{T}\left(\boldsymbol{P} + \frac{\partial \tilde{f}}{\partial \boldsymbol{\mathcal{E}}}\right)\cdot\dot{\boldsymbol{\mathcal{E}}} - \frac{1}{T}\left(\boldsymbol{\mathcal{M}} + \frac{\partial \tilde{f}}{\partial \boldsymbol{B}}\right)\cdot\dot{\boldsymbol{B}} - \bar{\boldsymbol{J}}_{\mathrm{q}}\cdot\frac{\boldsymbol{\nabla}T}{T^2} \\ - \sum_i \left[\boldsymbol{\nabla}\left(\frac{\mu_i}{T}\right) - \frac{z_i F\boldsymbol{\mathcal{E}}}{T} - \frac{M_i\boldsymbol{b}_i}{T}\right]\cdot\boldsymbol{J}_i \geq 0\ .\end{aligned} \tag{2.97}$$

If we assume there are no dissipation processes associated with polarization or magnetization, we may define

$$\begin{aligned}\boldsymbol{P} &= -\left(\frac{\partial \tilde{f}}{\partial \boldsymbol{\mathcal{E}}}\right)_{T,c_1,c_2,\ldots,c_N,\boldsymbol{B}}\ , \\ \boldsymbol{\mathcal{M}} &= -\left(\frac{\partial \tilde{f}}{\partial \boldsymbol{B}}\right)_{T,c_1,c_2,\ldots,c_N,\boldsymbol{\mathcal{E}}}\ .\end{aligned} \tag{2.98}$$

This brings the second and third terms of Eq. (2.97) to zero, giving

$$\rho\sigma_{\mathrm{i}} = \frac{\boldsymbol{\tau}:\boldsymbol{\nabla v}}{T} - \bar{\boldsymbol{J}}_{\mathrm{q}}\cdot\frac{\boldsymbol{\nabla}T}{T^2} - \sum_i \left[\boldsymbol{\nabla}\left(\frac{\mu_i}{T}\right) - \frac{z_i F\boldsymbol{\mathcal{E}}}{T} - \frac{M_i\boldsymbol{b}_i}{T}\right]\cdot\boldsymbol{J}_i \geq 0\ . \tag{2.99}$$

Specialization to the case of negligible magnetic field effects. For most electrolyte systems of interest, it may be reasonable to neglect all contributions of the magnetic field to the entropy balance expression. This may be argued using dimensional analysis of Maxwell's equations [49], although rigorous formulation of such arguments is beyond the scope of this dissertation. In the case where $\boldsymbol{B} = \boldsymbol{0}$, $\boldsymbol{\mathcal{E}} = \boldsymbol{E} = -\boldsymbol{\nabla}\phi$ and Eq. (2.94) reduces to

$$\begin{aligned}\rho\dot{s} = -\boldsymbol{\nabla}\cdot\left(\frac{\bar{\boldsymbol{J}}_{\mathrm{q}} - \sum_i \mu_i\boldsymbol{J}_i}{T}\right) + \frac{\rho r}{T} + \frac{\boldsymbol{\tau}:\boldsymbol{\nabla v}}{T} - \bar{\boldsymbol{J}}_{\mathrm{q}}\cdot\frac{\boldsymbol{\nabla}T}{T^2} \\ - \sum_i \left[\boldsymbol{\nabla}\left(\frac{\mu_i}{T}\right) + \frac{z_i F\boldsymbol{\nabla}\phi}{T} - \frac{M_i\boldsymbol{b}_i}{T}\right]\cdot\boldsymbol{J}_i\ .\end{aligned} \tag{2.100}$$

Furthermore, $\boldsymbol{\tau}$ is now

$$\begin{aligned}\boldsymbol{\tau} =& \boldsymbol{T} + \left(\sum_i \mu_i c_i - \tilde{f}\right)\boldsymbol{I} - \boldsymbol{E}\otimes\boldsymbol{P} \\ =& \bar{\boldsymbol{T}} - \epsilon_0\boldsymbol{E}\otimes\boldsymbol{E} + \frac{1}{2}\epsilon_0 E^2\boldsymbol{I} + \left(\sum_i \mu_i c_i - \tilde{f}\right)\boldsymbol{I} - \boldsymbol{E}\otimes\boldsymbol{P}\ .\end{aligned} \tag{2.101}$$

In this case, internal entropy production is

$$\rho\sigma_{\mathrm{i}} = \frac{\boldsymbol{\tau}:\boldsymbol{\nabla v}}{T} - \bar{\boldsymbol{J}}_{\mathrm{q}}\cdot\frac{\boldsymbol{\nabla}T}{T^2} - \sum_i \left[\boldsymbol{\nabla}\left(\frac{\mu_i}{T}\right) + \frac{z_i F\boldsymbol{\nabla}\phi}{T} - \frac{M_i\boldsymbol{b}_i}{T}\right]\cdot\boldsymbol{J}_i \geq 0 \tag{2.102}$$

We can further simplify this expression by assuming that thermodynamic forces and fluxes of different tensorial characters do not couple with each other in isotropic systems, also called the Curie principle [26, 50]. Thus, we can split our entropy production inequality as follows:

$$\begin{aligned} \frac{\boldsymbol{\tau} : \boldsymbol{\nabla} \boldsymbol{v}}{T} &\geq 0 \ , \\ -\bar{\boldsymbol{J}}_{\mathrm{q}} \cdot \frac{\boldsymbol{\nabla} T}{T^2} - \sum_i \left[\boldsymbol{\nabla} \left(\frac{\mu_i}{T} \right) + \frac{z_i F \boldsymbol{\nabla} \phi}{T} - \frac{M_i \boldsymbol{b}_i}{T} \right] \cdot \boldsymbol{J}_i &\geq 0 \ . \end{aligned} \tag{2.103}$$

Before proceeding, we must modify the second equality of Eq. (2.103) to account for the fact that a system of n components contains only $n-1$ independent fluxes due to the constraint that $\sum_i \boldsymbol{j}_i = \sum_i M_i \boldsymbol{J}_i = 0$, i.e., we can express the solvent flux, $\boldsymbol{J}_0$, as $\boldsymbol{J}_0 = -\sum_{i \neq 0} \frac{M_i}{M_0} \boldsymbol{J}_i$. Inclusion of this constraint into the second equality of Eq. (2.103) yields an expression of the form

$$-\bar{\boldsymbol{J}}_{\mathrm{q}} \cdot \frac{\boldsymbol{\nabla} T}{T^2} - \sum_{i \neq 0} \left[\boldsymbol{\nabla} \left(\frac{\mu_i - \frac{M_i}{M_0} \mu_0}{T} \right) + \frac{(z_i - \frac{M_i}{M_0} z_0) F \boldsymbol{\nabla} \phi}{T} - \frac{M_i (\boldsymbol{b}_i - \boldsymbol{b}_0)}{T} \right] \cdot \boldsymbol{J}_i \geq 0 \ . \tag{2.104}$$

Note that in most cases the solvent charge valency z_0 will be equal to zero.

For the remainder of our analysis we will consider the case of an isothermal system with no additional body forces $\boldsymbol{b}_i$, in which case Eq. (2.104) reduces to

$$-\frac{1}{T} \sum_{i \neq 0} \left(\boldsymbol{\nabla} \overline{\mu}_i - \frac{M_i}{M_0} \boldsymbol{\nabla} \overline{\mu}_0 \right) \cdot \boldsymbol{J}_i \geq 0 \ . \tag{2.105}$$

In this final expression we have combined the chemical potential and the body force from the external electric field into a single term, the electrochemical potential: $\overline{\mu}_i \coloneqq \mu_i + z_i F \phi$. Note that it is only possible to directly combine these terms after assuming that temperature is constant.

In general, we expect to be able to write internal entropy production as the sum of thermodynamic driving forces, $\boldsymbol{X}_i$, and fluxes, $\boldsymbol{J}_i$ [25, 26]:

$$\sigma_{\mathrm{i}} = \sum_i \boldsymbol{J}_i \cdot \boldsymbol{X}_i \geq 0 \ . \tag{2.106}$$

It is clear from Eqs. (2.105) and (2.106) that for this system we can choose

$$\hat{\boldsymbol{X}}_i = -(\boldsymbol{\nabla} \overline{\mu}_i - \frac{M_i}{M_0} \boldsymbol{\nabla} \overline{\mu}_0) \tag{2.107}$$

and

$$\boldsymbol{J}_i = c_i (\boldsymbol{v}_i - \boldsymbol{v}) \ , \tag{2.108}$$

where $i \neq 0$. In Sec. 2.2, we will use these definitions to define transport coefficients.

In this section, we derived an expression for internal entropy production using the Helmholtz free energy. The entropy balance is more conventionally derived, however, using the local equilibrium hypothesis and the Gibbs equation [25, 26]. For mixtures subject to an electromagnetic field, we do not a priori know the form of the Gibbs equation and therefore could not begin with this approach. We can, however, use our final expressions for the energy and entropy balances to derive the Gibbs equation for these systems (see Appendix A.2). Equation (A.16) could be used as the starting point for deriving internal entropy production in a manner consistent with that presented in this section.

2.2 Linear constitutive relations and linear irreversible thermodynamics

In what follows, we consider the simplification of the momentum, energy, and entropy balances after proposing linear constitutive relations for the polarization and shear stress. In defining these linear relations, we will restrict our discussion to isotropic materials in the absence of a magnetic field. The assumption of isotropy allows us to make use of the representation theorem saying that any n-dimensional isotropic tensor can be generated using the Kronecker delta tensor δ_{ij} and the n-dimensional Levi-Civita tensor $\varepsilon_{i_1,i_2,...i_n}$ [51].

Linear isotropic dielectrics

In a linear isotropic dielectric with no dissipation effects, the polarization $\boldsymbol{P}$ is directly proportional to the electric field $\boldsymbol{E}$. The most general such linear relationship is given by a rank-2 isotropic tensor, which by the aforementioned representation theorem must be proportional to the Kronecker delta. This leads to

$$\boldsymbol{P} = (\epsilon - \epsilon_0)\boldsymbol{E} \ , \tag{2.109}$$

where ϵ is the dielectric constant of the medium. By Eq. (2.29) we also see that

$$\boldsymbol{D}^{\mathrm{f}} = \epsilon \boldsymbol{E} \ . \tag{2.110}$$

The assumption of a linear dielectric allows us to integrate the first equality of Eq. (2.98) to obtain

$$\tilde{f} - \tilde{f}_0 = -\int (\epsilon - \epsilon_0)\boldsymbol{E} \cdot d\boldsymbol{E} = -\frac{1}{2}(\epsilon - \epsilon_0)E^2 \ , \tag{2.111}$$

where $\tilde{f}_0(T, c_1, c_2, ..., c_N)$ is the Helmholtz free energy per volume in the absence of an electric field. Equation (2.111) can be used to evaluate the electromagnetic contribution to the pressure, p. Recall that the pressure is conventionally defined in terms of the total Helmholtz free energy $\mathcal{F} = \tilde{f}V$ as $p := -\frac{\partial \mathcal{F}}{\partial V}\Big|_{T,n_1,...,n_N,\boldsymbol{\mathcal{E}},\boldsymbol{B}}$, where V is volume. The pressure can be

expressed in terms of the free energy per volume as

$$p = -\frac{\partial}{\partial V}(\tilde{f}V) = -\tilde{f} - V\frac{\partial \tilde{f}}{\partial V} = -\tilde{f} - V\sum_i \frac{\partial \tilde{f}}{\partial c_i}\frac{\partial c_i}{\partial V} \ , \tag{2.112}$$

or

$$\tilde{f} = -p + \sum_i \mu_i c_i \ . \tag{2.113}$$

This is identical to the result derived using extensivity arguments in Appendix A.1 (Eq. (A.5)). Incorporating Eq. (2.111), we can alternatively write

$$\begin{aligned} p =& -\tilde{f} - V\frac{\partial(\tilde{f}_0 - \frac{1}{2}(\epsilon - \epsilon_0)E^2)}{\partial V} \\ =& -\tilde{f}_0 + \frac{1}{2}(\epsilon - \epsilon_0)E^2 - V\sum_i \frac{\partial \tilde{f}_0}{\partial c_i}\frac{\partial c_i}{\partial V} + V\frac{1}{2}E^2\frac{\partial \epsilon}{\partial V} \ . \end{aligned} \tag{2.114}$$

Defining $\mu_{i,0} \coloneqq \frac{\partial \tilde{f}_0}{\partial c_i}$ and $p_0 \coloneqq \sum_i \mu_{i,0}c_i - \tilde{f}_0$ to be the chemical potential of species i and the pressure in the absence of an electric field, respectively, allows us to rewrite Eq. (2.114) as

$$p = p_0 + \frac{1}{2}\left[\epsilon - \epsilon_0 - \rho\frac{\partial \epsilon}{\partial \rho}\right]E^2 \ . \tag{2.115}$$

Newtonian fluids

In a Newtonian fluid, the shear stress $\boldsymbol{\tau}$ is directly proportional to the velocity gradient: $\boldsymbol{\tau} = \boldsymbol{\eta}^{(4)}\boldsymbol{\nabla v}$, where $\boldsymbol{\eta}^{(4)}$ is the fourth order viscosity tensor. A general fourth order tensor in three dimensions can be written as $\eta_{ijkl} = \eta_1\delta_{ij}\delta_{kl} + \eta_2\delta_{ik}\delta_{jl} + \eta_3\delta_{il}\delta_{jk}$, with three independent parameters. Imposing the symmetry of the stress tensor derived from the angular momentum balance (Sec. 2.1) eliminates one of these parameters and reduces $\boldsymbol{\tau} = \boldsymbol{\eta}^{(4)}\boldsymbol{\nabla v}$ to

$$\boldsymbol{\tau} = 2\eta\boldsymbol{d} + \lambda(\boldsymbol{d} : \boldsymbol{I})\boldsymbol{I} \ , \tag{2.116}$$

where η and λ are the two coefficients of viscosity and $\boldsymbol{d}$ is the symmetric part of the velocity gradient tensor, $\boldsymbol{d} = \frac{\boldsymbol{\nabla v} + (\boldsymbol{\nabla v})^T}{2}$.

The expression for $\tilde{f}$ in Eq. (2.113) can be combined with the linear constitutive relation for shear stress to directly evaluate $\boldsymbol{T}$ and $\bar{\boldsymbol{T}}$ and thus write the momentum balances in more useful forms. Substituting Newton's law of viscosity (Eq. (2.116)) and Eqs. (2.113) and (2.115) into our expressions for $\boldsymbol{\tau}$ (Eqs. (2.90) and (2.91)) in the case of no magnetic field, we see that

$$\begin{aligned} \boldsymbol{T} &= 2\eta\boldsymbol{d} + \lambda(\boldsymbol{d} : \boldsymbol{I})\boldsymbol{I} - p\boldsymbol{I} + \boldsymbol{E} \otimes \boldsymbol{P} \\ &= 2\eta\boldsymbol{d} + \lambda(\boldsymbol{d} : \boldsymbol{I})\boldsymbol{I} - p_0\boldsymbol{I} - \frac{1}{2}\left(\epsilon - \epsilon_0 - \rho\frac{\partial \epsilon}{\partial \rho}\right)E^2\boldsymbol{I} + (\epsilon - \epsilon_0)\boldsymbol{E} \otimes \boldsymbol{E} \end{aligned} \tag{2.117}$$

and

$$\begin{aligned}\bar{\boldsymbol{T}} &= 2\eta\boldsymbol{d} + \lambda(\boldsymbol{d}:\boldsymbol{I})\boldsymbol{I} + \epsilon_0\boldsymbol{E}\otimes\boldsymbol{E} - \frac{1}{2}\epsilon_0 E^2\boldsymbol{I} - p\boldsymbol{I} + \boldsymbol{E}\otimes\boldsymbol{P} \\ &= 2\eta\boldsymbol{d} + \lambda(\boldsymbol{d}:\boldsymbol{I})\boldsymbol{I} - p_0\boldsymbol{I} + \epsilon\boldsymbol{E}\otimes\boldsymbol{E} - \frac{1}{2}\left[\epsilon - \rho\frac{\partial\epsilon}{\partial\rho}\right]E^2\boldsymbol{I}\ .\end{aligned} \tag{2.118}$$

We can substitute these expressions directly into the local momentum balances. Incorporation of Eq. (2.117) into Eq. (2.37) (when $\boldsymbol{B} = 0$ and dielectric constant does not vary with density) gives

$$\rho\dot{\boldsymbol{v}} = -\boldsymbol{\nabla}p_0 + \eta\nabla^2\boldsymbol{v} + (\eta+\lambda)\boldsymbol{\nabla}(\boldsymbol{\nabla}\cdot\boldsymbol{v}) + \sum_i \rho_i\boldsymbol{b}_i + q^f\boldsymbol{E}\ . \tag{2.119}$$

This expression is simply the Navier-Stokes equations with an additional body force acting on the free charges in the system. For an electroneutral system ($q^f = 0$) in a linear dielectric, it is therefore appropriate to use the standard Navier-Stokes equations to analyze momentum transport in an electrolyte.

Analogously, substituting Eq. (2.118) into the momentum balance in the form of Eq. (2.50) yields

$$\rho\dot{\boldsymbol{v}} = -\boldsymbol{\nabla}p_0 + \eta\nabla^2\boldsymbol{v} + (\eta+\lambda)\boldsymbol{\nabla}(\boldsymbol{\nabla}\cdot\boldsymbol{v}) + \boldsymbol{\nabla}\cdot\left[\epsilon\boldsymbol{E}\otimes\boldsymbol{E} - \frac{1}{2}\epsilon E^2\boldsymbol{I}\right] + \sum_i \rho_i\boldsymbol{b}_i\ . \tag{2.120}$$

We have used the fact that for the case of no magnetic field, $\dot{\boldsymbol{g}} = \dot{\boldsymbol{v}}$. Whichever form of the momentum balance is used, the boundary conditions for momentum transport are always obtained from $\bar{\boldsymbol{T}}\boldsymbol{n}$ (Eq. (2.118)), not from $\boldsymbol{T}\boldsymbol{n}$ (Eq. (2.117)).

Diffusive transport coefficients

Recall from Sec. 2.1 that internal entropy production can be written as a bilinear form relating thermodynamic driving forces and fluxes, i.e., $\sigma_{\mathrm{i}} = \sum_i \boldsymbol{J}_i\cdot\boldsymbol{X}_i$. We now postulate linear relations between these forces and fluxes of the following form:

$$\boldsymbol{J}_i = \sum_j \boldsymbol{L}^{ij}\boldsymbol{X}_j \tag{2.121}$$

and

$$\boldsymbol{X}_j = \sum_i \boldsymbol{M}^{ij}\boldsymbol{J}_i\ . \tag{2.122}$$

Each transport coefficient $\boldsymbol{L}^{ij}$ or $\boldsymbol{M}^{ij}$ is a second order tensor in three dimensions, which for an isotropic system may be expressed as $\boldsymbol{L}^{ij} = L^{ij}\boldsymbol{I}$ and $\boldsymbol{M}^{ij} = M^{ij}\boldsymbol{I}$. For the subsequent analysis we consider only the scalar transport coefficients L^{ij} and M^{ij}. Additionally, note

that $L^{ij} = L^{ji}$ and $M^{ij} = M^{ji}$ by the Onsager reciprocal relations [23,24], as will be apparent from the Green-Kubo relations derived in Sec. 3.1.

The second law dictates that

$$\sigma_{\mathrm{i}} = \sum_i \boldsymbol{J}_i \cdot \boldsymbol{X}_i = \sum_i \sum_j L^{ij} \boldsymbol{X}_j \cdot \boldsymbol{X}_i \geq 0 \ . \tag{2.123}$$

Thus the matrix $\boldsymbol{L}$ composed of each of the L^{ij} coefficients is positive semi-definite. This provides some information on the possible values for each L^{ij}, for example that the diagonal elements L^{ii} must be greater than or equal to zero and that $\sum_i \sum_j L^{ij} \geq 0$. Furthermore, the condition that the eigenvalues of $\boldsymbol{L}$ must be real and greater than or equal to zero tells us that the principal invariants of $\boldsymbol{L}$ are positive. Thus, the determinant of $\boldsymbol{L}$ is positive, for example $L^{++}L^{--} - L^{+-2} \geq 0$ for a binary electrolyte of a single type of cation (+) and anion (−).

The choices of force and flux defined in Eqs. (2.107) and (2.108) yield the following relations:[3]

$$c_i(\boldsymbol{v}_i - \boldsymbol{v}) = -\sum_{j\neq 0} L^{ij} \left(\boldsymbol{\nabla} \overline{\mu}_j - \frac{M_j}{M_0} \boldsymbol{\nabla} \overline{\mu}_0 \right) \tag{2.125}$$

and

$$-\left(\boldsymbol{\nabla} \overline{\mu}_i - \frac{M_i}{M_0} \boldsymbol{\nabla} \overline{\mu}_0 \right) = \sum_{j\neq 0} M^{ij} c_j (\boldsymbol{v}_j - \boldsymbol{v}) \ . \tag{2.126}$$

Note that based on this formulation, the transport coefficients L^{ij} and M^{ij} are not defined for i or j equal to the solvent, species 0. To reformulate Eqs. (2.125) and (2.126) when the solvent is also included as one of the species, one can define

$$L^{i0} = L^{0i} = -\sum_{j\neq 0} \frac{M_j}{M_0} L^{ij} \ , \tag{2.127}$$

which yields a simpler, more convenient equation:

$$c_i(\boldsymbol{v}_i - \boldsymbol{v}) = -\sum_j L^{ij} \boldsymbol{\nabla} \overline{\mu}_j \ , \tag{2.128}$$

where the summation is now over all species. Note that isotropy, the Onsager reciprocal relations, and the constraint that $\sum_i M_i L^{ij} = 0$ (Eq. (2.127)) implies that an n-component electrolyte has $n(n-1)/2$ independent transport coefficients.

[3]The linear laws can easily be generalized to the case of non-isothermal systems, where we could have

$$\boldsymbol{J}_i = c_i(\boldsymbol{v}_i - \boldsymbol{v}) = -\frac{L^{iT}}{T^2} \boldsymbol{\nabla} T - \sum_{j\neq 0} L^{ij} \left(\boldsymbol{\nabla} \left(\frac{\mu_j}{T} \right) + \frac{z_i F \boldsymbol{\nabla} \phi}{T} - \frac{M_j}{M_0} \left[\boldsymbol{\nabla} \left(\frac{\mu_0}{T} \right) + \frac{z_0 F \boldsymbol{\nabla} \phi}{T} \right] \right) \ , \tag{2.124}$$

which captures cross-coupling effects between temperature gradients and species flux, i.e., the Soret effect.

Equation (2.128), denoted here as the Onsager transport equations, provides a foundation for rigorous continuum-level modeling of electrolyte transport. In this chapter, we have demonstrated how these equations emerge from the combination of Maxwell's equations, balance laws, internal entropy production, and linear constitutive relations. While Eq. (2.128) only considers the impact of electrochemical potential gradients, the full set of equations presented in Chapter 2.1 enable treatment of a broad range of complex phenomena which feature the coupling of temperature gradients, bulk convection, and electromagnetic fields.

Chapter 3

Nonequilibrium Statistical Mechanics of Ion Transport[1]

The governing equations presented in the previous chapter allow us to describe macroscopic, boundary-driven transport phenomena in systems out of equilibrium. In this chapter, we will derive Green-Kubo relations [27, 28] to relate the diffusive transport coefficients L^{ij} to the decay of fluctuations at equilibrium. This connection between the deterministic, continuum level transport theory and the stochastic behavior observed at the molecular level is enabled by the Onsager regression hypothesis, one of the most important developments of nonequilibrium statistical mechanics [23, 24]. This hypothesis states that the relaxation, or regression, of spontaneous fluctuations in an aged system in equilibrium is governed by the same laws which describe the response to macroscopic perturbations away from equilibrium. The regression hypothesis was used by Kubo [28] to derive the Green-Kubo relations, which enable facile computation of transport coefficients from molecular dynamics simulations. This offers a means of rigorously studying transport in systems where experimental characterization may be challenging or impractical, for example in screening new electrolyte chemistries or studying systems with more than two types of ionic species. In Chapter 3.1, we begin by detailing a derivation for the Green-Kubo relation for L^{ij} which is based on the Onsager regression hypothesis. We subsequently describe an alternate derivation based on linear response theory in Chapter 3.2.

3.1 Green-Kubo relations: Derivation based on the Onsager regression hypothesis

Consider a system at equilibrium in which each species k has a mean concentration $\overline{c}_k$. Thermal fluctuations at equilibrium will induce small fluctuations in concentration, δc_k,

[1]This chapter is closely adapted from portions of Ref [1]: Fong, K. D., Bergstrom, H. K., McCloskey, B. D. & Mandadapu, K. K. Transport phenomena in electrolyte solutions: Non-equilibrium thermodynamics and statistical mechanics. *AIChE Journal* e17091 (2020).

about this mean value. The concentration of species k at any instant $c_k(\boldsymbol{x},t)$ may thus be expressed as $c_k(\boldsymbol{x},t) = \overline{c}_k + \delta c_k(\boldsymbol{x},t)$. The species mass balance (Eq. (2.5)) may be modified at equilibrium to be

$$\frac{\partial(\delta c_i)}{\partial t} = -\boldsymbol{\nabla}\cdot\boldsymbol{J}_i \ . \tag{3.1}$$

In writing Eq. (3.1) we have used the fact that $\boldsymbol{v} = 0$ for a system at equilibrium. Substituting the constitutive relation in Eq. (2.128) into Eq. (3.1) yields

$$\frac{\partial(\delta c_i)}{\partial t} = \boldsymbol{\nabla}\cdot\left[\sum_j L^{ij}\boldsymbol{\nabla}\overline{\mu}_j\right] . \tag{3.2}$$

Using Eq. (A.4) with constant temperature and the magnetic field $\boldsymbol{B} = 0$, the quantity $\boldsymbol{\nabla}\overline{\mu}_j$ can be written in terms of the electric field and concentration as

$$\boldsymbol{\nabla}\overline{\mu}_j = \boldsymbol{\nabla}\mu_j + z_jF\boldsymbol{\nabla}\phi = -\left(\frac{\partial \boldsymbol{P}}{\partial c_j}\right)_{T,c_{l\neq j},\boldsymbol{E}}\cdot\boldsymbol{\nabla}\boldsymbol{E} + \sum_k\left(\frac{\partial\mu_j}{\partial c_k}\right)_{T,c_{l\neq k},\boldsymbol{E}}\boldsymbol{\nabla}c_k + z_jF\boldsymbol{\nabla}\phi \ , \tag{3.3}$$

where as before $\boldsymbol{E} = -\boldsymbol{\nabla}\phi$. Using Eq. (2.109), we can write

$$\left(\frac{\partial \boldsymbol{P}}{\partial c_j}\right)_{T,c_{l\neq j},\boldsymbol{E}}\cdot\boldsymbol{\nabla}\boldsymbol{E} = -\left(\frac{\partial(\epsilon-\epsilon_0)\boldsymbol{E}}{\partial c_j}\right)_{T,c_{l\neq j},\boldsymbol{E}}\cdot\boldsymbol{\nabla}\boldsymbol{E} \ .$$

Assuming changes in dielectric constant with respect to concentration are negligible, this term can be eliminated. Thus, the gradient in electrochemical potential is

$$\boldsymbol{\nabla}\overline{\mu}_j = \sum_k\left(\frac{\partial\mu_j}{\partial c_k}\right)_{T,c_{l\neq k},\boldsymbol{E}}\boldsymbol{\nabla}c_k + z_jF\boldsymbol{\nabla}\phi \ . \tag{3.4}$$

Now, Eq. (3.2) becomes

$$\frac{\partial(\delta c_i)}{\partial t} = \boldsymbol{\nabla}\cdot\left[\sum_j L^{ij}\left(\sum_k\left.\frac{\partial\mu_j}{\partial c_k}\right|_{T,c_{l\neq k},\boldsymbol{E}}\boldsymbol{\nabla}c_k + z_jF\boldsymbol{\nabla}\phi\right)\right] . \tag{3.5}$$

The term $\frac{\partial\mu_j}{\partial c_k}$ can be rewritten in terms of δc_i at equilibrium (see Appendix A.3):

$$\frac{\partial\mu_j}{\partial c_k} = \frac{1}{\beta V}(\boldsymbol{K}_{\mathrm{CC}}^{-1})^{kj} \ , \tag{3.6}$$

where $\boldsymbol{K}_{\mathrm{CC}}$ is the covariance matrix with elements $\langle\delta c_i\delta c_j\rangle$ and $\beta = (k_{\mathrm{B}}T)^{-1}$, where k_{B} is the Boltzmann constant. We thus have

$$\frac{\partial(\delta c_i)}{\partial t} = \boldsymbol{\nabla}\cdot\left[\sum_j L^{ij}\left(\sum_k\frac{1}{\beta V}(\boldsymbol{K}_{\mathrm{CC}}^{-1})^{kj}\boldsymbol{\nabla}c_k + z_jF\boldsymbol{\nabla}\phi\right)\right] . \tag{3.7}$$

Expanding the right hand side yields

$$\frac{\partial(\delta c_i)}{\partial t} = \sum_j L^{ij}\left[\sum_k \frac{1}{\beta V}(\boldsymbol{K}_{\mathrm{CC}}^{-1})^{kj}\boldsymbol{\nabla}^2 c_k - z_j F \boldsymbol{\nabla}\cdot\boldsymbol{E}\right] + \sum_j \boldsymbol{\nabla} L^{ij}\cdot\left[\sum_k \frac{1}{\beta V}(\boldsymbol{K}_{\mathrm{CC}}^{-1})^{kj}\boldsymbol{\nabla} c_k - z_j F \boldsymbol{E}\right] . \tag{3.8}$$

By Eqs. (2.27) and (2.110) for a system with uniform dielectric constant, $\boldsymbol{\nabla}\cdot\boldsymbol{E} = q^{\mathrm{f}}/\epsilon$. Over length scales shorter than the Debye length, electroneutrality may be violated, yielding a nonzero value of q^{f}. In Green-Kubo relations, however, we are only interested in describing long wavelength fluctuations at equilibrium; thus, the quantity $\boldsymbol{\nabla}\cdot\boldsymbol{E}$ may be neglected.

The transport coefficients L^{ij} depend on concentration. Given that the concentration fluctuations at equilibrium are small, however, we can linearize L^{ij} around the mean solution concentration to obtain

$$L^{ij} = L^{ij}\Big|_{\bar{c}_m} + \sum_l \frac{\partial L^{ij}}{\partial c_l}\Big|_{\bar{c}_m}(\delta c_l) . \tag{3.9}$$

Using Eq. (3.9) and rewriting all terms in terms of concentration fluctuations, Eq. (3.8) becomes

$$\frac{\partial(\delta c_i)}{\partial t} = \sum_j \left(L^{ij}\Big|_{\bar{c}_m} + \sum_l \frac{\partial L^{ij}}{\partial c_l}\Big|_{\bar{c}_m}(\delta c_l)\right)\left(\sum_k \frac{(\boldsymbol{K}_{\mathrm{CC}}^{-1})^{kj}}{\beta V}\boldsymbol{\nabla}^2\delta c_k\right) + \sum_j\sum_l \frac{\partial L^{ij}}{\partial c_l}\Big|_{\bar{c}_m}(\boldsymbol{\nabla}\delta c_l)\left(\sum_k \frac{(\boldsymbol{K}_{\mathrm{CC}}^{-1})^{kj}}{\beta V}\boldsymbol{\nabla} c_k - z_j F\boldsymbol{E}\right) . \tag{3.10}$$

Eliminating the terms in Eq. (3.10) which are negligibly small leads to an evolution equation for the concentration:

$$\frac{\partial(\delta c_i)}{\partial t} = \sum_j\sum_k \frac{(\boldsymbol{K}_{\mathrm{CC}}^{-1})^{kj}}{\beta V} L^{ij}\boldsymbol{\nabla}^2(\delta c_k) , \tag{3.11}$$

where we have removed the subscript on $L^{ij}\big|_{\bar{c}_m}$ for simplicity.

Let us express the concentration as a Fourier series in terms of the wavevector $\boldsymbol{k}$:

$$\delta c_j = \sum_{\boldsymbol{k}} \delta c_j(\boldsymbol{k},t) e^{i\boldsymbol{k}\cdot\boldsymbol{x}} , \tag{3.12}$$

which leads to

$$\boldsymbol{\nabla}^2(\delta c_j) = \sum_{\boldsymbol{k}} -k^2 \delta c_j(\boldsymbol{k},t) e^{i\boldsymbol{k}\cdot\boldsymbol{x}} . \tag{3.13}$$

Equation (3.1) may be thus be written as

$$\delta\dot{c}_i(\boldsymbol{k},t) = -i\boldsymbol{k}\cdot\boldsymbol{J}_i(\boldsymbol{k},t) , \tag{3.14}$$

where we have used $\boldsymbol{J}_i = \sum_{\boldsymbol{k}} \boldsymbol{J}_i(\boldsymbol{k},t)e^{i\boldsymbol{k}\cdot\boldsymbol{x}}$. Analogously, Eq. (3.11) is transformed into

$$\delta\dot{c}_i(\boldsymbol{k},t) = -k^2\frac{k_\mathrm{B}T}{V}\left[\sum_j\sum_m(\boldsymbol{K}_\mathrm{CC}^{-1})^{mj}L^{ij}\delta c_m(\boldsymbol{k},t)\right] . \tag{3.15}$$

We now multiply both sides of Eq. (3.15) by $\delta c_l(-\boldsymbol{k},0)$ and take an ensemble average, giving

$$\left\langle\delta\dot{c}_i(\boldsymbol{k},t)\delta c_l(-\boldsymbol{k},0)\right\rangle = -k^2\frac{k_\mathrm{B}T}{V}\left[\sum_j\sum_m(\boldsymbol{K}_\mathrm{CC}^{-1})^{mj}L^{ij}\left\langle\delta c_m(\boldsymbol{k},t)\delta c_l(-\boldsymbol{k},0)\right\rangle\right] . \tag{3.16}$$

Defining the correlation function $A^{ij} = \left\langle\delta c_i(\boldsymbol{k},t)\delta c_j(-\boldsymbol{k},0)\right\rangle$, Eq. (3.16) can be rewritten as

$$\frac{dA^{il}}{dt} = -k^2\frac{k_\mathrm{B}T}{V}\left[\sum_j\sum_m(\boldsymbol{K}_\mathrm{CC}^{-1})^{mj}L^{ij}A^{ml}(\boldsymbol{k},t)\right] . \tag{3.17}$$

We proceed by taking a Laplace transform of Eq. (3.17), defining the Laplace transform $\widetilde{A}(s)$ of a quantity $A(t)$ to be $\widetilde{A}(s) = \int_0^\infty dte^{-st}A(t)$, where s is a complex frequency parameter. Using integration by parts, the left hand side of Eq. (3.17) becomes

$$\int_0^\infty dte^{-st}\frac{dA^{il}}{dt} = e^{-st}A^{il}\Big|_0^\infty - \int_0^\infty dte^{-st}(-s)A^{il} = s\widetilde{A}^{il}(\boldsymbol{k},s) - A^{il}(\boldsymbol{k},0) , \tag{3.18}$$

and the right side of the equation is

$$\begin{aligned}\int_0^\infty dte^{-st}\bigg(-k^2\frac{k_\mathrm{B}T}{V}\left[\sum_j\sum_m(\boldsymbol{K}_\mathrm{CC}^{-1})^{mj}L^{ij}A^{ml}(\boldsymbol{k},t)\right]\bigg)& \\ = -k^2\frac{k_\mathrm{B}T}{V}\sum_j\sum_m(\boldsymbol{K}_\mathrm{CC}^{-1})^{mj}L^{ij}\widetilde{A}^{ml}(\boldsymbol{k},s) .&\end{aligned} \tag{3.19}$$

Combining Eqs. (3.18) and (3.19), Eq. (3.17) reduces to

$$s\widetilde{A}^{il}(\boldsymbol{k},s) - A^{il}(\boldsymbol{k},0) = -k^2\frac{k_\mathrm{B}T}{V}\sum_j\sum_m(\boldsymbol{K}_\mathrm{CC}^{-1})^{mj}L^{ij}\widetilde{A}^{ml}(\boldsymbol{k},s) . \tag{3.20}$$

Solving for the transport coefficient L^{il} yields

$$L^{il} = \frac{s\widetilde{A}^{il}(\boldsymbol{k},s) - A^{il}(\boldsymbol{k},0) + k^2\frac{k_\mathrm{B}T}{V}\sum_{j\neq l}\sum_m(\boldsymbol{K}_\mathrm{CC}^{-1})^{mj}L^{ij}\widetilde{A}^{ml}(\boldsymbol{k},s)}{-k^2\frac{k_\mathrm{B}T}{V}\sum_m(\boldsymbol{K}_\mathrm{CC}^{-1})^{ml}\widetilde{A}^{ml}(\boldsymbol{k},s)} . \tag{3.21}$$

Now consider a new function, $\phi^{ij}(\boldsymbol{k},t)$, defined as

$$\phi^{ij}(\boldsymbol{k},t) \coloneqq \left\langle\delta\dot{c}_i(\boldsymbol{k},t)\delta\dot{c}_j(-\boldsymbol{k},0)\right\rangle = -\frac{d^2A^{ij}}{dt^2} . \tag{3.22}$$

The Laplace transform of $\phi^{ij}(\boldsymbol{k},t)$ is

$$-\widetilde{\phi}^{ij}(\boldsymbol{k},s) = s^2\widetilde{A}^{ij}(\boldsymbol{k},s) - sA^{ij}(\boldsymbol{k},0)\ , \tag{3.23}$$

where we used the relation $\dot{A}^{ij}(0)=0$. Substituting $\phi^{ij}(\boldsymbol{k},t)$ into Eq. (3.21) yields

$$L^{il} = \frac{-\widetilde{\phi}^{il}(\boldsymbol{k},s)/s + k^2\frac{k_\mathrm{B}T}{V}\sum_{j\neq l}\sum_m(\boldsymbol{K}^{-1}_{\mathrm{CC}})^{mj}L^{ij}\big(-\widetilde{\phi}^{ml}(\boldsymbol{k},s)/s^2 + A^{ml}(\boldsymbol{k},0)/s\big)}{-k^2\frac{k_\mathrm{B}T}{V}\sum_m(\boldsymbol{K}^{-1}_{\mathrm{CC}})^{ml}\big(-\widetilde{\phi}^{ml}(\boldsymbol{k},s)/s^2 + A^{ml}(\boldsymbol{k},0)/s\big)}\ . \tag{3.24}$$

Let us consider large wavelength fluctuations, corresponding to the limit of $\boldsymbol{k}$ tending to zero. Under this limit, Equation (3.24) simplifies to:

$$\begin{aligned} L^{il} &= \lim_{\boldsymbol{k}\to 0}\frac{\widetilde{\phi}^{il}(\boldsymbol{k},s)}{k^2\frac{k_\mathrm{B}T}{V}\sum_m(\boldsymbol{K}^{-1}_{\mathrm{CC}})^{ml}(-\widetilde{\phi}^{ml}(\boldsymbol{k},s)/s + A^{ml}(\boldsymbol{k},0)\big)} \\ &= \lim_{\boldsymbol{k}\to 0}\frac{\int_0^\infty dt e^{-st}\big\langle\delta\dot{c}_i(\boldsymbol{k},t)\delta\dot{c}_l(-\boldsymbol{k},0)\big\rangle}{k^2\frac{k_\mathrm{B}T}{V}\sum_m(\boldsymbol{K}^{-1}_{\mathrm{CC}})^{ml}(-\int_0^\infty dte^{-st}/s\big\langle\delta\dot{c}_m(\boldsymbol{k},t)\delta\dot{c}_l(-\boldsymbol{k},0)\big\rangle + A^{ml}(\boldsymbol{k},0))}\ . \end{aligned} \tag{3.25}$$

Further simplification by substituting Eq. (3.14) leads to

$$L^{il} = \lim_{\boldsymbol{k}\to 0}\frac{\frac{V}{k_\mathrm{B}T}\int_0^\infty dte^{-st}\big\langle\big[(-i\boldsymbol{k})\cdot\boldsymbol{J}_i(\boldsymbol{k},t)\big]\big[(i\boldsymbol{k})\cdot\boldsymbol{J}_l(-\boldsymbol{k},0)\big]\big\rangle}{k^2\sum_m(\boldsymbol{K}^{-1}_{\mathrm{CC}})^{ml}(-\int_0^\infty dte^{-st}/s\big\langle\big[(-i\boldsymbol{k})\cdot\boldsymbol{J}_m(\boldsymbol{k},t)\big]\big[(i\boldsymbol{k})\cdot\boldsymbol{J}_l(-\boldsymbol{k},0)\big]\big\rangle + A^{ml}(\boldsymbol{k},0))}\ . \tag{3.26}$$

We now invoke the assumption that the system is isotropic and continue by using $\boldsymbol{k}=k\boldsymbol{e}_x$, which yields

$$\begin{aligned} L^{il} &= \lim_{\boldsymbol{k}\to 0}\frac{k^2\frac{V}{k_\mathrm{B}T}\int_0^\infty dte^{-st}\big\langle J_{i,x}(\boldsymbol{k},t)J_{l,x}(-\boldsymbol{k},0)\big\rangle}{k^2\sum_m(\boldsymbol{K}^{-1}_{\mathrm{CC}})^{ml}\big(k^2\int_0^\infty dte^{-st}/s\big\langle J_{m,x}(\boldsymbol{k},t)J_{l,x}(-\boldsymbol{k},0)\big\rangle + A^{ml}(\boldsymbol{k},0)\big)} \\ &= \lim_{\boldsymbol{k}\to 0}\frac{\frac{V}{k_\mathrm{B}T}\int_0^\infty dte^{-st}\big\langle J_{i,x}(\boldsymbol{k},t)J_{l,x}(-\boldsymbol{k},0)\big\rangle}{\sum_m(\boldsymbol{K}^{-1}_{\mathrm{CC}})^{ml}A^{ml}(\boldsymbol{k},0)}\ . \end{aligned} \tag{3.27}$$

Note that $A^{ml}(0,0)=\boldsymbol{K}^{ml}_{\mathrm{CC}}$; thus the quantity $\sum_m(\boldsymbol{K}^{-1}_{\mathrm{CC}})^{ml}A^{ml}(0,0)=1$. Further, taking the limit as s tends to zero (corresponding to the long-time limit of equilibrium processes) yields the Green-Kubo expression

$$L^{il} = \frac{V}{k_\mathrm{B}T}\int_0^\infty dt\big\langle J_{i,x}(0,t)\cdot J_{l,x}(0,0)\big\rangle\ . \tag{3.28}$$

Equivalent expressions can be obtained using the y- or z-components of $\boldsymbol{J}_i$ as well. We can thus average over all three spatial dimensions to obtain (after a change of indices) the final form of the Green-Kubo relations for transport coefficients L^{ij} as

$$L^{ij} = \frac{V}{3k_\mathrm{B}T}\int_0^\infty dt\big\langle\boldsymbol{J}_i(t)\cdot\boldsymbol{J}_j(0)\big\rangle\ . \tag{3.29}$$

Our definition for L^{i0} in Eq. (2.127) is automatically satisfied by Eq. (3.29):

$$L^{i0} = \frac{V}{3k_{\mathrm{B}}T}\int_0^\infty dt\big\langle \boldsymbol{J}_i(t)\cdot\boldsymbol{J}_0(0)\big\rangle \ . \tag{3.30}$$

Incorporating the constraint that all fluxes sum to zero yields

$$\begin{aligned} L^{i0} &= \frac{V}{3k_{\mathrm{B}}T}\int_0^\infty dt\Big\langle \boldsymbol{J}_i(t)\cdot\Big(-\sum_{j\neq 0}\frac{M_j}{M_0}\boldsymbol{J}_j(0)\Big)\Big\rangle \\ &= -\frac{V}{3k_{\mathrm{B}}T}\sum_{j\neq 0}\frac{M_j}{M_0}\int_0^\infty dt\big\langle \boldsymbol{J}_i(t)\cdot\boldsymbol{J}_j(0)\big\rangle = -\sum_{j\neq 0}\frac{M_j}{M_0}L^{ij} \ . \end{aligned} \tag{3.31}$$

In summary, we note that the derivation presented in this section has made use of the following assumptions: the system is an isotropic, isothermal, linear dielectric; there is no applied magnetic field; and changes in the dielectric constant with concentration are negligible. Furthermore, the final Green-Kubo relations capture only long wavelength fluctuations, i.e., they are valid on larger length scales for which we may assume electroneutrality.

3.2 Linear response theory

For systems which can be described with a Hamiltonian, the Green-Kubo relations for the transport coefficients L^{ij} can also be derived through linear response theory, where we couple the system to a weak external perturbation and observe the resulting response. This derivation parallels that of Evans and Morriss [52] as well as Wheeler and Newman [53].

Let a system in equilibrium be described by a Hamiltonian $H = H_0(\{\boldsymbol{r}^\alpha, \boldsymbol{p}^\alpha\})$, where $\{\boldsymbol{r}^\alpha, \boldsymbol{p}^\alpha\}$ is the set of all particle positions and momenta. For a conservative system, H_0 gives the sum of the kinetic and potential energy of the system. Time evolution of the system is governed by Hamilton's equations of motion, $\dot{\boldsymbol{r}}^\alpha = \frac{\partial H_0}{\partial \boldsymbol{p}^\alpha}$ and $\dot{\boldsymbol{p}}^\alpha = -\frac{\partial H_0}{\partial \boldsymbol{r}^\alpha}$.

We now introduce a small, constant external force on the equilibrium ensemble. The Hamiltonian for this perturbed system H is

$$H = H_0 - \sum_j \boldsymbol{\mathcal{R}}_j\cdot\boldsymbol{\mathcal{F}}_j \ , \tag{3.32}$$

where $\boldsymbol{\mathcal{F}}_j$ is a force acting on species j and $\boldsymbol{\mathcal{R}}_j$ is a function of the position of species j. For sufficiently small $\boldsymbol{\mathcal{F}}_j$, the expectation value of any observable $\boldsymbol{\mathcal{B}}$ in this perturbed system (derived in Evans and Morriss [52]) is:

$$\big\langle \boldsymbol{\mathcal{B}}(t)\big\rangle = \big\langle \boldsymbol{\mathcal{B}}(0)\big\rangle_0 + \beta\int_0^t ds\big\langle \boldsymbol{\mathcal{B}}(s)\sum_j \dot{\boldsymbol{\mathcal{R}}}_j(0)\cdot\boldsymbol{\mathcal{F}}_j\big\rangle_0 \ , \tag{3.33}$$

where the notation $< >_0$ denotes an average over the equilibrium ensemble corresponding to H_0.

For electrolyte solutions, we choose $\boldsymbol{\mathcal{F}}_j = \boldsymbol{X}_j c_j V$, where once again $\boldsymbol{X}_j = -\boldsymbol{\nabla}\overline{\mu}_j$, and $\boldsymbol{\mathcal{R}}_j = \overline{\boldsymbol{r}}_j - \overline{\boldsymbol{r}}$. The quantity $\overline{\boldsymbol{r}}_j$ is the average position of species j, i.e., $\overline{\boldsymbol{r}}_j = \frac{1}{N_j}\sum_\alpha \boldsymbol{r}_j^\alpha$, where the notation $\boldsymbol{r}_j^\alpha$ refers to an atom/molecule α of type j and N_j is the number of particles of species j. The quantity $\overline{\boldsymbol{r}}$ is the center-of-mass position of the system, defined using the mass of each particle α, m^α, as $\overline{\boldsymbol{r}} = (\sum_\alpha m^\alpha \boldsymbol{r}^\alpha)/\sum_\beta m^\beta$. This choice of $\boldsymbol{\mathcal{F}}_j$ and $\boldsymbol{\mathcal{R}}_j$ corresponds to a perturbed Hamiltonian of

$$H = H_0 - \sum_j (\overline{\boldsymbol{r}}_j - \overline{\boldsymbol{r}}) \cdot \boldsymbol{X}_j c_j V \ . \tag{3.34}$$

This perturbation to the Hamiltonian modifies both the energy of the system as well as the equations of motion, which can now be written as $\dot{\boldsymbol{r}}^\alpha = \frac{\partial H_0}{\partial \boldsymbol{p}^\alpha}$ and $\dot{\boldsymbol{p}}^\alpha = -\frac{\partial H_0}{\partial \boldsymbol{r}^\alpha} - \boldsymbol{\nabla}\overline{\mu}_i$, where the additional force $-\boldsymbol{\nabla}\overline{\mu}_i$ is only applied to atoms α corresponding to type i. It is clear how the presence of $\boldsymbol{\nabla}\overline{\mu}_i$ results in an additional force driving the acceleration of particle α down its electrochemical potential gradient. In the absence of chemical potential gradients, the second equation of motion simply reduces to $\dot{\boldsymbol{p}}^\alpha = -\frac{\partial H_0}{\partial \boldsymbol{r}^\alpha} + \hat{q}^\alpha \boldsymbol{E}$.

Noting that $\dot{\boldsymbol{\mathcal{R}}}_j = \boldsymbol{v}_j - \boldsymbol{v}$, the quantity $\sum_j \dot{\boldsymbol{\mathcal{R}}}_j(0) \cdot \boldsymbol{\mathcal{F}}_j$ appearing in Eq. (3.33) is

$$\sum_j \dot{\boldsymbol{\mathcal{R}}}_j(0) \cdot \boldsymbol{\mathcal{F}}_j = \sum_j c_j V (\boldsymbol{v}_j(0) - \boldsymbol{v}(0)) \cdot \boldsymbol{X}_j \ . \tag{3.35}$$

Recalling the definition of species flux, $\boldsymbol{J}_i = c_i(\boldsymbol{v}_i - \boldsymbol{v})$, we can rewrite Eq. (3.35) as

$$\sum_j \dot{\boldsymbol{\mathcal{R}}}_j(0) \cdot \boldsymbol{\mathcal{F}}_j = \sum_j \boldsymbol{J}_j(0) \cdot \boldsymbol{X}_j V \ . \tag{3.36}$$

Substituting Eq. (3.36) into Eq. (3.33) gives

$$\big\langle \boldsymbol{\mathcal{B}}(t) \big\rangle = \big\langle \boldsymbol{\mathcal{B}}(0) \big\rangle_0 + V\beta \int_0^t ds \big\langle \boldsymbol{\mathcal{B}}(s) \sum_j \boldsymbol{J}_j(0) \cdot \boldsymbol{X}_j \big\rangle_0 \ . \tag{3.37}$$

We proceed by choosing $\boldsymbol{\mathcal{B}} = \boldsymbol{J}_i$, yielding

$$\big\langle \boldsymbol{J}_i(t) \big\rangle = \big\langle \boldsymbol{J}_i(0) \big\rangle_0 + V\beta \int_0^t ds \big\langle \boldsymbol{J}_i(s) \sum_j \boldsymbol{J}_j(0) \cdot \boldsymbol{X}_j \big\rangle_0 \ . \tag{3.38}$$

The quantity $\big\langle \boldsymbol{J}_i(0) \big\rangle_0$ is equal to zero, as there is no net flux of any species at equilibrium. Furthermore, $\boldsymbol{X}_j$ is time-independent and can be written outside the time integral. Thus, Eq. (3.38) can be written as

$$\big\langle \boldsymbol{J}_i(t) \big\rangle = V\beta \int_0^t ds \big\langle \sum_j \boldsymbol{J}_i(s) \otimes \boldsymbol{J}_j(0) \big\rangle_0 \boldsymbol{X}_j = \sum_j \boldsymbol{L}^{ij} \boldsymbol{X}_j \ , \tag{3.39}$$

where in the last equality we have incorporated Eq. (2.121). Taking the limit as t approaches infinity to get the long-time behavior of the system allows us to obtain an expression for $\boldsymbol{L}^{ij}$:

$$\boldsymbol{L}^{ij} = V\beta \int_0^\infty dt \big\langle \boldsymbol{J}_i(t) \otimes \boldsymbol{J}_j(0) \big\rangle_0 \ . \tag{3.40}$$

Once again assuming isotropy, we reach the same Green-Kubo relations as obtained previously (Eq. (3.29)):

$$L^{ij} = \frac{V}{3k_\mathrm{B}T} \int_0^\infty dt \big\langle \boldsymbol{J}_i(t) \cdot \boldsymbol{J}_j(0) \big\rangle \ , \tag{3.41}$$

where we have now omitted the subscript 0 on the equilibrium ensemble average.

Note that the derivation presented in this section is contingent on choosing the correct form of the modified Hamiltonian. Here, we chose the positions and force ($\boldsymbol{\mathcal{R}}_j$ and $\boldsymbol{\mathcal{F}}_j$) specifically so that the final Green-Kubo relations would be equivalent to that derived in Sec. 3.1. These $\boldsymbol{\mathcal{R}}_j$ and $\boldsymbol{\mathcal{F}}_j$ are not known *a priori*, however, and therefore a fully rigorous derivation of the Green-Kubo relations should be done using the mass balance, as in Sec. 3.1.

Chapter 4

Contextualization of the Onsager Transport Framework[1]

In this chapter, we provide a summary of the Onsager transport framework derived in the previous chapters and provide additional contextualization regarding its relation to other transport frameworks. We begin in Chapter 4.1 by describing the physical interpretation of the Onsager transport coefficients, L^{ij}, which capture correlations in ion motion. We subsequently describe how the Onsager framework maps onto other common ways of analyzing electrolyte transport, including the Stefan-Maxwell equations and the limit of infinite dilution (Chapter 4.2). In Chapter 4.3 we derive relations between L^{ij} and experimentally-relevant quantities such as the conductivity and salt diffusion coefficient, then in Chapter 4.4 we present governing equations for mass transport in electrolytes in terms of these experimental transport parameters. Finally, in Chapter 4.5 we demonstrate application of the Onsager framework to a model electrolyte, LiCl in dimethyl sulfoxide. Here, we use molecular simulations and experimental measurements to demonstrate how L^{ij} may look in a simple system and what insights we can gain from analyzing these transport coefficients.

4.1 Physical interpretation of the Onsager transport coefficients

The physical interpretation of the Onsager transport coefficients, L^{ij}, is readily apparent given the Green-Kubo relations (Eq. (3.29)):

$$L^{ij} = \frac{V}{3k_{\mathrm{B}}T}\int_0^\infty dt \big\langle \boldsymbol{J}_i(t)\cdot\boldsymbol{J}_j(0)\big\rangle \ .$$

[1]This chapter is closely adapted from portions of Ref. [1]: Fong, K. D., Bergstrom, H. K., McCloskey, B. D. & Mandadapu, K. K. Transport phenomena in electrolyte solutions: Non-equilibrium thermodynamics and statistical mechanics. *AIChE Journal* e17091 (2020), and Ref. [54]: Fong, K. D., Self, J., McCloskey, B. D. & Persson, K. A. Ion correlations and their impact on transport in polymer-based electrolytes. *Macromolecules* **54**, 2575–2591 (2021)

As these expressions consist of correlation functions between fluxes, it is clear that L^{ij} captures the extent of correlation between the motion of species i and j. Further insight into these equations can be obtained by noting that the Green-Kubo relations of Eq. (3.29) may be equivalently written in terms of particle positions, rather than velocities. This form of the equation is analogous to computing self-diffusion coefficients from the mean-squared displacement of particle positions:

$$L^{ij} = \frac{1}{6k_{\mathrm{B}}TV} \lim_{t\to\infty} \frac{d}{dt} \Big\langle \sum_{\alpha} [\boldsymbol{r}_i^{\alpha}(t) - \boldsymbol{r}_i^{\alpha}(0)] \cdot \sum_{\beta} [\boldsymbol{r}_j^{\beta}(t) - \boldsymbol{r}_j^{\beta}(0)] \Big\rangle. \tag{4.1}$$

Here, and throughout the remainder of this dissertation, $\boldsymbol{r}_i^{\alpha}$ denotes the position of particle α relative to the center-of-mass position of the entire system. Let us consider the diagonal terms of the transport matrix, L^{ii}:

$$L^{ii} = \frac{1}{6k_{\mathrm{B}}TV} \lim_{t\to\infty} \frac{d}{dt} \sum_{\alpha} \sum_{\beta} \big\langle [\boldsymbol{r}_i^{\alpha}(t) - \boldsymbol{r}_i^{\alpha}(0)] \cdot [\boldsymbol{r}_i^{\beta}(t) - \boldsymbol{r}_i^{\beta}(0)] \big\rangle. \tag{4.2}$$

These transport coefficients are composed of two contributions: when $\alpha = \beta$, we take the autocorrelation function of the flux of particle α, and when $\alpha \neq \beta$, we compute the cross-correlations between two distinct particles. These two contributions may be denoted as self and distinct terms, respectively:

$$L^{ii}_{\mathrm{self}} = \frac{1}{6k_{\mathrm{B}}TV} \lim_{t\to\infty} \frac{d}{dt} \sum_{\alpha} \big\langle [\boldsymbol{r}_i^{\alpha}(t) - \boldsymbol{r}_i^{\alpha}(0)]^2 \big\rangle, \tag{4.3}$$

$$L^{ii}_{\mathrm{distinct}} = \frac{1}{6k_{\mathrm{B}}TV} \lim_{t\to\infty} \frac{d}{dt} \sum_{\alpha} \sum_{\beta\neq\alpha} \big\langle [\boldsymbol{r}_i^{\alpha}(t) - \boldsymbol{r}_i^{\alpha}(0)] \cdot [\boldsymbol{r}_i^{\beta}(t) - \boldsymbol{r}_i^{\beta}(0)] \big\rangle. \tag{4.4}$$

Note that $L^{ii} = L^{ii}_{\mathrm{self}} + L^{ii}_{\mathrm{distinct}}$. From this decomposition, we can further interpret the physical significance of L^{ii}: it includes both correlations between particles of the same species (non-idealities, captured in the distinct terms) as well as ideal, uncorrelated particle motion captured in the self terms. The latter corresponds to simple Brownian motion of each ion and may be directly related to the self-diffusion coefficient by

$$L^{ii}_{\mathrm{self}} = \frac{D_i c_i}{k_{\mathrm{B}}T} \ . \tag{4.5}$$

As noted in Chapter 2.2, the second law of thermodynamics imposes some restrictions on the possible values of each transport coefficient. While the distinct terms may take on positive or negative values, the self terms and the overall L^{++} and L^{--} must always be positive.

The physical interpretations of L^{ij}, L^{ii}_{self}, and $L^{ii}_{\mathrm{distinct}}$ are illustrated schematically in Figure 4.1. Although these schematics are for the specific case of a polyanionic system, the discussion below is readily generalized to any binary electrolyte. Let us first consider $L^{++}_{\mathrm{distinct}}$ (upper middle panel). In general, two distinct cations will move in an anti-correlated

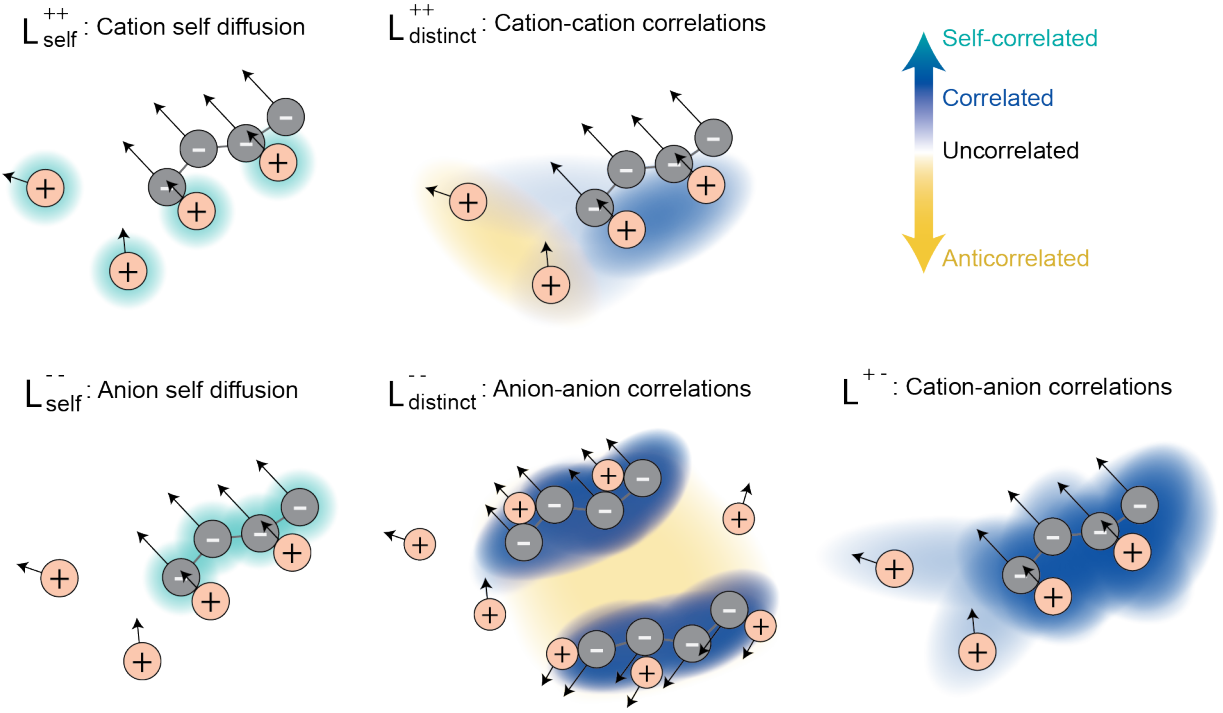

Figure 4.1: Schematic illustration of the types of ion motion and correlations captured by each transport coefficient L^{ij}. The colorbar in the upper right qualitatively indicates the type of ion correlation (or lack thereof), and the arrows on each ion indicate direction of motion.

manner due to electrostatic repulsion, as illustrated by the yellow shading between the two free cations in the figure. This will yield a negative contribution to L^{++}_{distinct}. The motion of two cations which are part of the same aggregate (in this case ionically bound to the same polyanion chain), however, will be positively correlated ($L^{++}_{\text{distinct}} > 0$, indicated by blue shading in the figure). The intuition governing L^{--}_{distinct} (Figure 4.1, lower middle panel) is similar. Distinct polyanionic chains will electrostatically repel and thus be anti-correlated, whereas anions within a given chain will be very strongly correlated.

The transport coefficients in which $i \neq j$ quantify correlations between different types of species. Herein we consider only L^{+-}, describing cation-anion correlation in a binary salt solution. With the exception of certain systems which will be discussed below, L^{+-} is generally positive due to the electrostatic attraction between cations and anions (Figure 4.1, lower right panel). This correlation will be strongest for ions that are directly paired, although long-range electrostatic interactions will also contribute to L^{+-}. Note that L^{+-} captures the total extent of correlation between all cation-anion pairs, i.e., the sum of all individual cation-anion correlations, rather than the average correlation between any given ion pair.

4.2 Relating various frameworks for electrolyte transport

The Onsager framework is advantageous in that (i) it emerges directly from the theory of linear irreversible thermodynamics and (ii) it yields transport coefficients (L^{ij}) which possess clear physical interpretation, as described in the previous section. However, the transport relations between $\boldsymbol{X}_i$ and $\boldsymbol{J}_i$ (Eq. (2.128)) derived in this work differ from the most common conventions describing transport phenomena in electrolytes and those typically analyzed in experiments [2, 21]. In this section, we briefly summarize these other major conventions, then give relations for interconverting between them.

I. Stefan-Maxwell equations. As described in Chapter 1, the most ubiquitous convention for electrolyte transport is the Stefan-Maxwell equations for multi-component diffusion,

$$c_i \boldsymbol{\nabla} \overline{\mu}_i = \sum_{j \neq i} K^{ij} (\boldsymbol{v}_j - \boldsymbol{v}_i) \ , \tag{4.6}$$

which describe the force on species i as linearly proportional to the relative friction between species i and each of the other species in the system. Rather than describing particle motion with respect to a reference velocity such as $\boldsymbol{v}$, the Stefan-Maxwell framework is written in terms of the relative velocity of two species. Recall that K^{ij} may be written in terms of the binary interaction diffusion coefficients D^{ij}, also called the Stefan-Maxwell diffusion coefficients, as $K^{ij} = \frac{RTc_i c_j}{c_{\mathrm{T}} D^{ij}}$. Physically, K^{ij} may be interpreted as quantifying the friction between species i and j. For gaseous systems, this friction has a clear atomistic interpretation in terms of collisions between particles. The connection between K^{ij} and molecular-level motion in a liquid electrolyte, however, is more complex.

II. Solvent velocity reference system. It is also common to choose yet another convention, with $\boldsymbol{X}_i^{\mathrm{s}} = -c_i \boldsymbol{\nabla} \overline{\mu}_i$ and $\boldsymbol{J}_i^{\mathrm{s}} = (\boldsymbol{v}_i - \boldsymbol{v}_0)$, where we use the superscript s to denote that the flux of species i ($\boldsymbol{J}_i^{\mathrm{s}}$) is described with respect to the solvent velocity $\boldsymbol{v}_0$ [2, 32, 53]. The use of $\boldsymbol{v}_0$ as the reference velocity is sometimes referred to as the Hittorf reference system [55]. The choice of $\boldsymbol{X}_i^{\mathrm{s}}$ as $-c_i \boldsymbol{\nabla} \overline{\mu}_i$ is particularly convenient given the form of the chemical potential in the dilute/ideal limit (discussed in more detail in the following section): $\mu_i = \mu_i^o + RT \ln c_i$. In this case, $-c_i \boldsymbol{\nabla} \mu_i = -RT \boldsymbol{\nabla} c_i$, and we recover the familiar result from Fick's law, in which the negative gradient of concentration is the driving force for diffusive flux.

The expressions for $\boldsymbol{X}_i^{\mathrm{s}}$ and $\boldsymbol{J}_i^{\mathrm{s}}$ can also be motivated directly from our entropy production expression (Eq. (2.103)) if we apply the Gibbs-Duhem equation for electroneutral systems at constant temperature, pressure, and electric field, i.e., $\sum_i c_i \boldsymbol{\nabla} \overline{\mu}_i = 0$ or $\boldsymbol{\nabla} \overline{\mu}_0 = -\sum_{i \neq 0} \frac{c_i}{c_0} \boldsymbol{\nabla} \overline{\mu}_i$ (Eq. (A.27)), instead of applying the constraint that all mass fluxes must sum to zero. In this case, the entropy production in Eq. (2.103) at constant tempera-

ture and $\boldsymbol{b}_i = 0$ becomes

$$\sigma_{\mathrm{i}} = -\sum_i \boldsymbol{\nabla}\overline{\mu}_i \cdot \boldsymbol{J}_i = -\sum_{i\neq 0} \boldsymbol{\nabla}\overline{\mu}_i \cdot (\boldsymbol{J}_i - \boldsymbol{J}_0) = -\sum_{i\neq 0} \boldsymbol{\nabla}\overline{\mu}_i \cdot [c_i(\boldsymbol{v}_i - \boldsymbol{v}_0)] \ . \tag{4.7}$$

From Eq. (4.7) it is clear that both $\boldsymbol{X}_i$ and $\boldsymbol{J}_i$ as well as $\boldsymbol{X}_i^{\mathrm{s}}$ and $\boldsymbol{J}_i^{\mathrm{s}}$ yield the same total entropy production and are thus both consistent with linear irreversible thermodynamics. The choices of $\boldsymbol{X}_i^{\mathrm{s}}$ and $\boldsymbol{J}_i^{\mathrm{s}}$, and corresponding linear relations, yield the following transport coefficient equations:

$$c_i \boldsymbol{\nabla}\overline{\mu}_i = \sum_{j\neq 0} M^{ij^{\mathrm{s}}}(\boldsymbol{v}_j - \boldsymbol{v}_0) \ , \tag{4.8}$$

and

$$(\boldsymbol{v}_i - \boldsymbol{v}_0) = -\sum_{j\neq 0} L^{ij^{\mathrm{s}}} c_j \boldsymbol{\nabla}\overline{\mu}_j \ . \tag{4.9}$$

Note that, by convention, the negative sign in the thermodynamic driving force has been absorbed into $M^{ij^{\mathrm{s}}}$, and therefore $\boldsymbol{L}^{\mathrm{s}} = -\boldsymbol{M}^{\mathrm{s}^{-1}}$.

Although both reference velocities give equivalent entropy production, only the mass-averaged velocity reference system can be cleanly integrated into the mass balance, which forms the basis for the regression hypothesis and derivations of the Green-Kubo relations in Sec. 3.1. Wheeler and Newman [53] have obtained Green-Kubo expressions for $L^{ij^{\mathrm{s}}}$ using the linear response approach of Sec. 3.2; their choice of modified Hamiltonian yields expressions for $L^{ij^{\mathrm{s}}}$ in terms of $\boldsymbol{J}_i^{\mathrm{s}}$, the species flux with respect to the solvent velocity. This Hamiltonian may not be consistent with conservation of mass as written in Eq. (2.5), which is with respect to the barycentric velocity and not the solvent velocity. Indeed, the $L^{ij^{\mathrm{s}}}$ obtained from our L^{ij} by the mapping described in the following sections (Secs. 4.2 and 4.2) may not be consistent with $L^{ij^{\mathrm{s}}}$ given by Wheeler and Newman's Green-Kubo relations. Their expressions thus may not correspond to true diffusive transport in the system.

III. Infinitely dilute solutions. While the Stefan-Maxwell equations and solvent velocity reference systems aim to fully capture solution non-idealities (correlations in ion motion), it is also very common to analyze transport by neglecting all solution non-idealities, i.e., $L^{ij} = 0$ for $i \neq j$ and $L^{ii}_{\mathrm{distinct}} = 0$. This analysis is only rigorously correct in the limit of infinite dilution but is routinely applied to non-dilute electrolyte as well, as it greatly simplifies both computational and experimental analysis of the system. This approximation is referred to as the Nernst-Einstein assumption.

Relating the Onsager transport and Stefan-Maxwell equations

In this section we provide a mapping between the Onsager transport coefficients L^{ij} in Eq. (2.128) and the Stefan-Maxwell transport coefficients K^{ij} (Eq. (4.6)). The methodology to obtain this mapping parallels that described by Bird for non-electrolyte multicomponent systems [56].

We begin by rewriting Eq. (2.128) as

$$\boldsymbol{v}_i - \boldsymbol{v} = -\sum_k \hat{L}^{ik} c_k \boldsymbol{\nabla} \overline{\mu}_k \ , \tag{4.10}$$

where, for convenience, we have defined the quantity $\hat{L}^{ik} = \frac{L^{ik}}{c_i c_k}$. Subtracting Eq. (4.10) for species i and j and multiplying by K^{ij} gives

$$K^{ij}(\boldsymbol{v}_j - \boldsymbol{v}_i) = K^{ij} \sum_k \left[\hat{L}^{ik} - \hat{L}^{jk}\right] c_k \boldsymbol{\nabla} \overline{\mu}_k \ . \tag{4.11}$$

Summing over $j \neq i$ yields

$$\sum_{j \neq i} K^{ij}(\boldsymbol{v}_j - \boldsymbol{v}_i) = \sum_k \sum_{j \neq i} K^{ij} \left[\hat{L}^{ik} - \hat{L}^{jk}\right] c_k \boldsymbol{\nabla} \overline{\mu}_k \ . \tag{4.12}$$

This equation takes on the form of the Stefan-Maxwell equations (Eq. (4.6)) if

$$\sum_k \sum_{j \neq i} K^{ij} \left[\hat{L}^{ik} - \hat{L}^{jk}\right] c_k \boldsymbol{\nabla} \overline{\mu}_k = c_i \boldsymbol{\nabla} \overline{\mu}_i \ , \tag{4.13}$$

subject to the additional constraint that $\sum_i M_i L^{ij} = 0$. Following Bird [56], we observe that these equations can be satisfied if we choose

$$\sum_{j \neq i} K^{ij} \left[\hat{L}^{ik} - \hat{L}^{jk}\right] = \delta_{ik} - \omega_i \ , \tag{4.14}$$

where $\omega_i = \rho_i / \rho$ is the mass fraction of species i. We first verify that Eq. (4.14) transforms Eq. (4.12) into the Stefan-Maxwell equations:

$$\sum_{j \neq i} K^{ij}(\boldsymbol{v}_j - \boldsymbol{v}_i) = \sum_k \delta_{ik} c_k \boldsymbol{\nabla} \overline{\mu}_k - \sum_k \omega_i c_k \boldsymbol{\nabla} \overline{\mu}_k = c_i \boldsymbol{\nabla} \overline{\mu}_i \ , \tag{4.15}$$

where the last equality is obtained by invoking the Gibbs-Duhem equation. While Eq. (4.14) yields the Stefan-Maxwell equations without the inclusion of the ω_i term, we require the latter to satisfy the constraint $\sum_i M_i L^{ij} = 0$. We verify that this constraint is satisfied by multiplying Eq. (4.14) by $M_k c_k$ and summing over k, resulting in

$$\sum_k M_k c_k \sum_{j \neq i} K^{ij} \left[\hat{L}^{ik} - \hat{L}^{jk}\right] = \sum_k M_k c_k \delta_{ik} - \sum_k M_k c_k \omega_i \ . \tag{4.16}$$

Rearranging and noting that $\sum_k M_k c_k = \sum_k \rho_k = \rho$, we obtain

$$\sum_{j \neq i} K^{ij} \left[\frac{1}{c_i} \sum_k M_k L^{ik} - \frac{1}{c_j} \sum_k M_k L^{jk}\right] = \rho_i - \rho_i \ , \tag{4.17}$$

where invoking the constraint $\sum_i M_i L^{ij} = 0$ gives $0 = 0$, as required.

To convert Eq. (4.14) into a more useful form, let us define the matrix $\boldsymbol{W}_i$ with components $(\boldsymbol{W}_i)_{jk} = \hat{L}^{jk} - \hat{L}^{ik}$ $(j, k \neq i)$. We can rewrite Eq. (4.14) in terms of $\boldsymbol{W}_i$ as

$$\sum_{j \neq i} K^{ij} (\boldsymbol{W}_i)_{jk} = \omega_i \qquad (i \neq k) \ . \tag{4.18}$$

Multiplying by $(\boldsymbol{W}_i^{-1})_{kl}$ and summing over k gives (after a change of indices)

$$K^{ij} = \omega_i \sum_{k \neq i} (\boldsymbol{W}_i^{-1})_{kj} \qquad (i \neq j) \ . \tag{4.19}$$

Analogously, the constraint $\sum_j M_j L^{jk} = 0$ can be rewritten as

$$\sum_j M_j c_j c_k [\hat{L}^{jk} - \hat{L}^{ik}] + \sum_j M_j c_j c_k \hat{L}^{ik} = 0 \ , \tag{4.20}$$

or, upon rearranging:

$$\sum_{j \neq i} \omega_j (\boldsymbol{W}_i)_{jk} = -\hat{L}^{ik} \qquad (i \neq k) \ . \tag{4.21}$$

Equivalently,

$$\sum_{k \neq i} \hat{L}^{ik} (\boldsymbol{W}_i^{-1})_{kj} = -\omega_j \qquad (i \neq j) \ . \tag{4.22}$$

Combining Eqs. (4.19) and (4.22) yields our final equation mapping K^{ij} and L^{ij}:

$$\frac{1}{K^{ij}} = -\frac{1}{\omega_i \omega_j} \frac{\sum_{k \neq i} \hat{L}^{ik} (\boldsymbol{W}_i^{-1})_{kj}}{\sum_{k \neq i} (\boldsymbol{W}_i^{-1})_{kj}} \qquad (i \neq j) \ . \tag{4.23}$$

For a two-component electrolyte such as an ionic liquid, the mapping in Eq. (4.23) can be written as

$$K^{+-} = \frac{-\omega_+ \omega_-}{\hat{L}^{+-}} = \frac{\omega_-^2}{\hat{L}^{++}} = \frac{\omega_+^2}{\hat{L}^{--}} \ , \tag{4.24}$$

where in the second and third equalities we have used the constraint $\sum_i M_i L^{ij} = 0$. For a three-component system, such as an electrolyte with binary salt and solvent, we obtain

$$\begin{aligned} K^{+-} &= \omega_+ \omega_- \frac{\hat{L}^{00} + \hat{L}^{+-} - \hat{L}^{+0} - \hat{L}^{-0}}{\hat{L}^{+0} \hat{L}^{-0} - \hat{L}^{+-} \hat{L}^{00}} \ , \\ K^{+0} &= \omega_+ \omega_0 \frac{\hat{L}^{--} + \hat{L}^{+0} - \hat{L}^{+-} - \hat{L}^{-0}}{\hat{L}^{+-} \hat{L}^{-0} - \hat{L}^{+0} \hat{L}^{--}} \ , \\ K^{-0} &= \omega_- \omega_0 \frac{\hat{L}^{++} + \hat{L}^{-0} - \hat{L}^{+-} - \hat{L}^{+0}}{\hat{L}^{+-} \hat{L}^{+0} - \hat{L}^{-0} \hat{L}^{++}} \ . \end{aligned} \tag{4.25}$$

Equation (4.23) may be used to obtain analogous expressions for systems with an arbitrary number of ionic components. Unlike L^{ij}, there is no Green-Kubo relation to directly compute K^{ij} from molecular dynamics simulations. Those works which do report Stefan-Maxwell coefficients from simulations do so by first computing the Onsager transport coefficients then mapping from L^{ij} to K^{ij} [53, 57–59]. Alternative methods for computing the Stefan-Maxwell coefficients directly have been proposed [60,61], although their accuracy is somewhat contentious [53].

Finally, we note that both the Onsager and Stefan-Maxwell equations can be used for continuum-level transport modeling [62–65] to predict concentration and potential profiles at a system level and can be used to obtain experimentally-measurable quantities [2]. However, doing so is more challenging in the Stefan-Maxwell framework. Formulating the governing equations for macroscopic transport or writing expressions for experimentally measured properties relies on solving for the velocities of each species in solution; while this is trivial in the Onsager transport equations (Eq. (2.128)), it requires extensive algebra in the Stefan-Maxwell equations (inverting the matrix of all K^{ij}). This yields more complex expressions in the Stefan-Maxwell framework. The ionic conductivity of a binary salt in terms of D^{ij}, for example, is [2]

$$\kappa = \left[\frac{-RT}{c_{\mathrm{T}} z_+ z_- F^2}\left(\frac{1}{D^{+-}} - \frac{c_0 z_-}{c_+(z_+ D^{0+} - z_- D^{0-})}\right)\right]^{-1} . \tag{4.26}$$

This relation is substantially more complex than that emerging from the Onsager framework (Eq. (4.53)). Generalizations to multicomponent solutions beyond a binary salt, while trivial in terms of L^{ij}, are much more involved and rarely reported in the Stefan-Maxwell framework.

Relating the Onsager transport framework and the solvent reference velocity system

The relationship between the Onsager transport coefficients L^{ij} defined with reference to the barycentric velocity (Eq. (2.128)) and those of the solvent reference velocity system $L^{ij^{\mathrm{s}}}$ (Eq. (4.9)) are not straightforward. We can, however, easily map between the Stefan-Maxwell and solvent reference velocity frameworks. This mapping, in conjunction with Eq. (4.23) relating the Stefan-Maxwell and Onsager transport coefficients, allows us to connect L^{ij} and $L^{ij^{\mathrm{s}}}$.

The mapping between the Stefan-Maxwell coefficients K^{ij} and $M^{ij^{\mathrm{s}}}$ of the solvent reference velocity conventions is well-established [2]:

$$M^{ij^{\mathrm{s},0}} = K^{ij} - \delta_{ij}\sum_k K^{ik} , \tag{4.27}$$

where the superscript 0 indicates that the matrix $\boldsymbol{M}^{\mathrm{s},0}$ includes components from all species, including the solvent. As discussed previously, when all species are included, the components

of the transport matrix are not all independent due to the fact that there are only $n-1$ independent force/flux equations for an n-component system (as seen by either the Gibbs-Duhem equation or the fact that all fluxes must sum to zero). The independent components of the transport matrix are given by the submatrix eliminating the row and column corresponding to one species, typically the solvent. The components of this submatrix are the $M^{ij^{\mathrm{s}}}$ defined in Eq. (4.8). Recall that the submatrix $\boldsymbol{M}^{\mathrm{s}}$ is related to $\boldsymbol{L}^{\mathrm{s}}$ via $\boldsymbol{L}^{\mathrm{s}} = -\boldsymbol{M}^{\mathrm{s}^{-1}}$. Thus, L^{ij} may be mapped to $L^{ij^{\mathrm{s}}}$ via the following process: L^{ij} may be related to K^{ij} using Eq. (4.23), K^{ij} may be related to $M^{ij^{\mathrm{s},0}}$ with Eq. (4.27), $\boldsymbol{M}^{\mathrm{s},0}$ may be converted into the submatrix with components $M^{ij^{\mathrm{s}}}$, and finally $\boldsymbol{M}^{\mathrm{s}}$ may be inverted to give $L^{ij^{\mathrm{s}}}$.

In what follows, we demonstrate this mapping procedure for a binary electrolyte, consisting of a single cation, single anion, and solvent. The relation between the Stefan-Maxwell and Onsager transport coefficients have already been written for a binary electrolyte in Eq. (4.25). All that remains is to explicitly write $L^{ij^{\mathrm{s}}}$ in terms of the Stefan-Maxwell coefficients. We choose to give this mapping in terms of the Stefan Maxwell diffusion coefficients, D^{ij}, rather than K^{ij}, as this will be useful in a later section. Writing out the components of $\boldsymbol{K}$ in terms of D^{ij} gives

$$\boldsymbol{K} = \frac{RT}{c_{\mathrm{T}}} \begin{bmatrix} \frac{c_+^2}{D^{++}} & \frac{c_+c_-}{D^{+-}} & \frac{c_+c_0}{D^{+0}} \\ \frac{c_+c_-}{D^{+-}} & \frac{c_-^2}{D^{--}} & \frac{c_-c_0}{D^{-0}} \\ \frac{c_+c_0}{D^{+0}} & \frac{c_-c_0}{D^{-0}} & \frac{c_0^2}{D^{00}} \end{bmatrix} . \tag{4.28}$$

Now applying the mapping of Eq. (4.27), we obtain

$$\boldsymbol{M}^{\mathrm{s}^0} = \frac{RT}{c_{\mathrm{T}}} \begin{bmatrix} -(\frac{c_+c_-}{D^{+-}} + \frac{c_+c_0}{D^{+0}}) & \frac{c_+c_-}{D^{+-}} & \frac{c_+c_0}{D^{+0}} \\ \frac{c_+c_-}{D^{+-}} & -(\frac{c_+c_-}{D^{+-}} + \frac{c_-c_0}{D^{-0}}) & \frac{c_-c_0}{D^{-0}} \\ \frac{c_+c_0}{D^{+0}} & \frac{c_-c_0}{D^{-0}} & -(\frac{c_+c_0}{D^{+0}} + \frac{c_-c_0}{D^{-0}}) \end{bmatrix} . \tag{4.29}$$

As mentioned before, not all components of $\boldsymbol{M}^{\mathrm{s}^0}$ are independent. The independent coefficients are obtained by eliminating the row and column corresponding to the solvent, given by the submatrix

$$\boldsymbol{M}^{\mathrm{s}} = \frac{RT}{c_{\mathrm{T}}} \begin{bmatrix} -(\frac{c_+c_-}{D^{+-}} + \frac{c_+c_0}{D^{+0}}) & \frac{c_+c_-}{D^{+-}} \\ \frac{c_+c_-}{D^{+-}} & -(\frac{c_+c_-}{D^{+-}} + \frac{c_-c_0}{D^{-0}}) \end{bmatrix} . \tag{4.30}$$

Inverting $\boldsymbol{M}^{\mathrm{s}}$ and simplifying, we obtain the following expression for $\boldsymbol{L}^{s}$.

$$\boldsymbol{L}^{\mathrm{s}} = \frac{c_{\mathrm{T}}}{RT\gamma} \begin{bmatrix} c_+c_-D^{-0}D^{+0} + c_-c_0D^{+-}D^{+0} & c_+c_-D^{+0}D^{-0} \\ c_+c_-D^{+0}D^{-0} & c_+c_-D^{-0}D^{+0} + c_+c_0D^{+-}D^{-0} \end{bmatrix} , \tag{4.31}$$

where $\gamma = c_+^2c_-c_0D^{-0} + c_+c_-^2c_0D^{+0} + c_+c_-c_0^2D^{+-}$.

We have now outlined mappings between the Onsager and the Stefan-Maxwell coefficients (Eq. (4.23)), as well as between the Stefan-Maxwell coefficients and those of the solvent reference velocity framework (Eq. (4.31)), thus providing a relation between the Onsager and solvent-reference transport coefficients as well.

Behavior in the limit of infinite dilution

Here we show how the Onsager transport equations (Eq. (2.128)) behave in the limit of infinite dilution, thereby recovering the familiar Nernst-Planck equation for transport in an ideal electrolyte solution. In the case of infinite dilution, we can rewrite our expressions for both L^{ij} and $L^{ij^{\mathrm{s}}}$ by assuming that $c_{\mathrm{T}} \approx c_0 >> c_+, c_-$ and $\boldsymbol{v} \approx \boldsymbol{v}_0$. Using the latter expression and multiplying by c_i, Eq. (4.9) containing $L^{ij^{\mathrm{s}}}$ can be rewritten as

$$c_i(\boldsymbol{v}_i - \boldsymbol{v}) = -\sum_{j\neq 0} L^{ij^{\mathrm{s}}}_{\mathrm{dilute}} c_i c_j \boldsymbol{\nabla}\overline{\mu}_j \ . \tag{4.32}$$

Comparing to Eq. (2.128) containing L^{ij}, we can conclude that

$$L^{ij}_{\mathrm{dilute}} = c_i c_j L^{ij^{\mathrm{s}}}_{\mathrm{dilute}} \tag{4.33}$$

for $i, j \neq 0$.

Relation to self-diffusion coefficients. As in the previous sections, for brevity we now consider only binary electrolytes. Extensions to multicomponent systems are straightforward. Simplifying Eq. (4.31) under the assumption that $c_{\mathrm{T}} \approx c_0 >> c_+, c_-$ yields

$$\boldsymbol{L}^{\mathrm{s}}_{\mathrm{dilute}} = \frac{1}{RTc_+c_-c_0}\begin{bmatrix} c_-c_0D^{+0} & c_+c_-D^{+0}D^{-0}/D^{+-} \\ c_+c_-D^{+0}D^{-0}/D^{+-} & c_+c_0D^{-0} \end{bmatrix} \ . \tag{4.34}$$

We can also infer that there will no be correlations between distinct ions at infinite dilution, i.e., the cross-correlated transport coefficient $L^{+-} = 0$. In order for these off-diagonal terms of Eq. (4.34) to tend to 0, we require that $D^{+-} \to \infty$, yielding

$$\boldsymbol{L}^{\mathrm{s}}_{\mathrm{dilute}} = \frac{1}{RT}\begin{bmatrix} \frac{D^{+0}}{c_+} & 0 \\ 0 & \frac{D^{-0}}{c_-} \end{bmatrix} \ , \tag{4.35}$$

or, using Eq. (4.33),

$$\boldsymbol{L}_{\mathrm{dilute}} = \frac{1}{RT}\begin{bmatrix} D^{+0}c_+ & 0 \\ 0 & D^{-0}c_- \end{bmatrix} \ . \tag{4.36}$$

Equations (4.33), (4.35), and (4.36) provide direct relations between transport coefficients from the different frameworks, L^{ij}, $L^{ij^{\mathrm{s}}}$, and D^{ij}, in the limit of infinite dilution. Finally, these multicomponent transport coefficients at infinite dilution may also be related to the self-diffusion coefficients[2] of each individual species. To do so, we rewrite the Green-Kubo

[2]In some texts, the term 'self-diffusion coefficient' refers specifically to the motion of a labeled particle in a pure liquid of identical, unlabeled particles [66], whereas the diffusion of a labeled particle in a multicomponent system is referred to as an intradiffusion coefficient. In this text, however, we refer to both of these scenarios as self-diffusion coefficients, as both can be computed based on the translational Brownian motion of the particles [67].

relations for L^{ii}:

$$L^{ii} = \frac{Vc_i^2}{3k_\mathrm{B}T}\int_0^\infty dt \left\langle \left(\frac{1}{N_i}\sum_\alpha \boldsymbol{v}_i^\alpha(t) - \boldsymbol{v}(t)\right)\cdot\left(\frac{1}{N_i}\sum_\beta \boldsymbol{v}_i^\beta(0) - \boldsymbol{v}(0)\right)\right\rangle . \tag{4.37}$$

In addition to substituting $\boldsymbol{J}_i = c_i(\boldsymbol{v}_i - \boldsymbol{v})$, we have decomposed $\boldsymbol{v}_i$ into $\frac{1}{N_i}\sum_\alpha \boldsymbol{v}_i^\alpha$, where the index α enumerates all atoms/molecules of species i. Simplifying Eq. (4.37) yields

$$L^{ii} = \frac{Vc_i^2}{3k_\mathrm{B}TN_i^2}\int_0^\infty dt \left\langle \sum_\alpha\sum_\beta \left(\left(\boldsymbol{v}_i^\alpha(t) - \boldsymbol{v}(t)\right)\cdot\left(\boldsymbol{v}_i^\beta(0) - \boldsymbol{v}(0)\right)\right)\right\rangle . \tag{4.38}$$

Splitting the double sum in Eq. (4.38) to distinguish between cases where $\alpha = \beta$ (the self terms) and those where $\alpha \neq \beta$ (the distinct terms) results in

$$\begin{aligned} L^{ii} = \frac{Vc_i^2}{3k_\mathrm{B}TN_i^2}\Bigg[&\int_0^\infty dt \left\langle \sum_\alpha \left(\left(\boldsymbol{v}_i^\alpha(t) - \boldsymbol{v}(t)\right)\cdot\left(\boldsymbol{v}_i^\alpha(0) - \boldsymbol{v}(0)\right)\right)\right\rangle + \\ &\int_0^\infty dt \left\langle \sum_\beta\sum_{\alpha\neq\beta} \left(\left(\boldsymbol{v}_i^\alpha(t) - \boldsymbol{v}(t)\right)\cdot\left(\boldsymbol{v}_i^\beta(0) - \boldsymbol{v}(0)\right)\right)\right\rangle\Bigg] . \end{aligned} \tag{4.39}$$

This analysis is equivalent to the decomposition of L^{ii} into self and distinct terms as given in Eqs. (4.3) and (4.4): the first term in this equation describes self-correlations, while the second term captures correlations between distinct particles of type i, which are negligible at infinite dilution. Therefore, we observe that

$$L^{ii}_\mathrm{dilute} = L^{ii}_\mathrm{self} = \frac{Vc_i^2}{3k_\mathrm{B}TN_i^2}\sum_\alpha\left[\int_0^\infty dt \left\langle \left(\boldsymbol{v}_i^\alpha(t) - \boldsymbol{v}(t)\right)\cdot\left(\boldsymbol{v}_i^\alpha(0) - \boldsymbol{v}(0)\right)\right\rangle\right] . \tag{4.40}$$

The term in the square brackets is the integral of the velocity autocorrelation function, which is simply three times the self-diffusion coefficient of species i, D_i [68]. This yields

$$L^{ii}_\mathrm{dilute} = \frac{Vc_i^2}{3k_\mathrm{B}TN_i^2}[3N_iD_i] , \tag{4.41}$$

where the additional factor of N_i comes from summing over all atoms/molecules α of species i. Incorporating the fact that $c_i = N_i/V$, Eq. (4.41) becomes

$$L^{ii}_\mathrm{dilute} = \frac{D_ic_i}{RT} . \tag{4.42}$$

We have thus derived Eq. (4.5) given in the previous section. Equation (4.42) shows the relations between L^{ii}_dilute and the self-diffusion coefficients and, with Eq. (4.36), also implies that the Stefan-Maxwell diffusion coefficients D^{+0} and D^{-0} approach the self-diffusion coefficients D_+ and D_-, respectively, in the limit of infinite dilution.

Derivation of the Nernst-Planck equation. The above simplifications allow facile derivation of the Nernst-Planck equation for the flux of species i, $\boldsymbol{N}_i \coloneqq c_i \boldsymbol{v}_i$, at infinite dilution. Simplification of Eq. (2.128) for the case where all but the diagonal terms of the transport matrix are zero gives

$$c_i(\boldsymbol{v}_i - \boldsymbol{v}) = -L^{ii}_{\text{dilute}} \boldsymbol{\nabla} \overline{\mu}_i \ . \tag{4.43}$$

Further simplification and incorporation of Eq. (4.42) yields

$$c_i \boldsymbol{v}_i = -\frac{D_i c_i}{RT}(\boldsymbol{\nabla}\mu_i + z_i F \boldsymbol{\nabla}\phi) + c_i \boldsymbol{v} \ . \tag{4.44}$$

We may now incorporate the definition of $\boldsymbol{N}_i$ as well as the definition of chemical potential for an ideal solution: $\mu_i = \mu_i^\theta + RT \ln c_i$, implying $\boldsymbol{\nabla}\mu_i = \frac{RT}{c_i}\boldsymbol{\nabla} c_i$. Thus,

$$\boldsymbol{N}_i = -D_i \boldsymbol{\nabla} c_i - \frac{D_i c_i z_i F}{RT} \boldsymbol{\nabla}\phi + c_i \boldsymbol{v} \ . \tag{4.45}$$

As a final step, we apply the Einstein relation to relate the self-diffusion coefficient to the electrophoretic mobility u_i ($u_i = \frac{D_i z_i F}{RT}$) [68] to recover the Nernst-Planck equation:[3]

$$\boldsymbol{N}_i = -D_i \boldsymbol{\nabla} c_i - u_i c_i \boldsymbol{\nabla}\phi + c_i \boldsymbol{v} \ . \tag{4.46}$$

4.3 Relation to experimentally-relevant quantities

The Onsager transport coefficients L^{ij} are not directly measurable from experiments. They may, however, be explicitly related to quantities which can be accessed experimentally, namely the ionic conductivity, electrophoretic mobility, transference number, and salt diffusion coefficient. In this section, we derive expressions for each of these experimentally measurable quantities in terms of L^{ij}. Utilizing our derived Green-Kubo relations for L^{ij} (Eq. (3.29)), we also provide Green-Kubo expressions for some of these experimentally measurable quantities so that they can be calculated directly in molecular simulations. Finally, we give expressions for L^{ij} in terms of the aforementioned experimentally measurable quantities for the special case of a binary solution.

Ionic conductivity

We begin by deriving an expression for the ionic conductivity in terms of L^{ij}. Consider a solution of uniform composition, i.e. with no gradients in chemical potential, such that

[3] In this work, the mobility is defined as $u_i = \frac{\boldsymbol{v}_i - \boldsymbol{v}}{\boldsymbol{E}}$, describing the velocity of a species in response to an electric field. In some texts [2], the mobility is instead defined as $u_i' = \frac{(\boldsymbol{v}_i - \boldsymbol{v})}{z_i F \boldsymbol{E}} = \frac{u_i}{z_i F}$. The Nernst-Planck equation using this convention is $\boldsymbol{N}_i = -D_i \boldsymbol{\nabla} c_i - z_i F u_i' c_i \boldsymbol{\nabla}\phi + c_i \boldsymbol{v}$.

$\boldsymbol{\nabla}\overline{\mu}_i = \boldsymbol{\nabla}\mu_i + z_i F\boldsymbol{\nabla}\phi = z_i F\boldsymbol{\nabla}\phi$. For conventional experimental conductivity measurements of electrolyte solutions, this condition of uniform composition is satisfied by applying a rapidly alternating voltage or current through the electrolyte about the open circuit voltage, the high frequency of which does not allow appreciable concentration gradients to form [69]. Rewriting the transport Eq. (2.128) under this condition leads to

$$c_i(\boldsymbol{v}_i - \boldsymbol{v}) = -\sum_j L^{ij} z_j F\boldsymbol{\nabla}\phi \ . \tag{4.47}$$

Multiplying by Fz_i and summing over all species i results in

$$\sum_i F z_i c_i \boldsymbol{v}_i - \sum_i F z_i c_i \boldsymbol{v} = -\sum_i \sum_j L^{ij} z_i z_j F^2 \boldsymbol{\nabla}\phi \ . \tag{4.48}$$

Note that the second term on the left side of the equation is zero due to electroneutrality, which dictates $\sum_i z_i c_i = 0$. Thus we will see that while L^{ij} depends on the chosen reference velocity (in this case $\boldsymbol{v}$), the ionic conductivity will be independent of the reference velocity, as expected.

Recall that the free current density $\tilde{\boldsymbol{j}}^{\mathrm{f}}$ may be written as

$$\tilde{\boldsymbol{j}}^{\mathrm{f}} = F\sum_i z_i c_i \boldsymbol{v}_i \ . \tag{4.49}$$

Equation (4.49) can also be written in terms of the fluxes of ions as

$$\tilde{\boldsymbol{j}}^{\mathrm{f}} = F\sum_i (z_i \boldsymbol{J}_i + z_i c_i \boldsymbol{v}) = F\sum_i z_i \boldsymbol{J}_i \ , \tag{4.50}$$

where in the second equality we have invoked the condition of electroneutrality. Using Eqs. (4.48) and (4.49), we obtain

$$\tilde{\boldsymbol{j}}^{\mathrm{f}} = -\sum_i \sum_j L^{ij} z_i z_j F^2 \boldsymbol{\nabla}\phi \ , \tag{4.51}$$

showing a linear relationship between the current density and the electric field. Using Ohm's Law to define the ionic conductivity κ from

$$\tilde{\boldsymbol{j}}^{\mathrm{f}} = -\kappa\boldsymbol{\nabla}\phi \tag{4.52}$$

yields our final relation between ionic conductivity and the transport coefficients L^{ij} as

$$\kappa = F^2 \sum_i \sum_j L^{ij} z_i z_j \ . \tag{4.53}$$

The Green-Kubo relation for ionic conductivity can be obtained from Eq. (3.29) as

$$\kappa = \frac{1}{3k_{\mathrm{B}}TV}\int_0^\infty dt \left\langle \sum_\alpha \hat{q}^\alpha(\boldsymbol{v}^\alpha(t) - \boldsymbol{v}(t)) \cdot \sum_\beta \hat{q}^\beta(\boldsymbol{v}^\beta(0) - \boldsymbol{v}(0)) \right\rangle \ , \tag{4.54}$$

where the summations are over all individual ions in the system (denoted by the indices α and β), rather than over all types of ions i as in Eq. (3.29). Recall that $\hat{q}^\alpha$ is the electronic charge of the ion α. With electroneutrality ($\sum_\alpha \hat{q}^\alpha = 0$), the reference velocity vanishes and we obtain the Green-Kubo equation commonly presented in other works [67]:

$$\kappa = \frac{1}{3k_\mathrm{B}TV}\int_0^\infty dt \left\langle \sum_\alpha \hat{q}^\alpha \boldsymbol{v}^\alpha(t) \cdot \sum_\beta \hat{q}^\beta \boldsymbol{v}^\beta(0) \right\rangle . \tag{4.55}$$

Electrophoretic mobility

We can also obtain expressions for the electrophoretic mobility of species i, u_i, defined as $\boldsymbol{v}_i - \boldsymbol{v} =: u_i \boldsymbol{E}$, in terms of L^{ij}. This quantity can be measured experimentally using techniques such as electrophoretic Nuclear Magnetic Resonance (NMR) spectroscopy [70] or capillary electrophoresis [71]. To this end, consider once again the case with no gradients in chemical potential. In this case, the definition of electrophoretic mobility can be compared with Eq. (2.128), yielding

$$u_i = \sum_j L^{ij} \frac{z_j F}{c_i} . \tag{4.56}$$

Based on Eq. (4.53), it follows that the ionic conductivity is related to mobility as $\kappa = \sum_i F z_i c_i u_i$. In molecular simulations, u_i can either be computed by separately calculating each L^{ij} term or by directly using the Green-Kubo relations emerging from substituting the Green-Kubo relations for L^{ij} (Eq. (3.29)) into Eq. (4.56):

$$u_i = \frac{1}{3k_\mathrm{B}T}\int_0^\infty dt \left\langle \sum_\alpha \hat{q}^\alpha (\boldsymbol{v}^\alpha(0) - \boldsymbol{v}(0)) \cdot (\boldsymbol{v}_i(t) - \boldsymbol{v}(t)) \right\rangle . \tag{4.57}$$

This result is consistent with the relation derived by Dünweg et al. [72] using linear response theory.

Transference number

The transference number of species i, t_i, can also be determined directly from L^{ij}. The transference number is defined as the fraction of current carried by species i in a system with no concentration gradients. Using Eq. (4.50), it is given by

$$t_i \coloneqq \frac{z_i \boldsymbol{J}_i}{\sum_j z_j \boldsymbol{J}_j} . \tag{4.58}$$

Equation (4.58) can be expressed in terms of electrophoretic mobility and conductivity as

$$t_i = \frac{F z_i c_i u_i}{\kappa} = \frac{\sum_j L^{ij} z_i z_j}{\sum_k \sum_l L^{kl} z_k z_l} . \tag{4.59}$$

From the first equality, it is clear that the transference number may equivalently be interpreted as the fraction of conductivity attributed to species i. The second equality has incorporated Eqs. (4.53) and (4.56) to give the transference number in terms of L^{ij}.

Experimentally, the transference number can be measured via a number of methods. The most common method is a potentiostatic polarization experiment, where a fixed potential is applied to a symmetric cell and the ratio of the achieved steady state current to the Ohmic current is equal to the transference number of the reactive species [73]. This method is only strictly valid in the infinite dilution limit. For concentrated electrolytes, additional information about the activity of the solution must be known in order to calculate transference numbers [74]. Using another common method, the Hittorf method, the transference number can be directly obtained by measuring the concentration of ions throughout multiple connected chambers in a symmetric cell after passing current through the electrolyte for a known amount time [75]. The transference number can also be obtained by measuring the electrophoretic mobility of each ionic species by the methods mentioned described above.

Salt/Electrolyte diffusion coefficient

The transport coefficients L^{ij} can also be related to the salt or electrolyte diffusion coefficient, following the derivation by Katchalsky [32]. For this derivation, we restrict ourselves to a binary electrolyte, with a single salt. Rather than considering a system with no chemical potential gradients as with κ, u_i, and t_i, here we consider the condition of no electrical current. Under this condition, the salt diffusion coefficient D_{el} is defined by

$$\boldsymbol{J}_{\text{el}} \coloneqq -D_{\text{el}} \boldsymbol{\nabla} c \ , \tag{4.60}$$

where the subscript 'el' denotes quantities pertaining to the overall electrolyte. The salt flux $\boldsymbol{J}_{\text{el}}$ is related to the fluxes of the cation and anion, $\boldsymbol{J}_+$ and $\boldsymbol{J}_-$, respectively, by $\boldsymbol{J}_{\text{el}} = \frac{\boldsymbol{J}_+}{\nu_+} = \frac{\boldsymbol{J}_-}{\nu_-}$, where ν_+ and ν_- are the stoichiometric coefficients of the cation and anion in the salt. The quantity c is the concentration of salt, $c = \frac{c_+}{\nu_+} = \frac{c_-}{\nu_-}$. Note that $z_+\nu_+ = -z_-\nu_-$ due to the condition of electroneutrality. In what follows, we aim to express the salt diffusion coefficient D_{el} in terms of L^{ij}.

Let us begin by considering the total current. By Eq. (4.50),

$$\tilde{\boldsymbol{j}}^{\text{f}} = z_+ F \boldsymbol{J}_+ + z_- F \boldsymbol{J}_- \ . \tag{4.61}$$

Incorporating the transport laws (Eq. (2.125)) into Eq. (4.61) yields

$$\begin{aligned} \tilde{\boldsymbol{j}}^{\text{f}}/F = -z_+ L^{++}\left(\boldsymbol{\nabla}\overline{\mu}_+ - \frac{M_+}{M_0}\boldsymbol{\nabla}\overline{\mu}_0\right) - z_+ L^{+-}\left(\boldsymbol{\nabla}\overline{\mu}_- - \frac{M_-}{M_0}\boldsymbol{\nabla}\overline{\mu}_0\right) \\ - z_- L^{--}\left(\boldsymbol{\nabla}\overline{\mu}_- - \frac{M_-}{M_0}\boldsymbol{\nabla}\overline{\mu}_0\right) - z_- L^{+-}\left(\boldsymbol{\nabla}\overline{\mu}_+ - \frac{M_+}{M_0}\boldsymbol{\nabla}\overline{\mu}_0\right) \ . \end{aligned} \tag{4.62}$$

Let us define the quantity $\mu_i' \coloneqq \boldsymbol{\nabla}\overline{\mu}_i - \frac{M_i}{M_0}\boldsymbol{\nabla}\overline{\mu}_0$ and rewrite Eq. (4.62) as

$$\tilde{\boldsymbol{j}}^{\mathrm{f}}/F = -z_+L^{++}\boldsymbol{\nabla}\mu_+' - z_+L^{+-}\boldsymbol{\nabla}\mu_-' - z_-L^{--}\boldsymbol{\nabla}\mu_-' - z_-L^{+-}\boldsymbol{\nabla}\mu_+' \ . \tag{4.63}$$

Further, it is convenient to define the chemical potential of the salt or electrolyte as $\mu_{\mathrm{el}} \coloneqq \nu_+\overline{\mu}_+ + \nu_-\overline{\mu}_-$, and analogously $\mu_{\mathrm{el}}' \coloneqq \nu_+\mu_+' + \nu_-\mu_-'$. Note that the Gibbs-Duhem relation ($\boldsymbol{\nabla}\overline{\mu}_0 = -\frac{c_+}{c_0}\boldsymbol{\nabla}\overline{\mu}_+ - \frac{c_-}{c_0}\boldsymbol{\nabla}\overline{\mu}_-$) allows us to write $\boldsymbol{\nabla}\mu_{\mathrm{el}}' = \left(1+\frac{c}{c_0M_0}(\nu_+M_+ + \nu_-M_-)\right)\boldsymbol{\nabla}\mu_{\mathrm{el}}$. These definitions, along with Eqs. (4.53), (4.59), and (4.63), allow us to express the electrochemical potential of the ions as

$$\begin{aligned}\boldsymbol{\nabla}\mu_+' &= \frac{-\tilde{\boldsymbol{j}}^{\mathrm{f}}Fz_+}{\kappa} + \frac{t_-}{\nu_+}\boldsymbol{\nabla}\mu_{\mathrm{el}}' \ , \\ \boldsymbol{\nabla}\mu_-' &= \frac{-\tilde{\boldsymbol{j}}^{\mathrm{f}}Fz_-}{\kappa} + \frac{t_+}{\nu_-}\boldsymbol{\nabla}\mu_{\mathrm{el}}' \ .\end{aligned} \tag{4.64}$$

Combining Eqs. (2.125) and (4.64) allows us to write the ion fluxes in terms of $\boldsymbol{\nabla}\mu_{\mathrm{el}}'$ and L^{ij} as

$$\begin{aligned}\boldsymbol{J}_+ &= \frac{\tilde{\boldsymbol{j}}^{\mathrm{f}}t_+}{Fz_+} + \frac{z_+z_-\nu_+}{\nu_+\nu_-}\left(\frac{L^{--}L^{++} - L^{+-2}}{z_+^2L^{++} + 2z_+z_-L^{+-} + z_-^2L^{--}}\right)\boldsymbol{\nabla}\mu_{\mathrm{el}}' \ , \\ \boldsymbol{J}_- &= \frac{\tilde{\boldsymbol{j}}^{\mathrm{f}}t_-}{Fz_-} + \frac{z_+z_-\nu_-}{\nu_+\nu_-}\left(\frac{L^{--}L^{++} - L^{+-2}}{z_+^2L^{++} + 2z_+z_-L^{+-} + z_-^2L^{--}}\right)\boldsymbol{\nabla}\mu_{\mathrm{el}}' \ .\end{aligned} \tag{4.65}$$

Now let us consider the case of no net current which is relevant for determining the salt diffusion coefficient. When $\tilde{\boldsymbol{j}}^{\mathrm{f}} = 0$, we may write the salt flux $\boldsymbol{J}_{\mathrm{el}}$ as

$$\boldsymbol{J}_{\mathrm{el}} = \frac{z_+z_-}{\nu_+\nu_-}\left(\frac{L^{--}L^{++} - L^{+-2}}{z_+^2L^{++} + 2z_+z_-L^{+-} + z_-^2L^{--}}\right)\boldsymbol{\nabla}\mu_{\mathrm{el}}'. \tag{4.66}$$

Note that while all previous transport properties have been defined with respect to gradients in electrochemical potential (the true thermodynamic driving force), the salt diffusion coefficient is defined with respect to concentration gradients. Thus, to identify D_{el} from Eq. (4.66), we need a relation between $\boldsymbol{\nabla}\mu_{\mathrm{el}}'$ and $\boldsymbol{\nabla}c$. To this end, we invoke the form of the chemical potential,

$$\mu_{\mathrm{el}} = \mu_{\mathrm{el}}^o + \nu RT\ln(cf_{\mathrm{el}}) + RT\ln(\nu_+^{\nu_+}\nu_-^{\nu_-}) \ , \tag{4.67}$$

where $f_{\mathrm{el}} = (f_+^{\nu_+}f_-^{\nu_-})^{1/\nu}$ is the salt activity coefficient [2] and $\nu = \nu_+ + \nu_-$.[4] Thus,

$$\boldsymbol{\nabla}\mu_{\mathrm{el}} = \frac{\partial\mu_{\mathrm{el}}}{\partial c}\boldsymbol{\nabla}c = \frac{\nu RT}{c}\left[1 + \frac{d\ln f_{\mathrm{el}}}{d\ln c}\right]\boldsymbol{\nabla}c \ , \tag{4.68}$$

[4]The quantities μ_{el} and f_{el} are referred to in some texts as $\mu_\pm$ and $f_\pm$ [2].The salt chemical potential may also be written in terms of molal (as opposed to molar) activity coefficients, denoted γ_{el}. In this case, $\boldsymbol{\nabla}\mu_{\mathrm{el}} = \frac{\nu RT}{c}\left[1 + \frac{d\ln\gamma_{\mathrm{el}}}{d\ln m}\right]\left[1 - \frac{d\ln c_0}{d\ln c}\right]\boldsymbol{\nabla}c$, where m is molality.

and correspondingly

$$\boldsymbol{\nabla}\mu'_{\mathrm{el}} = \frac{\nu RT}{c}\left[1 + \frac{d\ln f_{\mathrm{el}}}{d\ln c}\right]\left(1 + \frac{c}{c_0 M_0}(\nu_+ M_+ + \nu_- M_-)\right)\boldsymbol{\nabla}c\ . \tag{4.69}$$

Combining Eqs. (4.60), (4.66) and (4.69), the salt diffusion coefficient is given by

$$D_{\mathrm{el}} = \frac{-z_+ z_-(L^{--}L^{++} - L^{+-^2})}{(z_+^2 L^{++} + 2z_+ z_- L^{+-} + z_-^2 L^{--})}\frac{\nu RT}{c\nu_+\nu_-}\left[1 + \frac{d\ln f_{\mathrm{el}}}{d\ln c}\right]\left(1 + \frac{c}{c_0 M_0}(\nu_+ M_+ + \nu_- M_-)\right)\ . \tag{4.70}$$

Experimentally D_{el} is typically measured via the restricted diffusion method, where a concentration gradient is built across a symmetric cell by applying a potential or fixed current density [76]. The potential or current is then stopped and the concentration gradient is monitored as it relaxes. The concentration can either be directly monitored using interferometry or other spectroscopic methods or can be indirectly observed by monitoring the changing open circuit potential [77, 78].

L^{ij} in terms of experimental quantities

The above relations enable us to compute conductivity, mobility, transference number, and salt diffusion coefficient from L^{ij} values obtained from molecular simulation. In contrast, we can also manipulate these equations to solve for L^{ij} in the case where the electrolyte has been characterized experimentally. Rearranging Eqs. (4.53), (4.59), and (4.70) and solving for L^{ij} in terms of the experimentally measurable quantities gives:

$$\begin{aligned}
L^{++} &= \frac{\nu_+^2 D_{\mathrm{el}}}{\frac{\nu RT}{c}\left[1 + \frac{d\ln f_{\mathrm{el}}}{d\ln c}\right]} + \kappa\left(\frac{t_+}{z_+ F}\right)^2\ , \\
L^{--} &= \frac{\nu_-^2 D_{\mathrm{el}}}{\frac{\nu RT}{c}\left[1 + \frac{d\ln f_{\mathrm{el}}}{d\ln c}\right]} + \kappa\left(\frac{t_-}{z_- F}\right)^2\ , \\
L^{+-} &= \frac{\nu_+\nu_- D_{\mathrm{el}}}{\frac{\nu RT}{c}\left[1 + \frac{d\ln f_{\mathrm{el}}}{d\ln c}\right]} + \frac{\kappa t_+ t_-}{z_+ z_- F^2}\ .
\end{aligned} \tag{4.71}$$

In summary, we have derived equations to enable inter-conversion between L^{ij} and experimentally relevant, macroscopic electrolyte transport quantities. This provides experimentalists with a means to quantitatively evaluate the extent of correlation between each of the ionic species in solution.

4.4 Governing equations for mass transport

In this section, we combine the mass balance of Chapter 2.1 and the linear laws of Chapter 2.2 to derive governing equations for mass transport in electrolytes, restricting to the special case of a binary electrolyte. These equations allow us to directly utilize experimentally-measurable transport properties to set up boundary value problems for the concentration profile of an electrolyte. Let us begin by substituting the expression for cation flux, $\boldsymbol{J}_+$ in Eq. (4.65) into the mass balance, Eq. (2.5), yielding

$$\frac{\partial c_+}{\partial t} + \boldsymbol{\nabla} \cdot (c_+ \boldsymbol{v}) = -\boldsymbol{\nabla} \cdot \left[\frac{\tilde{\boldsymbol{j}}^{\mathrm{f}} t_+}{F z_+} + \frac{z_+ z_- \nu_+}{\nu_+ \nu_-} \left(\frac{L^{--} L^{++} - L^{+-^2}}{z_+^2 L^{++} + 2 z_+ z_- L^{+-} + z_-^2 L^{--}} \right) \boldsymbol{\nabla} \mu'_{\mathrm{el}} \right] . \quad (4.72)$$

Incorporating the definition of the salt diffusion coefficient (Eq. (4.70)) and Eq. (4.69) gives

$$\frac{\partial c_+}{\partial t} + \boldsymbol{\nabla} \cdot (c_+ \boldsymbol{v}) = -\boldsymbol{\nabla} \cdot \left[\frac{\tilde{\boldsymbol{j}}^{\mathrm{f}} t_+}{F z_+} - \nu_+ D_{\mathrm{el}} \boldsymbol{\nabla} c \right] . \quad (4.73)$$

Finally, we may write the governing equation for the total salt concentration, $c = \frac{c_+}{\nu_+} = \frac{c_-}{\nu_-}$:

$$\frac{\partial c}{\partial t} + \boldsymbol{\nabla} \cdot (c \boldsymbol{v}) = -\boldsymbol{\nabla} \cdot \left[\frac{\tilde{\boldsymbol{j}}^{\mathrm{f}} t_+}{F z_+ \nu_+} - D_{\mathrm{el}} \boldsymbol{\nabla} c \right] . \quad (4.74)$$

Equation (4.74) is analogous to the governing equation for concentration presented in Newman's textbook [2] derived from the Stefan-Maxwell framework:

$$\frac{\partial c}{\partial t} + \boldsymbol{\nabla} \cdot (c \boldsymbol{v}_0) = \boldsymbol{\nabla} \cdot \left[D_{\mathrm{el}}^{\mathrm{SM}} \left(1 - \frac{d \ln c_0}{d \ln c} \right) \boldsymbol{\nabla} c \right] - \frac{\tilde{\boldsymbol{j}}^{\mathrm{f}} \cdot \boldsymbol{\nabla} t_+^0}{z_+ \nu_+ F} . \quad (4.75)$$

Here, the transference number t_+^0 is defined with reference to the solvent velocity, rather than the center of mass velocity, and the salt diffusion coefficient $D_{\mathrm{el}}^{\mathrm{SM}}$ is defined in terms of Stefan-Maxwell diffusion coefficients. The additional factor of $\left(1 - \frac{d \ln c_0}{d \ln c}\right)$ arises from defining the salt diffusion coefficient in terms of molal, as opposed to molar, activity coefficients.

Let us simplify Eq. (4.74) in the limit of infinite dilution, where we assume that $c << c_0$, $f_{\mathrm{el}} = 1$, and $L^{+-} = 0$. Under these conditions, the diffusion coefficient (Eq. (4.70)) becomes

$$D_{\mathrm{el,dilute}} = \frac{-z_+ z_- L^{--} L^{++}}{(z_+^2 L^{++} + z_-^2 L^{--})} \frac{\nu R T}{c \nu_+ \nu_-} . \quad (4.76)$$

Further, we may invoke Eq. (4.42) to write $D_{\mathrm{el,dilute}}$ in terms of self-diffusion coefficients:

$$D_{\mathrm{el,dilute}} = \frac{D_+ D_- \nu}{\nu_- D_+ + \nu_+ D_-} = \frac{D_+ D_- (z_+ - z_-)}{z_+ D_+ - z_- D_-} . \quad (4.77)$$

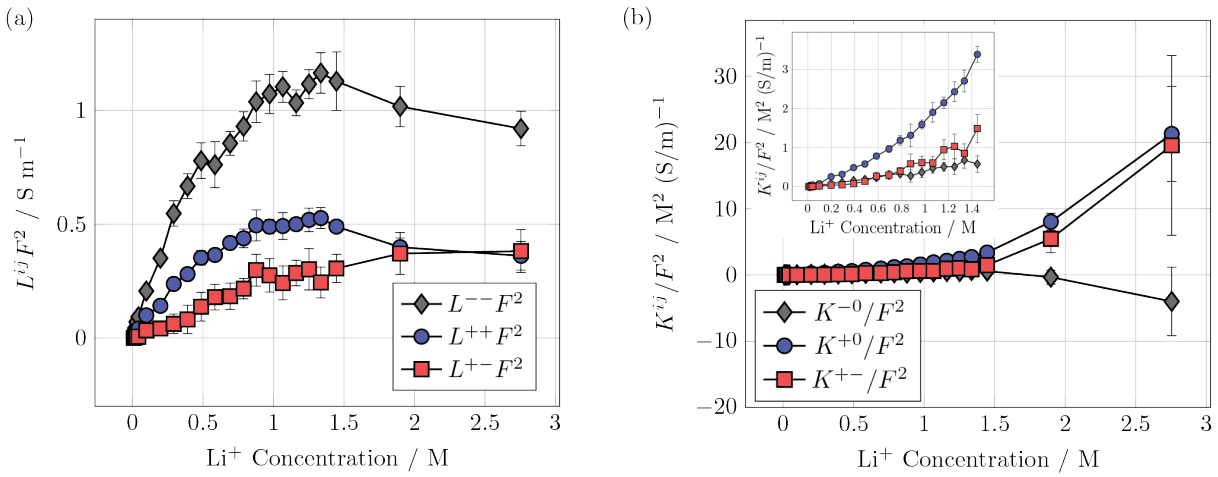

Figure 4.2: Transport coefficients for LiCl in DMSO solutions. (a) Onsager transport coefficients ($L^{ij}F^2$) and (b) Stefan-Maxwell transport coefficients (K^{ij}/F^2) of each pair of ionic species versus concentration. The inset in (b) shows the data at low concentrations. Transport coefficients are divided or multiplied by a factor of F^2 (where F is Faraday's constant) such that the units are related to those commonly used for ionic conductivity.

Analogously, the cation transference number in ideal solutions is

$$t_{+,\text{dilute}} = \frac{z_+ D_+}{z_+ D_+ - z_- D_-} \ . \tag{4.78}$$

Incorporating Eqs. (4.77) and (4.78) into Eq. (4.74) give the following governing equation for transport in dilute, binary electrolytes:

$$\frac{\partial c}{\partial t} + \boldsymbol{\nabla} \cdot (c\boldsymbol{v}) = -\boldsymbol{\nabla} \cdot \left[\frac{\tilde{\boldsymbol{j}}^{\text{f}} z_+ D_+}{F z_+ \nu_+ (z_+ D_+ - z_- D_-)} - \frac{D_+ D_- (z_+ - z_-)}{z_+ D_+ - z_- D_-} \boldsymbol{\nabla} c \right] . \tag{4.79}$$

4.5 Applications to a model electrolyte: LiCl in dimethyl sulfoxide

In what follows, we use the Green-Kubo relations (Eq. (3.29)) derived herein to compute the transport coefficients L^{ij} in a model electrolyte system using classical molecular dynamics (MD) simulations (methods are described in Appendix B.1). Our model system consists of LiCl salt, chosen for its structural simplicity, in dimethyl sulfoxide (DMSO) solvent. DMSO was chosen over an aqueous solution to avoid the complications associated with the self-ionization of water, which introduces additional charge carrying species into solution.

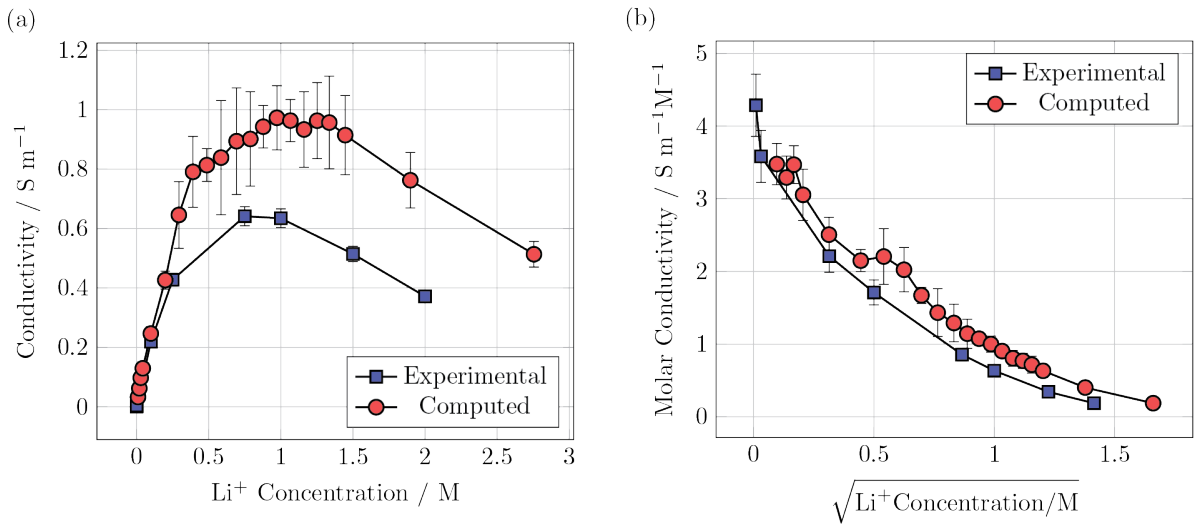

Figure 4.3: Conductivity of LiCl in DMSO. (a) Ionic conductivity versus concentration, with comparison to experimental data obtained from AC impedance measurements (see Appendix B.1). (b) Molar conductivity versus the square root of concentration, with comparison to experimental data.

As the dielectric constant and donor number of DMSO are relatively high, this solvent is commonly used for its effectiveness in dissolving and dissociating salts [55].

Figure 4.2a shows the transport coefficients L^{ij} from the Green-Kubo relations as a function of salt concentration. The Stefan-Maxwell coefficients K^{ij}, obtained from L^{ij} using the mapping in Eq. (4.25), are also given for comparison in Figure 4.2b. The error bars reported here are the standard deviation of ten independent replicate simulations, although we note that the true error based on Zwanzig and Ailawadi theory [79] and its extension [80] is likely smaller. We observe that the anionic term L^{--} is consistently the largest of the three transport coefficients. This more facile motion of the anion relative to the cation is consistent with the lithium ion's bulky solvation shell [81]. Based on the fact that L^{ij} is directly proportional to $c_i c_j$ (Eq. (3.29)), one might expect a monotonic increase in each of the transport coefficients with concentration. The non-monotonic trends in L^{++} and L^{--} reflect an increase in inter-ionic friction as concentration increases as a result of electrophoretic and relaxation effects [82]. These effects, along with ion pairing or aggregation, also contribute to correlated cation-anion motion, captured by L^{+-}. We note that the magnitude of L^{+-} increases monotonically with concentration, which is consistent with an increase in the number of ion pairs in solution.

In Figures 4.3 and 4.4, we demonstrate how the computed transport coefficients L^{ij} can be combined to yield experimentally relevant properties. The total ionic conductivity

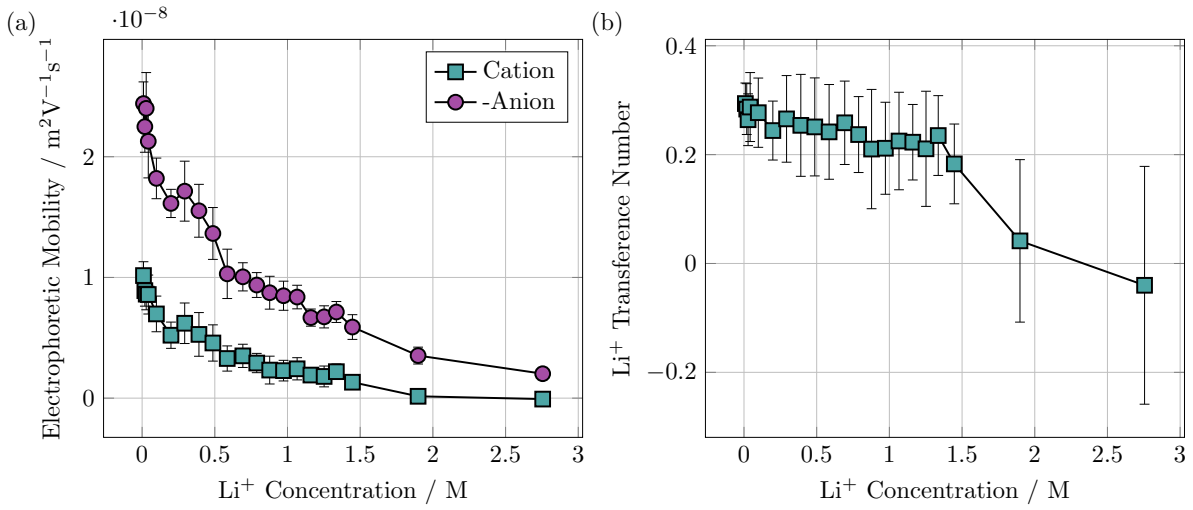

Figure 4.4: Mobility and transference numbers of LiCl in DMSO. (a) Electrophoretic mobility u of each ion. As the mobility of the anion is negative, for this species we show $-u$. (b) Cation transference number as a function of concentration.

computed from Eq. (4.53) is shown in Figure 4.3a. We also measure the conductivity experimentally using AC impedance spectroscopy (see Appendix B.1 for a detailed description of methods). The computed values and the experimental data show reasonable agreement both qualitatively and quantitatively, showing the molecular model to be reasonable for studying transport phenomena of LiCl in DMSO. Figure 4.3b shows the same experimental and computed conductivity data as in Figure 4.3a but is plotted as molar conductivity Λ (concentration-normalized conductivity) versus the square root of concentration. The Debye-Hückel-Onsager theory [82] predicts that for low concentrations $\Lambda = \Lambda^0 - \xi\sqrt{c}$, where Λ^0 is the limiting molar conductivity and ξ is a constant accounting for electrophoretic and relaxation effects. As can be seen in Figure 4.3b, the linear dependence of molar conductivity on $\sqrt{c}$ is only approximately followed at the most dilute concentrations; deviations from the predicted trend can likely be attributed to incomplete dissociation of the salt [83]. As the predicted $\sqrt{c}$ dependence is built upon Debye-Hückel theory, which is only valid for very dilute electrolytes, it is no surprise that we observe the molar conductivity to deviate substantially from the Debye-Hückel-Onsager equation at higher concentrations.

We also present the electrophoretic mobility and cation transference number in Figure 4.4a and b, respectively. In Figure 4.4a, we observe that the mobility of both the cation and anion decrease monotonically, once again due to more inter-ionic friction at higher concentrations. The magnitude of the anion mobility is larger than that of the cation, as required by the fact that $L^{--} > L^{++}$ at all concentrations (Figure 4.2). The transference number in Figure 4.4b is observed to remain relatively constant with respect to concentration

until approximately 1.5 M, after which it decreases sharply. The onset of the decrease in the lithium transference number roughly coincides with that of the ionic conductivity in Figure 4.3a. This shift likely reflects a change in the solvation environment of the lithium ions, i.e., a change in the most common ion aggregates present in solution. Note that although the transference number is defined as the fraction of conductivity attributed to a given species, it is not necessarily bounded between zero and one. Indeed, in this LiCl in DMSO system, the lithium transference number may become negative above 2.5 M. This phenomena, which has been observed in systems such as solid polymer electrolytes [84] and ionic liquids [85], corresponds to lithium moving towards more positive potential under an applied electric field and may be due to the presence of negatively charged aggregates in solution. It is important to note that the transference number is challenging to measure experimentally and is rarely reported without the use of ideal solution approximations [3]. In contrast, the Onsager framework and associated Green-Kubo relations allow for facile computation of the transference number at a computational cost equivalent to that of conventional MD calculations such as the diffusion coefficient or total ionic conductivity.

In summary, this chapter has provided an intuitive picture of the Onsager transport framework for electrolyte solutions and has related the Onsager transport coefficients L^{ij} to other common transport frameworks as well as experimentally-measurable properties. In the following chapters, we will demonstrate how this understanding of L^{ij} will enable us to gain useful insights as to the molecular-level mechanisms of ion motion in Li-ion battery electrolytes.

Chapter 5

Nonaqueous Polyelectrolyte Solutions for Lithium Ion Batteries[1]

In this chapter, we demonstrate application of the Onsager transport framework developed in the previous sections to an emerging class of electrolytes for Li-ion batteries: nonaqueous polyelectrolyte solutions. We describe the motivation for using these polyelectrolytes as potential high transference number alternatives to conventional battery electrolytes, then explore the structural and dynamic properties of a model nonaqueous polyelectrolyte using all-atom molecular dynamics (MD) simulations. We find that static structural analysis of Li^+ ion pairing is insufficient to fully explain the overall conductivity trend in this system, necessitating a dynamic analysis of the diffusion mechanism, in which we observe a shift from largely vehicular transport to more structural diffusion as Li^+ concentration increases. Furthermore, we demonstrate that despite the significantly higher diffusion coefficient of the lithium ion, the negatively-charged polyion is responsible for the majority of the solution conductivity at all concentrations, corresponding to Li^+ transference numbers much lower than previously estimated experimentally. We quantify the ion-ion correlations unique to polyelectrolyte systems which are responsible for this surprising behavior. These results highlight the need to reconsider the approximations typically made for transport in polyelectrolyte solutions.

5.1 Li-ion batteries and the cation transference number

As introduced in Chapter 1, the performance of conventional lithium-ion batteries (LIBs) is limited by their low cation transference number (t_+), defined as the fraction of ionic conductivity imparted by the lithium ion rather than its counterion [2]. These low t_+ values

[1]This chapter is closely adapted from Ref [86]: Fong, K. D.et al. Ion transport and the true transference number in nonaqueous polyelectrolyte solutions for lithium ion batteries. *ACS Central Science* **5**, 1250–1260 (2019).

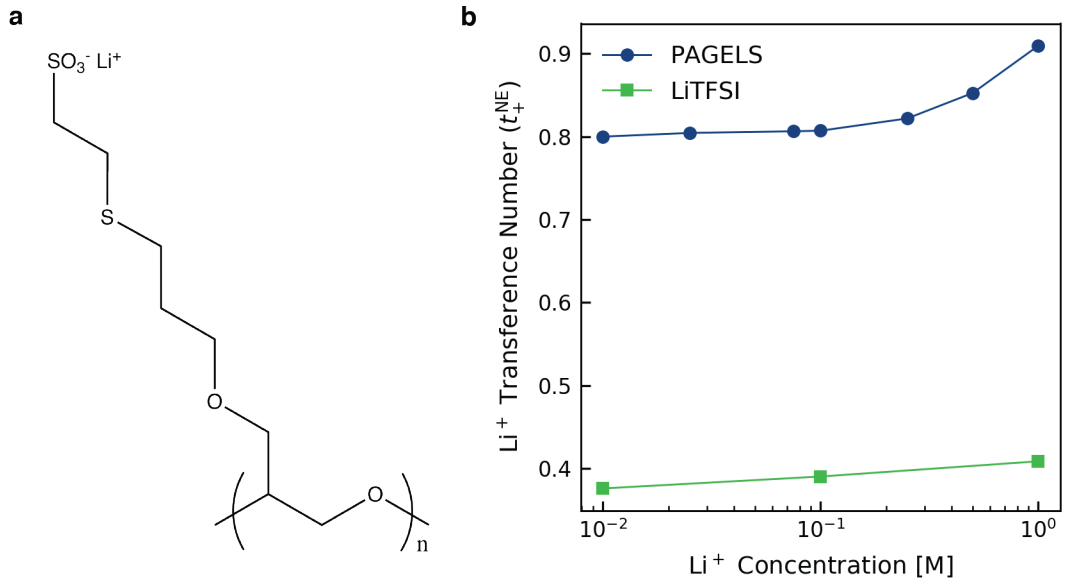

Figure 5.1: Properties of the PAGELS polyelectrolyte. (a) Chemical structure. (b) Experimental values of the Nernst-Einstein transference number of PAGELS in DMSO, compared to a conventional salt, LiTFSI [96].

(typically about 0.4) [9] correspond to electrolytes in which the anion is highly mobile, whereas the electrochemically active Li^+ moves more sluggishly due to its bulky solvation shell [81]. As a result, concentration gradients form in the electrolyte, which limit material utilization, promote lithium plating, and generate concentration overpotentials, all of which contribute to lower power density, energy density, and lifetime of the cell [3, 4, 87].

Strategies towards increasing t_+ typically focus on immobilizing the anion, for example via lithium-conducting ceramics [88–91] or single-ion conducting solid polymer electrolytes [92–95]. However, the mechanical properties of ceramics make thin film processing difficult, and polymer electrolytes suffer from poor conductivity, particularly at room temperature and below. Alternatively, it has been recently proposed that t_+ could be increased by covalently appending the anion to the backbone of a polymer, which is then dissolved in nonaqueous solvent to form a lithium-neutralized polyelectrolyte solution [96–99]. As these polyelectrolytes are entirely in the liquid phase, they could serve as a means to increase transference number without drastic conductivity losses and be directly used in existing cell designs. Indeed, initial studies have reported transference numbers as high as 0.8 to 0.98 depending on the polymer chemistry, solvent, and ion concentration [96, 97, 99, 100]. Experimental data [96] for one such polyelectrolyte solution, poly(allyl glycidyl ether-lithium sulfonate) (PAGELS) in dimethyl sulfoxide (DMSO), is given in Figure 5.1, with comparison to a conventional Li-ion battery salt, LiTFSI, in the same solvent.

While these results suggest that such polyelectrolyte solutions could be very promising options for high-transference number battery electrolytes, it is important to note that the transference number is very difficult to determine unequivocally from experiments [3]. Most reported electrochemical t_+ measurements (namely those using the Bruce and Vincent method [101]) assume ideal solutions of non-interacting ions, while those that incorporate the effects of non-idealities are typically challenging to execute experimentally. Balsara and Newman′s [74] generalization of the Bruce and Vincent method to concentrated solutions, for example, requires a restricted diffusion experiment as well as determination of the salt activity coefficient. Other techniques, such as the Hittorf or Tubandt method [75], are associated with large statistical uncertainties due to noisy data [9, 102]. As a result, true transference numbers are rarely measured directly [3].

The existing experimental studies [96, 97, 99, 100] which report high t_+ in a nonaqueous polyelectrolyte have not measured the rigorous transference number, but have rather estimated t_+ by assuming that the solution behaves ideally. As discussed in Chapter 4.2, this Nernst-Einstein (NE) approximation assumes there are no correlations between ions in the electrolyte, thereby eliminating the off-diagonal components of the transport matrix (L^{+-}) as well as the distinct terms. Incorporating this approximation into Eq. (4.59) yields an expression for the Nernst-Einstein transference number of species i, t_i^{NE}, in terms of only the self transport coefficients:

$$t_i^{\mathrm{NE}} = \frac{z_i^2 L_{\mathrm{self}}^{ii}}{\sum_j z_j^2 L_{\mathrm{self}}^{jj}}. \tag{5.1}$$

For the cation transference number of a binary electrolyte, incorporating Eq. (4.5) and the condition of electroneutrality, $\sum_i z_i c_i = 0$, yields an expression for transference number in terms of the self-diffusion coefficients of the cation and anion, D_+ and D_-, respectively:

$$t_+^{\mathrm{NE}} = \frac{z_+ D_+}{z_+ D_+ - z_- D_-} \ . \tag{5.2}$$

The self-diffusion coefficients in this expression can be easily obtained experimentally from pulsed-field gradient nuclear magnetic resonance (PFG-NMR). In a polyelectrolyte, there exists some ambiguity as to the value of z_-. Noting that all anions on the chain must move collectively over long timescales, one may interpret z_- as the net charge of the polymer (z_{polymer}). Conversely, the experimental works which have characterized these systems to-date [96–99] have assumed $z_- = -1$, i.e., that each monomer is considered to be an independent anionic species. These works thus use the following equation to estimate the transference number of a polyelectrolyte solution:

$$t_+^{\mathrm{NE}} = \frac{D_+}{D_+ + D_-} \ . \tag{5.3}$$

We will discuss the implications of each of these choices for z_- in the following sections. We also note that that t_+^{NE} is sometimes referred to as a transport number, rather than a transference number [103].

The Nernst-Einstein approximation typically yields reasonable results for conventional electrolyte solutions, but we lack insight as to how well this assumption holds for polyelectrolytes. More broadly, development of these systems is hindered by a lack of fundamental understanding of ion transport phenomena in these solutions. Many of the properties beyond the transference number which most strongly govern battery electrolyte performance, such as ion speciation and diffusion mechanisms, are challenging to precisely access experimentally [104]. We further note that the majority of theoretical work on polyelectrolyte solutions has focused on the properties of the polyion chain alone, rather than the behavior of the counterion, which is the electroactive species of interest for batteries [105, 106].

Simulation techniques such as molecular dynamics are well-suited to address many of the unanswered questions surrounding these nonaqueous polyelectrolytes. As the time and length scales associated with ion transport are compatible with those accessible by MD, this technique has been used extensively to gain insight into the properties of conventional binary lithium salts such as lithium bis(trifluoromethanesulfonyl)imide (LiTFSI) or lithium hexafluorophosphate ($LiPF_6$) [107, 108] as well as solid polymer electrolytes [109–113]. MD has also been successfully applied to polyelectrolytes, although these studies have been performed almost exclusively in aqueous systems [114–116], for example on biological polyelectrolytes such as DNA [117, 118], or in solvent-free ionomer melts [119–122]. Others have performed polyelectrolyte simulations in non-explicit continuum solvents [123–125], but this approach often fails to adequately capture trends in chain conformation and ion dissociation [97, 126]. Of the MD simulations in explicit nonaqueous solvents [98,127], we are unaware of any which characterize the battery-relevant transport properties (such as t_+) of the solution.

Herein, we employ all-atom classical MD simulations of PAGELS in DMSO, a model polyelectrolyte system for battery applications. Several of the most important transport properties of this system have been investigated experimentally [96], enabling validation of the computational model. We characterize the structural properties of a single chain in solution, demonstrating the intuitive connection between ion pairing behavior and polyion conformation. Next, we explore the dynamic mechanisms for lithium ion diffusion and migration, focusing specifically on ion-ion correlations and their impact on conductivity and transference number. This work illuminates some of the fundamental atomistic processes governing transport in these nonaqueous polyelectrolyte solutions, which has implications not only for the design of enhanced LIB electrolytes but also for improved understanding of polyelectrolyte dynamics in general.

5.2 Structural properties

Ion Speciation

One of the most deciding aspects of the performance of a battery electrolyte is ion speciation: the extent of ion pairing in an electrolyte governs the number of charge-carrying species, thereby directly influencing the conductivity, transference number, and other crucial

electrolyte properties [6,128,129]. Using a distance criterion obtained from the cation-anion radial distribution function (RDF), we classify each Li^+ ion as either free, in a solvent-separated ion pair (SSIP), or in a contact ion pair (CIP) or larger aggregate (AGG) with the sulfonate ions, the anionic moiety of the polyion (Figure 5.2a). The nomenclature used here is common in the field of battery electrolytes, but in the polyelectrolyte literature this phenomenon is typically referred to as counterion condensation [130]. The CIPs referred to here are analogous to Manning's "site" bound ions, whereas SSIPs are similar to "territorially" bound condensed counterions [131]. Consistent with the various theories of counterion condensation in polyelectrolytes [132,133], here we observe that the fraction of free Li^+ ions (Figure 5.2b) decreases as concentration increases, ranging from 72% at 0.05 M down to 5% at 1.0 M, while the extent of ion pairing and aggregation increases. The coordination number of anions within the first Li^+ shell (plotted in Figure B.2) yield a similar trend.

While this initial analysis provides a general picture of ion speciation trends in the polyelectrolyte, the data in Figure 5.2b does not distinguish between CIPs and AGGs. We quantify the relative significance of these AGGs in Figure 5.2c, which gives the probability of observing aggregates of different sizes for each concentration. We observe that the probability of ion aggregates to form decreases approximately exponentially with aggregate size, a trend which has been observed for conventional LIB electrolytes [108]. As fewer than 2.5% of the observed aggregates consist of three or more ions, we expect the bulk behavior of the system to be dictated primarily by the free ions, SSIPs, and CIPs.

To further visualize the most prevalent solvation structures and aggregate types in the polyelectrolyte solution, we employ a graph theory approach analogous to that of Tenney et al. [134], in which we translate the positions of the system's atoms at any given time into a graph composed of nodes and vertices. The nodes in this case represent Li^+, S (SO_3^-), or O (DMSO) atoms, and the edges give connectivity between Li^+-S (SO_3^-) or Li^+-O (DMSO) pairs which are coordinated in their first solvation shell. Analysis of the connectivities at each time step allows for determining the most common topologies observed over the course of the simulation, as shown in Figure 5.2d. The area of the nodes in this figure are proportional to the logarithm of the frequency at which the topology appears in the system, averaged over all concentrations. As expected, the most frequently-observed topologies are the free ion and CIP (SSIPs are not captured in this analysis), while clusters with more ions are significantly less common.

Polymer Conformation

In this section we focus on the polymer conformation, which is closely tied to ion speciation. At low concentrations, when contact ion pairing is negligible, the polymer chain is highly charged. In this state, electrostatic repulsion between charged monomers extends the chain into a predominantly linear conformation. As concentration increases and more counterions (Li^+) bind to the chain, the repulsion between the monomers decreases and the polymer adopts a more entropically favorable, globular conformation. [104]. This trend is apparent in the snapshots shown in Figure 5.3a. The linear to coiled transformation with concentration

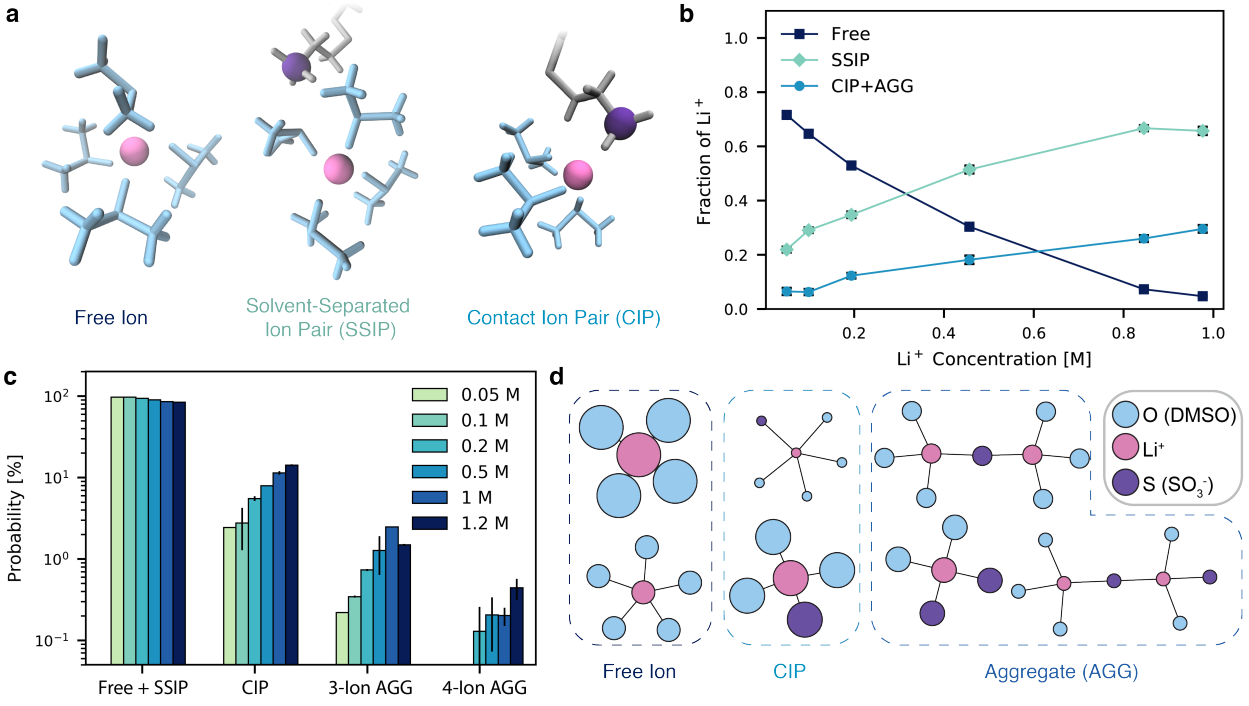

Figure 5.2: Ion speciation trends. (a) Schematics of the three most common states of ion speciation: free ions, solvent-separated ion pairs (SSIPs), and contact ion pairs (CIPs). (b) Fraction of lithium ions in each speciation state as a function of concentration. (c) Probability of observing ion clusters of different sizes. (d) Most commonly observed topologies representing the connectivity of Li^+ to neighboring sulfur (SO_3^-) and oxygen (DMSO) atoms, averaged over all concentrations. Node area is proportional to the logarithm of the probability of observing each topology.

can be observed quantitatively in both the end-to-end distance (Figure 5.3b) as well as the radius of gyration (Figure 5.3c), which both decrease as concentration increases.

Changes in the polyion's persistence length (Figure 5.3d) are also consistent with our trends in ion pairing described in the previous section. The persistence length reflects the extent of orientational correlation along the backbone of the chain. For polyelectrolytes, the overall persistence length is a combination of orientational correlations from the inherent flexibility of the uncharged backbone as well as electrostatic correlations induced by repulsion of the charged monomers [135]. Hence changes in electrostatic correlations dictate the trend in persistence length with concentration, such that the highly charged chains at lower concentrations yield the greatest persistence lengths. Our results are in qualitative agreement with the classical Odijk-Skolnick-Fixman (OSF) theory [136, 137], which predicts

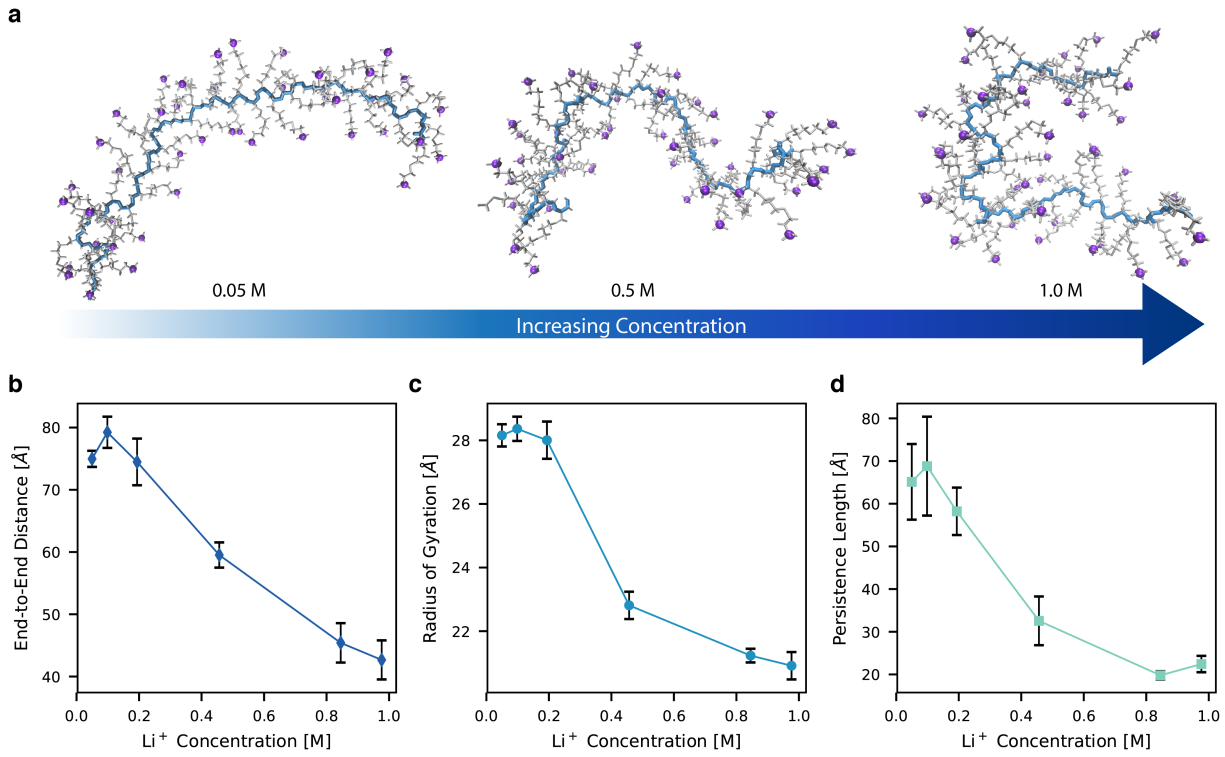

Figure 5.3: Polymer structure as a function of concentration. (a) Example configurations of polymer conformation at 0.05 M, 0.5 M, and 1.0 M. (b) End-to-end distance, (c) radius of gyration, and (d) persistence length at each concentration. Sulfur atoms on the sulfonate anion are depicted in purple, the chain backbone is blue, and the sidechains are gray. Solvent molecules and lithium ions are omitted for clarity.

that persistence length should be proportional to the square of the Debye screening length, or inversely proportional to the solution ionic strength. Quantitative agreement with this model should not be expected, however, given the oligomeric nature of the chain (here 43 monomers, chosen to match available experimental data — see Appendix B.2 for details on system setup) as well as the presence of the long sidechains, which render the distribution of anionic charges on the chain somewhat irregular. Similar limitations prevent us from comparing other structural or dynamic properties of the polyion to known polyelectrolyte scaling laws, which typically assume infinitely long chains with uniform charge distributions [138].

5.3 Dynamic properties

Before extracting atomistic transport motifs for the PAGELS polyelectrolyte, we validate the dynamics produced by our MD force field against experimental data [96]. The calcu-

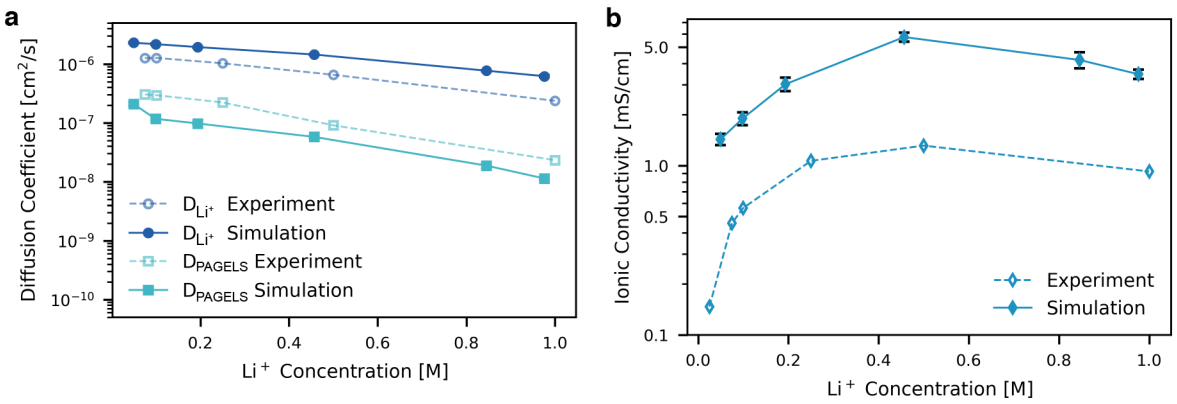

Figure 5.4: Comparison of calculated dynamic properties with experimental values. (a) Diffusion coefficients of Li^+ and the polyelectrolyte (PAGELS) center of mass. (b) Ionic conductivity. Experimental values are taken from Buss et al. [96]

lated self-diffusion coefficients and those measured experimentally in previous work using pulsed-field gradient nuclear magnetic resonance (PFG-NMR) are given in Figure 5.4a. In addition to reproducing the experimental trend in which both the lithium ions and polyion diffuse more slowly as concentration increases, the diffusion coefficients match to within less than half of an order of magnitude — well within the errors commonly observed for MD simulations using non-polarizable force fields [139, 140]. Some of the observed discrepancy, particularly for the polyion, may be attributed to finite size effects from our simulations of a single polymer chain. These effects are well-known to result in slower diffusion relative to an infinitely large simulation box [141]. While we have performed simulations with two chains at the highest concentrations which suggest that these finite size effects are relatively small (Figure B.1), it is possible that significantly larger simulation sizes could yield better agreement with experimental diffusion data. The experimental ionic conductivity κ is also reproduced within reasonable error (Figure 5.4b). Our overestimation of the total conductivity suggests that the force field may underestimate the effects of ion pairing in the actual system. Regardless, the relative changes in conductivity with concentration show excellent agreement with experimental trends.

Lithium Diffusion Mechanisms

To characterize lithium ion transport within this polyelectrolyte system, we consider not only the static picture of the lithium ion coordination environments but also the dynamic trends governing the motion of Li^+ relative to its surroundings. Diffusion of Li^+ relative to another species can be characterized as either vehicular, in which Li^+ diffuses together with its solvation shell as a single complex, or structural, where neighboring species do not move together for appreciable distances. In the latter case, the Li^+ solvation shell molecules are

frequently exchanged [142]. Identification of these mechanisms has been shown in previous works to be crucial for fully understanding trends in ionic conductivity [143, 144].

The diffusion mechanism of one species relative to another can be distinguished quantitatively by calculating the residence time (τ) for two neighboring species to move together [145, 146]. Herein we have evaluated residence times for Li^+ with respect to DMSO and SO_3^- (both CIPs in the first solvation shell and SSIPs in the second solvation shell) as well as for SO_3^- with respect to DMSO in its first solvation shell.

The residences times alone, however, cannot be used to compare diffusion mechanisms, as overall diffusion slows down at higher concentrations due to increased solution viscosity. Indeed, we observe that the residence times calculated for each pair of species (Figure 5.5a) generally increase as concentration increases. As the overall changes in system viscosity will be reflected in the solvent (DMSO) diffusion coefficient, we use this quantity to convert from residence time to diffusion length, $\mathcal{L}$, where $\mathcal{L} = \sqrt{6 D_{\mathrm{DMSO}} \tau}$. The calculated diffusion lengths (Figure 5.5b) enable a systematic comparison of changing diffusion mechanisms across concentration. This analysis demonstrates that the diffusion length generally decreases as concentration increases, corresponding to a shift in the diffusion mechanism towards more structural diffusion for all lithium species. The SO_3^--DMSO diffusion length, which stays relatively constant across concentration, is the only exception to this trend. The Li^+-SO_3^- (CIP) trend here is of particular interest. Although more ion pairs exist at higher concentrations (as shown by our static coordination environment analysis), the change in diffusion mechanism indicates that each of these ion pairs will travel a shorter distance as neighbors. We note that this observation has important implications for our analysis of cation-anion correlations and ionic conductivity in the following section.

While the aforementioned diffusion mechanism analysis has dealt exclusively with the *average* behavior of all lithium ions, we gain additional insight from analyzing the trajectories of individual Li^+. When mapping a given Li^+ trajectory over the scale of a few nanoseconds (shown for a representative Li^+ atom in Figure 5.5c), we observe discrete jumps of approximately 4-5 Å overlaid on the typical noise associated with molecular diffusion. Visualization of the lithium ion and its surroundings over this period reveals that these jumps correspond to ion hopping events between solvent-separated lithium and sulfonate ions, as pictured in Figure 5.5c. The average time between these hops is consistent with the residence time analysis of solvent-separated Li^+-SO_3^- pairs, as shown in Figure 5.5a. The residence time provides a quantitative measure of the average rate of hopping events, which can be interpreted as inversely proportional to τ [147].

This mechanism is reminiscent of the ion hopping behavior postulated for transport in solid polymer electrolytes [111,148] as well as organic liquid electrolytes at high concentration [149, 150]. In this polyelectrolyte, however, solvent-separated ion hopping is observed for all concentrations simulated, suggesting that hopping events may be facilitated by the presence of the polymer. Indeed, recent work [151] has generated evidence for substantial migration of territorially bound counterions (SSIPs) along polyelectrolyte backbones. It is possible that constraining the anion positions through their attachment to the chain backbone generates favorable anion-anion separation distances for the hopping to occur. Importantly, however,

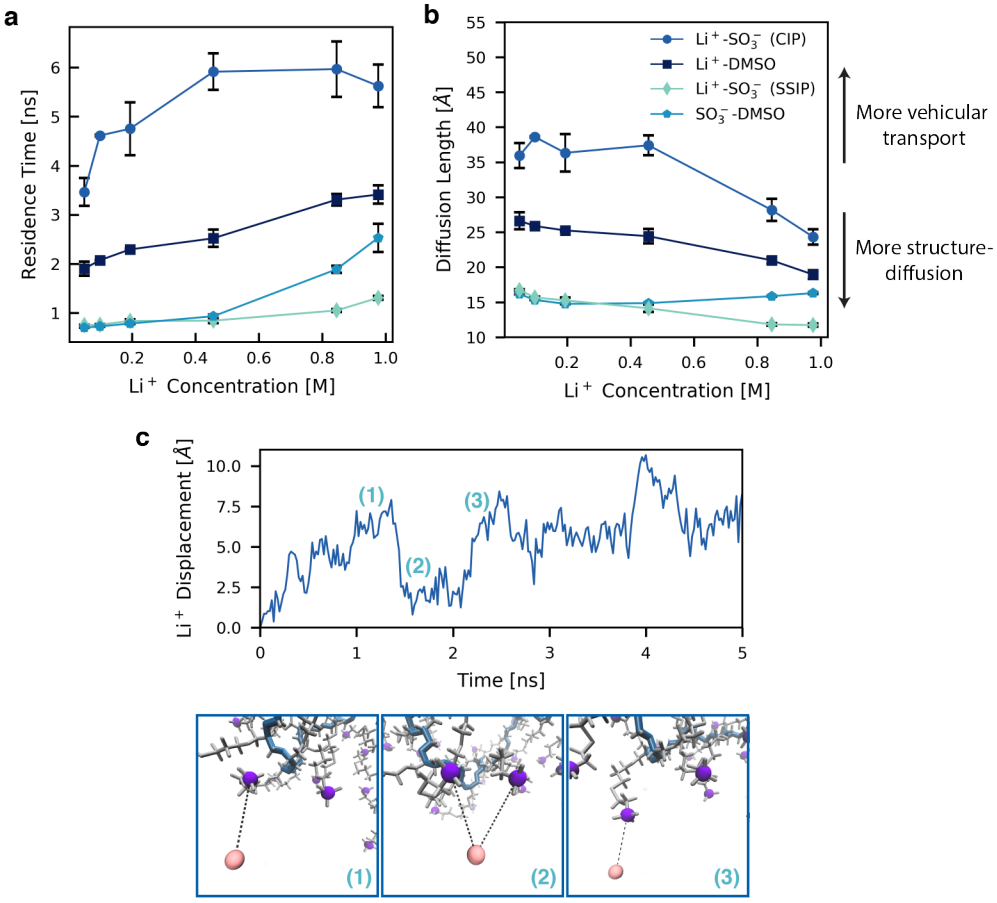

Figure 5.5: Characterization of lithium ion diffusion mechanisms. (a) Residence time (characteristic time travelled together by a pair of neighboring species before separating) as a function of concentration for various species. (b) Diffusion length as a function of concentration for various species. (c) Sample Li^+ trajectory with snapshots depicting the solvent-separated ion hopping process. Sulfur atoms on the sulfonate anion are depicted in purple, the lithium ion is pink, the chain backbone is blue, and the sidechains are gray. Solvent molecules are omitted for clarity.

we emphasize that the ion hopping diffusion mechanism is not the only process governing overall Li^+ motion. In addition to these hopping events, full trajectory inspection reveals that the overall movement of the ions is heavily influenced by free diffusion in DMSO as well as co-diffusion of CIPs with the polymer.

Ionic Conductivity and Transference Number

Given that the main motivation for polyelectrolyte solutions as battery electrolytes is their predicted high lithium transference number, in this section we aim to evaluate the transference number as well as elucidate the physical mechanisms which govern it. Unlike experimental measurements, MD trajectories and the Onsager transport framework described in Chapters 2-4 afford us the ability to calculate t_+ without having to make any assumptions about the ideality of the solution. This framework allows us to gain more insight into the physical processes governing the ionic conductivity trends as a whole by decomposing the total conductivity into separate contributions from the various types of correlated and uncorrelated ion motion in the system [152–155]:

$$\kappa = \kappa^{++}_{\text{self}} + \kappa^{--}_{\text{self}} + \kappa^{++}_{\text{distinct}} + \kappa^{--}_{\text{distinct}} + 2\kappa^{+-} \tag{5.4}$$

Here, and throughout this chapter, we consider the quantities κ^{ij}, related to L^{ij} via $L^{ij} = \frac{\kappa^{ij}}{z_i z_j F^2}$, such that the transport coefficients exhibit the dimensions of ionic conductivity. While we will return to the L^{ij} notation in the following chapter, working with κ^{ij} provides a more physically-intuitive means of analyzing the contributions to the conductivity. The two self-conductivity terms ($\kappa^{++}_{\text{self}}$ and $\kappa^{--}_{\text{self}}$) yield the conductivity from completely uncorrelated ion motion. The distinct terms ($\kappa^{++}_{\text{distinct}}$, $\kappa^{--}_{\text{distinct}}$, and κ^{+-}) capture ion-ion correlations between pairs of cations, pairs of anions, and cation-anion pairs, respectively. If the sum of all the distinct terms is zero, the resulting conductivity follows Nernst-Einstein or ideal solution behavior. In this case, t_+^{NE} will correspond to the true transference number. However, the distinct terms typically decrease both conductivity and cation transference number relative to the ideal case [155, 156].

While analysis of the conductivity in this manner is more common for conventional, low molecular weight salt electrolytes, the framework here is consistent with that often used in the polyelectrolyte community, in which the total conductivity is expressed as the product of the ideal solution conductivity and an interaction parameter capturing interionic friction and ion pairing effects [157]. It has been shown by Vink [158] that these expressions for polyelectrolyte conductivity can be derived from linear irreversible thermodynamics, the same starting point for deriving the Green-Kubo relations on which the conductivity analysis in this work is based. The analysis here, however, allows us to calculate the relative contribution of each type of ion-ion interaction to the total conductivity rather than only a single interaction parameter — an analysis which to our best knowledge has not been previously applied to any polyelectrolyte system. Note that in this analysis, we are considering the behavior of each individual sulfonate anion, rather than the center-of-mass motion of the entire

polyelectrolyte chain. Either choice of anion yields equivalent results for the computed total ionic conductivity, electrophoretic mobilities, and transference number (see Section B.3).

Figure 5.6a shows the contribution of each of the terms in Eq. (5.4) to the overall molar conductivity in this system. The two self-conductivity terms are closely related to the cation and anion self-diffusion coefficients, and thus their contribution to the total molar conductivity decreases as concentration increases. The Li^+-distinct conductivity is approximately zero at all concentrations, corresponding to uncorrelated ion motion, although at higher concentrations the relative contribution of $\kappa^{++}_{\text{distinct}}$ slightly decreases to become negative. Negative conductivity contributions signify anti-correlated motion, as Li^+ ions within close proximity repel each other. This trend is more apparent when plotting the fractional contribution of each conductivity term to the total conductivity (Figure 5.6b), rather than the molar conductivity.

The Li^+-SO_3^- distinct conductivity impacts the overall conductivity much more significantly. We find the calculated κ^{+-} for the PAGELS in DMSO system to be negative for all concentrations. As the anion and cation are oppositely charged, a negative κ^{+-} corresponds to correlated ion motion, for example through the joint movement of an ion pair. This negative contribution coincides with our intuitive understanding of ion pairing lowering the overall conductivity relative to the ideal case. Surprisingly, the negative contribution of κ^{+-} decreases in magnitude, signifying less correlated cation-anion motion, as concentration increases, despite the fact that the fraction of paired Li^+ ions increases with concentration. We rationalize this behavior at least in part through the aforementioned trends in diffusion mechanism. While the percentage of CIPs is higher at high concentrations, these ion pairs exhibit shorter diffusion lengths such that they diffuse through a more structural mechanism than ion pairs at low concentration. Indeed, shorter distances travelled as a single correlated entity are consistent with smaller contributions to κ^{+-}. We speculate that changes in Li^+-SO_3^- correlation with concentration may also be related to the decreased charge screening length at high concentrations, which limits electrostatic attraction between ions to shorter distances.

These results suggest that a purely static analysis of ion pairing, simply the spatial arrangement of atoms at any given time, is inadequate to fully understand trends in ionic conductivity. Importantly, this finding conflicts with the underlying assumptions of many polyelectrolyte conductivity theories, in which the fraction of uncondensed (free) counterions is often included as an adjustable parameter by which the entire conductivity is scaled [157, 159].

We further note that the trend of increasingly negative κ^{+-} at lower concentrations has been observed in MD simulations of non-polyelectrolyte systems, such as superconcentrated LiTFSI in tetraglyme as well as 1-butyl-3-methylimidazolium tetrafluoroborate ($[BMIM^+][BF_4^-]$) electrolytes in a variety of solvents [152,153]. Similarly, Haskins et al. [160] noted that the fraction of uncorrelated ionic motion ($\kappa_{\text{NE}}/\kappa$, where κ_{NE} is the Nernst-Einstein conductivity) increases with concentration for Li^+-doped ionic liquid electrolytes, i.e. the distinct conductivity terms decrease as concentration increases. In agreement with our observations, they attribute this trend to a change in diffusion mechanism from vehicular to

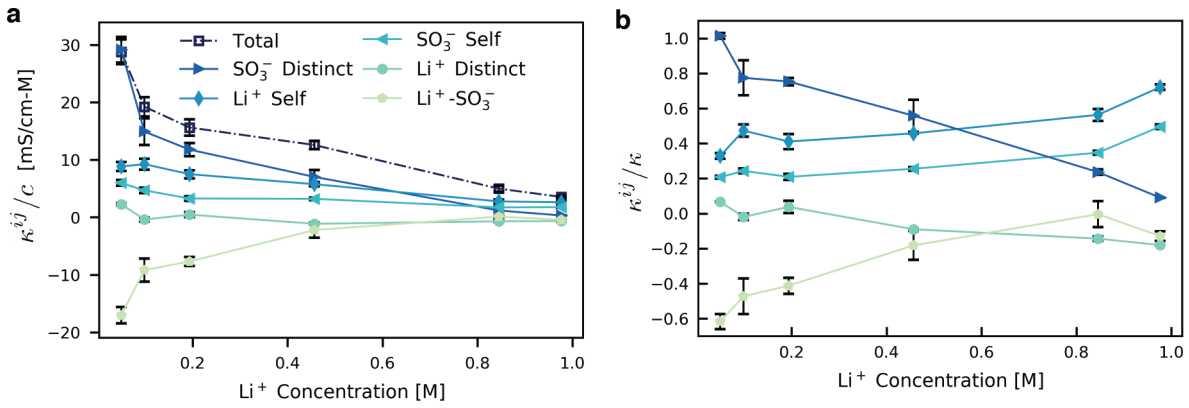

Figure 5.6: Transport coefficients for PAGELS in DMSO. (a) Contributions of each type of uncorrelated (self) or correlated (distinct) ion motion to the total molar conductivity (κ^{ij}/c). (b) Fractional contributions of each type of uncorrelated (self) or correlated (distinct) ion motion to the total conductivity (κ^{ij}/κ).

more structural as concentration increases.

While the aforementioned trends in self, cation-cation, and cation-anion conductivities are not unique to polyelectrolytes, the anion-anion correlation term introduces complexities not seen in conventional salt solutions. Typically, $\kappa^{--}_{\text{distinct}}$ does not contribute substantially to the overall conductivity [152, 153], analogous to $\kappa^{++}_{\text{distinct}}$. In anionic polyelectrolytes, however, each of the anions on a given chain is highly correlated to the others through their connection to the same polymer backbone. This correlated motion results in substantial positive contributions to the total ionic conductivity, which have important implications for analysis of the transference number (see below).

In addition to providing information on the mechanisms dictating ionic conductivity, dividing the conductivity into its constitutive elements also enables facile computation of the electrophoretic mobility of the ionic species based on Eq. (4.56):

$$\mu_+ = \frac{1}{Fc_+z_+}(\kappa^{++}_{\text{self}} + \kappa^{++}_{\text{distinct}} + \kappa^{+-}) \tag{5.5}$$

$$\mu_- = \frac{1}{Fc_-z_-}(\kappa^{--}_{\text{self}} + \kappa^{--}_{\text{distinct}} + \kappa^{+-}) \tag{5.6}$$

We note that the choice of z_- will not impact the final mobility, as the product c_-z_- is constant regardless of whether the individual anionic moieties or the polymer chain as a whole are considered. The mobility of both the polyion and Li^+ are shown in Figure 5.7a. As concentration increases, the mobility of both the polyelectrolyte chain and Li^+ decrease. As before, due to the short length of the polyion chain, the results do not coincide with

the classical polyelectrolyte scaling laws, which predict that polyelectrolyte mobility should be independent of concentration [161]. The mobilities can be converted to transference numbers using Eq. (4.59). In Figure 5.7b the calculated true transference numbers (denoted as t_+ in the figure) are overlaid with the diffusion coefficient-based transport numbers (t_+^{NE}) calculated from Eq. (5.2) using both $z_- = -1$ and $z_- = z_{\mathrm{polymer}} = -43$. As mentioned previously, the t_+^{NE} calculated using $z_- = -1$ is in agreement with the commonly-employed experimental analyses [96, 97] and yields very high transference number estimates which are relatively constant across concentrations. The true transference number, however, is significantly lower, ranging from 0.09 to 0.49; only the highest concentrations studied are predicted to exhibit transference numbers appreciably greater than those of conventional LIB electrolytes.

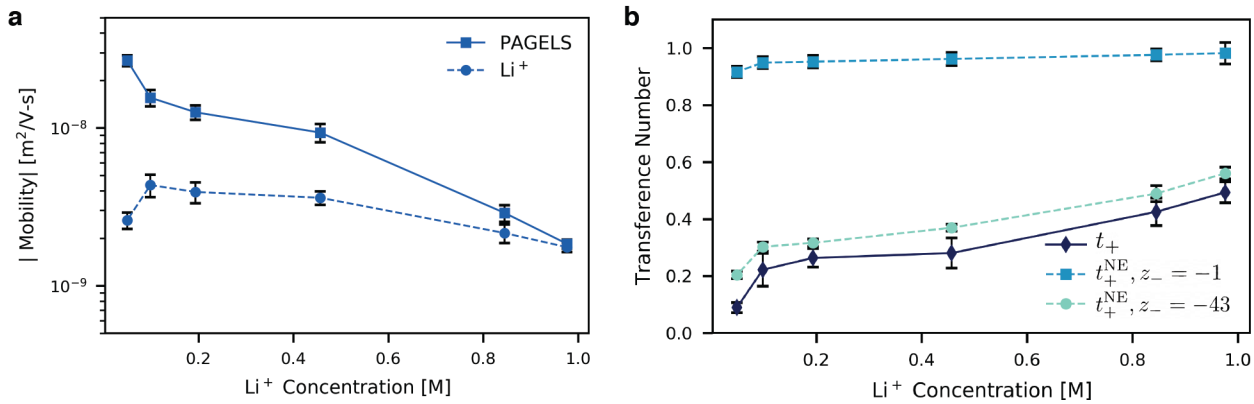

Figure 5.7: Mobility and transference numbers of PAGELS in DMSO. (a) Electrophoretic mobility of the PAGELS polymer and lithium ion as a function of concentration. The absolute value of the data is shown, as the anionic polymer mobility is negative. (b) Transference number as a function of concentration. The true transference number (t_+) calculated from ionic conductivity data is plotted along with the transport number (t_+^{NE}, an approximation of t_+ for ideal systems). Values for the charge of the anionic species (z_-) of both -1 and $z_{\mathrm{polymer}} = -43$ are used in calculating transport number.

These results demonstrate that the use of $z_- = -1$ in Eq. (5.2) severely overestimates the true transference number, and that the only correct interpretation of Eq. (5.2) is that using $z_- = z_{\mathrm{polymer}}$. Choosing $z_- = -1$ in the Nernst-Einstein equation assumes all ions in the system are completely uncorrelated, which simply cannot be true when all ions on a given chain are constrained to move together. In fact, anion-anion correlations ($\kappa^{--}_{\mathrm{distinct}}$) constitute the largest portion of the non-ideal distinct conductivity terms and are responsible for the majority of the discrepancy between t_+^{NE} ($z_- = -1$) and t_+. In contrast, t_+^{NE} ($z_- = z_{\mathrm{polymer}}$) treats the polymer collectively as a single unit and thus eliminates the need to account for

anion-anion correlations within a given chain, effectively combining the SO_3^- self and distinct contributions into a single term, the PAGELS self-conductivity. This data is in much closer agreement with the true t_+. In this case, the only component of the overall conductivity which is not accounted for is the cation-anion distinct conductivity (κ^{+-}). We note, however, that the calculated t_+ could be influenced by finite size effects. Our single-chain simulations may fail to capture important inter-chain interactions which may contribute to the overall distinct conductivity, although our preliminary tests using two chains (Figure B.1) suggest that these effects are unlikely to impact our main conclusions. Although we have modeled one specific polyelectrolyte system, the ion correlation and transference number analysis presented here has not made any assumptions regarding chain length or charge distribution of the polyelectrolyte and should thus be generally applicable. Hence, we recommend that experimentalists employing the Nernst-Einstein approximation and Eq. (5.2) to estimate transference number use $z_- = z_{\text{polymer}}$ in future work, rather than $z_- = -1$. This applies not only to polyelectrolyte systems but also to those which tether the anions together through other means, for example in polyoligomeric silsesquioxanes (POSS) functionalized with anionic moieties [162].

Although the cation transference number of the PAGELS in DMSO polyelectrolyte is not as promising as originally thought, optimization of chain length, concentration, and polymer chemistry may still yield systems with significantly higher t_+. Furthermore, the wide range in the true transference number as a function of concentration suggests that polyelectrolyte systems present an interesting means of tuning transference number in ways which cannot be accomplished in more conventional systems. Preliminary simulations suggest that decreasing polymer charge density, i.e. reducing the fraction of monomers with anionic moieties, may be a promising means of decreasing anion-anion correlations and thus increasing the transference number. The complex balance between charge density, total lithium concentration, viscosity, conductivity, and transference number in these solutions is the subject of future work.

In conclusion, we have investigated the structural and transport properties of a model nonaqueous polyelectrolyte solution, PAGELS in DMSO, through all-atom MD simulations. To validate the model, the calculated diffusion coefficients and ionic conductivity values were benchmarked against experimental results. We characterized the solvation structure and ion speciation behavior of the Li^+ in the electrolyte and demonstrated the clear relationship between ion pairing and polymer structure. Furthermore, analysis of the ion transport mechanisms in the solution revealed a shift towards more structural diffusion as concentration increases as well as the presence of a solvent-separated ion hopping motif. Finally, we deconvoluted the total ionic conductivity into contributions from each type of correlated and uncorrelated ion motion to demonstrate the substantial impact of cation-anion and anion-anion correlations. These non-ideal ion correlations substantially decrease the cation transference number relative to estimates based on experimentally measured diffusion coefficient data. We envision that the ion transport mechanisms elucidated in this work will inform design of improved polyelectrolyte systems for LIBs and enhance our understanding of charge transport in polyelectrolyte solutions in general.

Chapter 6

Onsager Transport Coefficients and Transference Numbers in Polyelectrolyte Solutions[1]

In the previous chapter, we demonstrated using all-atom molecular dynamics (MD) simulations that for one polyelectrolyte system, poly(allyl glycidyl ether-lithium sulfonate) (PAGELS) in dimethyl sulfoxide (DMSO), the Li-ion transference number is substantially lower than would be expected from the ideal solution (Nernst-Einstein) approximations ($t_+^{\mathrm{NE}} \gg t_+$). We demonstrated that although the PAGELS electrolyte had been presented in the literature [96] as having a very high transference number based on measurements of the Nernst-Einstein transference number, this electrolyte formulation may not in fact be promising for next-generation batteries. It remains to be seen, however, whether the failure of Eq. (5.3) generalizes beyond the PAGELS system, and whether we can make any more general claims about the extent of non-idealities (ion correlations) in polyelectrolytes which hold independent of the electrolyte chemistry. Furthermore, we wish to understand (i) the emergence of polyelectrolytes' unique transport properties as we transition from a conventional monomeric electrolyte to oligo- and polyanions and (ii) how transport properties change as a function of concentration, including the extreme limit of solvent-free systems or polymerized ionic liquids, which are also under investigation as LIB electrolyte alternatives [164–168]. While existing polyelectrolyte studies have extensively explored the polyion transport properties in these solutions [105,106], the behavior of the counterion and thus the battery-relevant transport properties of polyelectrolytes such as t_+ are largely unexplored.

Herein, we use coarse-grained molecular dynamics simulations with explicit solvent to systematically study transport as a function chain length and concentration for a generic polyelectrolyte solution. Making use of the Onsager transport framework described in Chapters 2-4, we present the Onsager transport coefficients L^{ij} computed for the coarse-grained

[1]This chapter is closely adapted from Ref [163]: Fong, K. D., Self, J., McCloskey, B. D. & Persson, K. A. Onsager transport coefficients and transference numbers in polyelectrolyte solutions and polymerized ionic liquids. *Macromolecules* **53**, 9503–9512 (2020).

polyelectrolyte model, gaining insight into the ion correlations between species in solution. We use these transport coefficients to calculate the transference number for the solutions, rationalizing the resulting trends based on ion correlations and ion pairing behavior. We find that the strong ion correlations in polyelectrolyte solutions generally yield conductivity and transference number values lower than in conventional monomeric electrolytes, suggesting that — from a transport perspective — polyelectrolytes may not be a promising alternative to conventional battery electrolytes.

6.1 Onsager transport coefficients in a coarse-grained polyelectrolyte model

Here we present the computed the Onsager transport coefficients for polyelectrolyte solutions using a coarse-grained molecular dynamics model based on the classical Kremer-Grest bead-spring chain [169, 170] with explicit solvent. We simulate chain lengths ranging from 1 to 25, noting that based on previous studies using similar polymer models we do not expect significant entanglement effects for these chain lengths [121,169,171]. These polyelectrolytes are studied at four concentrations ranging from 0.001 σ^{-3} to 0.05 σ^{-3}, where σ is the Lennard-Jones unit of distance and the diameter of each particle in the system. Mapping the size of one monomer bead to that of a polystyrene sulfonate monomer (2.5 Å), this concentration range approximately corresponds to 0.1 to 5 M (see Appendix B.3) section for a more detailed discussion).

In this section, we discuss the transport coefficients in these solutions and show how they may be interpreted to gain physical insight into transport phenomena in polyelectrolytes. Each of the transport coefficients L^{ij} quantifies a different aspect of ion motion or ion-ion correlation, illustrated qualitatively in Figure 4.1. Let us analyze L^{ij} as a function of chain length: these transport coefficients are given directly for a concentration of 0.01 σ^{-3} in Figure 6.1a and with diagonal terms L^{ii} split into self and distinct components in Figure 6.1b. The latter will provide more intuitive insight into the transport behavior of these systems.

The two self terms (L^{++}_{self} and L^{--}_{self}) given in Figure 6.1b are proportional to the self-diffusion coefficients (Eq. (4.5)). For the monomeric systems ($N = 1$) corresponding to conventional binary electrolytes, L^{++}_{self} is necessarily equal to L^{--}_{self}, as the cation and anion in the model are equivalent in their mass, size, and excluded volume (Lennard-Jones) interactions. As N increases, both L^{++}_{self} and L^{--}_{self} decrease, a trend which aligns with the intuitive expectation of diffusion coefficients to decrease as the chain becomes larger and the overall solution more viscous. The decrease in L^{--}_{self} is more pronounced due to the bulky nature of the polymer chain.

The L^{+-} transport coefficient captures correlations between cations and anions. The value of L^{+-} is much lower than that of either L^{++} or L^{--} for the $N = 1$ system but becomes increasingly significant as chain length increases. This trend suggests an increased prevalence of ion pairing at higher N, as expected from theories for counterion condensation

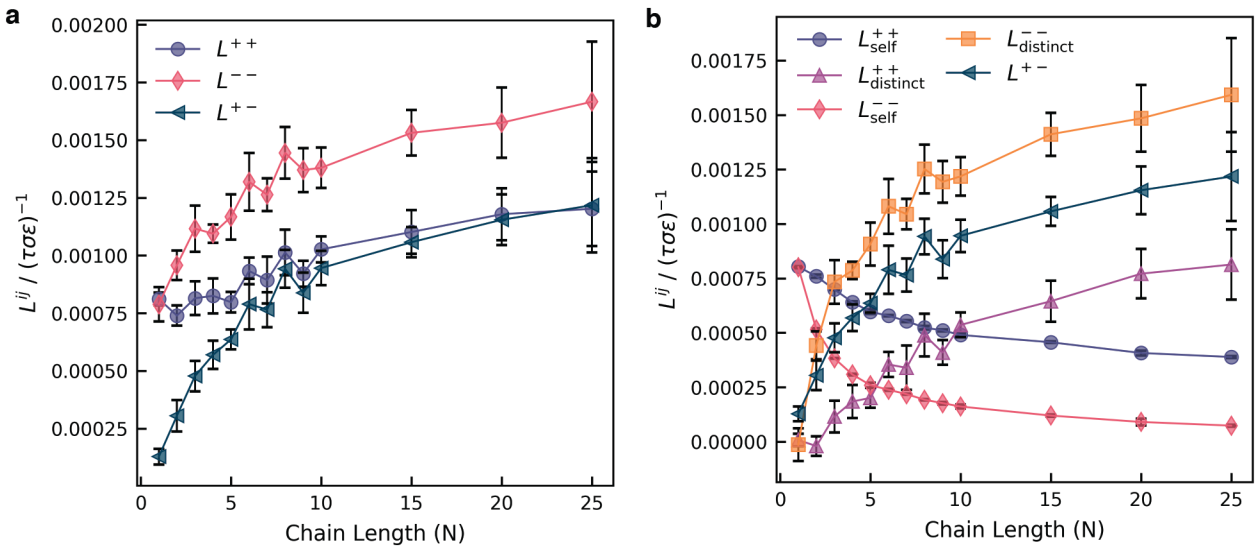

Figure 6.1: Transport coefficients as a function of chain length for a concentration of 0.001 σ^{-3}, including (a) total L^{ij} and (b) L^{ij} with diagonal terms decomposed into self and distinct contributions.

in polyelectrolytes [132] and confirmed directly in these simulations *vide infra*. Note that when computing ionic conductivity via Eq. (4.53), the L^{+-} term will be subtracted from the total value. Thus, as expected, cation-anion correlations decrease the overall conductivity.

Let us now turn to the distinct terms, L^{++}_{distinct} and L^{--}_{distinct}, which describe cation-cation and anion-anion correlations, respectively. In general, one would expect distinct ions of the same species to interact very little, in which case the distinct terms would be approximately zero, or to repel, leading to negative values of the distinct terms reflecting anti-correlated motion. Indeed, the monomeric ($N = 1$) systems studied here show very small contributions of L^{++}_{distinct} and L^{--}_{distinct}, with the values at high concentration being slightly negative. As chain length increases, however, we deviate from this expected behavior and observe that L^{++}_{distinct} and L^{--}_{distinct} increase with chain length. These very positive values suggest highly correlated motion, i.e. groups of like-charge ions moving together for appreciable periods of time. Like the trend in L^{+-}, this behavior can be rationalized by increased ion aggregation. The increase of L^{++}_{distinct} with chain length reflects the presence of multiple cations bound to the same chain, which will move together for the lifetime of the ion aggregate. As chain length increases (and with it the extent ion pairing), we expect more cations on average to be bound to a given chain, resulting in an increase in the correlations between distinct cations.

The increase in L^{--}_{distinct} with chain length is even more pronounced: for most chain lengths, this term dominates over all other transport coefficients and will thus strongly impact

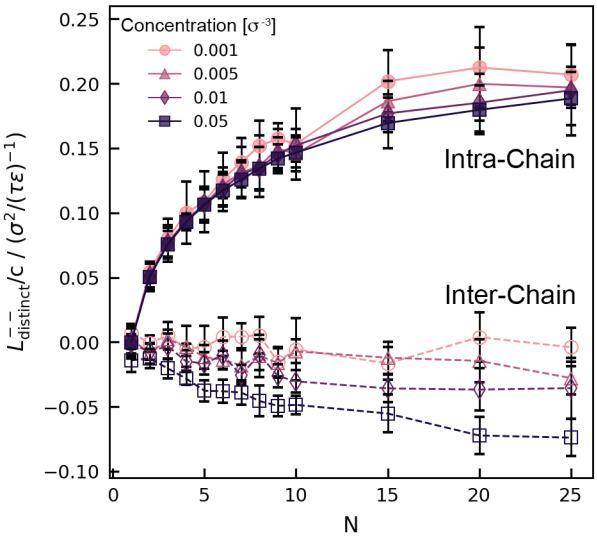

Figure 6.2: $L^{--}_{\text{distinct}}/c$ split into contributions from anion-anion correlations within chains (solid lines, filled markers) and between chains (dashed lines, open markers). The two curves sum to yield the total $L^{--}_{\text{distinct}}/c$.

conductivity and transference number. The total value of L^{--}_{distinct} contains contributions from correlations between anions tethered to the same chain as well as anions on different chains. The former will generate a positive contribution to L^{--}_{distinct}, as anions on a given chain are constrained to move together and are thus highly correlated, while the latter will give a negative contribution, as two negatively-charged macroions will repel each other and move in an anti-correlated manner. In all systems studied, we observe that intra-chain correlations dominate over inter-chain correlations (Figure 6.2), yielding the strong positive trend in L^{--}_{distinct} with chain length. Details on the decomposition of L^{--}_{distinct} into these two contributions are provided in Appendix B.3.

While the analysis of the Onsager transport coefficients presented in this section has provided detailed physical intuition as the the nature of ion motion in these polyelectrolyte systems, the reader may be more familiar with the Stefan-Maxwell equations for multicomponent diffusion, and by extension Newman's concentrated electrolyte theory [2], rather than the Onsager equations presented in this work. As discussed in Chapter 4, both frameworks are thermodynamically consistent, and it is possible to map between the transport coefficients from the two approaches (Eq. (4.25)). We thus provide the Stefan-Maxwell coefficients K^{ij} for the polyelectrolyte solutions studied at a concentration of 0.01 σ^{-3} for comparison (Figure 6.3). Note that for the more dilute concentrations studied K^{-0} transitions from positive to negative, corresponding to divergence of the Stefan-Maxwell diffusion coefficients D^{ij}, where $K^{ij} = \frac{RTc_ic_j}{c_{\text{T}}D^{ij}}$. The molecular-level interpretation of such behavior, which has been

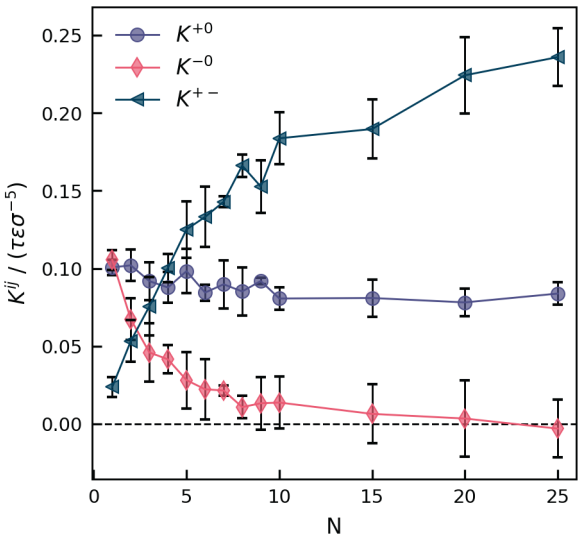

Figure 6.3: Stefan-Maxwell coefficients K^{ij} for a concentration of 0.01 σ^{-3}.

observed experimentally in solid polymer electrolytes as well [29], is the subject of ongoing work.

6.2 Transference numbers

Having computed the transport coefficients for a range of polyelectrolyte solutions, we may now combine these L^{ij} to obtain experimentally relevant quantities, specifically the cation transference number, shown in Figure 6.4a. We observe that for all concentrations studied, the transference number decreases as chain length increases, with the monomeric electrolyte having the highest transference number. Given that ionic conductivity generally decreases as chain length increases, these results suggest that the polyelectrolyte solutions studied herein would not yield any advantages in battery performance relative to a conventional monomeric electrolyte.

The values of the rigorously computed t_+ stand in stark contrast with the ideal solution transference number, t_+^{NE}. Recall from Eq. (5.2) that there are two options for computing t_+^{NE}: we may choose to treat each monomer as a separate ion, in which case the z_- appearing in Eq. (5.2) is -1, or we may treat the entire polymer chain as the anionic species, in which case $z_- = -N$. The resulting t_+^{NE} values based on each of these choices are given in Figures 6.4b and c. We observe that t_+^{NE} ($z_- = -N$) qualitatively reproduces the trend that transference number decreases as chain length increases, but in most cases it overestimates the rigorously computed t_+. This equation ignores correlations between different chains and between cations and anions, but it captures intra-chain correlations by treating the entire

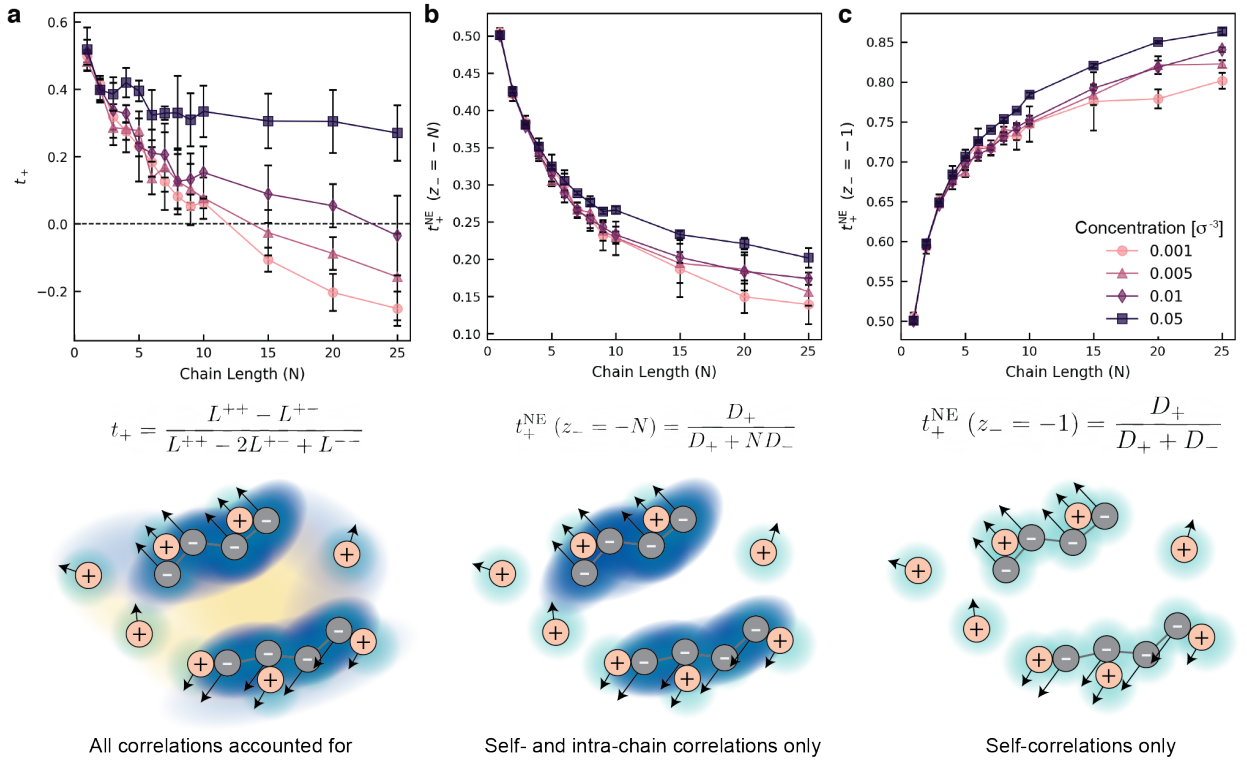

Figure 6.4: Cation transference number as a function of chain length. (a) Rigorously computed t_+ obtained from the Onsager transport coefficients and accounting for all ion correlations present in solution. (b) and (c) t_+^{NE}, the ideal solution transference number ignoring correlations between ions. These are written in terms of the self-diffusion coefficients, rather than Onsager transport coefficients, using Eq. (4.5). (b) Treating entire polymer chains as the anionic species ($z_- = -N$) accounts for intra-chain correlations but ignores correlations between chains and between cations and anions. (c) Treating individual monomers as the anionic species ($z_- = -1$) ignores all ionic correlations. Ion correlations are depicted according to the colormap in Figure 4.1.

chain as a single unit. In contrast, t_+^{NE} ($z_- = -1$) does not account for any correlations between ions, capturing only self-diffusion. This assumes that monomers on the same chain move completely independently, which is obviously incorrect given the fact that they are covalently bonded. The resulting values for t_+^{NE} ($z_- = -1$) in Figure 6.4c increase with chain length, reaching values as high as 0.86. This approximation drastically overestimates the true t_+ and clearly does not provide a physically meaningful estimate of transference number in polyelectrolytes. In experimental systems where the transference number cannot be rigorously measured and only self-diffusion coefficients are available, t_+^{NE} ($z_- = -N$) provides a much more reasonable estimate of t_+.

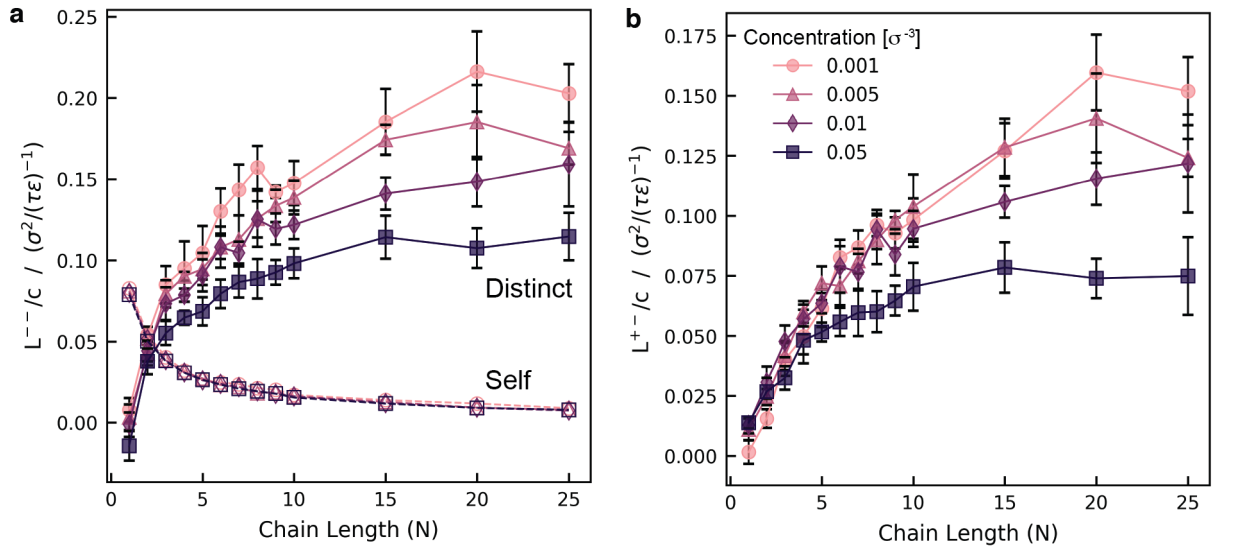

Figure 6.5: Comparison of anion transport coefficients for each concentration and chain length. (a) L^{--}_{self} (dashed lines) and L^{--}_{distinct} (solid lines), all divided by concentration to give the contributions to each transport coefficient per ion. (b) L^{+-} divided by concentration.

We now seek to rationalize the transference number trends in Figure 6.4 based on the ion correlations in the electrolyte. While each of the L^{ij} affect the observed trends in the transference number, the general decrease in t_+ with increasing chain length can be most directly understood through the trends in L^{--}_{self} and L^{--}_{distinct}, which are shown in Figure 6.5a. The data in this figure are divided by the total concentration to yield the contribution to each transport coefficient per ion. For each concentration, the L^{--}_{self} term (and thus the self-diffusion coefficient) decreases with N. Indeed, the fact that a long polymer chain moves more slowly than a monomer is the basis for the intuitive notion that the anion in a polyelectrolyte solution should carry less current than the cation to yield a high t_+. As Eq. (5.2) for t_+^{NE} includes only the self terms (assuming all distinct terms to be zero), it is clear why t_+^{NE} ($z_- = -1$) in Figure 6.4c exhibits such high values. In polyelectrolyte systems, however, it is unreasonable to ignore the distinct terms when estimating t_+, as we observe that the magnitude of L^{--}_{distinct} surpasses that of L^{--}_{self} for all but the shortest chain lengths (Figure 6.5a). As mentioned above, this increase in L^{--}_{distinct} is due to the fact that increasing N leads to more anions being covalently bound and thus constrained to move together, a phenomena which will be general to any polyelectrolyte regardless of the chemical properties of the polymer or solvent. The sum of the self and distinct terms, i.e., the overall L^{--}, increases with respect to chain length, corresponding to a decreasing cation transference number.

In addition to the trend with respect to chain length, we also note that t_+ increases with concentration, similarly to previous results obtained with all-atom simulations on PAGELS

in DMSO [86]. This can be most clearly understood in terms of cation-anion correlations, quantified in Figure 6.5b. The contribution to L^{+-} per ion decreases as the concentration increases, yielding higher t_+ for more concentrated solutions. In order to rationalize the trend of decreasing cation-anion correlations as concentration increases, let us consider the ion pairing behavior of the solutions. Ion pairing is conventionally defined based on a structural analysis of the solution: a cation is considered to be paired at a given time if it is within some specific distance of an anion. The fraction of cations in ion pairs or larger aggregates based on this type of analysis is given in Figure 6.6a. The resulting trend that ion pairing increases with concentration, however, is not consistent with the trend of decreasing L^{+-}/c with concentration, suggesting that this static structural analysis does not provide a meaningful assessment of ion correlations in the system. Instead, the trends in L^{+-}/c must be understood with a dynamic analysis of ion pairing, shown in Figure 6.6b. Here we quantify the ion pair residence time, or the characteristic time for an ion pair to exist before breaking apart [145,146,172]. Despite the fact that more ions are paired at high concentrations, each of these pairs has a shorter lifetime, resulting in overall less correlated cation-anion motion and higher cation transference number. This phenomenon is illustrated schematically in Figures 6.6c and d. The negative correlation between static ion pairing fraction and dynamic ion pair lifetime was similarly observed in MD simulations of PAGELS in DMSO [86], suggesting that this may be a common phenomenon in polyelectrolyte solutions.

The lowest concentrations studied yield negative t_+ at high chain lengths. This phenomenon corresponds to the presence of negatively charged aggregates which contribute substantially to the conductivity. For example, if a single cation is bound to a polyanion chain to yield an aggregate with large negative charge, upon application of an electric field that bound cation will move along with the polymer towards higher electric potential (in the "wrong direction"). As these negatively-charged aggregates are a natural occurrence in polyelectrolytes, it is unsurprising that we observe $t_+ < 0$ (or equivalently $t_- > 1$) for cases at low concentration when ion pairs are long-lived. In fact, solutions with $t_- > 1$ have been widely reported experimentally for dilute, aqueous polyelectrolytes [173–177]. The phenomena of negative transference number is discussed in more detail in Chapter 7.2.

6.3 Extension to polymerized ionic liquids

Given the trend of increasing cation transference number with concentration, the question naturally arises as to whether further increasing concentration may yield polyelectrolytes with t_+ greater than that of the monomeric solution. We can answer this question by considering the limit of a solvent-free system, i.e., a polymerized ionic liquid.

We must first revisit our theoretical framework for the case of a solvent-free system. As mentioned above, a system with n components will have $n(n-1)/2$ independent transport coefficients. A two-component electrolyte will thus only have one independent transport coefficient. We remind the reader that $\sum_i M_i L^{ij} = 0$ as a consequence of our center-of-mass reference frame, where M_i is the molar mass of species i. Noting that the masses

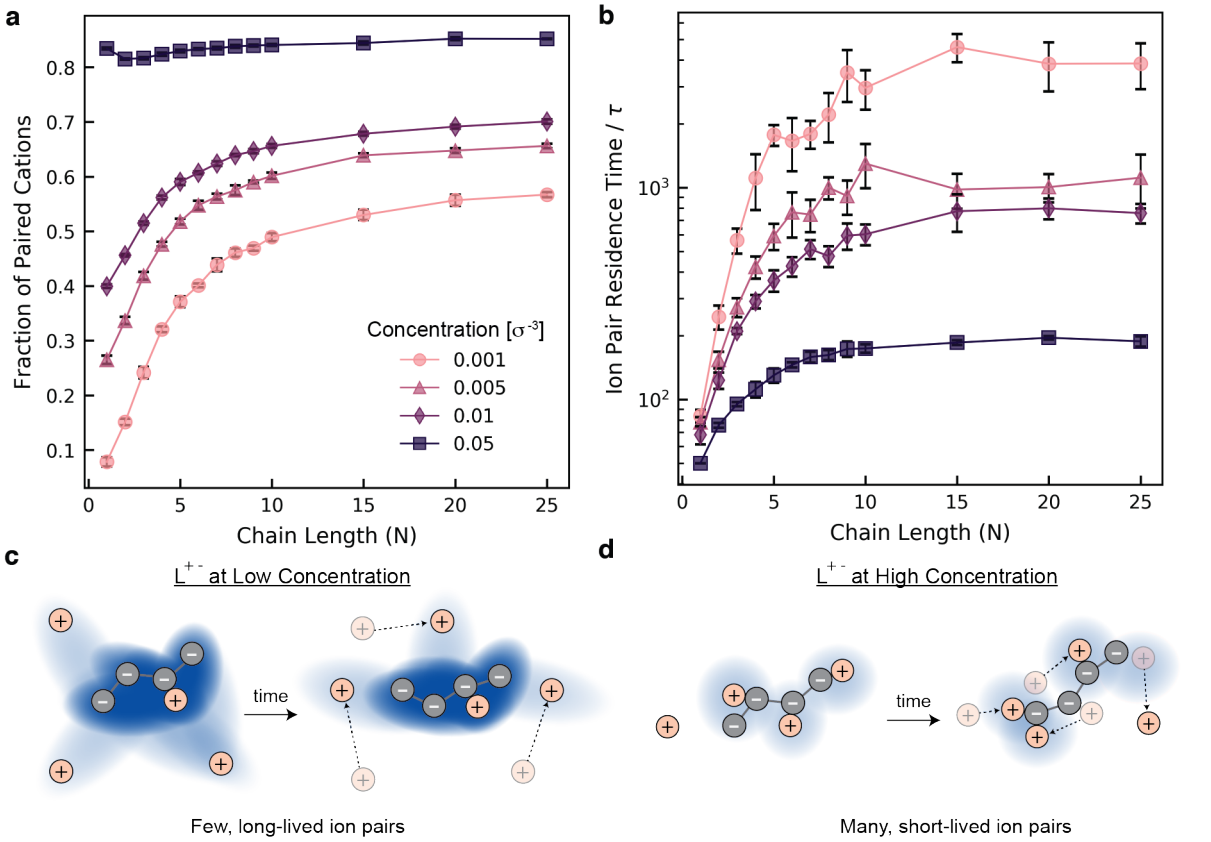

Figure 6.6: Ion pairing analysis. (a) Fraction of cations in ion pairs or aggregates based on static structural analysis. (b) Ion pair residence times. (c) and (d) Schematic illustration of cation-anion correlations (L^{+-}) at low (c) and high (d) concentrations. Ion correlations are depicted according to the colormap in Figure 6.1.

of all species in our system are equivalent, we can conclude that $L^{++} = L^{--} = -L^{+-}$ in these solvent-free systems. Indeed, the computed transport coefficients follow exactly this relation (Figure 6.7a; self and distinct transport coefficients for these systems, as well as the total ionic conductivity, are provided in Figure 6.8). The implications of this data are twofold. First, L^{+-} is necessarily negative in a two-component electrolyte, suggesting anti-correlated cation-anion motion. This phenomena has been previously noted in the ionic liquids literature [153, 154, 165]. Second, from Eq. (4.59) it can be shown that the transference number of these solvent-free solutions is determined solely by the ion charges and masses: $t_+ = z_+M_-/(z_+M_- - z_-M_+)$. This phenomenon, too, has been noted previously for polymerized ionic liquids [165] and molten salts [178,179]. In the polyelectrolyte solutions modeled here where the cation and monomer masses are the same, $t_+ = 0.5$ for all chain lengths (Figure 6.7b).

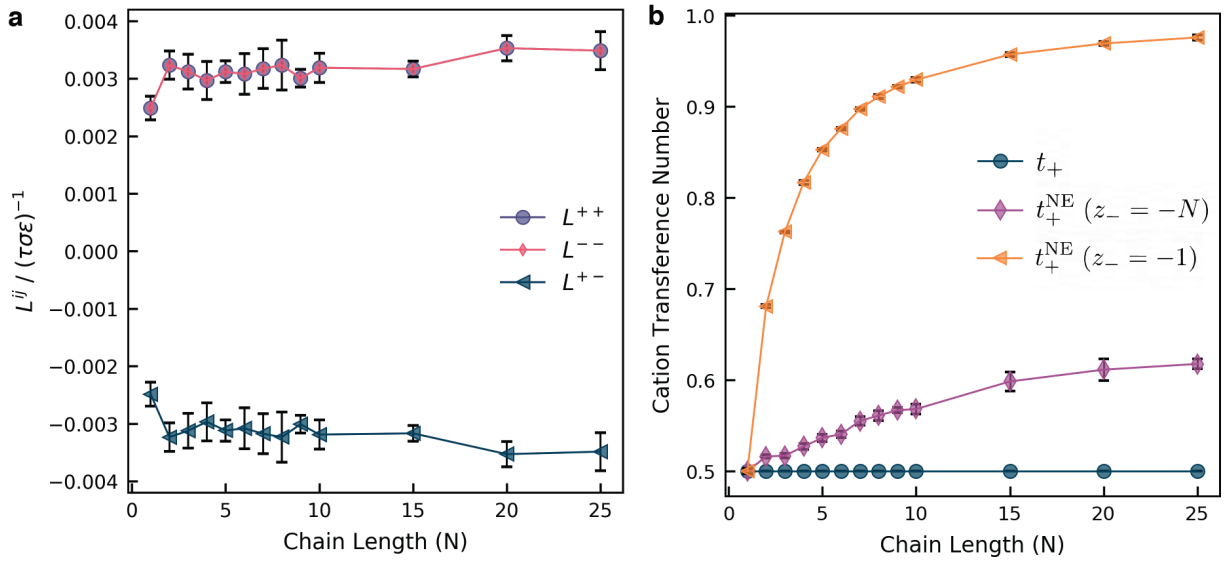

Figure 6.7: Transport data for the solvent-free solution. (a) Transport coefficients as a function of chain length. The markers for L^{++} and L^{--} directly overlap. (b) Transference number as a function of chain length, computed rigorously (t_+) and using the Nernst-Einstein approximation (t_+^{NE}).

Note that in most physically relevant polymerized ionic liquids or single-ion conductors, the cation and anion ratios are drastically different, and thus the computed transference number will deviate from the value of 0.5 reported for the systems studied here. In the polystyrene-TFSI-based systems commonly investigated experimentally [93, 180], for example, the anionic monomer has a molar mass of 314.28 g/mol, compared to the Li-ion mass of 6.94 g/mol. This mass discrepancy would translate to a transference number of 0.98 in a two-component solution of dry lithiated polystyrene-TFSI — in line with experimental characterization of these types of systems having very high t_+ [93, 180]. It is important to note that the main utility of the transference number is in dictating the extent of concentration gradients in an electrolyte, which limit a battery's rate capability [3]. As electroneutrality dictates that no concentration gradients may be formed in a solvent-free electrolyte, however, the transference number of these systems is of little physical relevance in predicting battery performance. Regardless, even in this superconcentrated limit, we do not observe any polyelectrolyte solutions with cation transference number greater than the conventional monomeric systems.

In summary, here we have computed the Onsager transport coefficients in polyelectrolyte solutions as a function of chain length and concentration using coarse-grained molecular dynamics simulations with explicit solvent. These transport coefficients provide insight into the correlations dictating ion motion and allow us to rigorously compute the transference

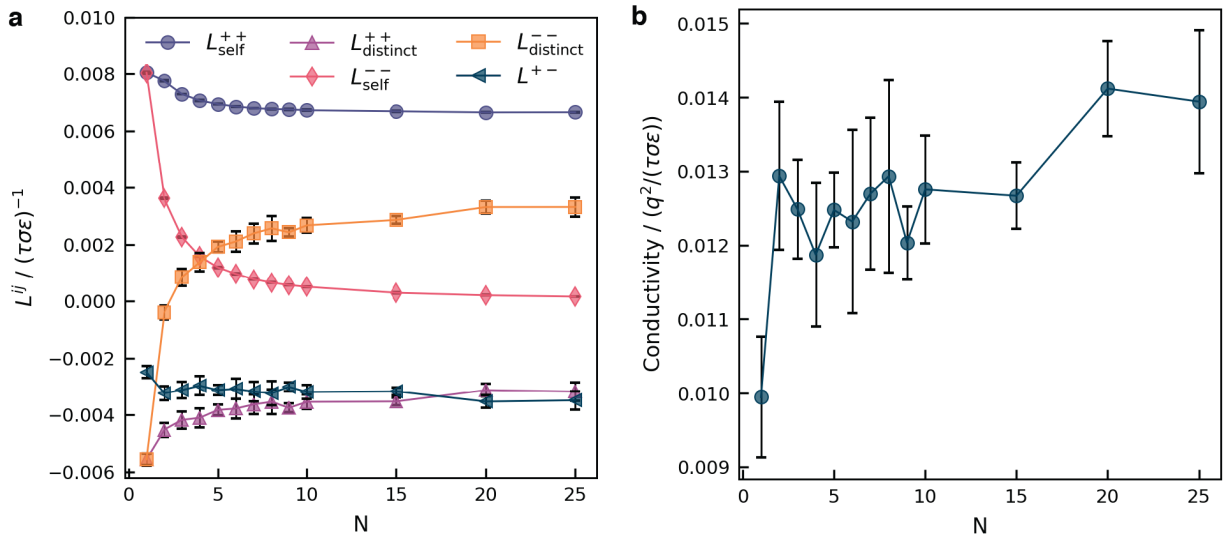

Figure 6.8: (a) Transport coefficients for the solvent-free system as a function of chain length, split into self and distinct terms. (b) Conductivity as a function of chain length for the solvent-free system.

number of the solutions. We demonstrate that the intrinsic anion-anion correlations within chains result in decreasing t_+ as chain length increases and cause substantial deviation between the true t_+ and the ideal solution quantity t_+^{NE}. Furthermore, the decrease in t_+ with decreasing concentration can be attributed to stronger cation-anion correlations for more dilute solutions. These stronger correlations are primarily attributed to the longer lifetime of existing ion pairs rather than an increased quantity of ion pairs (defined based on a structural picture of the solution). Even in the case of a solvent-free system (polymerized ionic liquid), we do not observe any polyelectrolyte solutions with transference number greater than that of a conventional monomeric electrolyte. These results suggest that unentangled, short-chain polyelectrolyte solutions may not be useful as high t_+ alternatives to conventional LIB electrolytes. It is possible that polyelectrolyte solutions or gel-like single-ion conductors may be able to attain high cation transference number if the chains are entangled or cross-linked such that the polymer is effectively immobile. Based on Eq. (3.29), we see that if the flux of the anion is zero, then L^{--} and L^{+-} will also tend to zero, in which case the transference number would approach unity. While these systems could have high transference number, these approaches typically yield very low conductivity [93,181]. Thus there exists a trade-off between cation transference number and conductivity which must be resolved in order to achieve promising single-ion conductors.

Chapter 7

Conclusions[1]

7.1 Dissertation summary

Herein, we have presented the development and application of the Onsager transport framework as a rigorous and intuitive theory for analyzing transport in electrolyte solutions. In Chapter 2, we derive the continuum-level governing equations for electrolyte transport and formulate linear laws relating the thermodynamic driving forces and fluxes in an electrolyte, giving rise to the Onsager transport coefficients L^{ij}. We establish the connection between these coefficients and equilibrium fluctuations in ion motion in Chapter 3, where we derive Green-Kubo relations for L^{ij}. Our code to use these relations to extract L^{ij} from molecular simulation data is available at `https://github.com/kdfong/transport-coefficients-MSD`.

We provide physical interpretation for the Onsager transport coefficients and relate them to experimentally-relevant quantities and other commonly used transport theories in Chapter 4. We emphasize that while the Onsager framework and the more ubiquitous Stefan-Maxwell equations are thermodynamically consistent, the Onsager framework possesses several key advantages, in that its transport coefficients (i) yield simpler relations for experimentally-relevant transport quantities than K^{ij}, which easily generalize to complex multicomponent solutions, (ii) are easier to compute from molecular simulations, and (iii) have a clearer physical interpretation, as they directly relate to ion correlations. We present simulations of a simple electrolyte solution, lithium chloride in dimethyl sulfoxide, to demonstrate the types of insights gained from analyzing transport through the lens of the Onsager transport coefficients.

In Chapter 5, we utilize the Onsager transport framework to demonstrate the dramatic failure of the Nernst-Einstein approximation in polyelectrolyte solutions. Using atomistic molecular dynamics simulations, we quantify the substantial contribution of ion-ion correla-

[1]Portions of this chapter are adapted from Ref. [54]: Fong, K. D., Self, J., McCloskey, B. D. & Persson, K. A. Ion correlations and their impact on transport in polymer-based electrolytes. *Macromolecules* **54**, 2575–2591 (2021)

tions in nonaqueous polyelectrolytes, which drastically decrease the true cation transference number relative to the Nernst-Einstein value. This work suggests that although multiple experimental studies have presented polyelectrolytes as promising high transference number systems based on the Nernst-Einstein approximation, these electrolytes may not actually possess favorable transport properties for battery applications. We demonstrate that these conclusions generalize to generic polyelectrolyte solutions using coarse-grained molecular dynamics simulations in Chapter 6. In this chapter we further demonstrate the presence of negative transference numbers in some polyelectrolyte solutions, and we elucidate the counterintuitive nature of transport in polymerized ionic liquids and other two-component electrolytes, where we observe anti-correlated cation-anion motion and transference numbers which are independent of chain length.

These investigations into polyelectrolyte transport have inspired new experimental efforts to verify the transference number behavior predicted by this theoretical and computational work. Experiments are currently ongoing to (i) systematically synthesize new model polyelectrolyte solutions with precisely controlled chain lengths, ranging from the monomer to the oligomeric regime, and (ii) develop electrophoretic NMR capabilities to rigorously measure the transference numbers of these solutions without resorting to ideal solution approximations. Preliminary measurements have confirmed the strong decrease in cation transference number as polymer chain length increases and the occurrence of negative transference numbers for longer chains.

7.2 Perspectives on the importance of ion correlations in electrolyte transport

The analyses presented herein on polyelectrolyte solutions give rise to more general conclusions regarding the significance of ion correlations in electrolyte solutions. In this section, we discuss the broader relevance of each of the various types of ion correlations that exist in an electrolyte. Although analysis of ion correlations and Onsager-type transport coefficients is rare in the literature, there exist a myriad of systems in which analyzing transport through this lens may yield important mechanistic insights and suggest design rules for electrolytes with enhanced transport properties. This section presents representative case studies of such systems from the literature and summarizes the central themes emerging from the transport coefficient analysis presented in this dissertation.

Cation-anion correlations

Understanding cation-anion correlations, captured in the transport coefficient L^{+-}, is crucial for the design of electrolytes for energy storage applications. As these correlations are induced by the inherent electrostatic attraction between cations and anions, L^{+-} will generally be non-negligible for most electrolytes used in energy storage applications, which typically

employ moderately high concentrations and/or a relatively low dielectric constant. In general, an optimal electrolyte will minimize cation-anion correlations, as a more positive value of L^{+-} will decrease the ionic conductivity of an electrolyte (Eq. 4.53), and, for the common case where the cation transference number is less than one half, a greater value of L^{+-} will also decrease t_+ (Eq. 4.59).

Static vs dynamic analyses of ion pairing

Cation-anion correlations are conventionally discussed in terms of ion pairing or aggregation, i.e., the fraction of ions which are bound to another ion at any given time [104]. In molecular simulations, it is common to use a distance criterion [86,182,183], such as the first minimum of the radial distribution function, to define an ion as either free, paired, or part of a higher order aggregate such as a triple ion. This offers a computationally inexpensive means of characterizing ionic interactions in an electrolyte, as the simulation timescales of this ion pairing analysis are generally much shorter than those required for dynamic analyses.

In some systems, the static picture of ion pairing adequately captures cation-anion correlations, and we will use this framework throughout this text to intuitively rationalize trends in ion correlations. France-Lanord and Grossman [129] developed an effective method for computing ionic conductivity from molecular simulations which accounts for ion correlations exclusively through analysis of ion aggregates. Each aggregate is considered a distinct charge carrier, and its diffusion coefficient is used in the Nernst-Einstein equation to compute conductivity. This method gives reasonable agreement with the rigorously-computed conductivity for LiTFSI in PEO. Burlatsky et al. used a simpler version of this approach for lithiated Nafion electrolytes containing nonaqueous solvents, in which the conductivity was estimated from the diffusion coefficient of only the free lithium ions and contributions from lithium ions paired to the Nafion polymer were ignored [127]. Furthermore, the static picture of ion pairing often forms the basis for theories of transport in polymer-based electrolytes, for example by assuming that bound ions do not contribute to conductivity [157,159,184]. In the polyelectrolyte literature, the fraction of free ions is a key parameter in theories describing diffusion, including the presence of diffusion coefficients several orders of magnitude greater than expected from the Stokes-Einstein equation (called the "fast" mode) [105,185,186].

Despite the aforementioned utility of analyzing ion speciation to understand cation-anion correlations, a growing body of work suggests that this static picture alone is inadequate in many electrolyte systems [187,188]. While the static picture analyzes the positions of the ions at a snapshot in time, the Green-Kubo relation for L^{+-} requires integrating the flux-flux correlation function over time, suggesting that a dynamic (time-dependent) analysis is necessary to understand how cation-anion interactions affect experimentally observable transport properties. The static ion pairing definition will generally overestimate cation-anion correlations: an ion pair that breaks apart immediately after forming, for example, will be accounted for in the static picture of ion pairing but will not contribute significantly to L^{+-}. Likewise, ions that hop directly between charged sites of a polyion (without first travelling through the surrounding dielectric medium) will contribute to the conductivity

despite the fact that the ions remain continuously paired. This type of ion transport has been observed as a crucial mechanism in a variety of systems, including polyelectrolytes [86, 151], polymerized ionic liquids [189], and ionomer melts [190–193]. The potential limitations of the static picture to describe cation-anion correlations have important implications for the interpretation of the ionicity (defined as $\kappa/\kappa^{\mathrm{NE}}$ to give the degree of uncorrelated ion motion) as well. It is often assumed that the ionicity corresponds to the fraction of free ions in the system, i.e., that the extent of ion correlation in an electrolyte is given directly by the degree of ion pairing [96, 194]. While there are some works in which the ionicity does indeed agree well with the fraction of free ions computed from molecular dynamics, for example in Borodin and Smith's simulations of LiTFSI in PEO [148], in what follows we discuss several instances in which this is not the case. As an extreme example, the ionicity of (polymerized) ionic liquids is often comparable to that of conventional liquid electrolytes [97, 195–199]; it is well-established that the static picture of ions as either bound or free fails for superconcentrated systems such as these [200–202].

Beyond the static fraction of ion pairing, further insight into cation-anion correlations can be obtained by analyzing the residence time of ion pairs, τ, or the average time that an ion pair persists before breaking apart. As in Chapters 5 and 6 of this work, τ may be computed from molecular dynamics simulations based on the autocorrelation function $P_{\alpha\beta}(t) = \left\langle H_{\alpha\beta}(t)H_{\alpha\beta}(0)\right\rangle$, where $H_{\alpha\beta}(t)$ equals one if particles α and β are neighbors at time t and zero otherwise. The decay time of $P_{\alpha\beta}(t)$, defined either by a stretched exponential fit or simply the time for the function to reach a certain value, yields τ [86,145,146,172,191,203].

Analysis of ion pair or cluster residence times has been shown to yield excellent correlation with the extent of ion correlations in an electrolyte. Shen and Hall [203], for example, compared the ionicity in salt-doped homopolymers and block copolymers with both the static fraction of ion pairs and the normalized cluster relaxation rate (defined as the inverse residence time of an ion cluster divided by the polymer relaxation rate) using coarse-grained MD simulations. Assuming that cation-cation and anion-anion interactions do not dominate transport in these systems of neutral polymer electrolytes, the ionicity provides indirect insight into L^{+-}. For a range of Coulomb strengths, the authors found that the normalized cluster relaxation rate correlated directly with the ionicity (Fig. 7.1a), while the fraction of free ions obtained from structural analysis was found to be anti-correlated with ionicity, as shown in Fig. 7.1b. This stands in direct contrast with the common interpretation of the ionicity as the fraction of free ions described above. The phenomenon of L^{+-} correlating with ion dynamics rather than statics has been demonstrated for polyelectrolyte solutions in this work as well. Our study of transport in short-chain polyelectrolyte solutions, using both atomistic (Chapter 5) and coarse-grained (Chapter 6) molecular dynamics, showed that changes in the contribution to L^{+-} per ion could not be rationalized by trends in the static fraction of ion pairs but rather paralleled the trends in ion pair residence times. In both Shen and Hall's solid polymers as well as the aforementioned polyelectrolyte solutions, cation-anion correlations (and correspondingly ion pair residence times) decrease as concentration increases, despite the fact that ion pairing from the static picture increases with concentration. Experimental measurements have similarly reported increasing ionicity

as concentration increases, i.e., less correlated ion motion at high concentrations [204–206]. This decrease in cation-anion correlations at high concentrations warrants further exploration, but it may be due to a shift in transport mechanisms or solvation environments and/or the fact all mass fluxes must sum to zero in the system, which place constraints on the relative values of the transport coefficients.

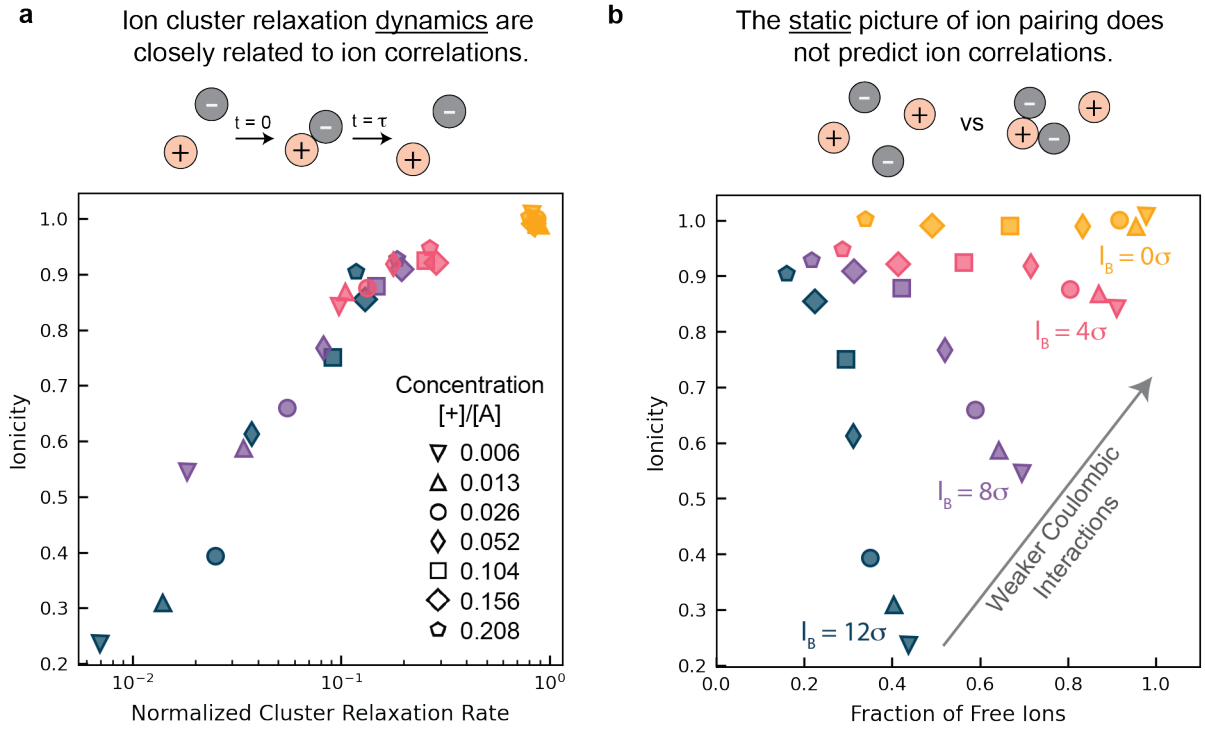

Figure 7.1: Demonstration that ion correlations in an electrolyte, as quantified by the ionicity, (a) correlate well with the relaxation time of ion clusters but (b) do not correlate well with the fraction of free ions determined from static structural analysis. Data is obtained from coarse-grained MD simulations of salt-doped homopolymers at varying concentration and Bjerrum length, l_B. Adapted with permission from Ref. [203].

Design principles for minimizing cation-anion correlations

Design of electrolytes with high ionic conductivity should aim to minimize cation-anion correlations. The simplest means of tuning the value of L^{+-} is to alter the charge density of the electrolyte ions. To this end, several recent computation works have investigated the effect of altering ionic size and/or ion dipole strength on ion transport [191, 207–211]. Cheng et al. [207], for example, suggested that optimal conductivity in polymerized ionic liquids could be obtained using large ions in the polymer chain and small counterions. Using

both coarse-grained and atomistic MD simulations, they found that this design choice led to optimal decoupling of ion motion and segmental dynamics. Molinari et al. [209] altered the charge density of $TFSI^-$ anions in MD simulations of LiTFSI in PEO by scaling the anion partial charges, finding that a more polar anion decreased Li^+ mobility and increased ion clustering, while an anion with a more uniform charge distribution had the opposite effect. This trend that increasing anion charge delocalization improves transport, specifically via a decrease in L^{+-}, is a general design rule that holds across many systems (Figure 7.2a).

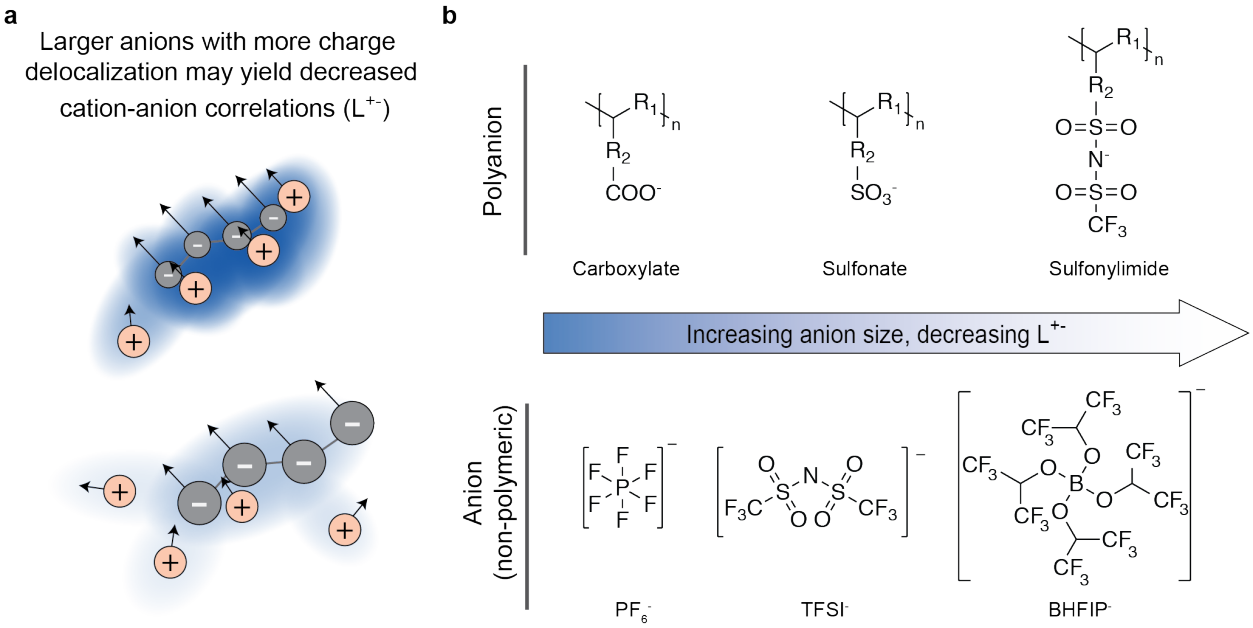

Figure 7.2: Design rules for minimizing L^{+-}. (a) Illustration of the weaker ion correlations expected in systems employing larger ions with greater charge delocalization. Correlations are colored according to the color bar in Figure 4.1. (b) Examples of common chemistries employed to increase anion charge delocalization in polyanions (top) and small-molecule anions (bottom).

Common chemistries used to enhance anion charge delocalization are presented in Figure 7.2b. In solid polymer electrolytes, anions such as PF_6^- and $TFSI^-$ are some of the most commonly studied [207]. It has been experimentally demonstrated in carbonate solvents [212] that $TFSI^-$ has a smaller thermodynamic ion association constant than PF_6^-, and that $TFSI^-$ exhibits higher t_+ in polymer-based electrolytes [213]. It is worth noting that recent studies on multivalent (non-polymeric) electrolytes for energy storage applications have also worked towards lowering cation-anion interaction via increased anion charge delocalization. One notable example is the fluorinated alkoxyborate $BHFIP^-$ anion, which allows for reduced ion pairing and thus improved transport and due to its large size [214–217]. Polyanionic single-ion conductors often employ sulfonylimide groups (analogous to the chemistry of a $TFSI^-$

anion), which provide more charge delocalization than sulfonate or carboxylate moieties. The greater charge delocalization in these anions has been shown to correlate with higher conductivity in a variety of systems [218–221]. For advances in synthesis strategies and further examples of successful single-ion conductor chemistries, we refer the reader to the recent review by Zhang et al. [93]

While the trend of decreased cation-anion correlation with greater anion charge delocalization holds for many systems, in some cases changes in the charge distribution of an ion can alter the transport mechanisms in an electrolyte, complicating the resulting changes in bulk transport. This has been observed in the MD simulations performed by Lin and Maranas [210] of PEO-based single ion conducting solid polymer electrolytes. Here, the cation-anion electrostatic interactions were tuned by changing the partial charges of the sulfonate anion appended to the polymer backbone. As expected, a more charge-delocalized anion (weaker electrostatic interactions) decreased ion aggregation. While one would intuitively expect this decreased aggregation to yield increased conductivity, it was observed that the mobility of the sodium cation in the system remained unchanged. The authors attribute this counterintuitive result to a changing diffusion mechanism: with weak electrostatic interactions, motion was dominated by free ions solvated by the EO backbone, whereas with stronger electrostatic interactions, hopping of the cation between sulfonate anions became the dominant process. In the work of Ma et al. reporting coarse-grained MD simulations of random ionomer melts [191], modifying the cation/anion size ratio resulted in substantial changes to both nanostructure and ion pair residence times. Depending on the dielectric constant and applied electric field, these changes in ion size sometimes increased and sometimes decreased cation mobility. Furthermore, we note that the impact of altering charge delocalization of the cation is often more complex than changing that of the anion, namely in solid polymer electrolytes where the cation and polymer host strongly interact. A larger cation has been shown to enhance transport in some cases [208, 222] by minimizing cation-anion correlation, whereas in other cases the presence of free cations can mediate cross-linking of polymer chains and lead to reduced mobility [223].

Cation-cation and anion-anion correlations

In dilute liquid electrolytes, cation-cation and anion-anion correlations (L^{++}_{distinct} and L^{--}_{distinct}) are not expected to contribute substantially to electrolyte transport. It is anticipated that like-ions will either interact very little or move in an anti-correlated manner due to electrostatic repulsion, yielding negative values of L^{ii}_{distinct} with small magnitude [153, 163]. In concentrated or polymer-based electrolytes, however, L^{ii}_{distinct} may contribute substantially. This contribution is most notable in (i) polyionic systems, where the covalent links between charged monomers create strong correlations between charges on a given chain, and (ii) systems with substantial ion aggregation such as low-permittivity polymer electrolytes. We address both cases in this section.

Polyions generate strong like-ion correlations

Covalent attachment of multiple ions to yield a polyion inevitably introduces strong like-ion correlations. As discussed in detail in Chapters 5 and 6, in oligomeric polyions all ions on a given chain are constrained to move together, i.e., over sufficiently long timescales the flux of any given monomer on a chain will be equal to that of the chain center of mass. For longer chains or systems with very slow dynamics, distinct monomers may not be perfectly correlated over the timescale of a simulation (or experiment), but substantial correlation will nevertheless exist between ions on nearby monomers. Our MD simulations of anionic polyelectrolytes have demonstrated that in many systems, L^{--}_{distinct} is the largest of all the transport coefficients. As these correlations are induced by the covalent bonding of the ions, this substantial contribution of L^{--}_{distinct} is expected for anionic polyelectrolytes regardless of the specific chain chemistry or solvent properties. As a result of the large magnitude of L^{--}_{distinct} in polyionic solutions, the Nernst-Einstein approximation (which assumes all L^{ii}_{distinct} and L^{+-} are zero) fails drastically for these systems. Several recent experimental works, however, have used the Nernst-Einstein assumption to characterize the transference number in nonaqueous polyionic systems for application in lithium-ion batteries [96, 97, 100, 224], using $t_+^{\text{NE}} = \frac{D_+}{D_+ + D_-}$. As the self-diffusion coefficient of the anion is much smaller than that of the counterion in these systems, the t_+^{NE} approximation typically yields very high cation transference numbers ($t_+^{\text{NE}} > 0.8$, compared to $t_+ \approx 0.4$ for conventional liquid electrolytes). We have found [86,163], however, that the true transference number incorporating ion correlations (which is the relevant quantity in predicting macroscopic concentration profiles and electrolyte performance) is drastically lower, and that t_+^{NE} does not even qualitatively reproduce the trend in the rigorously-computed t_+ due to the large values of L^{--}_{distinct} and L^{+-} in these systems. Importantly, for these polyionic solutions, incomplete characterization of ion correlations can lead to an incorrect understanding of ion transport — based on ideal solution (Nernst-Einstein) assumptions treating each charged monomer as an independent ion, these polyelectrolyte solutions seem like promising alternatives to conventional battery electrolytes, whereas in actuality their transport properties are substantially less favorable than standard electrolyte formulations.

The behavior of L^{ii}_{distinct} in two-component (solvent-free) systems such as polymerized ionic liquids is more complex, as the transport coefficients in these systems must satisfy the constraint $\sum_i M_i L^{ij} = 0$. Zhang et al. [165] performed atomistic MD simulations of polycationic polymerized ionic liquids and observed anti-correlated cation-cation motion, despite the fact that cations on a given chain were covalently constrained to move together. Our coarse-grained simulations of polymerized ionic liquids (Chapter 6), however, reported the opposite trend (positively correlated anion-anion motion for a negatively-charged polymer). We recommend further studies to reconcile the origin of these differences.

Strongly aggregating systems: the questions of near-unity ionicity and negative transference numbers

Distinct anion-anion or cation-cation correlations (L^{ii}_{distinct}) are also expected to be substantial in systems with low dielectric constant that have a high degree of ion aggregation, where ions of the same type in a given aggregate will move together in a correlated manner for the lifetime of the aggregate. Ion aggregation will simultaneously increase both cation-anion correlations (L^{+-}) and like-ion correlations (L^{ii}_{distinct}). While the former decreases the ionic conductivity, the latter will increase it. Thus the effect of ion aggregation on bulk conductivity may not be apparent a priori. Generally, aggregation is associated with slower dynamics and the formation of neutral clusters which do not contribute to conductivity [104]: in a long-lived, charge-neutral aggregate, the contributions of L^{+-} and L^{ii}_{distinct} to the overall conductivity should cancel out. In the case of charged aggregates or systems with frequent exchange/rearrangement of aggregate populations, however, strong aggregation may actually enhance conductivity. In some cases, extensive aggregation leads to the formation of percolating networks which yield facile ion transport, as observed in ionomers [120, 192, 193, 225, 226] and polymerized ionic liquids [207].

Due to the complex interplay of cation-anion, cation-cation, and anion-anion correlations, we could envision a system with very strong ion correlations that possesses ionicity close to unity due to the cancellation of contributions from L^{+-} and L^{ii}_{distinct} [154]. Care should thus be taken when interpreting the ionicity as the degree of ideal or uncorrelated transport in an electrolyte. Large L^{ii}_{distinct} may rationalize experimental [148, 227–229] and computational [230, 231] observations of relatively high ionicity in solid polymer electrolytes. As we are not aware of any works which have explicitly computed L^{ii}_{distinct} in these systems, quantification of the extent to which these correlations dictate ionicity and other bulk transport properties remains an interesting avenue for further study.

We also note that like-ion correlations (L^{ii}_{distinct}) and ion aggregation may be used to rationalize the phenomena of negative cation transference numbers, which have been measured experimentally [84] and from MD simulations [129] in PEO-based electrolytes. Qualitatively, negative transference numbers may be rationalized through the presence of negatively charged aggregates. Recall that the transference number is the fraction of conductivity attributed to a given species, which we may write using a ratio of electrophoretic mobilities: $t_i = Fz_ic_iu_i/(\sum_j Fz_jc_ju_j)$, where the electrophoretic mobility is defined as $u_i = (\boldsymbol{v}_i - \boldsymbol{v})/\boldsymbol{E}$. In general, we expect an anion to move toward more positive potential, corresponding to a negative mobility, and a cation to move toward more negative potential (positive mobility), such that the quantity z_iu_i and thus the transference number are generally positive. Consider, however, a cation which is part of a net-negative aggregate such as a triple ion with two anions and one cation. The aggregate as a whole will move towards more positive potential, so the cation in the aggregate will migrate in the "wrong" direction and have negative mobility [85]. As the total cation mobility is an average over all cations in the system, the overall average cation mobility can be negative (yielding a negative cation transference number) if enough cations are part of negatively charged aggregates and if the mobility of

those aggregates is sufficiently large. Mathematically, $t_+ < 0$ corresponds to a system where $L^{+-} > L^{++}$ (Eq. 4.59). This is also consistent with the presence of negatively charged aggregates, where L^{++}_{distinct} is small relative to L^{+-} and L^{--}_{distinct}. Although there remains some uncertainty based on measurement technique as to whether PEO-based electrolytes actually have negative t_+ [204], molecular simulations in PEO-based electrolytes have in certain circumstances observed negatively charged aggregates [209, 232]. Negative cation transference numbers have been observed through simulation [163] and experiment [173–177] in anionic polyelectrolyte solutions as well, where negatively charged aggregates are common (for example, a single cation bound to a polyanion chain).

Ion-solvent correlations

Bulk transport properties such as the conductivity and transference number are computed using only L^{++}, L^{--}, and L^{+-}. Transport coefficients for the solvent or polymer host (L^{+0}, L^{-0}, and L^{00}) are not only unnecessary to compute these quantities, but for a binary, single-solvent electrolyte they also can be computed directly from knowledge of L^{++}, L^{--}, and L^{+-}, i.e., they are not independent quantities. Using the aforementioned constraint $\sum_i M_i L^{ij} = 0$, the solvent transport coefficients of a binary electrolyte can be written as

$$\begin{aligned} L^{+0} &= -\frac{1}{M_0}(M_+ L^{++} + M_- L^{+-}) \ , \\ L^{-0} &= -\frac{1}{M_0}(M_+ L^{+-} + M_- L^{--}) \ , \\ L^{00} &= -\frac{1}{M_0}(M_+ L^{+0} + M_- L^{-0}) \ . \end{aligned} \tag{7.1}$$

Note that because L^{++}, L^{--}, and L^{+-} are generally positive, Eq. (7.1) implies that L^{+0} and L^{-0} will be negative (anti-correlated motion), while L^{00} will be positive. Although the solvent transport coefficients are not directly useful in obtaining experimentally-relevant transport properties, tuning ion-solvent interactions can have a substantial impact on L^{++}, L^{--}, and L^{+-}. Increasing cation-solvent correlation (making L^{+0} less negative), for example, would correspond to decreasing L^{++} (slower cation self-diffusion) and/or L^{+-} (weaker cation-anion correlations). In this section, we explore how changing various aspects of ion-solvent interactions affect the ion correlations discussed in the previous sections as well as how these modifications affect bulk transport properties.

One of the key solvent properties dictating correlations in an electrolyte is the dielectric constant ε. As would be expected from Coulomb's law, increasing the dielectric constant generally decreases cation-anion correlations L^{+-}. In solid polymer electrolytes, it has been observed using both atomistic [233] and coarse-grained [203, 211, 230, 231] MD that greater dielectric constant or polymer polarity increases ionicity and decreases ion aggregation. Similarly, in simulations of random ionomer melts, Ma et al. [191] observed shorter cation-anion residence times and higher ion mobility with higher dielectric constant. While the decreases in L^{+-} induced by higher dielectric constant will favor higher overall ionic conductivity,

several works have demonstrated non-monotonic trends in ion transport with respect to dielectric constant. This trend is clearly illustrated in the coarse-grained MD simulations of solid polymer electrolytes performed by Wheatle et al. [230], as shown in Figure 7.3. At low polymer polarity, ionicity data suggests that conductivity may be limited by high L^{+-} as a result of ion aggregation. At high polarity, however, the ionicity remains high but transport is limited by polymer segmental dynamics. The latter is expected to decrease self-diffusion of ions, especially that of the cation (L^{++}_{self}) due to the strong coupling of cation diffusion and polymer dynamics in most solid polymer electrolytes [148, 209]. Note that the overall dielectric constant of the solution in these simulations may also be affected by the polarity of ionic clusters (in addition to the polarity of the polymer itself), which has been found to significantly affect the dielectric constant of PEO-based electrolytes in experimental studies [229, 234, 235]. The trade-off between polymer segmental motion and dielectric constant has also been observed experimentally, for example by Choi et al. in polysiloxane-based single-ion conductors, where maximal conductivity was observed using plasticizers with intermediate glass transition temperature and dielectric constant [236]. Others have similarly observed that ion transport is optimized at intermediate dielectric constant but attribute the trend to changes in the ion transport mechanism with respect to ε. Gudla et al. [237] have found that polymer dielectric constant (tuned by scaling partial charges in atomistic MD) has a substantial impact on transport in LiTFSI-PEO. They suggest that as dielectric constant increases, Li^+ motion transitions from vehicular diffusion to primarily interchain hopping then ultimately to intrachain hopping, with the interchain hopping at intermediate ε yielding the fastest lithium diffusion. In ionomer melts, Bollinger et al. [193] have suggested that optimal conductivity can be reached when Coulombic interactions are strong enough to allow for a percolated aggregate structure but weak enough to favor ion dissociation and short residence times.

In addition to tuning bulk solution properties such as the dielectric constant, transport in polymer-based electrolytes may also be tuned via solvent/polymer chemistry, which alters short-range interactions between species. Computational methods are particularly well-suited to evaluating these effects, as they allow for precise control of chemical structure in materials that may be difficult to synthesize experimentally. In solid polymer electrolytes where strong cation-polymer interactions typically dictate transport [148, 209, 238], several works have explored the strategy of increasing polymer-anion interactions (L^{-0}) to improve transport properties. Savoie et al. [109], for example, simulated Lewis-acidic polymers (polyboranes) which preferentially coordinated with the anionic species, observing substantial decreases in anion diffusion (L^{--}_{self}) and increases in cation diffusion (L^{++}_{self}). Similarly, France-Lanord et al. [232] used classical MD to investigate a PEO variant with sulfonyl secondary sites, finding that the strong interaction between the sulfonyl group and the anion ($TFSI^-$) preferentially decreased anion transport and led to increased lithium ion transference number. These authors also studied the effect of carbonate secondary sites on the polymer chain, which increased polymer-cation interactions. In this carbonate-containing system, the increase in L^{+0} presumably decreased L^{+-}, as a substantial reduction in ion pairing was observed. Note that it may be impractical to attempt to tune polymer-ion inter-

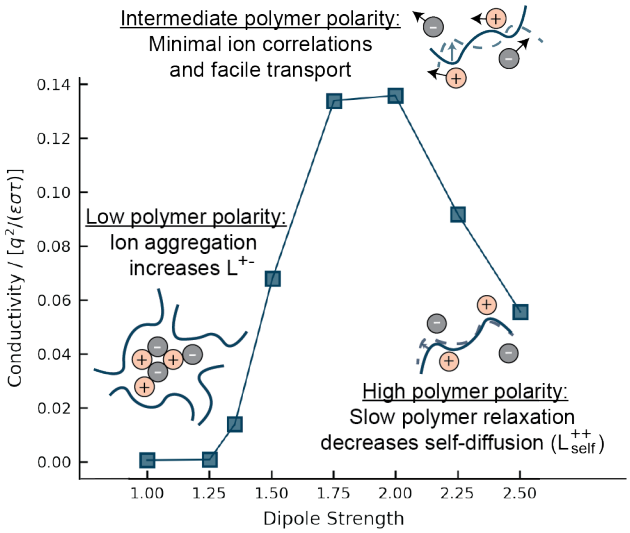

Figure 7.3: Ionic conductivity as a function of host polymer dipole strength obtained from coarse-grained molecular dynamics simulations of salt-doped solid polymer electrolytes. Adapted with permission from Ref. [230].

actions without inadvertently affecting ion transport mechanisms. In PEO, it is understood that lithium ions move through a well-connected network of solvation sites which promote facile intrachain hopping [111]. Alternate polymer structures may not be conducive to this mechanism. Classical MD simulations of polyester-based polymer electrolytes, for example, found mainly isolated clusters of polymer solvation sites, in which the main transport mechanisms were infrequent interchain hopping and co-diffusion with the polymer chain. These slower processes yielded ionic conductivities an order of magnitude lower than in PEO [111].

In this section, we have discussed how cation-anion, like-ion, and ion-solvent correlations impact transport in electrolyte solutions. We demonstrate the limitations of some of the conventional paradigms for analyzing ion correlations, for example using the static fraction of ion pairing as a proxy for cation-anion correlations and applying the Nernst-Einstein approximation to polyionic systems. Several design rules are suggested from our analysis, namely the use of ions with highly delocalized charge to decrease cation-anion correlations, as well as use of a solvent or polymer host with an intermediate value of dielectric constant to balance tradeoffs between ion aggregation and self-diffusion.

7.3 Recommendations for future work

We recommend that calculation of L^{ij} should become standard practice in characterization of electrolyte transport. There are several systems for which we anticipate insight

into transport coefficients and ion correlations from molecular dynamics simulations will be particularly valuable at addressing long-standing questions in the field. Of note are PEO-based electrolytes for lithium-ion batteries, where experimental studies have demonstrated a variety of complex transport phenomena such as negative cation transference number and diverging Stefan-Maxwell diffusion coefficients [29, 84]. Knowledge of L^{ij} could elucidate the molecular origins of these phenomena, which are still under debate. Additional attention should also be devoted to the study of L^{ij} in two-component systems such as polymerized ionic liquids, where the transport coefficients are all inter-dependent as a consequence of the barycentric reference frame. The counterintuitive relationships between L^{+-}, L^{ii}_{self}, and L^{ii}_{distinct} in these systems are still poorly understood, particularly with regards to the effect of changing chain length, dielectric constant, and ion chemistry. Furthermore, the Onsager transport framework is well-suited to treat multicomponent systems with more than one type of cation and/or anion, such as the complex solutions handled in the fields of biology, geochemistry, and water purification [239, 240]. We also note the widespread use of supporting electrolytes [241] in energy storage applications.

Finally, we emphasize that the adoption of the Onsager transport framework is not exclusive to molecular simulations. Just as we can compute experimentally-measurable transport quantities from knowledge of L^{ij} using the equations in Chapter 4.3, we may also compute L^{ij} from experimentally-measured quantities such as conductivity, transference number, and salt diffusion coefficient. The Onsager transport coefficients can serve as a powerful means of connecting observations from experiment and simulation. We believe this approach has the potential to enable both enhanced fundamental understanding and more rational design of new electrolyte formulations energy storage applications and beyond.

Bibliography

[1] Fong, K. D., Bergstrom, H. K., McCloskey, B. D. & Mandadapu, K. K. Transport phenomena in electrolyte solutions: Non-equilibrium thermodynamics and statistical mechanics. *AIChE Journal* e17091 (2020).

[2] Newman, J. & Thomas-Alyea, K. E. *Electrochemical Systems* (John Wiley & Sons, Inc., 2004), 3 edn.

[3] Diederichsen, K. M., McShane, E. J. & McCloskey, B. D. Promising routes to a high Li^+ transference number electrolyte for lithium ion batteries. *ACS Energy Letters* **2**, 2563–2575 (2017).

[4] Doyle, M., Fuller, T. F. & Newman, J. The importance of the lithium ion transference number in lithium/polymer cells. *Electrochimica Acta* **39**, 2073–2081 (1994).

[5] Li, M., Wang, C., Chen, Z., Xu, K. & Lu, J. New concepts in electrolytes. *Chemical Reviews* **120**, 6783–6819 (2020).

[6] Xu, K. Nonaqueous liquid electrolytes for lithium-based rechargeable batteries. *Chemical Reviews* **104**, 4303–4418 (2004).

[7] Zhang, S. S. A review on electrolyte additives for lithium-ion batteries. *Journal of Power Sources* **162**, 1379–1394 (2006).

[8] Haregewoin, A. M., Wotango, A. S. & Hwang, B.-J. Electrolyte additives for lithium ion battery electrodes: Progress and perspectives. *Energy & Environmental Science* **9**, 1955–1988 (2016).

[9] Valøen, L. O. & Reimers, J. N. Transport properties of $LiPF_6$-based li-ion battery electrolytes. *Journal of The Electrochemical Society* **152**, A882 (2005).

[10] Xu, K. Electrolytes and interphases in li-ion batteries and beyond. *Chemical Reviews* **114**, 11503–11618 (2014).

[11] Yao, P. *et al.* Review on polymer-based composite electrolytes for lithium batteries. *Frontiers in Chemistry* **7**, 522 (2019).

[12] Hallinan Jr, D. T. & Balsara, N. P. Polymer electrolytes. *Annual Review of Materials research* **43**, 503–525 (2013).

[13] Bachman, J. C. *et al.* Inorganic solid-state electrolytes for lithium batteries: mechanisms and properties governing ion conduction. *Chemical Reviews* **116**, 140–162 (2016).

[14] Minami, T., Hayashi, A. & Tatsumisago, M. Recent progress of glass and glass-ceramics as solid electrolytes for lithium secondary batteries. *Solid State Ionics* **177**, 2715–2720 (2006).

[15] Suo, L., Hu, Y.-S., Li, H., Armand, M. & Chen, L. A new class of solvent-in-salt electrolyte for high-energy rechargeable metallic lithium batteries. *Nature Communications* **4**, 1–9 (2013).

[16] Zeng, Z. *et al.* Non-flammable electrolytes with high salt-to-solvent ratios for li-ion and li-metal batteries. *Nature Energy* **3**, 674–681 (2018).

[17] Debye, P. & Hückel, E. Lowering of freezing point and related phenomena. *Physikalische Zeitschrift* **24**, 185–206 (1923).

[18] Onsager, L. The theory of electrolytes. *Physikalische Zeitschrift* **27**, 388–392 (1926).

[19] Onsager, L. On the theory of electrolytes. II. *Physikalische Zeitschrift* **28**, 277–298 (1927).

[20] Bird, R., Stewart, W. & Lightfoot, E. *Transport Phenomena* (John Wiley & Sons, Inc., 1960).

[21] Krishna, R. & Wesselingh, J. The Maxwell-Stefan approach to mass transfer. *Chemical Engineering Science* **52**, 861–911 (1997).

[22] Hirschfelder, J. O., Curtiss, C. F., Bird, R. B. & Mayer, M. G. *Molecular Theory of Gases and Liquids*, vol. 165 (John Wiley & Sons, Inc., 1964).

[23] Onsager, L. Reciprocal relations in irreversible processes. I. *Physical review* **37**, 405–426 (1931).

[24] Onsager, L. Reciprocal relations in irreversible processes. II. *Physical review* **38**, 2265–2279 (1931).

[25] Prigogine, I. *Introduction to Thermodynamics of Irreversible Processes* (Interscience Publishers, Inc., New York, 1967), 3 edn.

[26] de Groot, S. R. & Mazur, P. *Non-Equilibrium Thermodynamics* (Interscience Publishers, Inc., New York, 1969).

[27] Green, M. S. Markoff random processes and the statistical mechanics of time-dependent phenomena. II. Irreversible processes in fluids. *The Journal of Chemical Physics* **22**, 398–413 (1954).

[28] Kubo, R. Statistical-mechanical theory of irreversible processes. I. General theory and simple applications to magnetic and conduction problems. *Journal of the Physical Society of Japan* **12**, 570–586 (1957).

[29] Villaluenga, I. *et al.* Negative Stefan-Maxwell diffusion coefficients and complete electrochemical transport characterization of homopolymer and block copolymer electrolytes. *Journal of The Electrochemical Society* **165**, A2766–A2773 (2018).

[30] Kedem, O. & Katchalsky, A. A physical interpretation of the phenomenological coefficients of membrane permeability. *The Journal of General Physiology* **45**, 143–179 (1961).

[31] Kedem, O. & Katchalsky, A. Thermodynamic analysis of the permeability of biological membranes to non-electrolytes. *Biochimica et biophysica Acta* **27**, 229–246 (1958).

[32] Katchalsky, A. & Curran, P. F. *Nonequilibrium Thermodynamics in Biophysics* (Harvard University Press, 1967).

[33] Kjelstrup, S. & Bedeaux, D. *Non-equilibrium thermodynamics of heterogeneous systems*, vol. 20 (World Scientific, 2020).

[34] Newman, J. Transport processes in electrolytic solutions. *Advances in Electrochemistry and Electrochemical Engineering* **5**, 87–136 (1967).

[35] Bernardi, D., Pawlikowski, E. & Newman, J. A general energy balance for battery systems. *Journal of the Electrochemical Society* **132**, 5 (1985).

[36] Kovetz, A. *Electromagnetic Theory*, vol. 975 (Oxford University Press Oxford, 2000).

[37] Jackson, J. D. *Classical Electrodynamics* (John Wiley & Sons, Inc., 2007).

[38] Cohen-Tannoudji, C., Dupont-Roc, J. & Grynberg, G. *Photons and Atoms: Introduction to Quantum Electrodynamics* (John Wiley & Sons, Inc., 1997).

[39] Bjorken, J. D. & Drell, S. D. *Relativistic Quantum Mechanics* (McGraw-Hill, 1964).

[40] Schwinger, J. *Classical Electrodynamics* (CRC Press, 2019).

[41] Griffiths, D. J. *Introduction to Electrodynamics* (Prentice Hall, 1999).

[42] Steigmann, D. J. On the formulation of balance laws for electromagnetic continua. *Mathematics and Mechanics of Solids* **14**, 390–402 (2009).

[43] Luo, Z.-X., Xing, Y.-Z., Ling, Y.-C., Kleinhammes, A. & Wu, Y. Electroneutrality breakdown and specific ion effects in nanoconfined aqueous electrolytes observed by NMR. *Nature Communications* **6**, 6358 (2015).

[44] Levy, A., de Souza, J. P. & Bazant, M. Z. Breakdown of electroneutrality in nanopores. *Journal of Colloid and Interface Science* (2020).

[45] Feynman, R. P. Feynman lectures on physics. Volume 2: Mainly electromagnetism and matter. *Reading, Ma.: Addison-Wesley, 1964, edited by Feynman, Richard P.; Leighton, Robert B.; Sands, Matthew* (1964).

[46] Sahu, A., Sauer, R. A. & Mandadapu, K. K. Irreversible thermodynamics of curved lipid membranes. *Physical Review E* **96**, 042409 (2017).

[47] Mandadapu, K. K. *Homogeneous Non-Equilibrium Molecular Dynamics Methods for Calculating the Heat Transport Coefficient of Solids and Mixtures*. Ph.D. thesis, UC Berkeley (2011).

[48] Landau, L. D. *et al. Electrodynamics of Continuous Media*, vol. 8 (Elsevier, 2013).

[49] Castellanos, A. *Electrohydrodynamics*, vol. 380 (Springer Science & Business Media, 1998).

[50] Curie, P. *Oeuvres Publiées par les Soins de la Société Française de Physique* (Gauthier-Villars, Paris, 1908).

[51] Epstein, J. M. & Mandadapu, K. K. Time-reversal symmetry breaking in two-dimensional nonequilibrium viscous fluids. *Physical Review E* **101**, 052614 (2020).

[52] Morriss P., G. & Evans J., D. *Statistical Mechanics of Nonequilbrium Liquids* (ANU Press, 2007).

[53] Wheeler, D. R. & Newman, J. Molecular dynamics simulations of multicomponent diffusion. 1. Equilibrium method. *Journal of Physical Chemistry B* **108**, 18353–18361 (2004).

[54] Fong, K. D., Self, J., McCloskey, B. D. & Persson, K. A. Ion correlations and their impact on transport in polymer-based electrolytes. *Macromolecules* **54**, 2575–2591 (2021).

[55] Barthel, J. M., Krienke, H. & Kunz, W. *Physical Chemistry of Electrolyte Solutions: Modern Aspects*, vol. 5 (Springer Science & Business Media, 1998).

[56] Bird, R. B. & Klingenberg, D. J. Multicomponent diffusion — a brief review. *Advances in Water Resources* **62**, 238–242 (2013).

[57] Jamali, S. H. *et al.* Finite-size effects of binary mutual diffusion coefficients from molecular dynamics. *Journal of Chemical Theory and Computation* **14**, 2667–2677 (2018).

[58] Liu, X., Vlugt, T. J. & Bardow, A. Predictive Darken equation for Maxwell-Stefan diffusivities in multicomponent mixtures. *Industrial & Engineering Chemistry Research* **50**, 10350–10358 (2011).

[59] Krishna, R. & Van Baten, J. The Darken relation for multicomponent diffusion in liquid mixtures of linear alkanes: An investigation using molecular dynamics (MD) simulations. *Industrial & Engineering Chemistry Research* **44**, 6939–6947 (2005).

[60] van de Ven-Lucassen, I. M., Vlugt, T. J., van der Zanden, A. J. & Kerkhof, P. J. Using molecular dynamics to obtain Maxwell-Stefan diffusion coefficients in liquid systems. *Molecular Physics* **94**, 495–503 (1998).

[61] van de Ven-Lucassen, I. M., Otten, A. M., Vlugt, T. J. & Kerkhof, P. J. Molecular dynamics simulation of the Maxwell-Stefan diffusion coefficients in lennard-jones liquid mixtures. *Molecular Simulation* **23**, 43–54 (1999).

[62] Doyle, M., Fuller, T. F. & Newman, J. Modeling of galvanostatic charge and discharge of the lithium/polymer/insertion cell. *Journal of the Electrochemical society* **140**, 1526 (1993).

[63] Crothers, A. R., Darling, R. M., Kusoglu, A., Radke, C. J. & Weber, A. Z. Theory of multicomponent phenomena in cation-exchange membranes: Part II. Transport model and validation. *Journal of The Electrochemical Society* **167**, 013548 (2020).

[64] Schammer, M., Horstmann, B. & Latz, A. Theory of transport in highly concentrated electrolytes. *Journal of The Electrochemical Society* **168**, 026511 (2021).

[65] Smith, R. B. & Bazant, M. Z. Multiphase porous electrode theory. *Journal of The Electrochemical Society* **164**, E3291 (2017).

[66] Tyrrell, H. & Harris, K. *Diffusion in Liquids* (Butterworths Monographs in Chemistry, 1984).

[67] Hansen, J.-P. & McDonald, I. R. *Theory of Simple Liquids* (Elsevier, 1990).

[68] Frenkel, D. & Smit, B. *Understanding Molecular Simulation: From Algorithms to Applications*, vol. 50 (Academic Press, 2001), 2 edn.

[69] Barsoukov, E. & Macdonald, J. R. *Impedance Spectroscopy: Theory, Experiment, and Application* (John Wiley & Sons, Inc., 2005).

[70] Holz, M. Electrophoretic NMR. *Chemical Society Reviews* **23**, 165–174 (1994).

[71] Whatley, H. Basic principles and modes of capillary electrophoresis. In *Clinical and Forensic Applications of Capillary Electrophoresis*, 21–58 (Springer, 2001).

[72] Dünweg, B., Lobaskin, V., Seethalakshmy-Hariharan, K. & Holm, C. Colloidal electrophoresis: Scaling analysis, Green-Kubo relation, and numerical results. *Journal of Physics: Condensed Matter* **20**, 404214 (2008).

[73] Evans, J., Vincent, C. & Bruce, P. Electrochemical measurement of transference numbers in polymer electrolytes. *Polymer* **28**, 2324–2328 (1987).

[74] Balsara, N. P. & Newman, J. Relationship between steady-state current in symmetric cells and transference number of electrolytes comprising univalent and multivalent ions. *Journal of the Electrochemical Society* **162**, A2720 (2015).

[75] Bruce, P., Hardgrave, M. & Vincent, C. The determination of transference numbers in solid polymer electrolytes using the hittorf method. *Solid State Ionics* **53-56**, 1087–1094 (1992).

[76] Harned, H. & French, D. A conductance method for the determination of the diffusion coefficients of electrolytes. *Annals of the New York Academy of Sciences* **46**, 267–284 (1945).

[77] Newman, J. & Chapman, T. Restricted diffusion in binary solutions. *AIChE Journal* **19**, 343–348 (1973).

[78] Ehrl, A., Landesfeind, J., Wall, W. & Gasteiger, H. Determination of transport parameters in liquid binary lithium ion battery electrolytes. *Journal of The Electrochemical Society* **164**, A826–A836 (2017).

[79] Zwanzig, R. & Ailawadi, N. K. Statistical error due to finite time averaging in computer experiments. *Physical Review* **182**, 280–283 (1969).

[80] Jones, R. E. & Mandadapu, K. K. Adaptive Green-Kubo estimates of transport coefficients from molecular dynamics based on robust error analysis. *The Journal of Chemical Physics* **136**, 154102 (2012).

[81] Gering, K. L. Prediction of electrolyte conductivity: Results from a generalized molecular model based on ion solvation and a chemical physics framework. *Electrochimica Acta* **225**, 175–189 (2017).

[82] Onsager, L. & Fuoss, R. Irreversible processes in electrolytes. Diffusion, conductance and viscous flow in arbitrary mixtures of strong electrolytes. *The Journal of Physical Chemistry* **36**, 2689–2778 (1932).

[83] Wright, M. R. *An Introduction to Aqueous Electrolyte Solutions* (John Wiley, 2007).

[84] Pesko, D. M. *et al.* Negative transference numbers in poly (ethylene oxide)-based electrolytes. *Journal of The Electrochemical Society* **164**, E3569–E3575 (2017).

[85] Gouverneur, M., Schmidt, F. & Schönhoff, M. Negative effective Li transference numbers in Li salt/ionic liquid mixtures: Does Li drift in the "wrong" direction? *Physical Chemistry Chemical Physics* **20**, 7470–7478 (2018).

[86] Fong, K. D. *et al.* Ion transport and the true transference number in nonaqueous polyelectrolyte solutions for lithium ion batteries. *ACS Central Science* **5**, 1250–1260 (2019).

[87] Lu, Y. *et al.* Stable cycling of lithium metal batteries using high transference number electrolytes. *Advanced Energy Materials* **5**, 1402073 (2015).

[88] Murugan, R., Thangadurai, V. & Weppner, W. Fast lithium ion conduction in garnet-type $Li_7La_3Zr_2O_{12}$. *Angewandte Chemie - International Edition* **46**, 7778–7781 (2007).

[89] Aono, H. Ionic conductivity of the lithium titanium phosphate ($Li_{1+X}M_XTi_{2-X}(PO_4)_3$, M = Al, Sc, Y, and La) systems. *Journal of The Electrochemical Society* **136**, 590 (1989).

[90] Kamaya, N. *et al.* A lithium superionic conductor. *Nature Materials* **10**, 682–686 (2011).

[91] Kato, Y. *et al.* High-power all-solid-state batteries using sulfide superionic conductors. *Nature Energy* **1**, 16030 (2016).

[92] Matsumi, N., Sugai, K. & Ohno, H. Ion conductive characteristics of alkylborane type and boric ester type polymer electrolytes derived from mesithylborane. *Macromolecules* **36**, 2321–2326 (2003).

[93] Zhang, H. *et al.* Single lithium-ion conducting solid polymer electrolytes: Advances and perspectives. *Chemical Society Reviews* **46**, 797–815 (2017).

[94] Kobayashi, N., Uchiyama, M. & Tsuchida, E. Poly[lithium methacrylate-co-oligo(oxyethylene)methacrylate] as a solid electrolyte with high ionic conductivity. *Solid State Ionics* **17**, 307–311 (1985).

[95] Klein, R. J., Welna, D. T., Weikel, A. L., Allcock, H. R. & Runt, J. Counterion effects on ion mobility and mobile ion concentration of doped polyphosphazene and polyphosphazene ionomers. *Macromolecules* **40**, 3990–3995 (2007).

[96] Buss, H. G., Chan, S. Y., Lynd, N. A. & McCloskey, B. D. Nonaqueous polyelectrolyte solutions as liquid electrolytes with high lithium ion transference number and conductivity. *ACS Energy Letters* **2**, 481–487 (2017).

[97] Diederichsen, K. M., Fong, K. D., Terrell, R. C., Persson, K. A. & McCloskey, B. D. Investigation of solvent type and salt addition in high transference number nonaqueous polyelectrolyte solutions for lithium ion batteries. *Macromolecules* **51**, 8761–8771 (2018).

[98] Smiatek, J., Wohlfarth, A. & Holm, C. The solvation and ion condensation properties for sulfonated polyelectrolytes in different solvents - A computational study. *New Journal of Physics* **16**, 025001 (2014).

[99] Kreuer, K.-D., Wohlfarth, A., de Araujo, C. C., Fuchs, A. & Maier, J. Single alkaline-ion (li^+, na^+) conductors by ion exchange of proton-conducting ionomers and polyelectrolytes. *ChemPhysChem* **12**, 2558–2560 (2011).

[100] Dewing, B. L., Bible, N. G., Ellison, C. J. & Mahanthappa, M. K. Electrochemically stable, high transference number lithium bis (malonato) borate polymer solution electrolytes. *Chemistry of Materials* **32**, 3794–3804 (2020).

[101] Bruce, P. G. & Vincent, C. A. Steady state current flow in solid binary electrolyte cells. *Journal of Electroanalytical Chemistry and Interfacial Electrochemistry* **225**, 1–17 (1987).

[102] Fritz, H. P. & Kuhn, A. Comparative determination of effective transport numbers in solid lithium electrolytes. *Journal of Power Sources* **41**, 253–261 (1993).

[103] Walls, H. J. Anion and cation transference numbers determined by electrophoretic NMR of polymer electrolytes sum to unity. *Electrochemical and Solid-State Letters* **3**, 321 (1999).

[104] Marcus, Y. & Hefter, G. Ion pairing. *Chemical Reviews* **106**, 4585–4621 (2006).

[105] Muthukumar, M. 50th anniversary perspective: A perspective on polyelectrolyte solutions. *Macromolecules* **50**, 9528–9560 (2017).

[106] Dobrynin, A. V. Solutions of charged polymers. In *Polymer Science: A Comprehensive Reference, 10 Volume Set*, vol. 1, 81–132 (Elsevier, 2012).

[107] Borodin, O. & Smith, G. D. Quantum chemistry and molecular dynamics simulation study of dimethyl carbonate: Ethylene carbonate electrolytes doped with $LiPF_6$. *Journal of Physical Chemistry B* **113**, 1763–1776 (2009).

[108] Borodin, O. & Smith, G. D. LiTFSI structure and transport in ethylene carbonate from molecular dynamics simulations. *Journal of Physical Chemistry B* **110**, 4971–4977 (2006).

[109] Savoie, B. M., Webb, M. A. & Miller, T. F. Enhancing cation diffusion and suppressing anion diffusion via Lewis-acidic polymer electrolytes. *Journal of Physical Chemistry Letters* **8**, 641–646 (2017).

[110] Müller-Plathe, F. & Van Gunsteren, W. F. Computer simulation of a polymer electrolyte: Lithium iodide in amorphous poly(ethylene oxide). *The Journal of Chemical Physics* **103**, 4745–4756 (1995).

[111] Webb, M. A. *et al.* Systematic computational and experimental investigation of lithium-ion transport mechanisms in polyester-based polymer electrolytes. *ACS Central Science* **1**, 198–205 (2015).

[112] Diddens, D. & Heuer, A. Simulation study of the lithium ion transport mechanism in ternary polymer electrolytes: The critical role of the segmental mobility. *Journal of Physical Chemistry B* **118**, 1113–1125 (2014).

[113] Webb, M. A., Yamamoto, U., Savoie, B. M., Wang, Z. G. & Miller, T. F. Globally suppressed dynamics in ion-doped polymers. *ACS Macro Letters* **7**, 734–738 (2018).

[114] Ennari, J., Elomaa, M. & Sundholm, F. Modelling a polyelectrolyte system in water to estimate the ion-conductivity. *Polymer* **40**, 5035–5041 (1999).

[115] Carrillo, J. M. Y. & Dobrynin, A. V. Detailed molecular dynamics simulations of a model NaPSS in water. *Journal of Physical Chemistry B* **114**, 9391–9399 (2010).

[116] Wohlfarth, A. *et al.* Proton dissociation of sulfonated polysulfones: Influence of molecular structure and conformation. *Macromolecules* **48**, 1134–1143 (2015).

[117] Lyubartsev, A. P. & Laaksonen, A. Molecular dynamics simulations of DNA in solution with different counter-ions. *Journal of Biomolecular Structure and Dynamics* **16**, 579–592 (1998).

[118] Yang, L., Weerasinghe, S., Smith, P. & Pettitt, B. Dielectric response of triplex DNA in ionic solution from simulations. *Biophysical Journal* **69**, 1519–1527 (1995).

[119] Frischknecht, A. L. & Winey, K. I. The evolution of acidic and ionic aggregates in ionomers during microsecond simulations. *Journal of Chemical Physics* **150**, 064901 (2019).

[120] Ting, C. L., Stevens, M. J. & Frischknecht, A. L. Structure and dynamics of coarse-grained ionomer melts in an external electric field. *Macromolecules* **48**, 809–818 (2015).

[121] Hall, L. M. *et al.* Ionic aggregate structure in ionomer melts: Effect of molecular architecture on aggregates and the ionomer peak. *Journal of the American Chemical Society* **134**, 574–587 (2012).

[122] Ma, B., Nguyen, T. D., Pryamitsyn, V. A. & Olvera de la Cruz, M. Ionic correlations in random ionomers. *ACS nano* **12**, 2311–2318 (2018).

[123] Micka, U., Holm, C. & Kremer, K. Strongly charged, flexible polyelectrolytes in poor solvents: Molecular dynamics simulations. *Langmuir* **15**, 4033–4044 (1999).

[124] Liao, Q., Dobrynin, A. V. & Rubinstein, M. Molecular dynamics simulations of polyelectrolyte solutions: Nonuniform stretching of chains and scaling behavior. *Macromolecules* **36**, 3386–3398 (2003).

[125] Stevens, M. J. & Kremer, K. The nature of flexible linear polyelectrolytes in salt free solution: A molecular dynamics study. *The Journal of Chemical Physics* **103**, 1669–1690 (1995).

[126] Chremos, A. & Douglas, J. The influence of polymer and ion solvation on the conformational properties of flexible polyelectrolytes. *Gels* **4**, 20 (2018).

[127] Burlatsky, S. *et al.* Molecular dynamics modeling of the conductivity of lithiated nafion containing nonaqueous solvents. *Journal of The Electrochemical Society* **163**, A2232 (2016).

[128] Johansson, P. Electronic structure calculations on lithium battery electrolyte salts. *Physical Chemistry Chemical Physics* **9**, 1493–1498 (2007).

[129] France-Lanord, A. & Grossman, J. C. Correlations from ion pairing and the Nernst-Einstein equation. *Physical Review Letters* **122**, 136001 (2019).

[130] Manning, G. S. Limiting laws and counterion condensation in polyelectrolyte solutions I. Colligative properties. *The Journal of Chemical Physics* **51**, 924–933 (1969).

[131] Manning, G. S. Counterion binding in polyelectrolyte theory. *Accounts of Chemical Research* **12**, 443–449 (1979).

[132] Nyquist, R. M., Ha, B. Y. & Liu, A. J. Counterion condensation in solutions of rigid polyelectrolytes. *Macromolecules* **32**, 3481–3487 (1999).

[133] González-Mozuelos, P. & De La Cruz, M. O. Ion condensation in salt-free dilute polyelectrolyte solutions. *The Journal of Chemical Physics* **103**, 3145–3157 (1995).

[134] Tenney, C. M. & Cygan, R. T. Analysis of molecular clusters in simulations of lithium-ion battery electrolytes. *The Journal of Physical Chemistry C* **117**, 24673–24684 (2013).

[135] Ullner, M. & Woodward, C. E. Orientational correlation function and persistence lengths of flexible polyelectrolytes. *Macromolecules* **35**, 1437–1445 (2002).

[136] Odijk, T. Polyelectrolytes near the rod limit. *Journal of Polymer Science: Polymer Physics Edition* **15**, 477–483 (1977).

[137] Skolnick, J. & Fixman, M. Electrostatic persistence length of a wormlike polyelectrolyte. *Macromolecules* **10**, 944–948 (1977).

[138] Hara, M. *Polyelectrolytes: Science and Technology* (Marcel Dekker, New York, 1993).

[139] Salanne, M. Simulations of room temperature ionic liquids: From polarizable to coarse-grained force fields. *Physical Chemistry Chemical Physics* **17**, 14270–14279 (2015).

[140] Rajput, N. N. *et al.* Elucidating the solvation structure and dynamics of lithium polysulfides resulting from competitive salt and solvent interactions. *Chemistry of Materials* **29**, 3375–3379 (2017).

[141] Dünweg, B. & Kremer, K. Molecular dynamics simulation of a polymer chain in solution. *The Journal of Chemical Physics* **99**, 6983–6997 (1993).

[142] Castiglione, F. *et al.* Molecular environment and enhanced diffusivity of Li^+ ions in lithium-salt-doped ionic liquid electrolytes. *Journal of Physical Chemistry Letters* **2**, 153–157 (2011).

[143] Sorte, E. G. *et al.* Impact of hydration and sulfonation on the morphology and ionic conductivity of sulfonated poly(phenylene) proton exchange membranes. *Macromolecules* **52**, 857–876 (2019).

[144] Kreuer, K.-D., Paddison, S. J., Spohr, E. & Schuster, M. Transport in proton conductors for fuel-cell applications: Simulations, elementary reactions, and phenomenology. *Chemical Reviews* **104**, 4637–4678 (2004).

[145] Solano, C. J., Jeremias, S., Paillard, E., Beljonne, D. & Lazzaroni, R. A joint theoretical/experimental study of the structure, dynamics, and Li^+ transport in bis([tri]fluoro[methane]sulfonyl)imide [T]FSI-based ionic liquids. *Journal of Chemical Physics* **139**, 034502 (2013).

[146] Borodin, O., Smith, G. D. & Henderson, W. Li^+ cation environment, transport, and mechanical properties of the LiTFSI doped N-methyl-N-alkylpyrrolidinium$^+$TFSI$^-$ ionic liquids. *Journal of Physical Chemistry B* **110**, 16879–16886 (2006).

[147] Druger, S. D., Nitzan, A. & Ratner, M. A. Dynamic bond percolation theory: A microscopic model for diffusion in dynamically disordered systems. I. Definition and one-dimensional case. *The Journal of Chemical Physics* **79**, 3133–3142 (1983).

[148] Borodin, O. & Smith, G. D. Mechanism of ion transport in amorphous poly (ethylene oxide)/LiTFSI from molecular dynamics simulations. *Macromolecules* **39**, 1620–1629 (2006).

[149] Reger, A., Peled, E. & Gileadi, E. Mechanism of high conductivity in a medium of low dielectric constant. *The Journal of Physical Chemistry* **83**, 873–879 (1979).

[150] Hwang, S. *et al.* Ionic conduction and solution structure in $LiPF_6$ and $LiBF_4$ propylene carbonate electrolytes. *Journal of Physical Chemistry C* **122**, 19438–19446 (2018).

[151] Kamcev, J., Paul, D. R., Manning, G. S. & Freeman, B. D. Ion diffusion coefficients in ion exchange membranes: significance of counterion condensation. *Macromolecules* **51**, 5519–5529 (2018).

[152] Dong, D. & Bedrov, D. Charge transport in [li (tetraglyme)][bis (trifluoromethane) sulfonimide] solvate ionic liquids: Insight from molecular dynamics simulations. *The Journal of Physical Chemistry B* **122**, 9994–10004 (2018).

[153] McDaniel, J. G. & Son, C. Y. Ion correlation and collective dynamics in bmim/bf4-based organic electrolytes: From dilute solutions to the ionic liquid limit. *The Journal of Physical Chemistry B* **122**, 7154–7169 (2018).

[154] Kashyap, H. K., Annapureddy, H. V., Raineri, F. O. & Margulis, C. J. How is charge transport different in ionic liquids and electrolyte solutions? *The Journal of Physical Chemistry B* **115**, 13212–13221 (2011).

[155] Dong, D., Sälzer, F., Roling, B. & Bedrov, D. How efficient is li^+ ion transport in solvate ionic liquids under anion-blocking conditions in a battery? *Physical Chemistry Chemical Physics* **20**, 29174–29183 (2018).

[156] Molinari, N., Mailoa, J. P. & Kozinsky, B. General trend of negative transference number in Li salt / ionic liquid mixtures. *ChemRxiv* 1–21 (2019).

[157] Vink, H. Conductance of polyelectrolyte solutions, anisotropy and other anomalies. In *Physical Chemistry of Polyelectrolytes*, chap. 7, 225–244 (CRC Press, Boca Raton, 2001), 1 edn.

[158] Vink, H. The dynamic frictional theory of transport processes in relation to nonequilibrium thermodynamics. *Journal of Colloid And Interface Science* **160**, 51–58 (1993).

[159] Colby, R. H., Boris, D. C., Krause, W. E. & Tan, J. S. Polyelectrolyte conductivity. *Journal of Polymer Science Part B: Polymer Physics* **35**, 2951–2960 (1997).

[160] Haskins, J. B. *et al.* Computational and experimental investigation of li-doped ionic liquid electrolytes:[pyr14][tfsi],[pyr13][fsi], and [emim][bf4]. *The Journal of Physical Chemistry B* **118**, 11295–11309 (2014).

[161] Muthukumar, M. Dynamics of polyelectrolyte solutions. *Journal of Chemical Physics* **107**, 2619–2635 (1997).

[162] Chatare, V. *et al.* An alternative route to single ion conductivity using multi-ionic salts. *Materials Horizons* **5**, 461–473 (2018).

[163] Fong, K. D., Self, J., McCloskey, B. D. & Persson, K. A. Onsager transport coefficients and transference numbers in polyelectrolyte solutions and polymerized ionic liquids. *Macromolecules* **53**, 9503–9512 (2020).

[164] Qian, W., Texter, J. & Yan, F. Frontiers in poly(ionic liquid)s: Syntheses and applications. *Chemical Society Reviews* **46**, 1124–1159 (2017).

[165] Zhang, Z., Wheatle, B. K., Krajniak, J., Keith, J. R. & Ganesan, V. Ion mobilities, transference numbers, and inverse haven ratios of polymeric ionic liquids. *ACS Macro Letters* **9**, 84–89 (2019).

[166] Yu, Y. *et al.* Single lithium-ion polymer electrolytes based on poly(ionic liquid)s for lithium-ion batteries. *Soft Matter* **14**, 6313–6319 (2018).

[167] Kisliuk, A., Bocharova, V., Popov, I., Gainaru, C. & Sokolov, A. P. Fundamental parameters governing ion conductivity in polymer electrolytes. *Electrochimica Acta* **299**, 191–196 (2019).

[168] Gainaru, C. *et al.* Mechanism of conductivity relaxation in liquid and polymeric electrolytes: Direct link between conductivity and diffusivity. *The Journal of Physical Chemistry B* **120**, 11074–11083 (2016).

[169] Kremer, K. & Grest, G. S. Dynamics of entangled linear polymer melts: A molecular-dynamics simulation. *The Journal of Chemical Physics* **92**, 5057–5086 (1990).

[170] Grest, G. S. & Kremer, K. Molecular dynamics simulation for polymers in the presence of a heat bath. *Physical Review A* **33**, 3628 (1986).

[171] Hoy, R. S., Foteinopoulou, K. & Kröger, M. Topological analysis of polymeric melts: Chain-length effects and fast-converging estimators for entanglement length. *Physical Review E* **80**, 031803 (2009).

[172] Self, J., Fong, K. D. & Persson, K. A. Transport in superconcentrated $LiPF_6$ and $LiBF_4$/propylene carbonate electrolytes. *ACS Energy Letters* **4**, 2843–2849 (2019).

[173] Joshi, Y. & Kwak, J. C. Transference numbers, polyion mobilities, and charge fractions in aqueous solutions of lithium, sodium, and potassium dextransulfate. *Biophysical Chemistry* **12**, 323–328 (1980).

[174] Jordan, D., Kurucsev, T. & Martin, M. Comparative physical chemical study of isotactic and atactic poly (styrene sulphonic acid) solutions. Part 2. Electrical conductance and transference measurements in salt-free aqueous solutions. *Transactions of the Faraday Society* **65**, 606–611 (1969).

[175] De, R., Lee, H. & Das, B. Exploring the interactions in binary mixtures of polyelectrolytes: Influence of mixture composition, concentration, and temperature on counterion condensation. *Journal of Molecular Liquids* **251**, 94–99 (2018).

[176] Kuznetsov, I., Vorontsova, O. & Kozlov, A. Polyelectrolyte properties of biopolymers: Conductivity and secondary structure of polyriboadenylic acid and its salts in solutions. *Biopolymers: Original Research on Biomolecules* **31**, 65–76 (1991).

[177] Overbeek, J. T. G. Polyelectrolytes, past, present and future. In *Macromolecular Chemistry–11*, 91–101 (Elsevier, 1977).

[178] Matsunaga, S., Koishi, T. & Tamaki, S. Velocity correlation functions and partial conductivities of molten AgI-AgBr by molecular dynamics simulation. *Materials Science and Engineering: A* **449**, 693–698 (2007).

[179] Koishi, T. & Tamaki, S. Partial conductivities of a molten salt based on Langevin equation. *Journal of the Physical Society of Japan* **68**, 964–971 (1999).

[180] Bouchet, R. *et al.* Single-ion bab triblock copolymers as highly efficient electrolytes for lithium-metal batteries. *Nature Materials* **12**, 452–457 (2013).

[181] Bocharova, V. & Sokolov, A. P. Perspectives for polymer electrolytes: A view from fundamentals of ionic conductivity. *Macromolecules* **53**, 4141–4157 (2020).

[182] Ravikumar, B., Mynam, M. & Rai, B. Effect of salt concentration on properties of lithium ion battery electrolytes: A molecular dynamics study. *The Journal of Physical Chemistry C* **122**, 8173–8181 (2018).

[183] Samuel, D. *et al.* Ion pairing and diffusion in magnesium electrolytes based on magnesium borohydride. *ACS Applied Materials & Interfaces* **9**, 43755–43766 (2017).

[184] Manning, G. S. Limiting laws and counterion condensation in polyelectrolyte solutions ii. self-diffusion of the small ions. *The Journal of Chemical Physics* **51**, 934–938 (1969).

[185] Muthukumar, M. Ordinary–extraordinary transition in dynamics of solutions of charged macromolecules. *Proceedings of the National Academy of Sciences* **113**, 12627–12632 (2016).

[186] Dobrynin, A. V., Colby, R. H. & Rubinstein, M. Scaling theory of polyelectrolyte solutions. *Macromolecules* **28**, 1859–1871 (1995).

[187] Payne, V. A. *et al.* Simulations of structure and transport in polymer electrolytes. *Solid State Ionics* **81**, 171–181 (1995).

[188] Harris, K. R. Relations between the fractional Stokes-Einstein and Nernst-Einstein equations and velocity correlation coefficients in ionic liquids and molten salts. *The Journal of Physical Chemistry B* **114**, 9572–9577 (2010).

[189] Mogurampelly, S., Keith, J. R. & Ganesan, V. Mechanisms underlying ion transport in polymerized ionic liquids. *Journal of the American Chemical Society* **139**, 9511–9514 (2017).

[190] Frischknecht, A. L. *et al.* Chain and ion dynamics in precise polyethylene ionomers. *Macromolecules* **52**, 7939–7950 (2019).

[191] Ma, B., Nguyen, T. D. & Olvera de la Cruz, M. Control of ionic mobility via charge size asymmetry in random ionomers. *Nano letters* **20**, 43–49 (2019).

[192] Hall, L. M., Stevens, M. J. & Frischknecht, A. L. Dynamics of model ionomer melts of various architectures. *Macromolecules* **45**, 8097–8108 (2012).

[193] Bollinger, J. A., Stevens, M. J. & Frischknecht, A. L. Quantifying single-ion transport in percolated ionic aggregates of polymer melts. *ACS Macro Letters* **9**, 583–587 (2020).

[194] Aihara, Y., Sugimoto, K., Price, W. S. & Hayamizu, K. Ionic conduction and self-diffusion near infinitesimal concentration in lithium salt-organic solvent electrolytes. *The Journal of Chemical Physics* **113**, 1981–1991 (2000).

[195] Borodin, O., Gorecki, W., Smith, G. D. & Armand, M. Molecular dynamics simulation and pulsed-field gradient nmr studies of bis(fluorosulfonyl)imide (FSI) and bis[(trifluoromethyl)sulfonyl]imide (TFSI)-based ionic liquids. *The Journal of Physical Chemistry B* **114**, 6786–6798 (2010).

[196] Li, Z., Smith, G. D. & Bedrov, D. Li^+ solvation and transport properties in ionic liquid/lithium salt mixtures: A molecular dynamics simulation study. *The Journal of Physical Chemistry B* **116**, 12801–12809 (2012).

[197] Picalek, J. & Kolafa, J. Molecular dynamics study of conductivity of ionic liquids: The Kohlrausch law. *Journal of Molecular Liquids* **134**, 29–33 (2007).

[198] Lesch, V. *et al.* A combined theoretical and experimental study of the influence of different anion ratios on lithium ion dynamics in ionic liquids. *The Journal of Physical Chemistry B* **118**, 7367–7375 (2014).

[199] Hayamizu, K. Temperature dependence of self-diffusion coefficients of ions and solvents in ethylene carbonate, propylene carbonate, and diethyl carbonate single solutions and ethylene carbonate + diethyl carbonate binary solutions of $LiPF_6$ studied by nmr. *Journal of Chemical & Engineering Data* **57**, 2012–2017 (2012).

[200] Gebbie, M. A. *et al.* Ionic liquids behave as dilute electrolyte solutions. *Proceedings of the National Academy of Sciences* **110**, 9674–9679 (2013).

[201] Lee, A. A., Perez-Martinez, C. S., Smith, A. M. & Perkin, S. Scaling analysis of the screening length in concentrated electrolytes. *Physical Review Letters* **119**, 026002 (2017).

[202] Jones, P., Coupette, F., Härtel, A. & Lee, A. A. Bayesian unsupervised learning reveals hidden structure in concentrated electrolytes. *The Journal of Chemical Physics* **154**, 134902 (2021).

[203] Shen, K.-H. & Hall, L. M. Ion conductivity and correlations in model salt-doped polymers: Effects of interaction strength and concentration. *Macromolecules* **53**, 3655–3668 (2020).

[204] Rosenwinkel, M. P. & Schönhoff, M. Lithium transference numbers in PEO/LiTFSA electrolytes determined by electrophoretic nmr. *Journal of The Electrochemical Society* **166**, A1977 (2019).

[205] Schmidt, F. & Schönhoff, M. Solvate cation migration and ion correlations in solvate ionic liquids. *The Journal of Physical Chemistry B* **124**, 1245–1252 (2020).

[206] Grundy, L. S. *et al.* Impact of frictional interactions on conductivity, diffusion, and transference number in ether-and perfluoroether-based electrolytes. *Journal of The Electrochemical Society* **167**, 120540 (2020).

[207] Cheng, Y., Yang, J., Hung, J.-H., Patra, T. K. & Simmons, D. S. Design rules for highly conductive polymeric ionic liquids from molecular dynamics simulations. *Macromolecules* **51**, 6630–6644 (2018).

[208] Yeager, H. & Kratochvil, B. Conductance study of ion pairing of alkali metal tetrafluoroborates and hexafluorophosphates in acetonitrile. *Canadian Journal of Chemistry* **53**, 3448–3451 (1975).

[209] Molinari, N., Mailoa, J. P. & Kozinsky, B. Effect of salt concentration on ion clustering and transport in polymer solid electrolytes: A molecular dynamics study of PEO-LiTFSI. *Chemistry of Materials* **30**, 6298–6306 (2018).

[210] Lin, K.-J. & Maranas, J. K. Does decreasing ion-ion association improve cation mobility in single ion conductors? *Physical Chemistry Chemical Physics* **15**, 16143–16151 (2013).

[211] Shen, K.-H. & Hall, L. M. Effects of ion size and dielectric constant on ion transport and transference number in polymer electrolytes. *Macromolecules* **53**, 10086–10096 (2020).

[212] Ue, M. Mobility and ionic association of lithium and quaternary ammonium salts in propylene carbonate and γ-butyrolactone. *Journal of the Electrochemical Society* **141**, 3336 (1994).

[213] Tominaga, Y., Yamazaki, K. & Nanthana, V. Effect of anions on lithium ion conduction in poly (ethylene carbonate)-based polymer electrolytes. *Journal of the Electrochemical Society* **162**, A3133 (2015).

[214] Zhang, Z. *et al.* Novel design concepts of efficient mg-ion electrolytes toward high-performance magnesium–selenium and magnesium–sulfur batteries. *Advanced Energy Materials* **7**, 1602055 (2017).

[215] Shyamsunder, A., Blanc, L. E., Assoud, A. & Nazar, L. F. Reversible calcium plating and stripping at room temperature using a borate salt. *ACS Energy Letters* **4**, 2271–2276 (2019).

[216] Hahn, N. T. *et al.* The influence of ether solvent and anion coordination on electrochemical behavior in calcium battery electrolytes. *ACS Applied Energy Materials* **3**, 8437–8447 (2020).

[217] Li, Z., Fuhr, O., Fichtner, M. & Zhao-Karger, Z. Towards stable and efficient electrolytes for room-temperature rechargeable calcium batteries. *Energy & Environmental Science* **12**, 3496–3501 (2019).

[218] Ma, Q. *et al.* Impact of the functional group in the polyanion of single lithium-ion conducting polymer electrolytes on the stability of lithium metal electrodes. *RSC Advances* **6**, 32454–32461 (2016).

[219] Ma, Q. *et al.* Single lithium-ion conducting polymer electrolytes based on a super-delocalized polyanion. *Angewandte Chemie International Edition* **55**, 2521–2525 (2016).

[220] Meziane, R., Bonnet, J.-P., Courty, M., Djellab, K. & Armand, M. Single-ion polymer electrolytes based on a delocalized polyanion for lithium batteries. *Electrochimica Acta* **57**, 14–19 (2011).

[221] Ito, K. & Ohno, H. Design of highly ion conductive polyether/salt hybrids. *Electrochimica Acta* **43**, 1247–1252 (1998).

[222] Benrabah, D., Sylla, S., Alloin, F., Sanchez, J.-Y. & Armand, M. Perfluorosulfonate-polyether based single ion conductors. *Electrochimica Acta* **40**, 2259–2264 (1995).

[223] Kim, H.-T. & Park, J.-K. Effects of cations on ionic states of poly (oligo-oxyethylene methacrylate-co-alkali metal acrylamidocaproate) single-ion conductor. *Solid State Ionics* **98**, 237–244 (1997).

[224] Zhang, W. *et al.* Molecularly tunable polyanions for single-ion conductors and poly (solvate ionic liquids). *Chemistry of Materials* **33**, 524–534 (2021).

[225] Abbott, L. J. & Lawson, J. W. Effects of side chain length on ionic aggregation and dynamics in polymer single-ion conductors. *Macromolecules* **52**, 7456–7467 (2019).

[226] Chen, X., Chen, F., Liu, M. S. & Forsyth, M. Polymer architecture effect on sodium ion transport in pstfsi-based ionomers: A molecular dynamics study. *Solid State Ionics* **288**, 271–276 (2016).

[227] Timachova, K. *et al.* Mechanism of ion transport in perfluoropolyether electrolytes with a lithium salt. *Soft Matter* **13**, 5389–5396 (2017).

[228] Timachova, K., Watanabe, H. & Balsara, N. P. Effect of molecular weight and salt concentration on ion transport and the transference number in polymer electrolytes. *Macromolecules* **48**, 7882–7888 (2015).

[229] Lascaud, S. *et al.* Phase diagrams and conductivity behavior of poly (ethylene oxide)-molten salt rubbery electrolytes. *Macromolecules* **27**, 7469–7477 (1994).

[230] Wheatle, B. K., Lynd, N. A. & Ganesan, V. Effect of polymer polarity on ion transport: a competition between ion aggregation and polymer segmental dynamics. *ACS Macro Letters* **7**, 1149–1154 (2018).

[231] Wheatle, B. K., Fuentes, E. F., Lynd, N. A. & Ganesan, V. Influence of host polarity on correlating salt concentration, molecular weight, and molar conductivity in polymer electrolytes. *ACS Macro Letters* **8**, 888–892 (2019).

[232] France-Lanord, A. *et al.* Effect of chemical variations in the structure of poly (ethylene oxide)-based polymers on lithium transport in concentrated electrolytes. *Chemistry of Materials* **32**, 121–126 (2019).

[233] Wheatle, B. K., Keith, J. R., Mogurampelly, S., Lynd, N. A. & Ganesan, V. Influence of dielectric constant on ionic transport in polyether-based electrolytes. *ACS Macro Letters* **6**, 1362–1367 (2017).

[234] Borodin, O., Douglas, R., Smith, G., Eyring, E. M. & Petrucci, S. Microwave dielectric relaxation, electrical conductance, and ultrasonic relaxation of $LiPF_6$ in poly (ethylene oxide) dimethyl ether-500. *The Journal of Physical Chemistry B* **106**, 2140–2145 (2002).

[235] Petrucci, S., Masiker, M. C. & Eyring, E. M. The possible presence of triple ions in electrolyte solutions of low dielectric permittivity. *Journal of Solution Chemistry* **37**, 1031–1035 (2008).

[236] Choi, U. H., Liang, S., Chen, Q., Runt, J. & Colby, R. H. Segmental dynamics and dielectric constant of polysiloxane polar copolymers as plasticizers for polymer electrolytes. *ACS Applied Materials & Interfaces* **8**, 3215–3225 (2016).

[237] Gudla, H., Zhang, C. & Brandell, D. Effects of solvent polarity on Li-ion diffusion in polymer electrolytes: An all-atom molecular dynamics study with charge scaling. *The Journal of Physical Chemistry B* **124**, 8124–8131 (2020).

[238] McBreen, J., Lee, H., Yang, X. & Sun, X. New approaches to the design of polymer and liquid electrolytes for lithium batteries. *Journal of Power Sources* **89**, 163–167 (2000).

[239] Werber, J. R., Osuji, C. O. & Elimelech, M. Materials for next-generation desalination and water purification membranes. *Nature Reviews Materials* **1**, 1–15 (2016).

[240] Bone, S. E., Steinrück, H.-G. & Toney, M. F. Advanced characterization in clean water technologies. *Joule* **4**, 1637–1659 (2020).

[241] Faulkner, L. R. & Bard, A. J. *Electrochemical Methods: Fundamentals and Applications* (John Wiley and Sons, 2002).

[242] Chandler, D. *Introduction to Modern Statistical Mechanics* (Oxford University Press, New York, 1987).

[243] Plimpton, S. Fast parallel algorithms for short-range molecular dynamics. *Journal of Computational Physics* **117**, 1–19 (1995).

[244] http://lammps.sandia.gov (accessed aug 11, 2017).

[245] Martínez, L., Andrade, R., Birgin, E. G. & Martínez, J. M. PACKMOL: A package for building initial configurations for molecular dynamics simulations. *Journal of Computational Chemistry* **30**, 2157–2164 (2009).

[246] Banks, J. L. *et al.* Integrated modeling program, applied chemical theory (IMPACT). *Journal of Computational Chemistry* **26**, 1752–1780 (2005).

[247] Leontyev, I. & Stuchebrukhov, A. Accounting for electronic polarization in non-polarizable force fields. *Physical Chemistry Chemical Physics* **13**, 2613–2626 (2011).

[248] Toukmaji, A. Y. & Board, J. A. Ewald summation techniques in perspective: A survey. *Computer Physics Communications* **95**, 73–92 (2003).

[249] Michaud-Agrawal, N., Denning, E. J., Woolf, T. B. & Beckstein, O. MDAnalysis: A toolkit for the analysis of molecular dynamics simulations. *Journal of Computational Chemistry* **32**, 2319–2327 (2011).

[250] Gowers, R. *et al.* MDAnalysis: A Python package for the rapid analysis of molecular dynamics simulations. In *Proceedings of the 15th Python in Science Conference*, 98–105 (2016).

[251] Andersen, H. C. Rattle: A "velocity" version of the shake algorithm for molecular dynamics calculations. *Journal of Computational Physics* **52**, 24–34 (1983).

[252] Ryckaert, J. P., Ciccotti, G. & Berendsen, H. J. Numerical integration of the cartesian equations of motion of a system with constraints: molecular dynamics of n-alkanes. *Journal of Computational Physics* **23**, 327–341 (1977).

[253] Schrödinger. MacroModel (2018).

[254] Hagberg, A. A., Schult, D. A. & Swart, P. J. Exploring network structure, dynamics, and function using NetworkX. In Varoquaux, G., Vaught, T. & Millman, J. (eds.) *Proceedings of the 7th Python in Science Conference*, 11–15 (Pasadena, CA, 2008).

[255] Shannon, P. *et al.* Cytoscape: a software environment for integrated models of biomolecular interaction networks. *Genome Research* **13**, 2498–504 (2003).

[256] Kaburagi, M. *et al.* Molecular dynamics simulation of telomeric single-stranded DNA and POT1. *Polymer Journal* **48**, 189–195 (2016).

[257] Ha, B. Y. & Thirumalai, D. Electrostatic persistence length of a polyelectrolyte chain. *Macromolecules* **28**, 577–581 (1995).

[258] Carrillo, J.-M. Y. & Dobrynin, A. V. Polyelectrolytes in salt solutions: Molecular dynamics simulations. *Macromolecules* **44**, 5798–5816 (2011).

[259] Gubarev, A., Carrillo, J.-M. Y. & Dobrynin, A. V. Scale-dependent electrostatic stiffening in biopolymers. *Macromolecules* **42**, 5851–5860 (2009).

[260] Bačová, P. *et al.* Double-exponential decay of orientational correlations in semiflexible polyelectrolytes. *The European Physical Journal E* **35**, 53 (2012).

[261] Manghi, M. & Netz, R. R. Variational theory for a single polyelectrolyte chain revisited. *The European Physical Journal E* **14**, 67–77 (2004).

[262] Kowsari, M. H. *et al.* Molecular dynamics simulations of the structure and transport properties of tetra-butylphosphonium amino acid ionic liquids. *Physical Chemistry Chemical Physics* **13**, 8826 (2011).

[263] Rumble, C. A., Uitvlugt, C., Conway, B. & Maroncelli, M. Solute rotation in ionic liquids: size, shape, and electrostatic effects. *The Journal of Physical Chemistry B* **121**, 5094–5109 (2017).

[264] Kremer, F. & Schönhals, A. (eds.) *Broadband Dielectric Spectroscopy* (Springer Berlin Heidelberg, Berlin, Heidelberg, 2011).

[265] Flyvbjerg, H. & Petersen, H. G. Error estimates on averages of correlated data. *The Journal of Chemical Physics* **91**, 461–466 (1989). arXiv:`arXiv:1011.1669v3`.

[266] Grossfield, A. & Zuckerman, D. M. Quantifying uncertainty and sampling quality in biomolecular simulations. *Annual Reports in Computational Chemistry* **5**, 23–48 (2009).

[267] Chang, R. & Yethiraj, A. Strongly charged flexible polyelectrolytes in poor solvents: Molecular dynamics simulations with explicit solvent. *The Journal of chemical physics* **118**, 6634–6647 (2003).

[268] Yao, N., Li, J., Gu, F., Wang, H. & Liao, Q. Relaxation time spectrum and dynamics of stretched polymer chain in dilute θ solution: Implicit solvent model versus explicit solvent model. *Macromolecular Theory and Simulations* **29**, 1900064 (2020).

[269] Grass, K. & Holm, C. Polyelectrolytes in electric fields: Measuring the dynamical effective charge and effective friction. *Soft Matter* **5**, 2079–2092 (2009).

[270] Chang, R. & Yethiraj, A. Dilute solutions of strongly charged flexible polyelectrolytes in poor solvents: Molecular dynamics simulations with explicit solvent. *Macromolecules* **39**, 821–828 (2006).

[271] Hall, D. S., Self, J. & Dahn, J. Dielectric constants for quantum chemistry and li-ion batteries: Solvent blends of ethylene carbonate and ethyl methyl carbonate. *The Journal of Physical Chemistry C* **119**, 22322–22330 (2015).

[272] Lo, T. S., Khusid, B. & Koplik, J. Dynamical clustering of counterions on flexible polyelectrolytes. *Physical review letters* **100**, 128301 (2008).

[273] Chremos, A. & Douglas, J. F. Counter-ion distribution around flexible polyelectrolytes having different molecular architecture. *Soft Matter* **12**, 2932–2941 (2016).

[274] Carrillo, J.-M. Y., Brown, W. M. & Dobrynin, A. V. Explicit solvent simulations of friction between brush layers of charged and neutral bottle-brush macromolecules. *Macromolecules* **45**, 8880–8891 (2012).

Appendix A

Supplementary Thermodynamic Derivations[1]

In this appendix, we provide additional derivations related to the thermodynamics of electrolyte solutions which are relevant to Chapters 2 and 3.

A.1 Thermodynamic potentials

Deriving the internal entropy production in Chapter 2.1 relied on using the Helmholtz free energy per volume, $\tilde{f}$. In this section we begin with system-level thermodynamics to derive an expression for $\tilde{f}$ in a mixture subject to an electromagnetic field and infer the quantities on which $\tilde{f}$ depends. We then perform Legendre transforms to develop analogous expressions for the internal energy and Gibbs free energy densities.

At the system level, changes in the Helmholtz free energy $\mathcal{F} = \tilde{f}V$ can be written as [48]

$$d\mathcal{F} = -pdV - \mathcal{S}dT + \sum_i \mu_i dN_i - \int \boldsymbol{P} dV \cdot d\boldsymbol{\mathcal{E}} - \int \boldsymbol{\mathcal{M}} dV \cdot d\boldsymbol{B} \,, \tag{A.1}$$

where $\mathcal{S}$ is entropy and each of the other quantities has been defined in the main text. Consider the case where the polarization and Lorentz magnetization are uniform in the system, such that $\int \boldsymbol{P} dV = \boldsymbol{P}V$ and $\int \boldsymbol{\mathcal{M}} dV = \boldsymbol{\mathcal{M}}V$. Note that Eq. (A.1) is only valid in equilibrium. We therefore invoke the local equilibrium hypothesis: although irreversible processes may be taking place in the system as a whole, we can isolate a small region of the system which can be treated as though it were in equilibrium with respect to time. This region must be of an intermediate asymptotic length scale: small enough that its intensive properties such as T and p are uniform throughout the region but not so small that it captures fluctuations at the atomic level.

[1]This appendix is closely adapted from portions of Ref [1]: Fong, K. D., Bergstrom, H. K., McCloskey, B. D. & Mandadapu, K. K. Transport phenomena in electrolyte solutions: Non-equilibrium thermodynamics and statistical mechanics. *AIChE Journal* e17091 (2020).

In working with electromagnetic quantities, it is most convenient to consider quantities per unit volume. We recast Eq. (A.1) in terms of the free energy density $\tilde{f}$ and entropy per unit volume $\tilde{s}$ as

$$V d\tilde{f} + \tilde{f} dV = -p dV - \tilde{s} V dT + \sum_i \mu_i \left[d\left(\frac{N_i}{V}\right) V + \left(\frac{N_i}{V}\right) dV \right] - \boldsymbol{P} V \cdot d\boldsymbol{\mathcal{E}} - \boldsymbol{\mathcal{M}} V \cdot d\boldsymbol{B} \ . \quad \text{(A.2)}$$

Grouping terms, we obtain

$$V(d\tilde{f} + \tilde{s} dT - \sum_i \mu_i dc_i + \boldsymbol{P} \cdot d\boldsymbol{\mathcal{E}} + \boldsymbol{\mathcal{M}} \cdot d\boldsymbol{B}) + dV(\tilde{f} + p - \sum_i \mu_i c_i) = 0 \ , \quad \text{(A.3)}$$

leading to

$$d\tilde{f} = -\tilde{s} dT + \sum_i \mu_i dc_i - \boldsymbol{P} \cdot d\boldsymbol{\mathcal{E}} - \boldsymbol{\mathcal{M}} \cdot d\boldsymbol{B} \quad \text{(A.4)}$$

and

$$\tilde{f} = -p + \sum_i \mu_i c_i \ . \quad \text{(A.5)}$$

Equation (A.4) shows that $\tilde{f}$ is a function [T, $c_1, c_2, ..., c_N$, $\boldsymbol{\mathcal{E}}$, $\boldsymbol{B}$]. Equation (A.5) provides the integrated form of the thermodynamic relation for $\tilde{f}$ and is used in Chapter 2.2 to derive the forms of the pressure and stress tensor.

Now let us develop expressions for the internal energy and Gibbs free energy per volume specifically in the case of no applied magnetic field, when $\boldsymbol{\mathcal{E}} = \boldsymbol{E}$. Performing a Legendre transform ($\tilde{u} = \tilde{f} + T\tilde{s} + \boldsymbol{P} \cdot \boldsymbol{E}$), we can get an expression for the internal energy analogous to Eq. (A.4):

$$d\tilde{u} = T d\tilde{s} + \sum_i \mu_i dc_i + \boldsymbol{E} \cdot d\boldsymbol{P} \ . \quad \text{(A.6)}$$

In this case, $\tilde{u}$ does not include the energy of the electric field in vacuum ($\frac{1}{2}\epsilon_0 E^2$) which would be present in the absence of the body. In some cases, it is advantageous to include this background energy and consider the quantity $\bar{\tilde{u}}$ given by

$$\bar{\tilde{u}} \coloneqq \tilde{u} + \frac{1}{2}\epsilon_0 E^2 \ . \quad \text{(A.7)}$$

Using $\boldsymbol{P} = \boldsymbol{D}^{\mathrm{f}} - \epsilon_0 \boldsymbol{E}$ (Eqs. (2.16) and (2.29)) yields an expression for $d\bar{\tilde{u}}$ in terms of the dielectric displacement rather than the polarization, i.e.,

$$d\bar{\tilde{u}} = T d\tilde{s} + \sum_i \mu_i dc_i + \boldsymbol{E} \cdot d\boldsymbol{D}^{\mathrm{f}} \ . \quad \text{(A.8)}$$

The quantity $\boldsymbol{E} \cdot d\boldsymbol{D}^{\mathrm{f}}$, the work done by the electric field, can be equivalently written as $\boldsymbol{E} \cdot d\boldsymbol{D}^{\mathrm{f}} = \phi dq^f = \sum_i z_i F \phi dc_i$ (see Section 10 of Landau and Lifshitz [48]), leading to

$$d\bar{\tilde{u}} = T d\tilde{s} + \sum_i (\mu_i + z_i F \phi) dc_i \ . \quad \text{(A.9)}$$

Another Legendre transform gives us Gibbs free energy ($\bar{\tilde{g}} = \bar{\tilde{u}} - T\tilde{s} + p$) as

$$d\bar{\tilde{g}} = -\tilde{s}dT + dp + \sum_i (\mu_i + z_i F\phi) dc_i \ . \tag{A.10}$$

This gives the Gibbs free energy in terms of the electrochemical potential ($\overline{\mu}_i = \mu_i + z_i F\phi$), as is commonly found and used in the electrochemistry literature.

A.2 Gibbs equation

Here, we derive the form of the Gibbs equation in a state of local equilibrium for mixtures subject to an electric field (assuming a linear dielectric with no magnetic field). It is typical in the framework of non-equilibrium thermodynamics to start with the Gibbs equation as a local equilibrium hypothesis to derive the rate of internal entropy production. While this approach should yield the same expression for entropy production as that used in Chapter 2.1, it is nontrivial to derive or propose the Gibbs equation at the outset, where we do not know a priori the role of the electric field at local equilibrium. The energy and entropy balances derived in the main text, however, can be used to derive the Gibbs equation in these systems as shown below.

Let us define the internal energy per unit mass u as

$$\begin{aligned} \rho u &= \rho e - \frac{1}{2}\rho \boldsymbol{v}\cdot\boldsymbol{v} \ , \\ \rho \dot{u} &= \rho \dot{e} - \rho \dot{\boldsymbol{v}}\cdot\boldsymbol{v} \ . \end{aligned} \tag{A.11}$$

Using this definition, the energy balance (Eq. (2.68) in the case where $\boldsymbol{B} = 0$) can be written as

$$\rho\dot{u} = [\boldsymbol{T} + (\boldsymbol{E}\cdot\boldsymbol{P})\boldsymbol{I} - \boldsymbol{E}\otimes\boldsymbol{P}] : \boldsymbol{\nabla v} + \rho r - \boldsymbol{\nabla}\cdot\bar{\boldsymbol{J}}_{\mathrm{q}} + \sum_i \boldsymbol{j}_i\cdot\boldsymbol{b}_i + \boldsymbol{\mathcal{J}}^{\mathrm{f}}\cdot\boldsymbol{E} + \boldsymbol{E}\cdot\dot{\boldsymbol{P}} \ . \tag{A.12}$$

The entropy balance for a linear dielectric (Eq. (2.89) with the linear dielectric assumptions of Chapter 2.2) reduces to

$$\rho\dot{s} = \frac{1}{T}[\boldsymbol{T} + p\boldsymbol{I} - \boldsymbol{E}\otimes\boldsymbol{P}] : \boldsymbol{\nabla v} + \frac{\rho r}{T} + \frac{\sum_i \boldsymbol{j}_i\cdot\boldsymbol{b}_i}{T} + \frac{1}{T}\sum_i \mu_i \boldsymbol{\nabla}\cdot\boldsymbol{J}_i - \frac{\boldsymbol{\nabla}\cdot\bar{\boldsymbol{J}}_{\mathrm{q}}}{T} + \frac{1}{T}\boldsymbol{\mathcal{J}}^{\mathrm{f}}\cdot\boldsymbol{E} \ . \tag{A.13}$$

Subtracting Eq. (A.12) from Eq. (A.13) leads to

$$T\rho\dot{s} = \rho\dot{u} + (p - \boldsymbol{E}\cdot\boldsymbol{P})\boldsymbol{I} : \boldsymbol{\nabla v} - \boldsymbol{E}\cdot\dot{\boldsymbol{P}} + \sum_i \mu_i \boldsymbol{\nabla}\cdot\boldsymbol{J}_i \ . \tag{A.14}$$

Using the overall mass balance (Eq. (2.6)), we can rewrite $\boldsymbol{I} : \boldsymbol{\nabla v} = \rho \dot{v}$, where $v = \frac{1}{\rho}$ is the specific volume. This relation and the species mass balance (Eq. (2.5)) give $\boldsymbol{\nabla} \cdot \boldsymbol{J}_i = -c_i \rho \dot{v} - \dot{c}_i$. These simplifications reduce Eq. (A.14) to

$$T\rho\dot{s} = \rho\dot{u} + \rho\dot{v}(p - \boldsymbol{E}\cdot\boldsymbol{P} - \sum_i \mu_i c_i) - \boldsymbol{E}\cdot\dot{\boldsymbol{P}} - \sum_i \mu_i \dot{c}_i \ . \tag{A.15}$$

Incorporating the linear relation between $\boldsymbol{P}$ and $\boldsymbol{E}$ (Eq. (2.109)) and the expression for pressure in Eq. (2.115), Eq. (A.15) becomes

$$T\rho\dot{s} = \rho\dot{u} + \rho\dot{v}\left(p_0 - \frac{1}{2}\left[\epsilon - \epsilon_0 + \rho\frac{\partial\epsilon}{\partial\rho}\right]E^2 - \sum_i \mu_i c_i\right) - (\epsilon - \epsilon_0)\boldsymbol{E}\cdot\dot{\boldsymbol{E}} - \sum_i \mu_i \dot{c}_i \ . \tag{A.16}$$

Multiplying both side of the equation by dt then yields

$$T\rho ds = \rho du + \rho dv\left(p_0 - \frac{1}{2}\left[\epsilon - \epsilon_0 + \rho\frac{\partial\epsilon}{\partial\rho}\right]E^2 - \sum_i \mu_i c_i\right) - (\epsilon - \epsilon_0)\boldsymbol{E}\cdot d\boldsymbol{E} - \sum_i \mu_i dc_i \ , \tag{A.17}$$

which is the Gibbs equation for a mixture subject to an electromagnetic field.

A.3 Concentration fluctuations

Here we derive the expression relating the quantity $\left(\frac{\partial\mu_j}{\partial c_i}\right)$ to concentration fluctuations δc_i. This derivation parallels that found in Chandler [242].

In the grand canonical ensemble, fluctuations in the number of particles of species i, N_i, can be expressed as

$$\left\langle \delta N_i^2 \right\rangle = \left\langle N_i^2 \right\rangle - \left\langle N_i \right\rangle^2 = \sum_o N_{i,o}^2 P_o - \sum_o \sum_{o'} N_{i,o} N_{i,o'} P_o P_{o'} \ , \tag{A.18}$$

where we have summed over all o microstates in the ensemble. Alternatively, we may consider the covariance of the number of particles of species i and j as

$$\left\langle \delta N_i \delta N_j \right\rangle = \left\langle N_i N_j \right\rangle - \left\langle N_i \right\rangle\left\langle N_j \right\rangle = \sum_o N_{i,o} N_{j,o} P_o - \sum_o \sum_{o'} N_{i,o} N_{j,o'} P_o P_{o'} \ . \tag{A.19}$$

The probability of observing microstate o, P_o, in the grand canonical ensemble is given by

$$P_o = \frac{\exp(-\beta E_o + \beta \sum_i \mu_i N_{i,o})}{\Xi} \ , \tag{A.20}$$

where $\beta = \frac{1}{k_B T}$ and $\Xi = \sum_o \exp(-\beta E_o + \beta \sum_i \mu_i N_{i,o})$ is the grand canonical partition function. Substituting this expression for P_o into Eq. (A.19), we obtain:

$$\left\langle \delta N_i \delta N_j \right\rangle = \frac{\partial}{\partial(\beta\mu_j)}\left(\left.\frac{\partial \ln \Xi}{\partial(\beta\mu_i)}\right|_{\beta,V,\mu_{k\neq i}}\right)_{\beta,V,\mu_{k\neq j}} = \left.\frac{\partial\left\langle N_i \right\rangle}{\partial\beta\mu_j}\right|_{\beta,V,\mu_{k\neq j}} , \tag{A.21}$$

which can be inverted to obtain an expression for $\left(\frac{\partial \mu_j}{\partial c_i}\right)$ as

$$\left.\frac{\partial \mu_j}{\partial c_i}\right|_{\beta,V,c_{k\neq i}} = \frac{1}{\beta V}(\boldsymbol{K}_{\mathrm{CC}}^{-1})^{ij} \ , \tag{A.22}$$

where $\boldsymbol{K}_{\mathrm{CC}}$ is the covariance matrix with elements $\left\langle \delta c_i \delta c_j \right\rangle$.

A.4 Gibbs-Duhem equation

To derive the Gibbs-Duhem equation for an electrolyte under no applied magnetic field, we begin with Eq. (A.5),

$$\tilde{f} = -p + \sum_i \mu_i c_i \ . \tag{A.23}$$

Taking the total differential yields

$$d\tilde{f} = -dp + \sum_i \mu_i dc_i + \sum_i c_i d\mu_i \ . \tag{A.24}$$

When compared with the expression for $d\tilde{f}$ in Eq. (A.4), we can conclude

$$-dp + \tilde{s}dT + \sum_i c_i d\mu_i + \boldsymbol{P}\cdot d\boldsymbol{E} = 0 \ . \tag{A.25}$$

For the case of constant temperature, pressure, and electric field, Eq. (A.25) simplifies to

$$\sum_i c_i \boldsymbol{\nabla}\mu_i = 0 \ . \tag{A.26}$$

In an electroneutral system where $\sum_i z_i c_i = 0$, the chemical potential in Eq. (A.26) can be replaced with the electrochemical potential to arrive at the final form of the Gibbs-Duhem equation presented in this work,

$$\sum_i c_i \boldsymbol{\nabla}\overline{\mu}_i = 0 \ . \tag{A.27}$$

We can gain further insight into Eq. (A.27) by rewriting it in terms of p_0 and $\mu_{i,0}$, the pressure and chemical potential respectively in the absence of an electric field. We have already established that $p = p_0 + \frac{1}{2}\left[\epsilon - \epsilon_0 - \rho\frac{\partial \epsilon}{\partial \rho}\right]E^2$ in Eq. (2.115). Analogously, μ_i can be related to $\mu_{i,0}$ using the definition $\mu_i := \left.\frac{\partial \tilde{f}}{\partial c_i}\right|_{T,c_{j\neq i},\boldsymbol{E}}$ and Eq. (2.111), which give

$$\mu_i = \frac{\partial \tilde{f}}{\partial c_i} = \frac{\partial(\tilde{f}_0 - \frac{1}{2}(\epsilon-\epsilon_0)E^2)}{\partial c_i} = \frac{\partial \tilde{f}_0}{\partial c_i} - \frac{1}{2}E^2\frac{\partial \epsilon}{\partial c_i} = \mu_{i,0} - \frac{1}{2}E^2\frac{\partial \epsilon}{\partial c_i} \ . \tag{A.28}$$

Since $\rho = \sum_i c_i M_i$, we can write $\sum_i c_i d\mu_i = \sum_i c_i d\mu_{i,0} - \frac{1}{2}\rho d(E^2 \frac{\partial \epsilon}{\partial \rho})$. Substituting Eqs. (2.115) and (A.28) into Eq. (A.25) yields

$$-dp_0 + \tilde{s}dT + \sum_i c_i d\mu_{i,0} - d\left(\frac{1}{2}\left[\epsilon - \epsilon_0 - \rho\frac{\partial \epsilon}{\partial \rho}\right]E^2\right) - \frac{1}{2}\rho d\left(E^2\frac{\partial \epsilon}{\partial \rho}\right) + (\epsilon - \epsilon_0)\boldsymbol{E}\cdot d\boldsymbol{E} = 0 \ . \quad \text{(A.29)}$$

It is clear that the last three terms on the left-hand side sum to zero for constant ϵ. Thus we obtain a Gibbs-Duhem equation equivalent to that without any electric field:

$$-dp_0 + \tilde{s}dT + \sum_i c_i d\mu_{i,0} = 0 \ . \quad \text{(A.30)}$$

Appendix B

Methods

B.1 Methods associated with Chapter 4[1]

Simulation methods

All-atom classical molecular dynamics (MD) simulations of LiCl in DMSO were performed using the LAMMPS [243,244] software. Most simulations consisted of 1000 DMSO molecules, with the number of ions adjusted to vary the salt concentration. The systems with the two lowest concentrations, 0.01 and 0.02 M, contained 3000 and 1500 DMSO molecules, respectively. Molecules in each simulation were initially randomly packed into a cubic box using PACKMOL [245]. Equilibration of the system consisted of (i) conjugate-gradient energy minimization, (ii) 3 ns of simulation in the isothermal-isobaric (NPT) ensemble at a pressure of 1 atm and temperature of 298 K, (iii) 2 ns simulated annealing at 400 K, and (iv) 3 ns cooling back to 298 K. Production runs consisted of 5 ns at 298 K in the canonical (NVT) ensemble using the Nosé-Hoover style thermostat and a time step of 2 fs. Force field parameters were all taken from the OPLS_2005 force field [246], with partial charges of the ionic species scaled by a factor of 0.7 to account for the fact that ion-ion interactions are typically overestimated in non-polarizable force fields [247]. Each simulation used the velocity-Verlet algorithm, periodic boundary conditions, and the PPPM method [248] to solve for long-range Coulombic interactions. Software for computing transport coefficients was written with the help of the Python package MDAnalysis [249, 250] and is available online at `https://github.com/kdfong/transport-coefficients`.

Experimental methods

LiCl (Sigma Aldrich, >99.0%) salt was dried over P_2O_5 while under vacuum for 24 hours and directly transferred under vacuum to an Argon glovebox (Vac Atmospheres) maintained

[1]This section is closely adapted from portions of Ref [1]: Fong, K. D., Bergstrom, H. K., McCloskey, B. D. & Mandadapu, K. K. Transport phenomena in electrolyte solutions: Non-equilibrium thermodynamics and statistical mechanics. *AIChE Journal* e17091 (2020).

below 5ppm O_2 and 1ppm H_2O. Anhydrous DMSO (Sigma Aldrich ≥99.9%) packaged under inert atmosphere was directly opened inside the glovebox. Electrolyte solutions were prepared in a volumetric flask and salts were allowed to completely dissolve before adjusting the final volume and decanting. Dilute samples (<5mM) were prepared via serial dilution of a 100 mM solution. All electrolyte solutions were stored and characterized inside of the Argon glovebox.

Solution conductivity measurements were performed with a Mettler Toledo InLab 751-4mm conductivity probe with platinum blocking electrodes. Samples were measured at 25 in a dry block (Torrey Pines) inside of the Argon glovebox. Temperature of the solution was verified by a thermocouple inside of the conductivity probe and was always within 0.6 of the set point. The conductivity probe was calibrated with 84 μS/cm, 1410 μS/cm, and 12.88 mS/cm aqueous conductivity standards (Mettler Toledo) prior to being brought inside the Argon glovebox. A 5% error in conductivity was assumed based off of multiple measurements.

B.2 Methods associated with Chapter 5[2]

Simulations

All-atom classical molecular dynamics (MD) simulations were performed using the LAMMPS [243,244] code. Simulations were carried out on the anionic polymer poly(allyl glycidyl ether-lithium sulfonate) (PAGELS, see Figure 5.4a for structural schematic) in dimethyl sulfoxide (DMSO). Each simulation consisted of one polyion chain with a degree of polymerization of 43, 43 lithium counterions, and a variable number of DMSO molecules, chosen to adjust the concentration of Li^+ in the system from 0.05 M to 1 M. See Table B.1 for details on the exact concentrations, numbers of solvent molecules, and simulation box sizes used.

[2]This section is closely adapted from Ref [86]: Fong, K. D.et al. Ion transport and the true transference number in nonaqueous polyelectrolyte solutions for lithium ion batteries. *ACS Central Science* **5**, 1250–1260 (2019).

Li^+ Concentration (mol/L)	Number of Solvent Molecules	Simulation Box Length (Å)
0.05	12108	112.87
0.10	6054	89.81
0.19	3027	71.70
0.47	1211	53.87
0.85	605	43.88
0.98	505	41.82

Table B.1: Details on simulation setup at each concentration.

While these simulations would ideally consist of many polymer chains to fully capture the effects of inter-chain interactions, we are limited by the large computational cost of these multi-chain simulations. To evaluate the impact of using just one chain, we have performed preliminary simulations with two chains at the two highest concentrations studied (these are the concentrations at which we would expect inter-chain interactions to be most significant). As shown in Figure B.1, the transport properties of the solution (diffusion coefficients, conductivity, and transference number) are not significantly altered between the one- and two-chain simulations, suggesting that our single-chain study here has adequately captured the most important physics underlying transport in these systems.

The molecules of each simulation were randomly packed into a cubic box using PACKMOL [245], with the polymer chain prepared in a linear conformation. This initial configuration was first relaxed using a conjugated-gradient energy minimization scheme with a convergence criterion, defined as the energy change between successive minimization iterations divided by the magnitude of the energy, of 1.0e-4. The system was then equilibrated in the isothermal-isobaric (NPT) ensemble at a pressure of 1 atm and temperature of 298 K for 3 ns, followed by simulated annealing at 400 K for 2 ns, then cooling back to 298 K over 3 ns. [140] A Nosé-Hoover style thermostat and barostat with damping parameters of 0.1 ps and 1 ps, respectively, were used. Production runs were subsequently carried out in the canonical (NVT) ensemble at 298 K using the Nosé-Hoover style thermostat and a time step of 2 fs. Simulations were carried out for 50 ns, with the last 40 ns used for analysis.

In each simulation, the equations of motion were numerically integrated using the velocity-Verlet algorithm. Each system was periodic in the x, y, and z directions and incorporated the PPPM method [248] with accuracy 1.0e-5 to compute long-range Coulombic interactions. A cutoff of 15 Å was used in computing short-ranged potentials. The length of the C-H bonds of the PAGELS chain were fixed by implementing the SHAKE algorithm [251, 252].

All force field parameters were taken from the OPLS_2005 force field [246], where atom type and partial charge assignment was automated using MacroModel and the Maestro graphical interface (Schrödinger) [253]. Partial charges of the ionic species were scaled by a

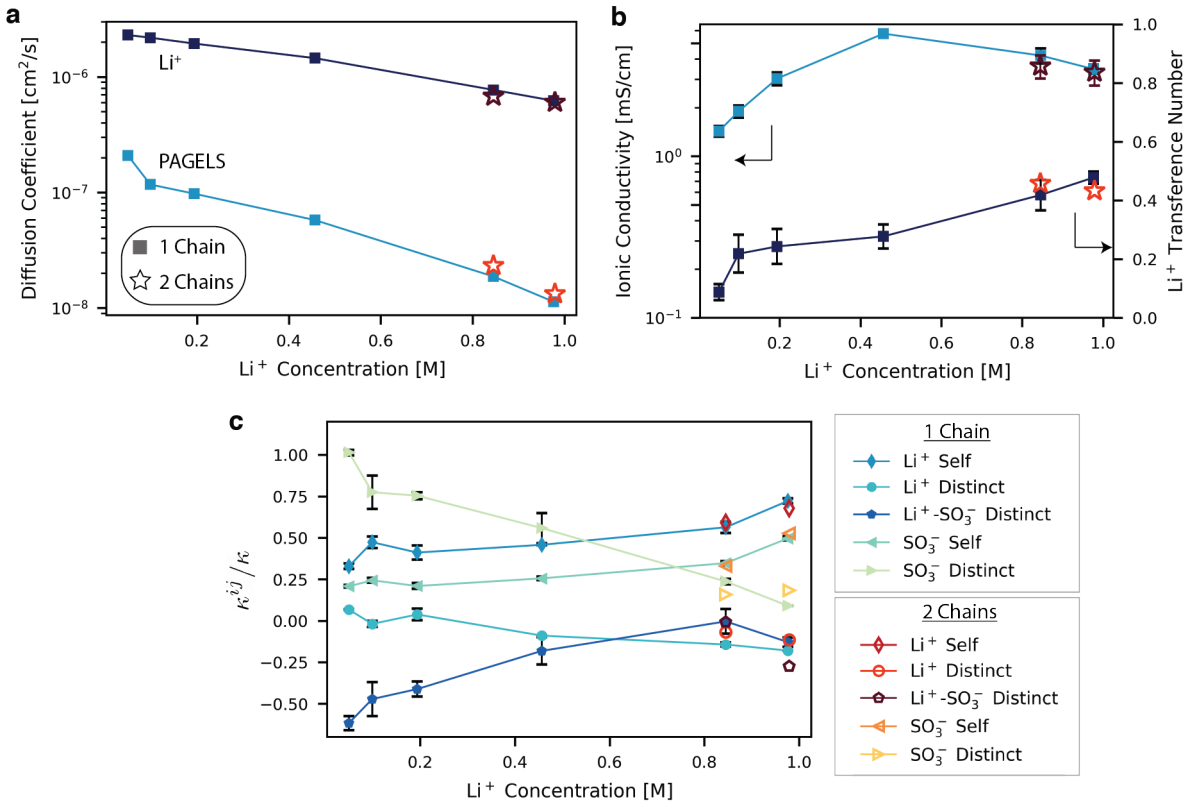

Figure B.1: Transport data for simulations using one versus two polymer chains at the two highest concentrations studied. (a) Diffusion coefficients. (b) Ionic conductivity and transference number. (c) Fractional contributions of each type of uncorrelated (self) or correlated (distinct) ion motion to the total conductivity.

factor of 0.7 to account for the fact that ion-ion interactions are typically overestimated in non-polarizable force fields [247].

Data analysis

Trajectories were analyzed using in-house code built with the help of the software MDAnalysis [249, 250].

Ion speciation

Free lithium ions, solvent-separated ion pairs (SSIPs), and contact ion pairs (CIPs) or larger aggregates (AGG) were identified from the cation-anion (Li^+-S (SO_3^-)) radial distribution functions (RDFs), plotted for each concentration in Figure B.2. A lithium ion is considered

part of a CIP or AGG if there is at least one sulfonate anion, specifically the sulfur atom, within the cutoff distance defined by the minimum after the first peak in the Li^+-S (SO_3^-) RDF (4.5 Å for all concentrations). SSIPs were defined analogously using the minimum after the second RDF peak (9.5-9.7 Å), and free lithium ions were those without any anions within the SSIP or CIP cutoff distances. Analysis of larger aggregate structures was undertaken with the aid of the Python package NetworkX [254], and visualizations of the most common Li^+ solvation environments were generated using the software Cytoscape [255].

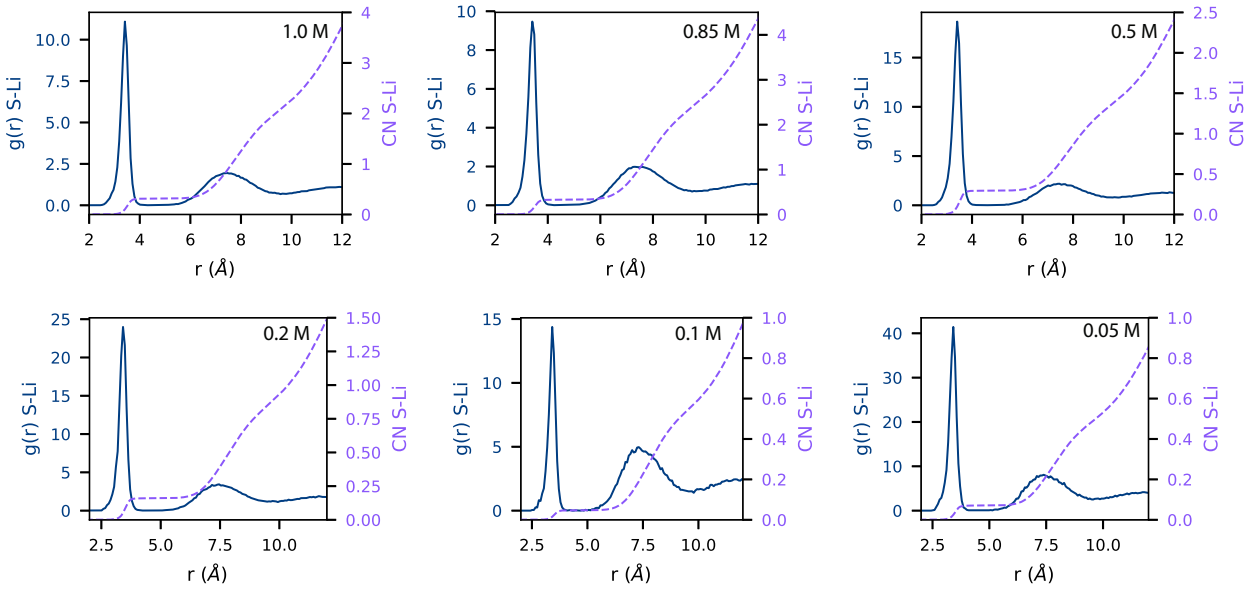

Figure B.2: Lithium-sulfur (SO_3^-) radial distribution functions (left axis) and coordination numbers (right axis) at each concentration studied.

Polymer conformation

Polyelectrolyte chain size was characterized using both the end-to-end distance as well as the radius of gyration, the latter of which is determined using [256]:

$$R_g^2 = \frac{1}{M}\left\langle \sum_{i=1}^{n} m_i \left| \boldsymbol{r}_i - \boldsymbol{r}_{\text{poly,cm}} \right|^2 \right\rangle \tag{B.1}$$

where n is the total number of atoms in the chain, M is the total mass of the polymer, m_i is the mass of atom i, $\boldsymbol{r}_i$ is the position vector of atom i, and $\boldsymbol{r}_{\text{poly,cm}}$ is the position vector of the polymer center of mass.

While a number of models exist to calculate the persistence length L_p of a polyelectrolyte chain [135, 257], the data presented in this work are calculated based on the orientational correlation function $G(l)$, which characterizes the orientational memory along the chain backbone [258]:

$$G(l) = \frac{1}{N_\mathrm{b} - l} \sum_{s=0}^{N_\mathrm{b}-l-1} \left\langle \boldsymbol{n}_s \cdot \boldsymbol{n}_{s+l} \right\rangle \tag{B.2}$$

Here $\boldsymbol{n}_s$ is the unit vector originating at backbone atom s and pointing along the polymer backbone, N_b is the total number of bonds in the polymer backbone, and l is the number of bonds separating unit vectors $\boldsymbol{n}_s$ and $\boldsymbol{n}_{s+l}$. The angular brackets denote an average of all chain conformations over time. To convert this orientational correlation function into a persistence length, it has been recently suggested that $G(l)$ should be fit to a biexponential function [258–260],

$$G(l) = (a) \exp\left(- \frac{|l|}{L_\mathrm{p}} \right) + (1 - a) \exp\left(- \frac{|l|}{L_\mathrm{short}} \right) \tag{B.3}$$

which is in good qualitative agreement with our calculated $G(l)$ functions. The first exponential decay constant, L_p, is the total persistence length of the chain, which is the sum of the intrinsic persistence length of the uncharged chain as well as the electrostatic persistence length. It is this L_p value which is the subject of our analysis in this work. The decay constant of the second exponential, L_short, describes additional orientational correlations present at short length scales, and a is an additional fitting parameter [261].

Diffusion coefficients

Diffusion coefficients of lithium ions and the polyelectrolyte center of mass were calculated based on the mean-square displacement (MSD, $\langle \Delta r(t)^2 \rangle$),

$$\langle \Delta r(t)^2 \rangle = \frac{1}{N} \left\langle \sum_{i=1}^{N} \left| \boldsymbol{r}_i(t) - \boldsymbol{r}_i(0) \right|^2 \right\rangle \tag{B.4}$$

where N is the total number of atoms/molecules and $\boldsymbol{r}_i(t)$ is the position vector of species i at time t relative to the center of mass of the entire system (included to correct for any drift in the center of mass of the simulation box). The angular brackets indicate the average over all time origins within the trajectory. From the MSD, the Einstein relation can be used to compute the self-diffusion coefficient D:

$$D = \frac{1}{6} \lim_{t \to \infty} \frac{d}{dt} \langle \Delta r(t)^2 \rangle \tag{B.5}$$

For an equilibrated system at sufficiently long simulation times, the system should be in the diffusive regime such that the MSD curve is linear with respect to time. That is, $\langle \Delta r(t)^2 \rangle \propto$

t^β, with $\beta = 1$. We ensure that all simulations in this work are run sufficiently long to achieve this linear behavior: we calculate average β values of 0.97 for Li^+ (ranging from 0.95 to 1.01) and 0.98 for the polyion center of mass (ranging from 0.87 to 1.06). Note that the statistics for the polymer are slightly inferior to that of the lithium ion: for Li^+ we average over all 43 ions in the system, which cannot be done for our single polymer chain. Nevertheless, our ranges of β are commonly accepted to be sufficiently linear for diffusion coefficient analysis [262]. Figure B.3a demonstrates this linear behavior for both the lithium ions and polymer for a representative simulation.

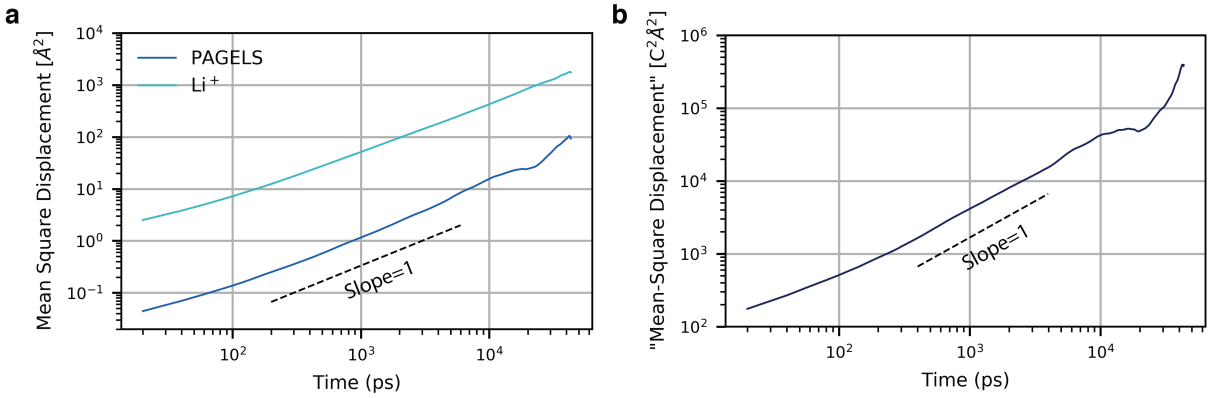

Figure B.3: Representative examples of the linear behavior required to calculate (a) diffusion coefficients and (b) ionic conductivity. A slope of one (corresponding to linear data on a log-log plot) is indicated on each plot. The effective "mean square displacement" on the y-axis of panel (b) is the quantity in angular brackets in Eq. (B.6). Data for these plots was for the system at a concentration of 0.85 M.

Note that data for our trajectory analysis has been collected every 20 ps. As a result, any non-Fickian diffusive processes present at very short times are not clearly shown in the MSD curve of Figure B.3a. As noted in previous MD simulations of polyelectrolytes, at short times we expect to see a ballistic regime with a log-log slope of 2, followed by a sub-diffusive regime with a slope less than one before finally reaching the Fickian regime with a log-log slope of one [192]. To demonstrate that we do indeed observe these phenomena, we have performed a simulation collecting data every 10 fs and plotted the polymer center of mass MSD data in Figure B.4.

Ionic conductivity

Ionic conductivity κ can be calculated from the following relation:

$$\kappa = \frac{1}{6k_\mathrm{B}TV} \lim_{t\to\infty} \frac{d}{dt} \left\langle \sum_i \sum_j q_i q_j [\boldsymbol{r}_i(t) - \boldsymbol{r}_i(0)] \cdot [\boldsymbol{r}_j(t) - \boldsymbol{r}_j(0)] \right\rangle \tag{B.6}$$

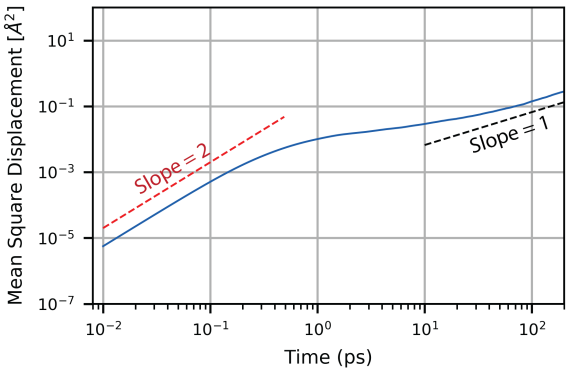

Figure B.4: Short-time behavior of the polymer center of mass mean-square displacement for the system at a concentration of 0.85 M.

where q_i is the charge of species i, $k_\mathrm{B}T$ is the thermal energy, and V is volume. This Einstein relation is derived from the Green-Kubo equation relating ionic conductivity with the microscopic charge current (Eq. (4.55)), derived in Section 4.3.

As is the case with diffusion coefficient calculations, a mathematically rigorous analysis of the conductivity requires the term enclosed in the angular brackets of Eq. (B.6) to be linear in time. The simulations performed here all reached the linear regime, with β values (defined as the extent of linearity analogously to the diffusion coefficient analysis above) between 0.84 and 1.04 for all concentrations. Results from a representative simulation are shown in Figure B.3b.

The ionic conductivity can be decomposed into separate terms, each corresponding to a different type of uncorrelated or correlated ion motion, namely the cation-self ($\kappa^{++}_\mathrm{self}$), anion-self ($\kappa^{--}_\mathrm{self}$), cation-distinct ($\kappa^{++}_\mathrm{distinct}$), anion-distinct($\kappa^{--}_\mathrm{distinct}$), and cation-anion-distinct (κ^{+-}) conductivities (see Eq. (5.4)). As described in Chapter 5, these partial conductivities may be directly related to the Onsager transport coefficients by $L^{ij} = \frac{\kappa^{ij}}{z_i z_j F^2}$; thus they may be computed using the Green-Kubo relations for L^{ij}. In this section, we use the form of these relations as presented in Eq. (4.1), which make use of the particle positions rather than velocities. Due to challenges in reaching the linear regime for some of these self- and distinct-conductivity terms, the derivatives in Eq. (4.1) were approximated by finite difference at $t = 2$ ns and $t = 0$ ns. Note that averaging is performed over all time origins in the trajectory (as denoted by the angular brackets in these equations). Hence the analysis averages the system behavior for all time differences of 2 ns within the entire 40 ns simulation. It was ensured that the choice of upper time bound in the finite difference calculation did not appreciably affect any trends as a function of concentration.

Diffusion mechanism

The diffusion mechanism of species i relative to species j (i.e. structure-diffusion versus vehicular motion) was evaluated by calculating the lifetime correlation function, $P_{ij}(t)$ [145, 146]:

$$P_{ij}(t) = \left\langle H_{ij}(t) H_{ij}(0) \right\rangle \tag{B.7}$$

Here $H_{ij}(t)$ is one if i and j are neighbors at time t and zero otherwise. Two species are considered neighbors if they are within a given cutoff distance. In this work, we calculate $P_{ij}(t)$ for three species pairs: Li^+-O (DMSO), Li^+- S (SO_3^-), and S (SO_3^-)-O (DMSO). The cutoff distance for these pairs was defined as the minimum after the first peak of the RDF to capture the first coordination shell. Additionally, the lifetime correlation function of lithium relative to sulfonate anions in the second coordination shell (i.e. solvent-separated ion pairs) was calculated by deeming two ions neighbors if the distance between them is between the first and second minima of the Li^+-S (SO_3^-) RDF.

The lifetime correlation function P_{ij} is subsequently converted into a residence time τ_{ij} of i and j neighbor pairs via a biexponential fit [263]:

$$P_{ij}(t) = \alpha \exp\left(\frac{-t}{\tau_{ij}}\right)^{\delta} + (1-\alpha)\exp\left(\frac{-t}{\tau_{ij,\text{short}}}\right) \tag{B.8}$$

where τ_{ij}, $\tau_{ij,\text{short}}$, α, and δ are fitting parameters. The first term in this expression gives the relevant residence time for inferring diffusion mechanisms, while the second term can be attributed to sub-diffusive processes at shorter timescales. The parameter δ varies between 0 and 1, with deviations from unity corresponding to the presence of multiple modes of diffusion with different timescales [264]. Here we observe $\delta > 0.99$ for all pairs of species, with the exception of Li^+- S (SO_3^-) (CIP), where δ varied between 0.8 and 1.

Finally, this residence time is expressed as a characteristic diffusion length $\mathcal{L}_{ij}$ by incorporating the diffusion coefficient of the solvent:

$$\mathcal{L}_{ij} = \sqrt{6 D_{\text{solvent}} \tau_{ij}} \tag{B.9}$$

This conversion corrects for the effect of changing overall solution viscosity across concentrations, enabling accurate comparison of diffusion mechanisms.

Error analysis

Statistical error values were obtained through a combination of independent simulation replicates and time averaging of individual simulations. Note that these are statistical errors due to the inherently limited sampling of an MD simulation, not errors arising from the model itself such as the choice of force field parameters.

The majority of the error data reported herein are obtained through block averaging [68, 265, 266]. For a given dynamical quantity, such as the fraction of free Li^+ ions or the polymer radius of gyration, we can calculate the statistical uncertainty of the average

value by computing the variance of multiple statistically independent observations of the quantity. Simply evaluating the variance of the data at every snapshot of the trajectory will underestimate the true error due to the inherent correlations within the system. Thus, to calculate the true statistical error, we must split the simulations into uncorrelated blocks, then compute the mean value of our quantity of interest for each block. Our final estimate of the uncertainty is then the standard deviation of these blocked averages (including both those from the same simulation as well as those from the independent duplicate run). The block length which yields uncorrelated data is not known a priori, so the error is analyzed over a range of block lengths. When the error becomes independent of block length, a suitable block length has been reached such that each block is uncorrelated from the rest.

Block averaging could not be performed for some quantities of interest (the self- and distinct-conductivities as well as the ion aggregate size distributions) due to poor statistics; proper fits to the data could only be obtained using the full 40 ns trajectory. For these quantities, the reported error bars are the standard deviation of the two independent 40 ns duplicates.

B.3 Methods associated with Chapter 6[3]

Coarse-grained polyelectrolyte model

Polyanions were represented by the Kremer-Grest bead-spring chain model [169, 170]. Adjacent beads, each representing one monomer, interacted via finitely extensible nonlinear elastic (FENE) bonds, where interaction energies take the form

$$U_{\mathrm{FENE}}(r) = -0.5KR_0^2 \ln\left[1 - \left(\frac{r}{R_0}\right)^2\right]. \tag{B.10}$$

Here r is the distance between two monomers, the spring constant $K = 30\ \varepsilon/\sigma^2$, and the maximum extension of the bond $R_0 = 1.5\ \sigma$. These bonding parameters yield an average bond length of $0.97\ \sigma$ and avoid unphysical crossing of bonds [191, 267].

Counterions and solvent molecules were modeled explicitly as charged and neutral beads, respectively. Although it increases the computational cost of the simulations, including explicit solvent has been shown in several works to be crucial for accurately capturing dynamics in the solution [268–270]. All particles (monomers, cations, and solvent) were subject to a truncated-shifted Lennard-Jones (LJ) potential to account for excluded volume,

$$U_{\mathrm{LJ}}(r) = \begin{cases} 4\varepsilon_{\mathrm{LJ}}\left[\left(\frac{\sigma_{\mathrm{LJ}}}{r}\right)^{12} - \left(\frac{\sigma_{\mathrm{LJ}}}{r}\right)^{6} - \left(\frac{\sigma_{\mathrm{LJ}}}{r_{\mathrm{cut}}}\right)^{12} + \left(\frac{\sigma_{\mathrm{LJ}}}{r_{\mathrm{cut}}}\right)^{6}\right] & r \le r_{\mathrm{cut}} \\ 0 & r > r_{\mathrm{cut}} \end{cases}. \tag{B.11}$$

[3]This section is closely adapted from Ref [163]: Fong, K. D., Self, J., McCloskey, B. D. & Persson, K. A. Onsager transport coefficients and transference numbers in polyelectrolyte solutions and polymerized ionic liquids. *Macromolecules* **53**, 9503–9512 (2020).

For all interactions, $\varepsilon_{\mathrm{LJ}} = \varepsilon$ (the LJ unit of energy) and $\sigma_{\mathrm{LJ}} = \sigma$, where σ is the LJ unit of distance and the diameter of each of the beads in the system. We choose $r_{\mathrm{cut}} = 2^{1/6}\sigma$, which yields good solvent conditions [123]. All species are given unit mass.

Cations and (poly)anions were additionally subject to the Coulomb potential,

$$U_{\mathrm{Coulomb}}(r) = \frac{z_i z_j e^2}{4\pi\epsilon_0\epsilon_{\mathrm{r}} r} = k_{\mathrm{B}}T\frac{l_{\mathrm{B}} z_i z_j}{r} \ , \tag{B.12}$$

where e is the elementary charge, ϵ_0 is the vacuum permittivity, ϵ_{r} is the dielectric constant of the medium, and z_i is the charge of species i. Each cation was assigned $z_+ = +1$ and each monomer was given $z_- = -1$. The quantity $l_{\mathrm{B}} = e^2/(4\pi\epsilon_0\epsilon_{\mathrm{r}}k_{\mathrm{B}}T)$ is the Bjerrum length, which defines the length scale at which the energy of electrostatic interactions is equal to the thermal energy, $k_{\mathrm{B}}T$. As the simulations in this work capture a wide range of polymer concentrations (from the semi-dilute regime to the limit of a solvent-free system), the dielectric constant was varied linearly as a function of fraction of solvent [271]. The lower limit of the dielectric constant, corresponding to a system with only solvent, was chosen to mimic the dielectric properties of water with a Bjerrum length of 7.1 Å. We follow the common procedure [123, 269] of mapping the average distance between polymers beads, 0.97 σ, to the size of a polystyrene sulfonate monomer, 2.5 Å, which yields a Bjerrum length of $l_{\mathrm{B}} = 7.1$ Å $\times$ (0.97 σ/2.5 Å) = 2.75 σ. The upper limit of the Bjerrum length for the system with no solvent was chosen to be 30 σ, in the range commonly chosen to study melts of charged polymers [121, 191].

Note that with the length scale mapping of 2.5 Å $\approx$ 0.97 σ, the ion concentrations simulated in this work (0.001, 0.005, 0.01, and 0.05 σ^{-3}) can be roughly mapped to concentrations of 0.1, 0.48, 0.97, and 4.8 M.

Simulation details

Polymer chains were initially prepared using a self-avoiding random walk. The polymers, cations, and solvent particles were randomly packed into a cubic simulation box using PACKMOL [245] at a density of 0.8 σ^{-3}, a value in the range commonly used to study both dilute polyelectrolyte solutions as well as polymer melts [121,191,192,272–274]. With the exception of the systems at the lowest concentration studied, 0.001 σ^{-3}, each simulation consisted of approximately 40,000 particles, with the exact number varied slightly to precisely reach the target concentration. It was verified that doubling the number of particles in the simulation box did not have any appreciable effect on the computed transport properties. At 0.001 σ^{-3}, however, finite size effects were more pronounced due to the smaller number of polymer chains in the system and the larger charge screening length. Simulations at this concentration were run with 80,000 particles, with one run using 120,000 particles verifying that there were no appreciable finite size effects with this larger box size. The systems with the longest chain length ($N = 25$) had 4, 10, 20, and 100 polymer chains for concentrations of 0.001, 0.005, 0.01, and 0.05 σ^{-3}, respectively.

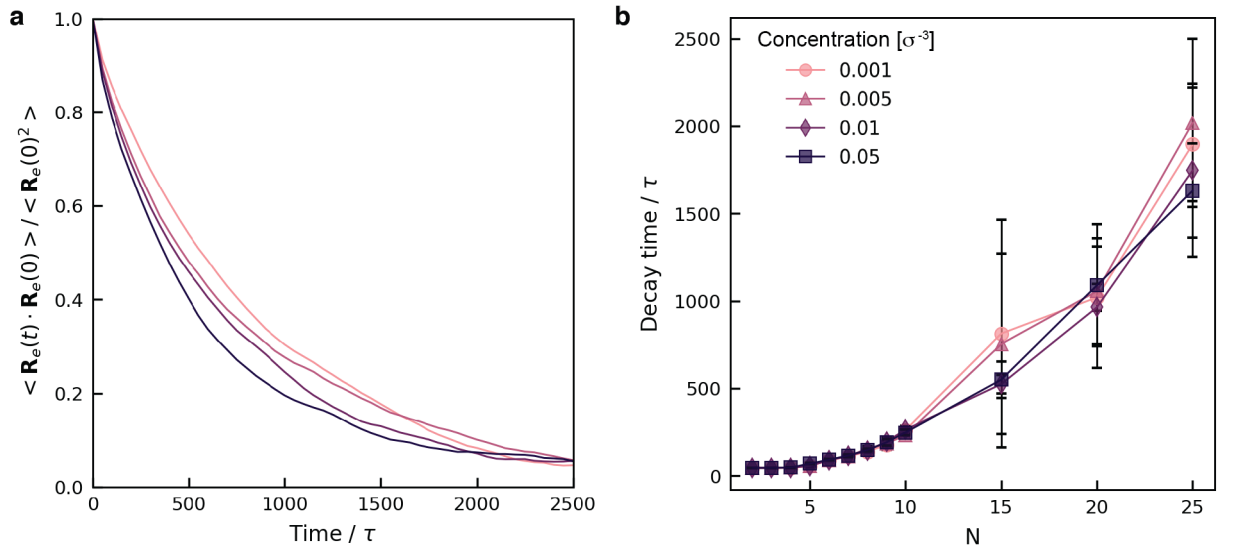

Figure B.5: End-to-end vector analysis. (a) End-to-end vector autocorrelation functions for $N = 25$ at each concentration. (b) Decay times of the end-to-end vector autocorrelation functions (defined as the time to reach a value of 0.1).

Molecular dynamics (MD) simulations were performed using the LAMMPS code [243, 244]. The as-prepared system was equilibrated using a conjugate gradient energy minimization. Simulations were run for a total of 10^7 steps, with a time step of 0.005 τ. The first 4×10^5 steps (2000 τ) were considered to be an equilibration period and not used for data analysis. This equilibration period was long enough for the polymer end-to-end vector autocorrelation function to decay to less than 0.1 for all systems (Figure B.5), suggesting that there were minimal effects of the initial system configuration by the time data collection began. We further confirmed that the polymers' radii of gyration and the total system energy had stabilized by the end of the equilibration period.

The equations of motion were numerically integrated using the velocity-Verlet algorithm, with periodic boundary conditions in all three spatial directions. A Nosé-Hoover style thermostat was used to maintain the temperature of the system at $k_\mathrm{B}T/\varepsilon = 1$. Long-range Coulombic interactions were evaluated using the PPPM method [248].

Data analysis

Transport coefficients were computed using Eq. (4.1):

$$L^{ij} = \frac{1}{6k_\mathrm{B}TV} \lim_{t\to\infty} \frac{d}{dt} \Big\langle \sum_\alpha [\boldsymbol{r}_i^\alpha(t) - \boldsymbol{r}_i^\alpha(0)] \cdot \sum_\beta [\boldsymbol{r}_j^\beta(t) - \boldsymbol{r}_j^\beta(0)] \Big\rangle.$$

The angular brackets denote averaging over all time origins within the trajectory. The self terms L^{ii}_{self} (and thus the diffusion coefficients, by Eq. (4.5)) are computed in an analogous manner using Eq. (4.3), and the distinct terms were computed by $L^{ii}_{\text{distinct}} = L^{ii} - L^{ii}_{\text{self}}$. All experimentally-relevant quantities such as the transference number were computed from L^{ij} using Eqs. (4.53)-(4.59).

In order to capture true diffusive transport, the term in angular brackets of Eqs. (4.1) or (4.3) must be linear with respect to time, i.e. $\left\langle \sum_\alpha [\boldsymbol{r}_i^\alpha(t) - \boldsymbol{r}_i^\alpha(0)] \cdot \sum_\beta [\boldsymbol{r}_j^\beta(t) - \boldsymbol{r}_j^\beta(0)] \right\rangle \propto t^\beta$ and $\sum_\alpha \left\langle [\boldsymbol{r}_i^\alpha(t) - \boldsymbol{r}_i^\alpha(0)]^2 \right\rangle \propto t^\beta$, with $\beta = 1$. For most simulations in this work, β was computed to be between 0.94 and 1.05, with analysis performed over at least a decade of time. This suggests that the simulations have been run long enough to reach and adequately sample the diffusive regime. Representative data demonstrating this linear behavior is given in Fig. B.6. There are a two classes of exceptions in which β deviates more substantially from unity. The first is for L^{+-} in the monomer simulations ($N = 1$) at the three lowest concentrations studied, in which case β became as low as 0.84. This deviation from linearity is due to the small overall magnitude of L^{+-}, which results in more noise in the fitting procedure. As $L^{+-} \approx 0$ for these systems, the fact that we do not observe linear behavior does not impact any of our conclusions. The second case where β departs from unity is for L^{--}_{self} in the solvent-free systems for chain lengths of 15, 20, and 25, where β reached as low as 0.73. This sub-diffusive behavior can be attributed to anion motion corresponding to intra-chain degrees of freedom, such as chain rotations. While the values of L^{--}_{self} for these three chain lengths presented in Fig. 6.8 can not be rigorously interpreted as transport coefficients due to this deviation from linearity, this does not affect any of the conclusions drawn in this work.

The extent of ion pairing as shown in Figure 6.6a was evaluated using a distance criterion: all cations within a given cutoff distance of any anion were considered paired. This cutoff distance was chosen as the first minimum of the cation-anion radial distribution function (1.6 σ, see Figure B.7), which was consistent across all chain lengths and concentrations. The residence times of ion pairs given in Figure 6.6b were evaluated by computing the lifetime correlation function $P_{\alpha\beta}(t) = \left\langle H_{\alpha\beta}(t) H_{\alpha\beta}(0) \right\rangle$, where $H_{\alpha\beta}(t)$ is one if particles α and β are neighbors at time t and zero otherwise [86,145,146,172]. Two particles are deemed neighbors if they fall within a distance cutoff, chosen based on the radial distribution function to be 2.5 σ to coincide with the minimum after the second solvation shell of the ions. This distance cutoff was larger than that used for the static evaluation of ion pairing, as we observed that ions moved very frequently back and forth between the first and second solvation shells. The residence time was defined as the time for $P_{\alpha\beta}(t)$ to decay to 10% of its original value.

Error bars throughout this text are given as the standard deviation of five independent replicates. Trajectories were analyzed using an in-house code which utilized the Python package MDAnalysis [249, 250]. Code is available at
`https://github.com/kdfong/transport-coefficients-MSD`.

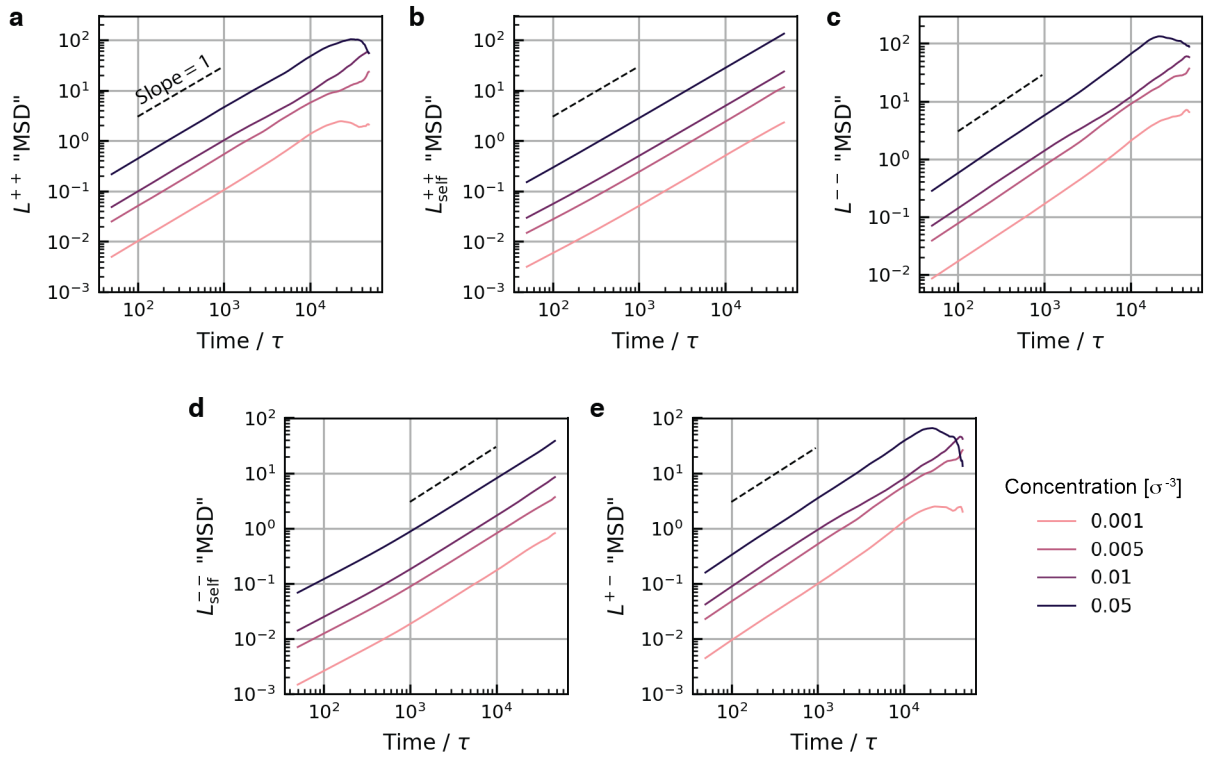

Figure B.6: Representative examples of data used to compute L^{ij} and L^{ii}_{self} using Eqs. (4.1) and (4.3), respectively. The quantity plotted is $\left\langle \sum_\alpha [\boldsymbol{r}_i^\alpha(t) - \boldsymbol{r}_i^\alpha(0)] \cdot \sum_\beta [\boldsymbol{r}_j^\beta(t) - \boldsymbol{r}_j^\beta(0)] \right\rangle$ for computing L^{ij} or $\sum_\alpha \left\langle [\boldsymbol{r}_i^\alpha(t) - \boldsymbol{r}_i^\alpha(0)]^2 \right\rangle$ for L^{ii}_{self}. Data for these plots is for a chain length of $N = 10$.

Analyzing monomer vs polymer motion

When computing the anion transport coefficients (L^{--} and L^{+-}) in a polyelectrolyte, we may treat either the polymer chain as a whole or individual monomers as the anionic species. The analysis presented in Chapters 5 and 6 uses the latter convention. In this section, we describe the relationship between the transport coefficients obtained from using each choice and show how the experimentally-relevant quantities (with the exception of the Nernst-Einstein transference number) are equivalent regardless of the analysis method. We show how combining both choices of anionic species can be used to decouple correlations between ions within a given chain and those between ions on different chains (intra- versus inter-chain interactions).

Let us denote the transport coefficients obtained by treating individual monomers as the anion with a subscript "m", and those obtained using the whole polymer chain with a subscript "p". The transport coefficients presented in the main text are L^{ij}_{m}. In order to

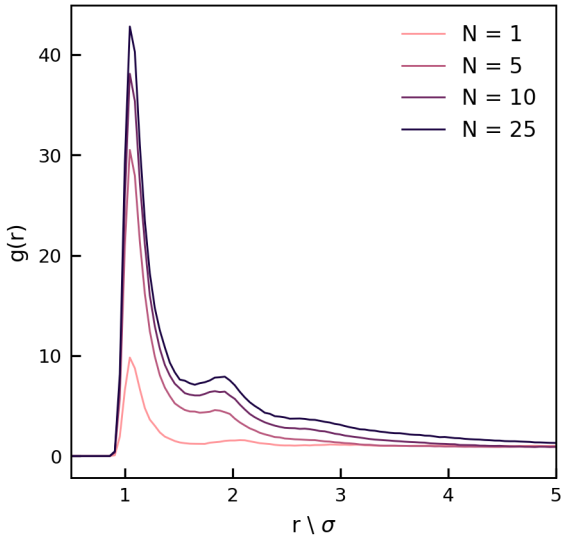

Figure B.7: Representative cation-anion radial distribution functions ($g(r)$) at a concentration of 0.01 σ^{-3} for four different chain lengths.

derive relations between L_{m}^{ij} and L_{p}^{ij}, we begin by writing the Green-Kubo relation for L_{p}^{--} as

$$L_{\mathrm{p}}^{--} = \frac{1}{6k_{\mathrm{B}}TV} \lim_{t\to\infty} \frac{d}{dt} \Big\langle \sum_a [\boldsymbol{r}_a(t) - \boldsymbol{r}_a(0)] \cdot \sum_b [\boldsymbol{r}_b(t) - \boldsymbol{r}_b(0)] \Big\rangle. \tag{B.13}$$

Here we use the indices a and b to denote a sum over each polymer chain, whereas we use the indices α and β to denote individual monomers. The quantity $\boldsymbol{r}_a$ is the center-of-mass position of the chain relative to the center of mass of the entire system, which can be written as $\boldsymbol{r}_a = \frac{1}{N}\sum_\alpha \boldsymbol{r}_a^\alpha$, noting that the masses of all monomers are equal. The quantity $\boldsymbol{r}_a^\alpha$ is the position (relative to the center of mass of the entire system) of monomer α on chain a. Equation (B.13) may be written in terms of individual monomer positions as

$$L_{\mathrm{p}}^{--} = \frac{1}{6k_{\mathrm{B}}TVN^2} \lim_{t\to\infty} \frac{d}{dt} \Big\langle \sum_a \sum_\alpha [\boldsymbol{r}_a^\alpha(t) - \boldsymbol{r}_a^\alpha(0)] \cdot \sum_b \sum_\beta [\boldsymbol{r}_b^\beta(t) - \boldsymbol{r}_b^\beta(0)] \Big\rangle. \tag{B.14}$$

Comparing to Eq. (4.1) in the main text, we can conclude that

$$L_{\mathrm{p}}^{--} = \frac{1}{N^2} L_{\mathrm{m}}^{--} \ . \tag{B.15}$$

Similar arguments allow us to relate L_{p}^{+-} and L_{m}^{+-} via

$$L_{\mathrm{p}}^{+-} = \frac{1}{N} L_{\mathrm{m}}^{+-} \ . \tag{B.16}$$

We can also relate the self anion transport coefficients, $L^{--}_{\mathrm{m,self}}$ and $L^{--}_{\mathrm{p,self}}$, by assuming that the self-diffusion coefficients of the polymer and monomer will be identical over long enough time scales, i.e., $D_{-,\mathrm{p}} = D_{-,\mathrm{m}}$. Further, note that the concentrations of polymer and monomer are related by by $c_m = Nc_p$. Using Eq. (4.5) of the main text, we can thus conclude that

$$L^{--}_{\mathrm{p,self}} = \frac{1}{N} L^{--}_{\mathrm{m,self}} \ . \tag{B.17}$$

As mentioned in the main text, the distinct anion transport coefficients obtained from analyzing monomer motion, $L^{--}_{\mathrm{m,distinct}}$, captures two forms of anion-anion correlations: those between anions on the same chain (intra-chain) and those between anions on different chains (inter-chain), i.e., $L^{--}_{\mathrm{m,distinct}} = L^{--}_{\mathrm{m,inter-chain}} + L^{--}_{\mathrm{m,intra-chain}}$. In contrast, the distinct anion transport coefficient from analyzing polymer center-of-mass motion gives only inter-chain correlations: $L^{--}_{\mathrm{p,distinct}} = L^{--}_{\mathrm{p,inter-chain}}$. Thus, if we seek to compare the relative magnitude of inter- and intra-chain correlations, we may compute $L^{--}_{\mathrm{m,inter-chain}} = N^2 L^{--}_{\mathrm{p,distinct}}$ and $L^{--}_{\mathrm{m,intra-chain}} = L^{--}_{\mathrm{m,distinct}} - L^{--}_{\mathrm{m,inter-chain}}$. These data are shown in Figure 6.2.

Using Eqs. (B.15) and (B.16), it is easy to demonstrate that the ionic conductivity, cation and anion mobilities, and transference number are equivalent regardless of whether the motion of the monomer (L^{ij}_{m}) or polymer center of mass (L^{ij}_{p}) is analyzed. Doing so requires us to note that the charge valencies of the polymer and monomer are related by the degree of polymerization N, i.e., $z_{\mathrm{p}} = Nz_{\mathrm{m}}$. For example, by Eq. (4.53) the conductivity is

$$\begin{aligned}
\kappa &= F^2 \sum_i \sum_j L^{ij} z_i z_j = F^2 (L^{++} z_+^2 + L^{--}_{\mathrm{p}} z_{\mathrm{p}}^2 - 2L^{+-}_{\mathrm{p}} z_+ z_{\mathrm{p}}) \\
&= F^2 (L^{++} z_+^2 + (L^{--}_{\mathrm{m}}/N^2)(Nz_{\mathrm{m}})^2 - 2(L^{+-}_{\mathrm{m}}/N) z_+ (Nz_{\mathrm{m}})) \\
&= F^2 (L^{++} z_+^2 + L^{--}_{\mathrm{m}} z_{\mathrm{m}}^2 - 2L^{+-}_{\mathrm{m}} z_+ z_{\mathrm{m}}) \ .
\end{aligned} \tag{B.18}$$

The only experimentally-relevant quantity which will change depending on whether we treat the monomer or polymer as the anionic species is $t_+^{\mathrm{NE}} = \frac{z_+ D_+}{z_+ D_+ - z_- D_-}$. The diffusion coefficients of the cation and anion will be equivalent regardless of whether the monomer or polymer center of mass is considered, but the anionic charge valence z_- will change. Using L^{ij}_{p} corresponds to including $z_- = -N$ in the equation, which will yield the t_+^{NE} values shown in Figure 6.4b, whereas with L^{ij}_{m}, $z_- = -1$ should be used, as in Figure 6.4c. As analyzing polymer center-of-mass motion implicitly captures intra-chain correlations, $t_+^{\mathrm{NE}}(z_- = -N)$ will provide a much more reasonable estimate for the true cation transference number than $t_+^{\mathrm{NE}}(z_- = -1)$, as is clear from Figure 6.4.